



PhD thesis

Development of Novel Methods for PET- Based Quantification of Drug Interactions in the Living Human Brain

Gjertrud Louise Laurell

Principal supervisor: Gitte Moos Knudsen

This thesis has been submitted to the Graduate School of the Faculty of Health and Medical Sciences, University of Copenhagen January 2, 2023

SUPERVISORS

Prof. Gitte Moos Knudsen
Neurobiology Research Unit,
Copenhagen University Hospital Rigshospitalet

Prof. R. Todd Ogden
Department of Biostatistics,
Columbia University

Dr. Martin Schain
Antaros Medical

Dr. Claus Svarer
Neurobiology Research Unit,
Copenhagen University Hospital Rigshospitalet

Dr. Pontus Plavén Sigray
Neurobiology Research Unit,
Copenhagen University Hospital Rigshospitalet

ASSESSMENT COMMITTEE

Prof. Henrik Bo Wiberg Larsson
Department of Clinical Medicine
University of Copenhagen

Prof. Ronald Boellaard
Department of Radiology and Nuclear Medicine
VU University Medical Center Amsterdam

Dr. Gaia Rizzo
Invicro

SUBMITTED

January 2nd, 2023.

DEFENSE

March 10th, 2023.

Cover page artwork by Terje Stenhaug (1949 – 2014).

I've got your dreams completely
I've got them locked away
That doesn't mean I own you
Or control a hair of your sweet head
— *I'll be your Pilot*, Belle & Sebastian

Grown-ups never understand anything by themselves, and it is
tiresome for children to be always and forever explaining things to
them.

— Antoine de Saint-Exupéry, *The Little Prince*

To Tarjei & Skule.

PREFACE

The work presented in this thesis was carried out at the Neurobiology Research Unit, Copenhagen University Hospital Rigshospitalet, between April 2019 and December 2022. In that period, the author, Gjertrud Louise Laurell, was employed, first as a research assistant, and later as a graduate student. The project was on hold for eight months between March and November 2021, while the author was on parental leave. The author has been enrolled as a PhD student in the Graduate Program in Neuroscience, at the Graduate School of Health and Medical Science, University of Copenhagen, since November 2020.

PUBLICATIONS

The following is a list of the papers that are included in the thesis. Throughout the text, they will be referred to by their roman numerals, as listed here.

- I **Gjertrud Louise Laurell**, Pontus Plavén-Sigra, Aurelija Jucaite, Andrea Varrone, Kelly P. Cosgrove, Claus Svarer, Gitte Moos Knudsen, Karolinska Schizophrenia Project Consortium, R. Todd Ogden, Francesca Zanderigo, Simon Cervenka, Ansel T. Hillmer, Martin Schain. Nondisplaceable binding is a potential confounding factor in ^{11}C -PBR28 translocator PET studies. *The Journal of Nuclear Medicine*. 2021; 62:412-417.
- II **Gjertrud Louise Laurell**, Pontus Plavén-Sigra, Claus Svarer, R. Todd Ogden, Gitte Moos Knudsen, Martin Schain. Designing drug occupancy studies with PET neuroimaging: Sample size, occupancy ranges and analytical methods. *NeuroImage*. 2022; 263:119620.
- III **Gjertrud Louise Laurell**, Pontus Plavén-Sigra, Annette Johansen, Nakul Ravi Raval, Arafat Nasser, Clara Aabye Madsen, Jacob Madsen, Hanne Demant Hansen, Lene Lundgaard Donovan, Gitte Moos Knudsen, Adriaan A. Lammertsma, R. Todd Ogden, Claus Svarer, Martin Schain. Kinetic Models for PET Displacement Studies. *In review at the Journal of Cerebral Blood Flow and Metabolism*.

All manuscripts can be found in the Appendix, where they are included in the same order as they are presented in the list above.

SUMMARY

Positron emission tomography (PET) is a medical imaging technique with a wide range of applications across several medical fields. By using radioactively labelled molecules (radiotracers), it is possible to map out and quantify biological processes.

In drug development and discovery, PET can aid in understanding the distribution and binding strength of a drug. By using a PET radiotracer that binds to the same target as the drug, and collecting data both before and after the drug is administered, it is possible to quantify occupancy (i. e. the fraction of targets that were bound by the drug).

The overarching goal of the PhD project was to improve the utility of PET for quantification of drug interactions in the brain. Throughout the project, common assumptions concerning both data analysis and study design were assessed. Further, new analytical methods are presented and evaluated.

In the first paper, the main question was whether the nondisplaceable (i. e. not bound to the intended target) component could be a confounding factor when making between-group comparisons of total binding. By estimating the non-displaceable uptake in four datasets with the PET tracer [^{11}C]PBR28, we found that both the alcohol use disorder and Parkinson's disease groups had significantly lower nondisplaceable uptake than their respective controls. While this study does not directly relate to estimation of occupancy, estimation of the nondisplaceable binding is closely linked to estimation of occupancy. Between-group differences in nondisplaceable binding will have confounding effects on both V_T and BP_{ND} , the two most frequently reported outcome measures from dynamic PET.

For the two other papers, the main emphasis has been on the estimation of drug interaction parameters. The goal of paper II was to provide data to guide the design of baseline-block PET studies. In this type of study, the goal is to quantify the occupancy of a drug by conducting two PET scans, one before, and one after administration of the drug. The observed difference in specific binding between the two scans represents the target occupancy in the post-drug scan. In a simulation framework based on the PET tracer [^{11}C]Cimbi-36, we evaluated the effect of the range of doses, number of included subjects, and choice of analytical method, on the accuracy of IC_{50} estimated from V_T . IC_{50} is the half-maximal inhibitory concentration, a measure of the binding strength of the drug. We evaluated the performance of two already established analytical methods: the Lassen plot and LEO. In addition, we introduce LEA, a new method for calcula-

tion of IC_{50} directly from PET outcome measures. LEA, like LEO, is based on maximum likelihood estimation. Quantification of the dose-occupancy relationship was substantially improved when using these likelihood-based methods. The Lassen plot required approximately four times the number of subjects to be as informative as LEO and LEA. We also found that acquiring data points where subjects were administered drug doses corresponding to less than approximately 40% occupancy contributed negligibly to IC_{50} estimation.

In the final paper, the focus was on calculation of occupancy from PET scans with in-scan drug intervention. In this experimental setup, the drug is administered during an ongoing scan, instead of the two-scan baseline-block setup. Because the steady-state assumption that forms the basis of most PET kinetic models is violated in a displacement scan, new models must be developed to quantify the data. We present a new model for input function-based quantification of displacement scan data, and solve it using both a numeric approach and simplified analytical approach. The performance of the model is tested in [^{11}C]UCB-J-based simulations, and in pig scans, where [^{11}C]UCB-J was displaced by brivaracetam. We demonstrated that the one-scan setup is a viable alternative to baseline-block studies. In simulations, the model returned unbiased occupancy estimates with both approaches, and the dose-occupancy relationship established from the pig data was consistent both with results from the Lassen plot, and with previously published results.

DANSK RESUMÉ

Positron-emissionstomografi (PET) er en molekylær billeddannelses-teknik, som ved brug af radioaktive sporstoffer muliggør billeddannelse og kvantificering af molekylære og metaboliske processer i kroppen. Som billeddiagnostisk teknik anvendes PET især til diagnostik af kræft. I centralnervesystemet kan PET blandt andet bruges til at måle koncentrationen af tilgængelige receptorer. Dette har flere spændende anvendelsesmuligheder, både i klinikken, hvor det kan anvendes diagnostisk og i forskning, hvor det kan bidrage til en større forståelse af hjernens funktion hos raske og syge mennesker.

PET kan også bruges til at undersøge optagelsen og bindingen af lægemidler i hjernen. For eksempel kan man ved hjælp af et radioaktivt sporstof, der binder til samme målprotein som lægemidlet foretage PET-scanninger både før og efter administration, beregne forholdet mellem indgivet dosis og optagelse i hjernen. Dette er bl.a. meget anvendt ved udvikling og evaluering af nye lægemidler med effekt i hjernen. I løbet af de sidste par årtier anvendes PET derfor i stigende grad af lægemiddelindustrien, blandt andet for at bekræfte, at potentielle nye lægemidler binder sig til det tilsigtede mål med tilstrækkelig specificitet, og for at beregne hvilken dosis af lægemidlet, der mest hensigtsmæssigt anvendes.

Dette PhD-projekt omhandler udvikling og evaluering af kvantitative metoder til analyse af hjerne-PET-data. I den første artikel har vi ved at bruge en ny analysemetode på flere eksisterende PET-datasæt udfordret en af de grundlæggende antagelser i kvantitativ PET. I de sidste to artikler fokuseres på såkaldte okkupansstudier, hvor PET bruges til at beregne i hvor høj grad lægemidlet i hjernen. I disse to artikler har vi brugt både simulerede og empiriske data til at undersøge forskellige studiedesigns, samt evaluere eksisterende og nye analysemetoder.

I artikel I anvendes en ny analysemetode, der gør det muligt at udskille den del af det samlede PET-signal, der kommer fra specifik binding af radioliganden til målproteinet. Den resterende del af signalet kan komme fra enten ubundet radioligand eller ikke-specifikt radioligand bundet i blod eller væv; sidstnævnte benævnes sommetider som 'ikke-fortrængelig' binding. I PET-studier, der sammenligner resultater mellem grupper (f.eks. patienter og kontroller), er det almindeligt at antage, at den ikke-fortrængelige del af signalet er konstant, og at eventuelle forskelle skyldes forskelle i den specifikke binding. Men vi viser her for sporstoffet [^{11}C]PBR28 – som bruges som en markør for neurobetændelse – at både grupperne med

alkoholafhængighed og Parkinsons sygdom havde signifikant lavere ikke-fortrængeligt signal end raske kontroller.

I artikel II anvendes simulerede data til at evaluere aspekter af studiedesign samt flere forskellige metoder til at analysere data fra det traditionelle PET-okkupans design, hvor der PET-skannes ved baseline og igen efter indgift af lægemidlet. Ved at simulere det samme undersøgelsesdesign 1000 gange kan vi påvise, hvordan selv små ændringer i eksempelvis antal af forsøgspersoner påvirker nøjagtigheden og præcisionen af de estimerede parametre. Disse resultater kan bidrage til planlægningen af fremtidige studier. Artikel II lancerer også en helt ny analysemetode, baseret på maximum likelihood-metoder. Maximum likelihood er en statistisk metode, hvor parametre estimeres ved at vælge den værdi, der bedst forklarer de observerede værdier. Brug af maximum likelihood-baserede metoder førte til bedre parameterestimer, men dette til trods gav den nye metode ikke bedre resultater end en eksisterende likelihood-baseret metode.

I artikel III anvender vi en alternativ metode til PET-okkupansmåling; her gives lægemidlet under en igangværende PET-scanning. På den måde kan man få et estimat for okkupans ud fra en enkelt PET-undersøgelse i stedet for to. Denne type eksperiment overtræder imidlertid nogle fundamentale antagelser i traditionelle kvantitative metoder til PET og derfor har vi udviklet en helt ny model til at håndtere dette samt to forskellige måder at løse det på. Modellen og løsningerne testes på både simulerede data og eksperimentelle målinger fra grise og viste sig at give gode mål for okkupansen.

CONTENTS

Preface	v
Publications	v
Summary	vii
Dansk resumé	ix
Abbreviations	xv
I INTRODUCTION	1
1 INTRODUCTION	3
II BACKGROUND	5
2 CENTRAL NERVOUS SYSTEM PHARMACOLOGY	7
2.1 Drug-Receptor Interactions	7
2.2 Pharmacokinetics	8
2.3 Drug Discovery and Development	9
3 POSITRON EMISSION TOMOGRAPHY	11
3.1 Basic principles of PET	11
3.2 Radionuclide and Radiotracer Production	12
3.3 The PET System	13
3.4 Data Acquisition	14
3.5 Data Reconstruction, Corrections and Sources of Noise	15
4 QUANTIFICATION OF BRAIN PET DATA	17
4.1 Data Preprocessing and Region of Interest Definition .	18
4.2 Tracer Kinetic Modelling	19
4.2.1 Key Parameters	20
4.2.2 Compartment Models	21
4.2.3 Reference Tissue Approaches	23
4.3 Quantifying Drug Occupancy	24
4.3.1 The Lassen Plot	25
4.3.2 Likelihood Estimation of Occupancy	25
4.3.3 In-Scan Intervention	26
4.4 Quantifying the Dose-Occupancy Relationship	27
5 CENTRAL NERVOUS SYSTEM APPLICATIONS OF PET	29
5.1 CNS PET Tracers	29
5.1.1 TSPO PET and [¹¹ C]PBR28	29
5.1.2 Serotonin 2A Receptor and [¹¹ C]Cimbi-36	31
5.1.3 Imaging Synaptic Density and [¹¹ C]UCB-J	31
5.2 PET Imaging in CNS Drug Development	32
III AIMS	35
6 AIMS	37

IV	PAPER I	39
7	METHODS	41
7.1	Data Acquisition	41
7.2	Estimation of V_T	41
7.3	Simultaneous Estimation of V_{ND}	43
7.4	Estimation of V_S	43
7.5	Statistical Analyses	43
8	RESULTS AND DISCUSSION	45
8.1	Lipopolysaccharide Challenge	45
8.2	Effect of Diagnosis	46
8.3	Effect of Genotype	49
8.4	The SIME method	52
V	PAPER II	53
9	METHODS	55
9.1	Simulation of Data	55
9.1.1	Simulation Experiment 1	55
9.1.2	Simulation Experiment 2	56
9.1.3	Simulation Experiment 3	56
9.1.4	Fixing True Parameter Values	57
9.1.5	Applying Unique and Realistic Noise to the Data	57
9.1.6	Simulating Baseline-Block Data	58
9.1.7	Simulating Test-Retest Data for Estimation of Covariance Structure	59
9.2	Analysis of Baseline-Block Data	59
9.2.1	The Lassen Plot	60
9.2.2	Likelihood Estimation of Occupancy	60
9.2.3	Dose-Occupancy Plot	60
9.2.4	Likelihood Estimation of Affinity	60
9.2.5	Comparison of Parameter Estimates	61
10	RESULTS AND DISCUSSION	63
10.1	Occupancy Range	63
10.2	Number of Subjects	65
10.3	Noise in Plasma Drug Concentration Measurements .	65
10.4	Analytical Methods	67
VI	PAPER III	69
11	METHODS	71
11.1	Kinetic Models for PET Displacement Studies	71
11.1.1	The Occupancy Model	72
11.1.2	The One-Tissue Compartment Displacement Model	72
11.1.3	The Two-Tissue Compartment Displacement Model	73
11.2	Simulation of PET TACs with Displacement	73
11.2.1	Generation of Noise-Free Time-Activity Curves	73
11.2.2	Adding Realistic Noise	74
11.3	Pig Displacement Experiments	74

11.4	Analysis of PET Displacement Scans	74
11.4.1	The Numerical Solution	75
11.4.2	The Single Step Approximation	75
12	RESULTS AND DISCUSSION	77
12.1	Estimation of Occupancy	77
12.2	The Model	78
12.3	Model Solutions	79
VII	CONCLUSION	81
13	CONCLUDING REMARKS AND FUTURE PERSPECTIVES	83
13.1	Nondisplaceable Binding	83
13.2	Drug Occupancy Studies	84
VIII	BIBLIOGRAPHY	87
IX	STATEMENTS	xvii
	Ethics Statement	xix
	Data Availability	xix
	Code Availability	xx
	Acknowledgements	xxi
X	APPENDICES	xxiii
A	PAPER I	xxv
B	PAPER II	xxxix
C	PAPER III	lv
D	DERIVATION OF THE LEA LOG-LIKELIHOOD FUNCTION	xcI

LIST OF FIGURES

Figure 1	PET compartment models	22
Figure 2	Paper I: V_{ND} of all controls	51
Figure 3	Paper I: Polymorphism plot	52
Figure 4	Paper III: Plasma brivaracetam concentration time course	78

LIST OF TABLES

Table 1	Paper I: Dataset summary	42
Table 2	Paper I: LPS results	46
Table 3	Paper I: AUD results	48
Table 4	Paper I: FEP results	49
Table 5	Paper I: PD results	50
Table 6	Paper II: Simulation experiment 1 design . . .	56
Table 7	Paper II: Hard-coded V_T values for [^{11}C]Cimbi- 36 simulations	58
Table 8	Paper II: Simulation Experiment 1 Results . . .	64
Table 9	Paper II: Simulation Experiment 2 Results . . .	66
Table 10	Paper II: Simulation Experiment 3 Results . . .	67

ABBREVIATIONS

^{11}C	Carbon-11
^{18}F	Fluorine-18
1TCM	One-tissue compartment model
2TCM	Two-tissue compartment model
5-HT _{2A} R	Serotonin 2A receptor
AIF	Arterial input function
ANOVA	Analysis of variance
AUD	Alcohol use disorder
BBB	Blood-brain barrier
BP _{ND}	Binding potential relative to the nondisplaceable component
C _P	Concentration of drug in plasma
C _A	Concentration of tracer in arterial plasma
C _{ND}	Concentration of tracer in the nondisplaceable tissue compartment
C _S	Concentration of tracer in the specific tissue compartment
C _T	Concentration of tracer in total tissue
CT	Computed tomography
FDG	Fluorodeoxyglucose
FEP	First-episode psychosis
FOV	Field of view
HAB	High-affinity binder
HRRT	High-resolution research tomograph
IC ₅₀	Half-maximal inhibitory concentration
IRF	Impulse response function
K _D	Equilibrium dissociation constant
LEA	Likelihood estimation of affinity
LEO	Likelihood estimation of occupancy

LPS	Lipopolysaccharide
LOR	Line of response
MAB	Mixed-affinity binder
MLE	Maximum likelihood estimation
MRI	Magnetic resonance imaging
PD	Parkinson's disease
PET	Positron Emission Tomography
ROI	Region of interest
RSS	Residual sum of squares
SIME	Simultaneous estimation of V_{ND}
SPECT	Single-photon emission computed tomography
SRTM	Simplified reference tissue model
SUV	Standardized uptake value
SUVR	Standardized uptake value ratio
SV2A	Synaptic vesicle protein 2A
TAC	Time-activity curve
TSPO	The 18-kDa translocator protein
v_B	Fractional blood volume
V_{ND}	Nondisplaceable distribution volume
V_S	Specific distribution volume
V_T	Total distribution volume
Δ	Occupancy
∂	Occupancy
∂^{max}	Maximal occupancy reached during a single PET scan
Δ_{max}	Maximal attainable occupancy

Part I

INTRODUCTION

A rock pile ceases to be a rock pile the moment a single man contemplates it, bearing within him the image of a cathedral.

— Antoine de Saint-Exupéry,
The Little Prince

INTRODUCTION

Development of novel drugs is tremendously costly and time consuming. Over the last decades, positron emission tomography (PET) has increasingly been used as a tool in the drug development process, especially for drugs targeting the central nervous system (CNS). By employing molecular imaging early in the drug development process, it is possible to confirm if the drug crosses the blood-brain barrier (BBB), and binds to its intended target with adequate *in vivo* affinity. Thus, drug candidates with low probability of success can be excluded before exhaustive and expensive clinical trials are initiated.

The focus of the work included in this thesis is model evaluation and development for PET. Specifically, the emphasis is on data analysis for PET studies including a drug intervention. When PET data is collected both before and after the administration of a drug, it is possible to estimate the percentage of targets that the drug binds to (i.e., the occupancy). Further, by pooling occupancy data from several subjects, it is possible to establish a dose-occupancy relationship, which allows the occupancy to be predicted from the drug exposure.

Depending on the drug target and PET radiotracer, different methods are available for quantifying binding of the tracer, and occupancy of the target by the drug. Further, the choice of analytical methods also depends on the experimental setup. In addition to the traditional baseline-block setup, where two separate PET scans are conducted, it is in some cases possible to displace the PET signal by administering a drug during an ongoing scan. The latter setup requires a different class of models than those that have traditionally been used to analyze PET data. The thesis work includes evaluation of both existing and novel models that can be applied both to the traditional baseline-block study design, and in-scan intervention studies.

Ultimately, the goal of the presented work is to provide information that can be used to improve the design of drug occupancy studies. We hypothesized that, by making informed decisions regarding experimental setup and analysis methods, it is possible to minimize both costs and radiation doses, without sacrificing the accuracy and precision of parameter estimates.

Part II

BACKGROUND

Well, I must endure the presence of a few caterpillars if I wish to become acquainted with the butterflies.

— Antoine de Saint-Exupéry,
The Little Prince

It has been estimated that, in Europe, brain diseases cause 50% of years lived with disability, and lead to costs of approximately €800 billion annually (Olesen et al., 2012; Olesen and Leonardi, 2003). In the US, drugs targeting the central nervous system (CNS) represent the most common type of prescription drugs among people under the age of 60 years, with CNS stimulants being the most commonly prescribed drug type in the 12 – 19 years age range, and antidepressants being the most commonly prescribed drug type in the 20 – 59 years age range (Martin and Ogden, 2019). In addition to their clinical importance, drugs targeting the CNS are also those that are most frequently self-administered for recreational use. (Ritter et al., 2020a)

With only a few exceptions, most drug targets are proteins. Proteins that are typically targeted by drugs include receptors, enzymes, transporters and ion channels. This is true both for drugs acting on the CNS and in the periphery. However, drug action in the CNS is often more complicated than outside. Not only is the CNS a very complex system, it is also uniquely protected by the blood-brain barrier (BBB). Even more than in other systems, there is often a lack of understanding of the events connecting drug action on a cellular level to their effects on brain function (Ritter et al., 2020a).

In this brief chapter, some key concepts in CNS pharmacology are described. The intention is not to give a complete overview, but to give some background that is relevant to the thesis work.

2.1 DRUG-RECEPTOR INTERACTIONS

The receptor concept has been called pharmacology's "big idea" (Rang, 2006). Neuroreceptors represent one of the most common types of targets for CNS drugs. Receptors are protein molecules found on cell membranes. When bound by a small molecule (ligand) with a specific chemical structure, they can cause a cellular response. When a ligand is bound to a receptor, we say that the receptor is occupied by the ligand.

Binding of ligands to receptors is governed by the concentrations of bound and free receptor and ligand, as well as the binding affinity of the ligand-receptor pair. Affinity is a measure of the propensity of the ligand and receptor to combine. It is inversely related to the equilibrium dissociation constant, K_D . The half-maximal inhibitory concentration, IC_{50} (see Section 4.4), is not the same as K_D . It offers

a more feasible, although less precise, measure of the *in vivo* binding strength of a ligand to a receptor.

Occupancy is governed by affinity. Higher affinity (lower K_D and IC_{50}) means that lower ligand concentrations are necessary to reach a certain occupancy.

Some, but not all, ligands binding to a receptor will activate the receptor, and cause a cellular response. Ligands that cause an activation of the receptor are referred to as agonists, while ligands that bind to receptors without causing activation are referred to as antagonists.

Full agonists produce the maximal possible response, while partial agonists only cause a partial response relative to that of a full agonist. The ability of a ligand to activate a receptor is referred to as the efficacy.

Drug action in a living organism is of course more intricate than a simple ligand-receptor interaction. Many complex molecular and physiological processes take place both before and after a drug binds to its target protein. Also, the binding might be enhanced or inhibited by the presence of other molecules.

2.2 PHARMACOKINETICS

The dynamic distribution of a drug within the body is referred to as pharmacokinetics. The human body is a complex system, and there are numerous factors that affect where, how, and how fast drugs move within a living organism.

The concentration of a drug in plasma (C_p) is often assumed to be related to the concentration of the drug at the target site (Ritter et al., 2020c). Often, and especially for drugs targeting the CNS, it is easier to measure the drug concentration in plasma than in the extracellular fluid of the target tissue. With intravenous administration of the drug, the plasma concentration will increase rapidly (with the rate of delivery), and then (for most drugs) decrease in an approximately exponential manner governed by the drug's elimination half-life (Hallare and Gerriets, 2022). For other administration methods, the shape and area of the plasma curve will also depend on the fraction and rate of absorption into the bloodstream (Holford, 2016).

Drug in the blood stream can be distributed across the body. Delivery of drug molecules to the CNS is complicated by the BBB. Some small, mostly lipophilic, molecules can traverse the BBB through passive diffusion (Abbott et al., 2010). Other molecules must rely on active transport mechanisms.

Inside the brain, the drug can be distributed in different concentrations in extracellular and intracellular fluid, brain microvasculature, and cerebrospinal fluid, and fluid flow within the brain will affect the drug distribution (Vendel, Rottschäfer, and de Lange, 2019). Non-

specific protein binding inside the brain can affect the drug activity (Srinivas, Maffuid, and Kashuba, 2018).

Drugs are eliminated from the body through metabolism and excretion.

Although a drug will undergo the same general processes in different people, there will always be inter-individual variability in pharmacokinetics. Factors such as health, age, sex, genetic variations, and interactions with other drugs can all affect how a drug is absorbed, distributed, metabolized and eliminated.

2.3 DRUG DISCOVERY AND DEVELOPMENT

Drug discovery and development is very costly and time consuming. Compared to drug development in general, development of CNS-targeting drugs faces lower success rates and longer development times (Mullard, 2016; Srinivas, Maffuid, and Kashuba, 2018).

In the discovery process, new candidate drugs are found. First, a suitable target must be identified. Then, thousands of molecules are screened, and the best candidates are optimized.

If promising leads are identified in the discovery process, they can be moved to preclinical development. This entails extensive testing, including studies on safety and toxicology, and pharmacokinetic and pharmacodynamic testing. Promising results in the preclinical phase are not a guarantee for success in humans (Srinivas, Maffuid, and Kashuba, 2018). In this phase, the feasibility of commercial-scale production is also evaluated (Ritter et al., 2020b).

Clinical development is the most time consuming and costly step, and only approximately 10% of all drugs entering clinical evaluation make it to market (Smietana, Siatkowski, and Møller, 2016). Phase I studies are small, and typically conducted in healthy populations, with a focus on pharmacology and side-effects. Phase II studies are conducted in patients, and are focused mainly on clinical effects. Dosing regimen for future studies is typically also determined in this step. In phase III the potential drug is evaluated in a large-scale, double-blinded, randomized clinical trial. For drugs that achieve approval for marketing, a fourth phase of post-marketing surveillance follows.

POSITRON EMISSION TOMOGRAPHY

Positron emission tomography (PET) is a molecular imaging technique which enables visualization and quantification of metabolic and molecular processes in the living human body. By labelling molecules with a positron-emitting radionuclide, the distribution of that molecule can be measured by an external detector. In theory, PET imaging could be used to track the *in vivo* movement of any molecule. The only constraint is whether it can be labelled with a positron-emitting radionuclide with a suitable half-life. Consequently, the potential applications of PET imaging are continuously expanding.

Unlike other medical imaging modalities like magnetic resonance imaging (MRI) and computed tomography (CT), PET does not inherently provide anatomical information. Instead, a PET image shows the distribution of the radiolabelled molecule (radiotracer). The spatial resolution of PET is substandard to that of MRI and CT. The strength of PET lies in its high molecular sensitivity. PET images are almost always combined with a structural imaging modality to assign spatial context. For brain applications, PET images are commonly co-registered to MR images.

The two most frequently used radionuclides for PET radiotracers targeting the CNS are Carbon-11 (^{11}C) and Fluorine-18 (^{18}F). Their half-lives are 20.3 min and 109.8 min, respectively. Other available radionuclides for PET include Nitrogen-13 (^{13}N), Oxygen-15 (^{15}O), Gallium-68 (^{68}Ga), Rubidium-82 (^{82}Rb), and Zirconium-89 (^{89}Zr).

PET is conceptually similar to Single photon-emission computed tomography (SPECT), which is also based on injecting radioactive tracers, and following their distribution with an external detector. However, SPECT uses a different class of radionuclides, and different detector setup and data acquisition. Also, unlike PET, SPECT is not inherently quantitative, because much of the signal is attenuated by collimators before reaching the detector.

3.1 BASIC PRINCIPLES OF PET

The PET scanner detects annihilation photons, originating from beta plus (β^+) decay events. In this type of radioactive decay, a proton in the nucleus of the proton-rich parent radionuclide is converted to a neutron. Simultaneously, a positron (e^+) and an electron neutrino (ν_e) are released. The result is a daughter nuclide with a lower atomic

number (Z) but the same mass number (A) as the parent. The generic equation for β^+ decay is:



where X is the radioactive parent nuclide, and X' is the resulting daughter nuclide. The energy, and initial velocity, of the released positron depends on the parent, but also differs from decay to decay (Knoll, 2010). Because the positron has a positive electric charge, it will be slowed down by interactions with negatively charged electrons. When sufficient kinetic energy has been lost, the positron will annihilate with a nearby electron, resulting in the release of two photons, each with an energy of 511 keV, at an approximate angle of 180° to each other. The 511 keV energy of the annihilation photons is linked to conservation of the mass of the annihilated electron and positron (Cherry, Sorenson, and Phelps, 2012b).

The distance that the positron travels after the beta decay depends both on its initial energy and random interactions with electrons. The density of the surrounding tissue will also affect the range. In water, the average positron range is 1.03 mm for ${}^{11}\text{C}$, and 0.64 mm for ${}^{18}\text{F}$ (Cherry, Sorenson, and Phelps, 2012a).

3.2 RADIONUCLIDE AND RADIOTRACER PRODUCTION

Positron-emitting radionuclides for PET are typically produced by cyclotrons, a type of particle accelerator. In the cyclotron, charged particles are accelerated by an alternating electric field, while being held to a spiral trajectory by a perpendicular magnetic field. The shape of the cyclotron is circular, and the electric field is applied to the particles through a gap across the center. A ion source is placed near the middle of the cyclotron. The result is a particle trajectory resembling a spiral, where particles travel with a fixed radius in a semicircle, before entering the gap, where it is accelerated, and travels with a slightly higher radius before again reaching the gap (Cherry, Sorenson, and Phelps, 2012e). When the particles have reached the maximum orbital radius, they are directed at a target, either inside or outside the cyclotron. For radionuclide production, the accelerated charged particles are aimed at a target consisting of a parent compound. When hit by the charged particle, the parent compound undergoes a nuclear reaction resulting in the desired radionuclide. Some common targets include nitrogen-14 for production of ${}^{11}\text{C}$, and oxygen-18 for production of ${}^{18}\text{F}$ (Radford and Lapi, 2019).

Following radionuclide production, a radiochemist combines it with a molecule to produce a radiotracer. For smaller molecules, radiolabelling is usually done by either direct substitution of an atom with a radioactive isotope of the same element, or by creating an analog molecule (Cherry, Sorenson, and Phelps, 2012e). Radionuclides such

as ^{11}C and ^{15}O are very useful, because they are easily incorporated into biologically relevant molecules. ^{18}F has very desirable imaging properties, but can often not be directly substituted into a molecule of interest without dramatically changing its characteristics (Ermert and Neumaier, 2019). Therefore, ^{18}F is often used to create analogs. For example, the most widely used PET tracer, 2-deoxy-2- ^{18}F fluoro-D-glucose (^{18}F FDG), is created by replacing a hydroxyl group with ^{18}F .

Another important consideration for radiotracer production is that the half-life of the radionuclide must match the time course of radiotracer distribution in the body. So, even though oxygen is suitable for direct substitution, the relatively short half-life of ^{15}O (2.03 min) greatly limits its possible applications (Gómez-Vallejo et al., 2019). Shorter-lived radionuclides also demand rapid synthesis techniques, further limiting their potential uses. Shorter half-lives can also limit transport of the radiotracer. Tracers labelled with shorter-lived radionuclides, such as ^{11}C and ^{15}O must be produced on site, while those labelled with longer-lived radionuclides, such as ^{18}F , can be transported to PET centers without an on site cyclotron and radiochemistry unit. On the other hand, longer half-lives result in larger radiation doses.

In the radiolabelling process, only a relatively small fraction of the product molecule will contain the radioactive nuclide (Antoni, 2019). When producing a radiotracer it is especially important that the product has a high specific activity (activity per unit mass), to ensure sufficient number of decay events without administering so much unlabelled compound that binding is saturated (see Chapter 4).

3.3 THE PET SYSTEM

A PET camera consists of blocks of scintillation detectors, placed in a cylinder surrounding the patient. The detectors are made of crystalline solids with high atomic mass. When a photon with sufficient energy hits the crystal it scintillates, meaning that light is produced. The amount of light emitted by the crystal is proportional to the energy of the photon (Cherry, Sorenson, and Phelps, 2012d). PET scintillation detectors are made of materials that have been specially designed to detect photons within an energy window surrounding the 511 keV of annihilation photons. The scintillating crystals are connected to either photomultiplier tubes or avalanche photodiodes, that produce an electric current in response to the light emitted in the crystal (Cherry, Sorenson, and Phelps, 2012d).

When two photons are detected by the PET system within a coincidence time window, typically in the order of nanoseconds, it can be assumed that an annihilation event took place somewhere along the line connecting the two detector elements where the photons were

detected. This line is often referred to as the line of response (LOR). In time-of-flight PET, the precision is increased by using the difference in detection times to give probabilistic evidence to the origin of the signal along the LOR (Vaquero and Kinahan, 2015).

Both the radius and axial length of the cylinder of detectors can differ immensely between scanners. The Siemens High-resolution research tomograph (HRRT) is a dedicated brain scanner with a field of view (FOV) designed to image the human brain. Small-animal PET scanners have smaller, both radial and axial, FOV. Longer axial FOVs have been limited by count-rate capabilities and timing resolution, as well as concerns regarding computational and economic costs (Poon et al., 2012). With recent improvements in detector technology and computational power, the last few years have seen the introduction of systems with increasing FOV, such as the EXPLORER total-body PET scanner, with a nearly 2-m axial length (Badawi et al., 2019).

PET has relatively poor spatial resolution compared to other medical imaging modalities, such as MRI and CT. Because positrons will travel a finite distance before an annihilation event occurs, PET images will always be somewhat blurred, even if the detector resolution were infinitely high. The resolution is also limited by the size of the detector elements, and the depth and material of the scintillator.

Coincidence detection obviates the need for collimators to determine the origin of a photon. For this reason, PET has much higher sensitivity than planar nuclear imaging modalities, such as SPECT, where collimators block a majority of emitted photons from being detected (Slomka et al., 2015). With 3D acquisition, the sensitivity is not uniform throughout the FOV, but is higher towards the middle, where events are more likely to be detected.

3.4 DATA ACQUISITION

The mode of delivery depends on the radiotracer, but typically it is administered by intravenous injection.

Prior to data collection, a transmission scan, with a radioactive rod source extending along the length of the scanner, is often performed (Cherry, Sorenson, and Phelps, 2012c). The objective of this is to obtain information that can be used to correct the PET data for different attenuation of photons originating at different depths and from different tissues. In hybrid imaging systems, information from the CT or MRI scan can instead be used to generate attenuation maps. This is relatively straight-forward for CT, because the pixel values in Hounsfield units have a simple bilinear relationship with the PET linear attenuation coefficient (Lee et al., 2016). MR-based attenuation maps rely on segmentation into different tissue classes, such as vasculature, fat, muscle, bone and air. Generally, MR-based attenuation

maps are more challenging to obtain, but vast improvements have been made in this field over the last few years (Olin et al., 2022).

In some applications of PET, for example in oncology, only the accumulation of radiotracer is of interest. In those cases, the tracer is administered some time before scanning to achieve some kind of steady state prior to data collection. The scan duration is usually relatively short. In these cases, data is acquired statically, meaning that only one image, showing the total accumulated activity in tissue over the course of the scan, is generated. Most clinical PET scanners have a relatively short FOV. In order to get a PET image that is longer than the field of view, the patient must be moved during the data acquisition by changing the bed position.

In other cases, we are more interested in how the radiotracer is delivered, distributed and metabolized in the body. This could be in cardiology to look at the function of the heart, or in neurology, to study cerebral blood flow, or distribution of proteins of interest. For these applications, the tracer is administered while the subject is already in the scanner, so that also the initial distribution of the tracer as it enters the body is recorded. Data is acquired dynamically, and the measured activity is divided into discrete time intervals, called frames. This results in time-activity curves (TAC), where the mean activity in each frame is plotted against the frame mid times. With dynamic acquisition it is not feasible to move the subject during an ongoing scan, and the image size is limited by the PET system's FOV.

For dynamic acquisitions, arterial blood is often collected throughout the scan to allow for full quantification.

3.5 DATA RECONSTRUCTION, CORRECTIONS AND SOURCES OF NOISE

In modern PET systems, acquisition is typically three-dimensional. With two-dimensional data acquisition, only coincidence events detected by the same detector ring are recorded, while in 3D acquisition any combination of detector elements in the cylinder can form a LOR. Some PET systems allow for list mode acquisition, where each coincidence event is sequentially recorded, along with information about time and involved detector pairs. For dynamic scans, this acquisition procedure allows the temporal framing to be decided and changed after the data acquisition is complete (Rahmim, Tang, and Zaidi, 2009).

Once the number and duration of the frames has been decided, they are individually reconstructed into tomographic images. The two most common approaches are filtered back projection and iterative reconstruction. Generally, iterative reconstruction is computationally heavier, but also gives better statistics and less artefacts (Vaquero

and Kinahan, 2015). Also, iterative reconstruction is compatible with more specialized detector geometries.

Not all pairs of detected photons originate from true coincidence events. Random coincidence is when two unrelated photons are detected within the same coincidence time window. This typically leads to a near-uniform blurring of the image. Scatter coincidence is when annihilation photons change direction when interacting with matter. This establishes an incorrect LOR, which is displaced from the true location of the annihilation event. Several correction strategies exist for both types of false coincidence events, but their effects cannot be completely removed (Cherry, Sorenson, and Phelps, 2012c).

Compared to scatter and random correction, attenuation correction is relatively easy. Because the probability for a pair of annihilation photons to both reach the detectors decreases with the distance travelled through matter, and the density of that matter, the likelihood of detection is not the same for all LORs. This is corrected based on transmission scans or CT- or MR-based attenuation maps.

Other factors that contribute to noise and reduced spatial resolution in PET include motion of the subject and partial volume effects (see Section 4.1).

QUANTIFICATION OF BRAIN PET DATA

For PET images to be useful for quantitative assessments, the system must be activity calibrated. By scanning a phantom with known activity concentration, a correction factor $[(\text{Bq cm}^{-3}) / (\text{counts voxel}^{-1})]$ can be obtained. The count rate of each voxel can then be multiplied with the correction factor to yield activity concentration (C_T) in Bq cm^{-3} . This correction is done automatically by the scanner.

When a decay event is detected by the scanner, information about the time and approximate position of that event is available. Radioactivity is a stochastic process, and the radionuclide could emit a positron at any given time. Thus, the detected activity could originate from tracer that is bound to its intended target, but also from tracer that is nonspecifically bound, or free in tissue or blood.

For full quantification of PET, it is necessary to collect data dynamically, and to start the data collection at, or before, the injection of the radiotracer. Detected events are binned into temporal frames. These frames are typically shorter (10 s – 1 min) in the beginning, when the activity concentrations in tissue change rapidly, and longer (5 – 15 min) towards the end of the scan, when much of the activity has decayed. Generally, framing is chosen so that the number of counts in each frame is relatively constant, with the aim of keeping the noise level consistent throughout the scan.

When PET data has been acquired statically, the binding is routinely expressed in standardized uptake value (SUV), which is the activity normalized by the injected dose and some measure of the subject's size, typically the body mass (Thie, 2004). SUV normalized by body mass is given by,

$$\text{SUV} = \frac{C_T \cdot \text{BM}}{A_{\text{inj}}}, \quad (2)$$

where C_T is the activity concentration in the target tissue, A_{inj} is the total injected activity, and BM is the body mass of the subject. By normalizing the activity, it becomes more comparable across subjects, but SUV is still just a measure of the total activity and cannot separate the specific signal from other sources. Simplified quantification methods and semi-quantitative outcome measures, such as the SUV, can in some cases be very useful. For example, in clinical settings, less invasive acquisition methods and shorter scan durations are often essential. Still, simplified methods must always be carefully validated against full quantification on a tracer-to-tracer basis (Lammertsma, 2017). Further, for many applications of PET, such as drug occupancy studies, there are no valid alternatives to full quantification.

For the kinetic modeling methods presented in this chapter to be valid, there are two especially important assumptions that must be adhered to (Lubberink and Heurling, 2019). The first is the tracer principle, which states that the concentration of radiotracer in the body must be low enough that the system is not perturbed by it. For compliance with the tracer principle it is important that the specific activity of the injected radiotracer is high. Often, it is assumed that less than 5% of the specific target is bound by the radiotracer, including also the administered unlabelled tracer. The second important principle is that the system should not change during an ongoing PET scan.

4.1 DATA PREPROCESSING AND REGION OF INTEREST DEFINITION

Before PET data can be quantified it has to go through some pre-processing steps. For dynamic PET data, the goal of this is to go from images of radioactivity in the brain to TACs, describing how the activity in a voxel, or a region of interest (ROI), changes over the course of the scan.

The first pre-processing step is often motion correction. Dynamic PET scans are usually relatively long (> 90 min), and some involuntary or voluntary motion during the course of the scan is difficult to avoid. For PET neuroimaging, it is common practice to fix or restrain the head to reduce motion. Often, this can be enough to limit the effects of motion, but at other times it might be necessary to do some motion correction. A number of different solutions for external motion tracking are available (Kyme and Fulton, 2021), but data-driven motion correction is more common. The frames are realigned by rigid registration to either a reference frame or a mean or sum image (Costes et al., 2009). Because of the low temporal resolution of PET, this approach does not necessarily correct for abrupt motions, but can cancel the effects of the position of the subject drifting during the course of the scan.

Because PET images do not inherently contain anatomical information, the images are almost always co-registered to anatomical images for spatial context. This step is a necessity for ROI-based quantification. In PET neuroimaging, a personal T₁-weighted MR image is typically co-registered to the PET image. Then, the MR data can be used to delineate ROIs, so that the PET signal in each voxel can be assigned to a region.

A number of different methods are available for ROI delineation. Regions can be drawn manually on each subject's MR image. This is a decreasingly common approach for anatomical regions, but can still be useful for smaller or non-anatomical regions, such as lesions and tumors. In general, MR atlases are used for automatic definition of anatomical ROIs (Svarer et al., 2005).

Another image processing step, which is especially important when using smaller ROIs is partial volume correction. Partial volume effects is the spillover of activity from tissues with high activity to an adjacent low-signal region, leading to an underestimation of the activity in the former and an overestimation of the activity in the latter (Rousset et al., 2007).

Many of the preprocessing steps are based on information from the MR image, and thus contribute to the total noise of the outcome parameters. The choice of pre-processing steps and methods can have a significant effect on the outcome of PET studies, and thus need to be considered carefully (Nørgaard et al., 2020).

4.2 TRACER KINETIC MODELLING

For tracer kinetic modelling, the radiotracer is typically administered as a bolus injection. That is, all the tracer is administered over a relatively short time at the beginning of the PET scan. The radiotracer can also be administered as bolus followed by constant infusion. The goal of this administration protocol is often to reach steady state conditions, which allows for more straightforward estimation of outcome parameters (Carson et al., 1993).

For full quantification of PET data, the tracer concentration both in the ROI and in plasma must be measured. For certain tracers, such as [^{15}O]water and [^{18}F]FDG, metabolite corrections are not necessary, which means that image-derived input functions are feasible (Okazawa et al., 2018; Zanotti-Fregonara et al., 2011). For most tracers however, arterial samples are necessary to calculate the radioactivity concentration in plasma. Only unmetabolized tracer in plasma is typically able to cross the BBB. Therefore, to calculate an arterial input function (AIF, C_p), the measured activity in blood is corrected both for the ratio of activity concentration in plasma to that in whole blood, and for the fraction of activity originating from radioactive metabolites of the parent tracer.

Often, but not always, kinetic models can also account for the presence of blood in the ROI. For this purpose, the total activity in blood (including both parent tracer and radiometabolites) is used. The fractional blood volume (v_B) can either be fitted or fixed (typically to 0.05 for the human brain). The total PET signal (C_{total}) can be expressed as the sum of the contributions from tissue and blood, as in the following equation,

$$C_{\text{total}}(t) = (1 - v_B) \cdot C_T(t) + v_B \cdot C_B(t),$$

where C_T is the activity concentration in tissue, and C_B is the activity concentration in blood.

Quantification methods based on AIFs are often referred to as invasive, reflecting the collection of arterial blood. For many radiotracers,

non-invasive quantification is also possible. These methods typically rely on the presence of a reference tissue: a region that is devoid of the tracer's specific target and with the same level of non-specific and free tracer concentrations. Before reference region approaches can be used, they should be carefully validated against full invasive quantification.

Depending on factors such as how data is collected, whether or not an AIF is available, and whether or not a reference region is available, people might choose to use different methods to quantify PET data, often resulting in different outcome measures. This variability of quantification methods can complicate comparison of results between studies.

4.2.1 Key Parameters

One of the most frequently reported outcome measures from PET ligand studies with full invasive quantification is the total distribution volume, V_T (Innis et al., 2007). The distribution volume, conceptually similar to a partition coefficient, is the ratio of tracer concentration in tissue (C_T) to that in plasma (C_P) at equilibrium,

$$V_T = \frac{C_T}{C_P}. \quad (3)$$

Thus, in an invasive bolus-infusion experiment at equilibrium conditions, V_T could be calculated directly by dividing the tissue concentration by the plasma concentration. In a bolus injection experiment, where equilibrium is not reached, other approaches to calculating V_T must be used. In these cases, it can be helpful that V_T is equal to the ratio of the area under the tissue curve to the area under the plasma curve,

$$V_T = \frac{\int_0^\infty C_T(t) dt}{\int_0^\infty C_P(t) dt}. \quad (4)$$

Because we only measure activity over a finite time this cannot be used to calculate V_T directly. However, for a given model, Equation 4 can be reworked to express V_T in terms of the model microparameters.

The specific distribution volume (V_S) and non-displaceable distribution volume (V_{ND}), are similarly defined to the total distribution volume, as the equilibrium ratio of the concentration of specifically bound tracer (C_S) and non-displaceable tracer (C_{ND}), respectively, to C_P . The total distribution volume is the sum of the non-displaceable and specific distribution volumes, $V_T = V_{ND} + V_S$.

Similar to distribution volumes, binding potentials (BP) are also equilibrium ratios of different states of the tracer. Specifically, they

are the ratio of the concentration of specifically bound tracer to something (Innis et al., 2007). Binding potentials are measures of the product of receptor density and affinity. Density and affinity cannot be disentangled by *in vivo* PET, and so binding potentials are the closest we can get to a measure of either (Mintun et al., 1984). The most frequently reported binding potential, the binding potential with respect to the non-displaceable compartment (BP_{ND}), is the equilibrium ratio of tracer concentration in the specific compartment to that in the non-displaceable compartment. BP_P is the equilibrium ratio of tracer concentration in the specific compartment to that in plasma (same as V_S), and BP_F is the equilibrium ratio of tracer concentration in the specific compartment to the concentration of free tracer in plasma. BP_{ND} can be expressed in terms of distribution volumes as, $BP_{ND} = V_S/V_{ND}$, or $BP_{ND} = V_T/V_{ND} - 1$.

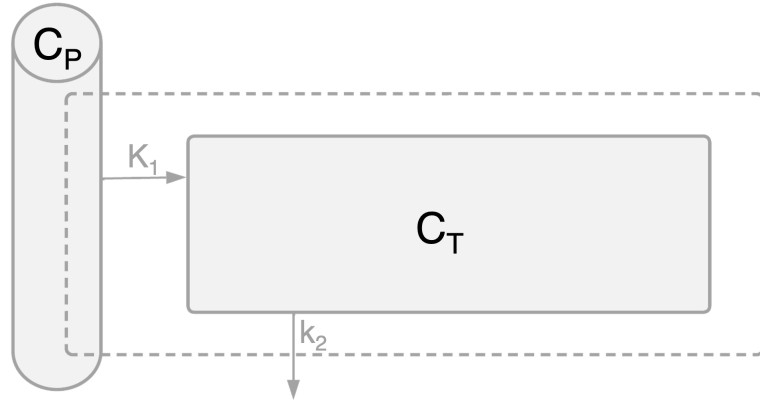
When V_T and BP_{ND} are used as outcome measures, changes are normally assumed to reflect changes in the specific signal only. However, both parameters are also dependent on the non-displaceable component. Before V_{TS} and BP_{ND} s can be compared across groups or before and after an intervention, it should be considered whether also the non-displaceable binding could differ between the two conditions.

4.2.2 Compartment Models

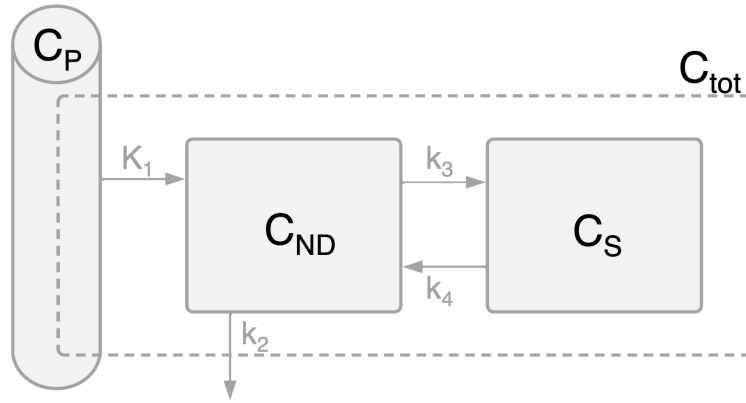
Compartment models are the most frequently used type of kinetic model for PET ligand quantification. A compartment represents an anatomical, physiological or biochemical state of the the PET radio-tracer. These models describe the transfer of the tracer between different compartments.

The goal of compartment models is not to accurately represent the underlying biology. Instead, they are meaningful approximations that provide solvable differential equations. All approximations and assumptions must be relevant to, and validated for, the specific tracer that they are applied to, and for some tracers the appropriate choice of model may vary between different regions. Irrespective of the number of compartments, the concentration of tracer within one single compartment is always assumed to be homogenous.

The most complex compartment model that can be reliably fitted to PET data is the two-tissue compartment model (2TCM). The 2TCM (Phelps et al., 1979), as illustrated in Figure 1b, has three compartments: one plasma compartment and two tissue compartments: the non-displaceable compartment and the specific compartment. The first compartment is the AIF (C_P). The non-displaceable compartment (C_{ND}) represents tracer that is either free in extracellular and intracellular fluid or non-specifically bound in tissue. It is a key assumption of this model that free and non-specifically bound tracer is in equi-



(a) The one-tissue compartment model (1TCM).



(b) The two-tissue compartment model (2TCM).

Figure 1: The two most common PET compartment models.

librium. For ligand studies, the specific compartment (C_S) represents tracer that is specifically bound to the target protein.

The 2TCM is described by the following system of differential equations:

$$\begin{aligned}\frac{dC_{ND}(t)}{dt} &= K_1 C_P(t) - (k_2 + k_3) C_{ND}(t) + k_4 C_S(t) \\ \frac{dC_S(t)}{dt} &= k_3 C_{ND}(t) - k_4 C_S(t).\end{aligned}$$

K_1 , k_2 , k_3 and k_4 are the kinetic rate constants describing the rate of transfer of tracer between the compartments. K_1 [$\text{mg min}^{-1} \text{mL}^{-1}$] represents the delivery of tracer across the BBB, and is the product of flow and extraction. k_2 [min^{-1}] represents the functional efflux of tracer out of the brain. k_3 [min^{-1}] is the combined forward rate constant ($k_3 = k_{on} f_{ND} B_{max}$, where k_{on} is the association constant of the ligand-target binding, f_{ND} is the fraction of free tracer in the non-

displaceable compartment, and B_{\max} is the concentration of available targets). k_4 [min^{-1}] is the dissociation constant k_{off} .

The rate constants are referred to as model microparameters. These parameters can often not be estimated with high precision or stability, which is why macroparameters, like V_T , are typically estimated instead. For the 2TCM, V_T is calculated from microparameters as,

$$V_T = \frac{K_1}{k_2} \left(1 + \frac{k_3}{k_4} \right).$$

If equilibrium between the non-displaceable and specific compartments can be assumed to be reached rapidly, a simpler compartment model, the one-tissue compartment model (1TCM), can be used. This model, as illustrated in Figure 1a, has only two compartments: the AIF (C_P) and tracer in total tissue ($C_T = C_{\text{ND}} + C_S$). The 1TCM is described by the differential equation,

$$\frac{dC_T(t)}{dt} = K_1 C_P(t) - k_2 C_T(t).$$

Changing the number of compartments in the model also changes the meaning of the model rate constants. Even though they have the same name, the 1TCM k_2 is not the same as the 2TCM k_2 .

The PET compartment models are linear systems with constant coefficients, and are relatively trivial to solve analytically, for example using the Laplace transform. For the 1TCM, the solution to the model ODE is

$$C_T(t) = K_1 C_P(t) \otimes e^{-k_2 t},$$

where \otimes is the convolution operator. This is the AIF (C_P) convoluted with the system's impulse response function (IRF). For increasing number of compartments the model solutions become much longer, but will always be the convolution of the AIF with the IRF, as long as the system is linear. For n tissue compartments, the IRF will be the sum of n exponential functions (Gunn, Gunn, and Cunningham, 2001).

4.2.3 Reference Tissue Approaches

Reliable estimation of specific binding measures normally requires the use of a reference region. A suitable reference tissue is a region that is devoid of the specific target of the radiotracer, but otherwise has the same characteristics as the target tissue (Heurling et al., 2017). In competition with another ligand for the same specific target as the PET tracer, the total binding in the reference region should ideally be unaltered. In other words, the binding in the reference region is said to be nondisplaceable, and ideally the reference region V_T should be the same as the V_{ND} of the target region.

Thus, if a reference region exists BP_{ND} or V_S can be calculated from the V_T s in the target (V_T^{ROI}) and reference region (V_T^{RR}) as $BP_{ND} = V_T^{ROI}/V_T^{RR} - 1$ and $V_S = V_T^{ROI} - V_T^{RR}$, respectively.

Further, the presence of a reference region also allows for noninvasive quantification, by using the reference region TAC as an indirect input function instead of the AIF. The full reference tissue model (Cunningham et al., 1991), assumes that the target tissue can be explained by a 2TC model and the reference tissue by a 1TC model, and rearranges the model differential equation in a way that allows the target tissue activity to be expressed as a function of the reference tissue activity.

More frequently, the simplified reference tissue model (SRTM; Lammertsma and Hume (1996)) is used for reference region based compartment modeling. The SRTM models the target tissue with a single compartment, and thus requires a rapid exchange of tracer between the nondisplaceable and specific compartments.

Reference tissues can also be used to calculate semi-quantitative outcome measures. Standardized uptake value ratios (SUVR) are calculated by dividing the SUV of the target tissue with that of the reference tissue. Because the tracer kinetics differ between the target and reference regions, the SUVR value will change throughout the scan, and deciding what part of the scan to use can be complicated (Luberink and Heurling, 2019).

4.3 QUANTIFYING DRUG OCCUPANCY

The percentage of targets that is blocked by a drug is referred to as the occupancy (Δ). For PET-based estimation of occupancy, the most frequently used experimental design is a baseline-block setup. It is important that a PET radiotracer that binds specifically to the same target as the drug is used. Each subject is scanned at least twice, once at baseline, and again after the drug has been administered. Frequently, the occupancy in the block scan is calculated as the fractional decrease in BP_{ND} between the two scans. However, this approach is only feasible for radiotracers with a suitable reference region. For the 2TCM it is technically possible to calculate BP_{ND} or BP_P/V_S directly from the model microparameters, but the standard error of those will usually be much higher than that of V_T . For the 1TCM, it is not possible to calculate binding potentials from the microparameters.

In the absence of a reference region, strategies to estimate occupancy rely on pooling multiple brain regions, and simultaneously estimating V_{ND} and Δ . The assumptions that V_{ND} and Δ are uniform across the brain, or at least across brain regions with similar tissue composition, is widespread and difficult to get around.

4.3.1 The Lassen Plot

The Lassen plot, often simply referred to as the occupancy plot, is a linear regression analysis technique for estimation of occupancy and V_{ND} from baseline-block PET data. It is based on the assumption that, within-subject, both V_{ND} and Δ are constant across the brain (Lassen et al., 1995). From these assumptions, it follows that the V_T s for the baseline and block scans can be expressed as,

$$V_T^{\text{baseline}} = V_{ND} + V_S + \epsilon \quad (5)$$

$$V_T^{\text{block}} = V_{ND} + (1 - \Delta)V_S + \epsilon, \quad (6)$$

where ϵ is noise.

The Lassen plot was first introduced by Lassen and colleagues in 1995, and later reformulated by Cunningham and colleagues to the form it is mostly encountered today (Cunningham et al., 2010):

$$V_T^{\text{baseline}} - V_T^{\text{block}} = \Delta \left(V_T^{\text{baseline}} - V_{ND} \right). \quad (7)$$

V_T^{baseline} and V_T^{block} are $k \times 1$ arrays of estimated V_T values in k ROIs for one subject. By plotting $V_T^{\text{baseline}} - V_T^{\text{block}}$ against V_T^{baseline} and fitting a line through the data, the occupancy in the block-scan can be estimated as the slope of the line, and the subject's V_{ND} as the line's x-intercept.

4.3.2 Likelihood Estimation of Occupancy

Likelihood estimation of occupancy (LEO; Schain, Zanderigo, and Ogden (2018)), is a maximum likelihood based estimator, founded on the same key assumptions as the Lassen plot. However, instead of using linear regression, LEO uses maximum likelihood estimation (MLE) techniques to estimate Δ and V_{ND} , accounting for the covariance of the regional V_T estimates. A major obstacle with using MLE approaches is to accurately approximate the covariance matrix (Σ). Different approaches have been evaluated in the past, such as estimating the covariance structure from test-retest datasets with the same radio-tracer. (Naganawa et al., 2019; Schain, Zanderigo, and Ogden, 2018).

Assuming Gaussian noise, the observed V_T values in ROI j can be regarded as being sampled from a normal distribution with mean according to the true V_T s as expressed in Equation 19, and standard deviation $\sqrt{\Sigma_{j,j}}$:

$$\begin{aligned} V_T^{\text{baseline}} &\sim N(V_{ND}\mathbf{1} + V_S, \Sigma) \\ V_T^{\text{block}} &\sim N(V_{ND}\mathbf{1} + (1 - \Delta)V_S, \Sigma). \end{aligned} \quad (8)$$

Then, the combined negative log-likelihood function for $\mathbf{V}_T^{\text{baseline}}$ and $\mathbf{V}_T^{\text{block}}$, will be,

$$\begin{aligned} \ell(\mathbf{V}_S, V_{\text{ND}}, \Delta \mid \mathbf{V}_T^{\text{b}}, \mathbf{V}_T^{\text{d}}) \\ = - \left(\mathbf{V}_T^{\text{baseline}} - (V_{\text{ND}} \mathbf{1} + \mathbf{V}_S) \right)^{\text{T}} \Sigma^{-1} \left(\mathbf{V}_T^{\text{baseline}} - (V_{\text{ND}} \mathbf{1} + \mathbf{V}_S) \right) \\ - \left(\mathbf{V}_T^{\text{block}} - (V_{\text{ND}} \mathbf{1} + (1 - \Delta) \mathbf{V}_S) \right)^{\text{T}} \Sigma^{-1} \left(\mathbf{V}_T^{\text{block}} - (V_{\text{ND}} \mathbf{1} + (1 - \Delta) \mathbf{V}_S) \right) \end{aligned} \quad (9)$$

Constant terms are excluded from Equation 9, because they will not affect the coordinates of the function minimum. The dimensionality of Equation 9 can be reduced by solving the partial derivative $\frac{\partial}{\partial \mathbf{V}_S} \ell = 0$, resulting in,

$$\mathbf{V}_S = \frac{\mathbf{V}_T^{\text{baseline}} - V_{\text{ND}} \mathbf{1} + (1 - \Delta) (\mathbf{V}_T^{\text{block}} - V_{\text{ND}} \mathbf{1})}{1 + (1 - \Delta)^2} \quad (10)$$

By substituting this expression into Equation 9, the LEO log-likelihood function becomes a two-dimensional function.

Minimizing $\ell(\Delta, V_{\text{ND}}, \mathbf{V}_S \mid \mathbf{V}_T^{\text{baseline}}, \mathbf{V}_T^{\text{block}})$ returns the most likely values for Δ , V_{ND} , and \mathbf{V}_S given the observed $\mathbf{V}_T^{\text{baseline}}$ and $\mathbf{V}_T^{\text{block}}$. Because the noise in the measurements are taken into consideration, this approach should yield unbiased estimates.

4.3.3 In-Scan Intervention

For PET tracers that can be displaced by a competing drug, it is possible to estimate target occupancy from a single PET scan. This experimental setup has many potential advantages over the traditional baseline-block study design. With one less scan, the radiation dose to the research subjects is considerably reduced, as is the financial costs of the experiment. Further, because both the baseline and block data is collected during the same scan, potential diurnal variations and test-retest effects could be avoided.

In previous work to model the in-scan displacement of PET radiotracer, the competing drug has often been an endogenous neurotransmitter. Existing models are rely on a reference region, and are based on the SRTM. The LSSRM (referred to as LSRRM in later publications), was introduced in 2003 (Alpert et al., 2003). It is a linear extension of the SRTM, where activation parameters are used to statistically detect the release of endogenous neurotransmitter. lp-ntPET (linear parametric neurotransmitter PET), introduced in 2012, is an extension of the LSSRM (Normandin, Schiffer, and Morris, 2012).

The extended simplified reference tissue model (ESRTM) was introduced in 2006 (Zhou et al., 2006). With this method, the SRTM is fitted to both the pre-intervention and post-intervention parts of the scan. The BP_{NDs} are estimated separately for each part, while the

other parameters (R_1 and k_2) are constrained to be constant throughout the entire scan. The target occupancy in the post-intervention part is calculated as the fractional decrease in BP_{ND} .

4.4 QUANTIFYING THE DOSE-OCCUPANCY RELATIONSHIP

When several occupancy datapoints, at different doses, have been collected, it is possible to quantify the relationship between drug exposure and target occupancy. Assuming a single binding site and non-cooperative binding, the relationship between plasma drug concentration (C_p) and target occupancy (Δ) can be expressed as,

$$\Delta = \Delta_{\max} \frac{C_p}{C_p + IC_{50}}, \quad (11)$$

Where Δ_{\max} is the maximal attainable occupancy, and IC_{50} is the half-maximal inhibitory concentration (i. e. plasma concentration corresponding to an occupancy of $\Delta_{\max}/2$), a measure of the protein-ligand binding strength. If the plasma drug concentration is not available, the administered dose can be used instead. In those cases, the dose required for half-maximal occupancy will be estimated in place of the IC_{50} . Equation 11 is sometimes referred to as the Emax model.

Δ_{\max} and IC_{50} are estimated by fitting the measured data to Equation 11. In theory, only two occupancy estimates are necessary to yield the parameter estimates, but because of the noisy nature of both PET data and plasma samples, several datapoints, ideally covering a wide range of occupancies, is typically used (Takano et al., 2016). To obtain the desired range of occupancies, it is routine to use an adaptive study design, where the administered dose is decided based on the occupancies estimated from previous scans.

CENTRAL NERVOUS SYSTEM APPLICATIONS OF PET

5.1 CNS PET TRACERS

PET neuroimaging is a wide field, spanning multiple radiotracers and applications. Some of the more common applications include [^{18}F]FDG PET to detect altered patterns of glucose metabolism, and imaging with radioligands for amyloid-beta and tau protein, both neuropathological hallmarks of Alzheimer's disease.

Radiotracing of neurotransmission can also be very useful, both to inform clinical practice, aid in drug discovery, and for better understanding of brain function. Neurotransmitter systems that can be imaged with PET include, among others, the dopaminergic, serotonergic, GABAergic, and glutamatergic systems (Gunn et al., 2015).

An ideal CNS PET tracer needs to cross the BBB. It should bind specifically to a target, with a suitable affinity. For quantitative imaging, it is important that the kinetic profile can be described by available mathematical models. Ideally, there should also be relatively little inter- and intra-subject variability in binding.

Here, some background is provided for the radiotracers that have been used in the studies included in the thesis.

5.1.1 TSPO PET and [^{11}C]PBR28

Neuroinflammation is a pathologic hallmark of several CNS diseases, including Alzheimer's, Parkinson's, Huntington's, and stroke (Belarbi et al., 2020; Minter, Taylor, and Crack, 2016; Palpagama et al., 2019; Stuckey et al., 2021). Although evidence suggests the involvement of neuroinflammation in these disorders, its role is often not fully understood.

Existing and emerging targets for PET imaging of neuroinflammation include the purinergic receptors P2X₇R and P2Y₁₂R, triggering receptor expressed on myeloid cells 1, cannabinoid receptor 2, and cyclooxygenase enzymes (Jain et al., 2020; Narayanaswami et al., 2018).

The most explored target for neuroinflammation PET imaging is the 18-kDa translocator protein (TSPO). TSPO is a mitochondrial protein, involved in several functions, including transmembrane transport of cholesterol. It is expressed on the outer mitochondrial membrane of glial cells (Casellas, Galiegue, and Basile, 2002). TSPO is over-expressed in activated microglia, but also present in other cells, in-

cluding astrocytes and endothelial cells (Cosenza-Nashat et al., 2009; Nutma et al., 2019).

Over the past three decades, numerous PET tracers targeting TSPO have been introduced. The first TSPO PET tracer to gain widespread popularity was [^{11}C]PK11195. PK11195 is a potent TSPO antagonist, which was first synthesised in 1983, and was first used as a ^{11}C -labelled PET tracer in 1986 (Benavides et al., 1983; Charbonneau et al., 1986). Some less favourable imaging characteristics of [^{11}C]PK11195, including low level of BBB penetration and high levels of non-specific binding in both plasma and tissue, motivated the development of numerous second-generation TSPO tracers (Lagarde, Sarazin, and Bottlaender, 2018), including [^{11}C]DPA-713, [^{11}C]ER176, and [^{18}F]FEPPA (Ikawa et al., 2017; Selleri et al., 2001; Wilson et al., 2008).

An issue with TSPO PET is that the reported results across studies are often conflicting (Dupont et al., 2017; Lagarde, Sarazin, and Bottlaender, 2018).

[^{11}C]PBR28 (Briard et al., 2008) is a very widely employed second-generation TSPO PET tracer. Compared to [^{11}C]PK11195, it has relatively higher specific signal (Fujita et al., 2017). For many second-generation tracers, including [^{11}C]PBR28, the affinity to TSPO is affected by a single nucleotide polymorphism on the TSPO gene (rs6971) (Owen et al., 2010, 2012). Subjects are genotyped before inclusion in PET studies, and are classified as either high-affinity (HAB), low-affinity (LAB), or mixed-affinity binders (MAB). For [^{11}C]PBR28, there is nearly a two-factor difference in V_T between HABs and MABs. For LABs, the specific binding is too low for clinical applicability (Fujita et al., 2017). It has also been shown that there are significant diurnal changes in [^{11}C]PBR28 V_T (Collste et al., 2016).

Quantification of TSPO PET data is complicated by several factors, including the presence of TSPO on the endothelium, and difficulties with obtaining accurate measurements of plasma free fractions (Collste et al., 2016; Rizzo et al., 2014). The [^{11}C]PBR28 kinetics are better described by the 2TCM than the 1TCM (Fujita et al., 2008). A 2TCM variation (2TCM-1K) that accounts for irreversible binding to endothelial TSPO has been proposed for quantification (Rizzo et al., 2014).

Because TSPO is expressed throughout the brain, no suitable reference region exists for TSPO PET tracers. Still, many attempts have been made at noninvasive quantification in TSPO PET. Several studies have employed supervised clustering methods to extract voxels with minimal specific binding. Others have calculated simple ratio-based outcome measures. Both approaches have been shown to produce outcomes that have very little association with AIF-based quantification (Albrecht et al., 2018; Matheson et al., 2017; Plavén-Sigray et al., 2018a).

5.1.2 Serotonin 2A Receptor and [¹¹C]Cimbi-36

Serotonin (5-hydroxytryptamine; 5-HT) has been linked to several CNS disorders. There are a total of fourteen serotonin receptor subtypes. Some important PET tracers targeting the serotonin system include [¹¹C]WAY-100635 and [¹¹C]CUMI-101 for serotonin 1A receptor, [¹¹C]AZ10419369 for serotonin 1B receptor, [¹¹C]SB207145 for serotonin 4 receptor, and [¹¹C]DASB for the serotonin transporter (Ginovart et al., 2001; Marnier et al., 2009; Milak et al., 2010; Pike et al., 1995; Varnäs et al., 2011).

The serotonin 2A receptor (5-HT_{2A}R) is one of three serotonin 2 receptor subtypes. The 5-HT_{2A}R is responsible for the hallucinogenic effects of some recreational drugs (Halberstadt, 2015), and changes in 5-HT_{2A}R levels has been linked with depression (Bhagwagar et al., 2006). 5-HT_{2A}R PET tracers include the antagonists [¹⁸F]Altanserin (Sadzot et al., 1995) and [¹¹C]MDL100907 (Talbot et al., 2012).

[¹¹C]Cimbi-36 was the first 5-HT_{2A}R agonist radiotracer to be validated for applications in human brain (Ettrup et al., 2014). It has a strong affinity to 5-HT_{2A}R (Ettrup et al., 2011), but also binds to the serotonin 2C receptor subtype (Ettrup et al., 2016; Finnema et al., 2014).

Early analyses showed that the *in vivo* kinetics of [¹¹C]Cimbi-36 were well-described by a 2TC model (Ettrup et al., 2014). In the same study, it was demonstrated that the cerebellum V_T was unchanged after blocking, indicating that it can be used as a reference region. In subsequent studies, reference tissue modeling with STRM has been frequently employed (da Cunha-Bang et al., 2019; Madsen et al., 2019; Yang et al., 2019). However, compared to the 2TCM, the SRTM slightly underestimates the BP_{ND} (Ettrup et al., 2014). The magnitude of the negative bias with SRTM quantification is comparable to that seen in other radioligands, such as [¹¹C]WAY-100635 (Parsey et al., 2000) and [¹⁸F]FE-PE2I (Sasaki et al., 2012). [¹¹C]Cimbi-36 BP_{NDs} calculated with SRTM has relatively low test-retest variability (Ettrup et al., 2016).

[¹¹C]Cimbi-36 has been shown to be sensitive to changes in endogenous serotonin levels, both in animals (Jørgensen et al., 2017; Yang et al., 2017) and in humans (Erritzoe et al., 2020).

Several psychedelic and antipsychotic drugs have a high affinity for 5-HT_{2A}R (González-Maeso and Sealfon, 2009), and [¹¹C]Cimbi-36 has been used to quantify 5-HT_{2A}R occupancy by psilocin (Madsen et al., 2019).

5.1.3 Imaging Synaptic Density and [¹¹C]UCB-J

The synaptic vesicle protein 2A (SV2A) is transmembrane protein found on synaptic vesicles. SV2 is present in all synaptic vesicles,

with very little intervesicle variation in numbers (Mutch et al., 2011). SV2A, the most widely distributed SV2 variant, has been assumed to be a marker of synaptic density - a concept that lacks an exact formal definition (Serrano et al., 2022).

PET tracers for SV2A have only recently been developed (Bretin et al., 2013), and the interest in SV2A PET escalated with the introduction of [^{11}C]UCB-J in 2014 (Mercier et al., 2014). Even though [^{11}C]UCB-J is still a relatively new PET tracer, it has already been used for a wide range of applications. Reduced SV2A measured by [^{11}C]UCB-J PET in humans has been reported in Alzheimer's disease, cannabis use disorder, depression, epilepsy, frontotemporal dementia, human immunodeficiency viruses, Parkinson's Disease, and schizophrenia (D'Souza et al., 2021; Finnema et al., 2020; Holmes et al., 2019; Malpetti et al., 2022; Radhakrishnan et al., 2021; Venkataraman et al., 2022; Weiss et al., 2021; Wilson et al., 2020).

Early preclinical evaluation showed that [^{11}C]UCB-J had excellent imaging characteristics (Nabulsi et al., 2016), which was later confirmed in humans (Finnema et al., 2016, 2018).

1TCM -based quantification of [^{11}C]UCB-J works better than 2TCM -based quantification, has low test-retest variability, and works very well with relatively short TACs (Finnema et al., 2018; Tuncel et al., 2021). [^{11}C]UCB-J V_T and BP_{ND} are not affected by altered blood flow (Smart et al., 2021). Efforts to move to noninvasive quantification of [^{11}C]UCB-J binding have been complicated by the ubiquitous expression of SV2A. [^{11}C]UCB-J signal is low, and only slightly displaceable, in white matter (Varnäs, Stepanov, and Halldin, 2020). The white matter region centrum semiovale has been proposed as a reference region, and used for SRTM-based estimation of [^{11}C]UCB-J BP_{ND} (Koole et al., 2019). However, as some portion of the centrum semiovale binding is displaceable, it does not represent an ideal reference region.

SV2A is also the target for the antiepileptic drugs levetiracetam and brivaracetam, making [^{11}C]UCB-J PET a suitable tool for quantifying the occupancy of these drugs.

5.2 PET IMAGING IN CNS DRUG DEVELOPMENT

In recent years, PET has become an important tool in drug development, especially for drugs targeting the CNS. Previously, the assessment of CNS drug candidates has had to rely on clinical outcomes and peripheral pharmacokinetic measures (Gunn and Rabiner, 2017). Because of the ability of PET to visualize and measure molecular processes *in vivo*, there are several useful applications of PET in the drug discovery and development processes. First, PET can be used to study the kinetics and distribution of the drug. Further, if a PET tracer binding to the same target as the drug is available, target engagement can

be confirmed by scanning subjects before and after administration of the drug. If several such scans are pooled, it is possible to establish a relationship between the administered dose and the target occupancy, which can guide dosing. Lastly, PET can also be used to monitor treatment effect, for example by measuring the extent of a tumor or lesion.

In clinical drug development, the costs increase with each consecutive phase of human testing. Therefore, it is very important to get good assessment of a drug candidate's likelihood for success as early as possible, and stop development of candidates that do not display the desired characteristics. Morgan's pillars of drug survival were first introduced in a study summarizing data from Phase II decisions at Pfizer (Morgan et al., 2012). The three pillars represent the most important characteristics of a drug that will define success in Phase II. In the words of Gunn and Rabiner (2017), they can be summarized as, (i) tissue exposure, (ii), target engagement, and (iii) pharmacological activity. PET imaging can aid in the assessment of all three pillars (Gunn and Rabiner, 2017).

Pillar i, tissue exposure, entails both that the drug must reach the target site, but also, that it is not washed out too quickly. For drugs targeting the CNS, the target is separated from the peripheral bloodstream by the BBB, and concentration in plasma cannot be used as evidence of available drug at its target site. If direct labeling of the drug candidate with a positron emitting radionuclide is possible, PET can be used to map its *in vivo* distribution (Varrone, Bundgaard, and Bang-Andersen, 2022). This type of PET experiment, not only contributes to confidence in BBB penetration, but kinetic modeling of the data can also inform on how the drug is transported across the BBB (Gunn and Rabiner, 2017). These distribution studies are best performed just after or during the first trials in humans. However, they are often also done pre-clinically before first-in-human studies (Varrone, Bundgaard, and Bang-Andersen, 2022). For drug targets in the periphery, direct radiolabeling of the drug can also be used to confirm that the drug does not cross the BBB, in order to make sure that CNS-related side-effects are unlikely (Varrone, Bundgaard, and Bang-Andersen, 2022).

Pillar ii, target engagement, points to occupancy of the intended target by the drug. For PET to contribute here, it is a requirement that a PET tracer with the same specific target as the drug exists. For new drug targets, development of suitable PET tracers to use for this purpose can be a part of the drug development process (Varrone, Bundgaard, and Bang-Andersen, 2022). In PET occupancy studies, subjects are scanned both before and after the administration of the drug. The target occupancy is calculated as the fractional decrease in specific binding between the two scans. When occupancy data is collected at several different doses, the dose-occupancy relationship can be established. This can assist with dosing in subsequent stud-

ies. Already in 1988, PET occupancy studies were used to establish the therapeutic occupancy range for antipsychotic drugs targeting the dopamine D₂ receptor (Farde et al., 1988). Occupancy is both a function of time and dose. For assessment of drug candidates, it can therefore be of value to study the occupancy at different time points after drug administration, especially if the free drug concentrations in plasma and brain are not in equilibrium (Gunn and Rabiner, 2017)

Pillar iii, pharmacological activity, entails the functional modulation of the target by the drug. Compared to the two first pillars, the use of PET to assess pharmacologic activity is not yet as widespread (Gunn and Rabiner, 2017). PET imaging can be used to detect downstream physiological changes induced by the drug. For example, dopamine transporter imaging has been used to monitor treatment response in Parkinson's disease, and amyloid-beta imaging to monitor treatment response in Alzheimer's disease (Parkinson Study Group, 2002; Rinne et al., 2010).

Part III

AIMS

"What makes the desert beautiful," said the little prince,
"is that somewhere it hides a well [...]"

— Antoine de Saint-Exupéry,
The Little Prince

AIMS

The overall aim of this thesis is to improve the utility of PET for quantification of drug interactions in the living human brain. This aim is reached by evaluating common assumptions concerning analytical methods and experimental design, and by developing new analytical methods, applicable for different types of tracers and study designs.

The specific objective for each paper is presented below.

- Paper I: To investigate the assumption that nondisplaceable binding is comparable across subjects. Specifically, we investigate whether the nondisplaceable component of the TSPO PET tracer [^{11}C]PBR28 is different between three clinical populations and their matched controls.
- Paper II: To provide evidence to guide the design of PET occupancy studies. Further, to develop a new likelihood-based estimator for drug interaction parameters.
- Paper III: To develop and evaluate a new class of kinetic models, which enables analysis of data from PET experiments where a drug is introduced during the PET scan.

Part IV

PAPER I

Words are the source of misunderstandings.

— Antoine de Saint-Exupéry,
The Little Prince

METHODS

In paper I, we compared the nondisplaceable, specific, and total distribution volumes (V_{ND} , V_S , V_T) of clinical populations with their matched controls.

7.1 DATA ACQUISITION

The data in paper I consisted of four previously published datasets with the TSPO PET tracer [^{11}C]PBR28. In one dataset, healthy subjects were scanned before and after an intervention with the neurotoxin lipopolysaccharide (LPS; Sandiego et al. (2015)). The three remaining datasets consisted of clinical subjects with indications for alcohol use disorder (AUD; Hillmer et al. (2017a)), first episode psychosis (FEP; Collste et al. (2017)), and Parkinson's disease (PD; Varnäs et al. (2019)), each with matched healthy controls. The LPS and AUD datasets were acquired at the Yale PET center (New Haven; Connecticut, US), and the FEP and PD datasets were acquired at Karolinska Institutet (KI, Solna, Stockholm, Sweden). An overview of the datasets, with summary of some key information, is presented in Table 1.

In all four datasets, PET data was acquired in a high-resolution research tomograph (HRRT; Siemens), and arterial blood was collected throughout the scans. The PET scan duration was 120 min for the LPS and AUD datasets, 90 min for the FEP dataset, and 72 min for the PD dataset. In addition, all subjects underwent T₁-weighted MRI scans for region of interest (ROI) delineation.

All subjects were genotyped for the rs6971 polymorphism, and low-affinity binders were excluded from all studies. Thus, all included subjects were either high-affinity binders (HABs) or mixed-affinity binders (MABs).

7.2 ESTIMATION OF V_T

V_T was estimated using the standard two-tissue compartment model (2TCM), with arterial plasma input functions (AIFs). The blood volume (v_B) was fitted. In all datasets, V_T values were reported for cerebellum and frontal cortex, except for the PD dataset, where striatum was reported instead of frontal cortex. In addition, V_T values in parietal cortex, occipital cortex, temporal cortex, putamen, caudate and thalamus were calculated.

Group	Genotype	Sex [F/M]	Age [mean±SD (range)]
Sandiego et al., 2015			
LPS challenge	3 HAB	0/3	28.0±6.0 (22.7 - 34.5)
	5 MAB	0/5	23.6±5.1 (19.1 - 31.1)
Hillmer et al., 2017			
AUD	7 HAB		40.9±7.9 (31.6 - 55.2)
	7 MAB		37.9±10.4 (26.9 - 51.0)
Controls	8 HAB		37.4±9.0 (26.3 - 48.4)
	7 MAB		32.8±14.6 (19.1 - 55.6)
Collste et al., 2017			
FEP	6 HAB	1/5	29.8±8.2 (20 - 40)
	10 MAB	4/6	27.7±8.8 (19 - 47)
Controls	9 HAB	5/4	27.8±9.3 (22 - 50)
	7 MAB	4/3	25.7±8.2 (20 - 43)
Varnäs et al., 2019			
PD	8 HAB	0/8	63.6±4.3 (57.1 - 69.1)
	8 MAB	1/7	63.4±6.4 (55.2 - 73.2)
Controls	8 HAB	1/7	64.9±4.9 (57.8 - 71.5)
	8 MAB	0/8	62.1±5.3 (56.1 - 72.0)

Table 1: Summary of datasets, with basic demographic information, from paper I.

F = female; M = male; SD = standard deviation; HAB = high-affinity binder; MAB = mixed-affinity binder; LPS = lipopolysaccharide; AUD = alcohol use disorder; FEP = first-episode psychosis; PD = Parkinson's Disease.

7.3 SIMULTANEOUS ESTIMATION OF V_{ND}

Brain-wide V_{ND} values for each subject were calculated using simultaneous estimation of V_{ND} (SIME; Ogden, Zanderigo, and Parsey (2015)). SIME works by predefining a grid of possible V_{ND} values. For each value on the grid, a 2TCM is fitted to a group of ROIs, with the constraint that $k_2 = K_1 \cdot V_{ND}$ in all regions. This reduces the number of estimated parameters from 4 to 3 for each ROI, making the V_{ND} estimation much more reliable than in the traditional 2TCM. The residual sum of squares (RSS) for all frames and ROIs is then computed for all V_{ND} values in the grid. Frames were weighted by the square root of the frame duration. No differential weighting was applied to the ROIs, because it has been shown for [^{11}C]WAY-100635 that size-based ROI weights have minimal effect on SIME V_{ND} (Schain et al., 2017). The V_{ND} value that minimizes the RSS is chosen as the brain-wide estimate for V_{ND} .

For our analyses we chose a V_{ND} grid ranging from 0 to 5, with a step size of 0.1. The range was chosen, because previous research suggests that this should comfortably cover potential V_{ND} values for [^{11}C]PBR28 (Plavén-Sigraý et al., 2019; Schain et al., 2018). In our implementation of SIME, we included eight regions; cerebellum, parietal cortex, frontal cortex, occipital cortex, temporal cortex, putamen, caudate and thalamus. v_B was fitted for each ROI separately.

7.4 ESTIMATION OF V_S

Regional V_S values were calculated from 2TCM- V_T s and SIME- V_{ND} s, as $V_S = V_T - V_{ND}$.

7.5 STATISTICAL ANALYSES

All statistical analyses were performed with MATLAB (version 9.5; MathWorks). For the LPS dataset, the percentage change in each outcome measure (V_T , V_S , V_{ND}) between the two scans, was calculated as $100 \cdot (\text{preLPS} - \text{postLPS})/\text{preLPS}$. A paired-sample t-test was applied to test the difference between the pre- and post-LPS scans.

For the three clinical datasets (AUD, FEP, and PD) a univariate 2-way analysis of variance (ANOVA) without interaction terms was used, where log-transformed outcome measures were the dependent variables, and diagnosis and genotype were fixed factors:

$$\log(Y) = \beta_0 + \beta_{\text{diagnosis}}x_{\text{diagnosis}} + \beta_{\text{control}}x_{\text{control}} + \beta_{\text{HAB}}x_{\text{HAB}} + \beta_{\text{MAB}}x_{\text{MAB}}.$$

Y represents the outcome measures (V_T , V_S , V_{ND}), and diagnosis is either AUD, FEP or PD. All x s indicate group assignment, as either 0 or 1. The percentage difference in each outcome measure between the

diagnosed groups and controls was calculated from the regression coefficients (β) as $100 \cdot e^{\beta_{\text{diagnosis}} - \beta_{\text{control}}} - 1$ (Schain et al., 2018). From the ANOVA model equation,

$$\frac{Y_{\text{diagnosis}}^{\text{HAB}}}{Y_{\text{control}}^{\text{HAB}}} = \frac{e^{\beta_0} e^{\beta_{\text{diagnosis}}} e^{\beta_{\text{HAB}}}}{e^{\beta_0} e^{\beta_{\text{control}}} e^{\beta_{\text{HAB}}}} = e^{\beta_{\text{diagnosis}} - \beta_{\text{control}}}$$

$$\frac{Y_{\text{diagnosis}}^{\text{MAB}}}{Y_{\text{control}}^{\text{MAB}}} = \frac{e^{\beta_0} e^{\beta_{\text{diagnosis}}} e^{\beta_{\text{MAB}}}}{e^{\beta_0} e^{\beta_{\text{control}}} e^{\beta_{\text{MAB}}}} = e^{\beta_{\text{diagnosis}} - \beta_{\text{control}}}.$$

It follows that the percentage difference in outcome measures between the diagnosis and control groups across genotypes can be calculated as,

$$100 \cdot \frac{Y_{\text{diagnosis}} - Y_{\text{control}}}{Y_{\text{control}}} = 100 \cdot (e^{\beta_{\text{diagnosis}} - \beta_{\text{control}}} - 1)$$

Percentage difference in outcome measures between HABs and MABs was computed in the same manner, as $100 \cdot e^{\beta_{\text{HAB}} - \beta_{\text{MAB}}} - 1$.

The ANOVA was later repeated with a diagnosis-genotype interaction term, revealing no significant effect interaction on any of the outcome measures in any of the datasets.

To exclude the possibility that atrophy was driving any between-group difference in V_{ND} , the ANOVA was rerun for V_{ND} on the AUD, FEP and PD datasets, with regional grey matter volume as an additional covariate.

Also, to test whether the results were sensitive to the choice of regions used to calculate the SIME V_{ND} , we reran the SIME analyses on a larger set of thirteen regions for the datasets acquired at KI (FEP and PD). The ANOVA was repeated on those V_{ND} estimates, resulting in the same conclusions as for the original eight regions.

Throughout all statistical analyses, an α -level of 0.05 was used. The reported p-values have not been corrected for multiple comparisons.

RESULTS AND DISCUSSION

$[^{11}\text{C}]\text{PBR28 } V_T$ has frequently been used as a direct measure of TSPO expression. This requires the assumption that any within-subject change or between-group difference in V_T arises exclusively from differences in the signal from specific binding to TSPO.

Globally uniform and unaltered nondisplaceable signal is one of the central assumptions in PET kinetic modeling. In the traditional compartment models the contributions from nondisplaceable and specific uptake cannot be reliably disentangled. Thus, the use of total binding as a proxy for specific binding, has been natural, given the limitations of the models. Still, very little research has been done to confirm that this substitute of outcome measures is valid.

With SIME, it is now possible to reliably estimate V_{ND} from a single PET scan. In paper I, we applied SIME to four different $[^{11}\text{C}]\text{PBR28}$ datasets to investigate whether the assumption that between-group differences in $[^{11}\text{C}]\text{PBR28 } V_T$ can be attributed exclusively to changes in TSPO expression is a valid one.

We found significant between-group differences in V_{ND} in two of the datasets. In this chapter, all results from Paper I are presented and discussed. Figures presenting the main findings can be found in the published manuscript (Appendix A). Here, the main findings are presented in tables, and figures are reserved for not previously published results.

8.1 LIPOPOLYSACCHARIDE CHALLENGE

In the first dataset, eight young males were scanned twice, before and after LPS administration. LPS is a toxin, and has previously been shown to result in higher signals with TSPO PET tracers in several different species, including mouse, rat, pig and non-human primates (de Lange et al., 2018; Dickens et al., 2014; Hillmer et al., 2017b; Vignal et al., 2018).

As expected, the mean V_T values were significantly increased following the LPS intervention. The SIME- V_{ND} s on the other hand, appeared to be unaffected by the toxin. By subtracting the nondisplaceable signal, the effect of the intervention becomes even more evident. Although the coefficients of variation were not different between V_T and V_S , there was a much higher mean percentage change from pre- to post-LPS in V_S compared to V_T . In frontal cortex, for example, the mean difference in V_T was 46% ($P=0.0012$), while the mean difference in V_S was 66% ($P=0.00026$). Mean percentage differences for all three

	Frontal cortex	Cerebellum
V_T	46% P = 0.0012	40% P = 0.016
V_S	66% P = 0.00026	59% P = 0.0052
V_{ND}	15% P = 0.38	

Table 2: Mean percentage difference in outcome measures between pre- and post-LPS scans. Positive values indicate that outcome measures are higher post-LPS. p-values (P) have not been corrected for multiple comparisons.

LPS = lipopolysaccharide; V_T = total distribution volume; V_S = specific distribution volume; V_{ND} = nondisplaceable distribution volume.

parameters, in frontal cortex and cerebellum, are presented in Table 2.

While these findings might seem unsurprising, they are very important. It has previously been demonstrated in simulations that high specific binding does not spill over and result in artificial overestimation of SIME- V_{ND} (Plavén-Sigray et al., 2019). With this dataset, we are able to demonstrate clearly, on real human data, that SIME can provide V_{ND} values that are uncorrelated with V_S .

Using the LPS dataset, we attempted to get an alternative estimate of V_{ND} by applying a modified variant of the Lassen plot. The rationale was that, by plotting the regional differences in V_T between pre- and post-LPS against the corresponding pre-LPS V_{TS} , similar to the Lassen plot, the x-intercept should reflect the V_{ND} . This approach did not result in reasonable V_{ND} estimates, and very poor R^2 values were observed when performing the linear fit. Although this could result from a number of reasons, a plausible explanation could be that the effect of LPS is not uniform throughout the brain, which would be a required assumption for this method to be meaningful.

8.2 EFFECT OF DIAGNOSIS

In the AUD dataset, all parameter values were on average lower for the AUD subjects compared to their controls. The results for this dataset is presented in Table 3. SIME revealed that the between-group difference in V_T seems to be mainly driven by V_{ND} (-34% , $P=0.00084$). A sizable but insignificant difference remains in V_S , especially in

frontal cortex where V_S was, on average, 19% lower in the AUD subjects compared to their matched controls ($P=0.065$).

The group effect on V_{ND} is very pronounced. However, the reason for this effect is not immediately obvious. One possible explanation is differences in brain tissue composition and condition. Prolonged abuse of alcohol is known to have degenerative effects on the brain (de la Monte and Kril, 2014). Rerunning the statistical analyses with gray matter volume as a covariate did not change the outcomes, suggesting that the lower V_{ND} of the AUD subjects is not caused by partial volume effects. However, this does not necessarily exclude the possibility that the difference is caused by excessive white matter atrophy in the AUD group. Significant age effects on V_T have previously been shown with several TSPO PET tracers, including [^{11}C]PBR28 (Guo et al., 2013; Kumar et al., 2012; Tuisku et al., 2019).

The trend-level group difference in frontal cortex V_S leaves the question regarding AUDs potential effect on TSPO expression fairly open. Previous TSPO PET studies on AUD have not been entirely conclusive. In animals, TSPO PET and autoradiography have generally show either no difference or higher TSPO binding in alcohol exposed animals (Kim et al., 2018; Saba et al., 2018; Tournier et al., 2021; Tyler et al., 2019). In humans, one study has found significantly lower hippocampal [^{11}C]PBR28 V_T in alcohol dependent subjects compared to controls (Kalk et al., 2017). However, V_T s were not significantly different in four other brain regions. In another study, MAB AUDs had significantly lower V_T s than MAB controls, but the same was not seen in HABs (Kim et al., 2018). Our findings offer a possible explanation for this. If the V_T difference is indeed driven by reduced V_{ND} , it should be easier to detect in MABs, as the V_{ND} represents a higher fraction of the total signal in this group.

In the FEP dataset we saw no evidence of different V_{ND} between patients and controls (14%, $P=0.30$). The FEP results are presented in Table 4. In frontal cortex, there was a statistically significant difference in both V_T (-36%, $P=0.045$) and V_S (-57%, $P=0.033$), while in cerebellum, p-values just above the α -level were observed for both V_T (-32%, $P=0.060$) and V_S (-44%, $P=0.054$). Although the same outcome is reached with both V_T and V_S again, like in the LPS dataset, the mean percentage separation between groups is much higher for V_S in both regions.

The question regarding neuroinflammation as quantified by TSPO PET in psychosis has been a polarizing one. Several attempts to quantify a potential inflammatory response in psychosis using TSPO PET have led to widely different conclusions. As of 2020, at least 14 original studies comparing TSPO PET outcomes between psychosis patients and controls had been published (De Picker and Morrens, 2020). In these studies, both methodological and demographic aspects of the study designs were widely varying, complicating the direct compari-

	Frontal cortex	Cerebellum
V_T	-23% P = 0.0048	-18% P = 0.012
V_S	-19% P = 0.065	-13% P = 0.15
V_{ND}	-34% P = 0.00084	

Table 3: Mean percentage difference in outcome measures between AUD subjects and their matched controls. Negative values indicate that outcome measures are lower for AUD compared to controls. p-values (P) have not been corrected for multiple comparisons. AUD = alcohol use disorder; V_T = total distribution volume; V_S = specific distribution volume; V_{ND} = nondisplaceable distribution volume.

son of studies. Two meta-analyses have been published on the topic, each reaching a different conclusion (Marques et al., 2019; Plavén-Sigra y et al., 2018b).

Since the publication of Paper I, a study has been published where SIME was used to calculate [^{11}C]PBR28 V_{ND} in schizophrenia (Marques et al., 2021). While that study did not include a control group, the SIME V_{ND} values obtained in that population was very well aligned with the FEP subjects included in Paper I. They also used pharmacological competition to estimate V_{ND} with the Lassen plot, and obtained near-identical mean V_{ND} to one that has previously been reported for healthy controls using the same approach (Marques et al., 2021; Owen et al., 2014).

In the PD dataset we observed a clear between-group difference in V_{ND} (-34%, $P=0.0032$), but no apparent effect on V_T or V_S , in either striatum or cerebellum (see Table 5). Like with AUD and psychosis, previous TSPO PET studies in PD have yielded mixed results. In studies using second generation TSPO tracers there is a tendency that no effect is seen when V_T is the reported outcome measure, while studies using ratio-based outcomes find higher binding in PD compared to controls (Ghadery et al., 2017; Koshimori et al., 2015; Lavis se et al., 2021; Terada et al., 2016). Given our finding of lower V_{ND} in PD, it is possible that the previous reports of higher ratio-based outcome measures in PD have in fact been driven by lower nondisplaceable concentrations rather than higher specific binding to TSPO. The lower nondisplaceable uptake we observed in PD does not necessarily exclude the possibility that specific binding is simultaneously higher. However, our results present no convincing evidence that this should be the case (for V_S $P=0.11$ in cerebellum, and $P=0.42$ in striatum).

	Frontal cortex	Cerebellum
V_T	-36% P = 0.045	-32% P = 0.060
V_S	-57% P = 0.033	-44% P = 0.054
V_{ND}	14% P = 0.30	

Table 4: Mean percentage difference in outcome measures between FEP subjects and their matched controls. Negative values indicate that outcome measures are lower for FEP compared to controls. p-values (P) have not been corrected for multiple comparisons.

FEP = first episode psychosis; V_T = total distribution volume; V_S = specific distribution volume; V_{ND} = nondisplaceable distribution volume.

We saw clear between-group differences in V_{ND} in two of the three included clinical datasets; V_{ND} was significantly lower for AUD and PD, but not for FEP. Like AUD, PD is also associated with accelerated brain tissue atrophy (Gao et al., 2017). However, again, including gray matter volume in the statistical analyses did not change the outcomes. Although schizophrenia by some is viewed as a neurodegenerative disorder, it does not belong to the same category as PD or AUD. Both PD and AUD are associated with reduced cerebral perfusion (Durazzo et al., 2010; Saeed, Lang, and Masellis, 2020). However, it has been shown in a simultaneous [^{11}C]PBR28 PET/MR study, that neither [^{11}C]PBR28 SUV nor SUVR are correlated with cerebral blood flow (Sander et al., 2021). Consequently, the underlying reasons for the observed group differences in the AUD and PD datasets remain unclear.

8.3 EFFECT OF GENOTYPE

A significant effect of genotype on V_{ND} was seen in the FEP and PD datasets, but not in the LPS and AUD datasets. Note that there is an overlap in the latter two, with five out of eight LPS baseline scans used as controls in the AUD study. The apparent genotype effect is difficult to conceptualize. The only difference between HABs and MABs is the molecular structure of their TSPO, and it is unclear how this could translate to a difference in V_{ND} . Because the difference is in the same direction as the expected difference in V_S (HABs higher than MABs), a tempting theory could be a spill-over effect from the specific compartment. However, this theory is not in line

	Striatum	Cerebellum
V_T	7.1% P = 0.32	2.2% P = 0.74
V_S	7.0% P = 0.42	15% P = 0.11
V_{ND}	-34% P = 0.0032	

Table 5: Mean percentage difference in outcome measures between PD subjects and their matched controls. Negative values indicate that outcome measures are lower for PD compared to controls. p-values (P) have not been corrected for multiple comparisons.

PD = alcohol use disorder; V_T = total distribution volume; V_S = specific distribution volume; V_{ND} = nondisplaceable distribution volume.

with the results of the LPS experiment, where V_{ND} was unaffected by the increase in V_S .

When all controls were pooled in one analysis the genotype-effect on V_{ND} was clear (P = 0.00016). However, when analyzing the controls from each PET centre separately, it was only evident in the datasets collected at KI. For the Yale controls there was no significant effect of genotype on V_{ND} . This data is presented in Figure 2. There are some key differences in the demographics of the two control populations. Most notably the KI controls span a much wider age range (20 – 72 years) compared to the Yale controls (19 – 55 years). Also, there is a slightly higher fraction of females among the KI controls (9 out of 31) than among to the Yale controls (4 out of 18). It has previously been shown that there is a sex effect on [^{11}C]PBR28 V_T , with higher V_T among females (Tuisku et al., 2019). This does not explain our results, as we see on average lower V_{ND} in the KI MABs than in the Yale MABs (see Figure 2).

Another difference between the datasets is scan duration. All scans from the Yale PET Centre had a duration of 120 min, while the scans conducted at KI ranged from 72 to 90 min. It is not entirely clear how a shorter scan duration would lead to differences in V_{ND} between HABs and MABs. However, this presents a potential avenue for further investigations. Rerunning the analyses on shortened versions of the 120-min TACs could give insight into how the SIME- V_{ND} estimates are affected by scan duration, and whether potential effects are different across genotypes.

If there is truly a genotype effect on V_{ND} , shedding light on the underlying causes could aid in understanding how and when nondisplaceable binding may have confounding effects. Currently, we have

no experimental evidence on the underlying causes, and we do not know whether they are biological or mathematical.

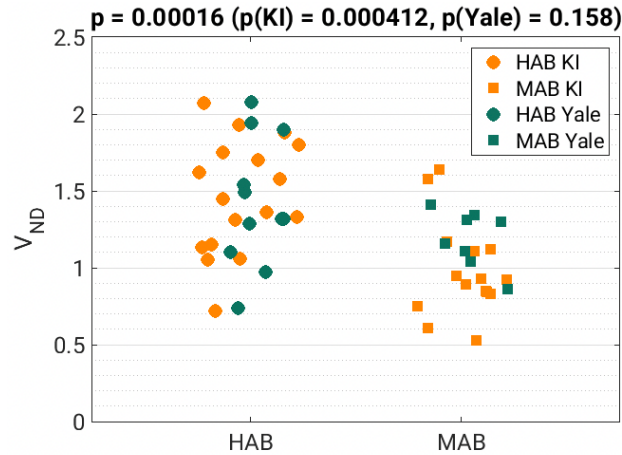


Figure 2: SIME V_{ND} estimates for all controls scanned at KI (orange) and Yale (green).

SIME = Simultaneous estimation of V_{ND} ; HAB = high-affinity binder; MAB = mixed-affinity binder.

Irrespective of cause, this finding emphasises the importance of balancing datasets with regards to genotype. All datasets used in this study were relatively well-balanced, and genotype was accounted for in the statistical analyses.

Previously, polymorphism plots have been used to estimate V_{ND} from TSPO PET data (Guo et al., 2013). The polymorphism plot is conceptually similar to the Lassen plot. The rationale is that by plotting the differences in regional V_T s between HABs and MABs against the HAB V_T s, and fitting a line through the points, the x-intercept should be an estimate of V_{ND} . This method relies on the assumption that V_{ND} is constant across genotypes. Consequently, if there is indeed a genotype effect on V_{ND} , the polymorphism plot is not a valid approach for estimation of V_{ND} .

Although the questions regarding the validity of the polymorphism plot remain unanswered, we have performed this analysis for the AUD, FEP and PD datasets, and found that the polymorphism plot V_{ND} is close to SIME V_{ND} . The mean SIME V_{ND} for each dataset falls within the 95% confidence interval of the polymorphism plot x-intercepts. However, these intervals were quite broad. To illustrate this point, the polymorphism plot for the PD dataset is presented in figure 3. This was the dataset where a polymorphism plot gave the best fit to the data with a R^2 of 0.97 (R^2 was 0.42 for the AUD dataset and 0.90 for the FEP dataset).

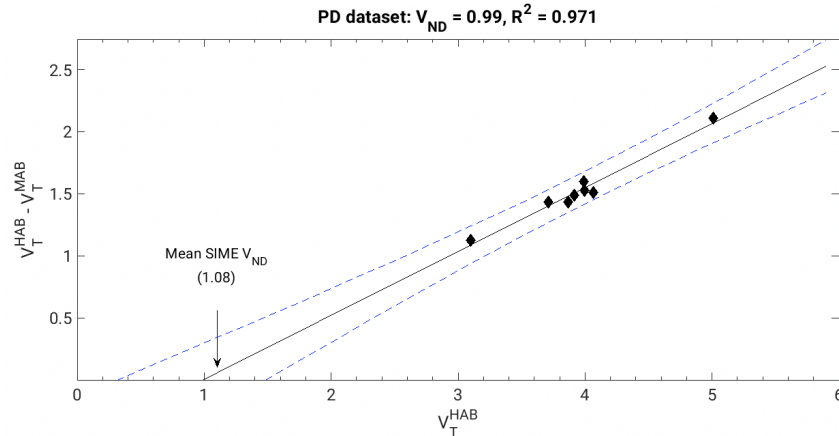


Figure 3: Polymorphism plot for the PD data. The solid black line is the fit through the datapoints, and the dashed blue lines illustrate the 95 % confidence interval of the fit. The mean SIME V_{ND} estimate in the dataset is indicated by an arrow.

PD = Parkinson’s Disease; SIME = Simultaneous estimation of V_{ND} ; HAB = high-affinity binder; MAB = mixed-affinity binder.

8.4 THE SIME METHOD

SIME is a relatively new method, and is not yet fully established in the field. For the case of $[^{11}\text{C}]\text{PBR28}$, it has been tested using simulations, blocking data, and test-retest data (Plavén-Sigray et al., 2019). SIME was concluded to be a useful method for estimation of V_{ND} . Still, further studies are warranted to establish the observed differences in V_{ND} . Pharmacokinetic competition studies could be used to confirm and quantify the between-group differences in V_{ND} that we saw in AUD and PD.

Currently, there is no validated procedure for selection of ROIs to include in the SIME analyses. The presented results were based on TACs from eight different ROIs. Rerunning the analyses on data from thirteen ROIs did not change the outcomes.

We initially did not weight the contributions from the different ROIs differently. Later, the SIME analyses were repeated with size-based ROI weights on all four datasets. Specifically, the contribution of each ROI was weighted by the relative ROI volume, compared to the largest included ROI. Differently weighting the contribution from each ROI did not change the outcome of the analyses.

SIME, as a variant of the 2TCM, relies on an AIF. Accurately defining the true input function is challenging in general, but especially so for TSPO ligands. The $[^{11}\text{C}]\text{PBR28}$ AIF shape depends on genotype (Plavén-Sigray et al., 2019), and it has previously been shown that SIME V_{ND} estimates are affected by AIF shape (Schain et al., 2017).

Part V

PAPER II

It is the time you have wasted for your rose that makes
your rose so important.

— Antoine de Saint-Exupéry,
The Little Prince

METHODS

9.1 SIMULATION OF DATA

In Paper II, simulations were used to assess different study designs for a PET baseline-block experiment, and different methods for analyzing the results from that type of study. For this purpose, we simulated V_T values with realistic and unique noise. The simulations were based on a [^{11}C]Cimbi-36 dataset, where healthy controls were scanned before and after a placebo intervention (da Cunha-Bang et al., 2019).

Throughout all simulations, the true underlying values for the key drug interaction parameters Δ_{max} (maximal attainable occupancy) and IC_{50} (half-maximal inhibitory concentration) were kept constant, at 85% and $2\mu\text{g}/\text{mg}$, respectively. The choice of these values was loosely based on the *in vivo* Δ_{max} and IC_{50} of psilocin binding to the serotonin 2A receptor, which has been estimated to be 76.7% and $1.95\mu\text{g}/\text{L}$ in a [^{11}C]Cimbi-36 baseline-block experiment in healthy humans (Madsen et al., 2019).

In three different simulation experiments, some key aspects of the study design were altered, to see how the estimation of IC_{50} was affected. Those were:

- 1 the range of occupancies in the dataset
- 2 the number of subjects in the dataset
- 3 the level of noise in the plasma drug concentration measurements

In all experiments, 1000 unique datasets were simulated for each condition.

9.1.1 Simulation Experiment 1

The design of simulation experiment 1 is illustrated in Table 6. We investigated the effect of the range of occupancies by simulating six different datasets with increasing dose range and increasing numbers of subjects. The first simulated dataset had five subjects, each receiving doses corresponding to occupancies evenly distributed between 53.3% and 80%. In the next simulation, a sixth subject, receiving a dose corresponding to 46.7% occupancy, was added. In each consecutive simulation, an additional subject with a dose corresponding to

N	INCLUDED OCCUPANCIES [%]
5	53.3, 60.0, 66.7, 73.3, 80.0
6	46.7, 53.3, 60.0, 66.7, 73.3, 80.0
7	40.0, 46.7, 53.3, 60.0, 66.7, 73.3, 80.0
8	33.3, 40.0, 46.7, 53.3, 60.0, 66.7, 73.3, 80.0
9	26.7, 33.3, 40.0, 46.7, 53.3, 60.0, 66.7, 73.3, 80.0
10	20.0, 26.7, 33.3, 40.0, 46.7, 53.3, 60.0, 66.7, 73.3, 80.0

Table 6: Design of simulation experiment 1. The table shows, for each of the six simulated datasets in simulation experiment 1, the number of included subjects (N), and the block-scan occupancies for those subjects.

6.7% occupancy lower than the lowest occupancy in the previous simulation was added. Thus, in the sixth and final simulation, 10 subjects received doses corresponding to occupancies ranging from 20% to 80%.

9.1.2 *Simulation Experiment 2*

In the second experiment, datasets with increasing numbers of subjects were simulated. A dose range corresponding to 40 – 80% occupancy was chosen, based on the results from the first experiment. In each simulation, subjects were administered doses corresponding to occupancies evenly distributed within this range. The sample size was increased from 5 to 25 in steps of one, and further up to 45 in steps of five.

9.1.3 *Simulation Experiment 3*

In the third experiment, we investigated the effect of noise in the measurements of plasma drug concentration (C_P). In the previous experiments, C_P was considered without noise. In this experiment, the C_P estimates (\hat{C}_P) were sampled from a normal distribution where the mean was the true C_P , and the standard deviation was the true C_P multiplied by a noise factor κ :

$$\hat{C}_P \sim N(C_P, \kappa C_P). \quad (12)$$

κ was increased from 0 to 1, in steps of 0.1, for a total of eleven different evaluated noise levels. All simulated datasets included 10 subjects, and a dose range corresponding to 40 – 80% occupancy was used.

9.1.4 Fixing True Parameter Values

True V_T values in seven regions were hard-coded for ten separate subjects. Those seven regions were thalamus, insula, anterior cingulate cortex, posterior cingulate cortex, orbitofrontal cortex, occipital cortex, and cerebellum. Cerebellum- V_T was used only as an estimate of brain-wide V_{ND} for each subject (Ettrup et al., 2014), so that for the other regions, the true underlying V_S would be the difference between V_T in that region and V_T in cerebellum.

The hardcoded V_T values were chosen based on seven healthy subjects, scanned with [^{11}C]Cimbi-36 before and after a placebo intervention (da Cunha-Bang et al., 2019). This dataset originally included eight subjects, but one was excluded from this study, due to missing frames in one of the scans. First, for each of the seven subjects, the true V_T in each region of interest (ROI) was defined as the mean of the two scans. For each ROI, those seven V_T s were combined, and used to calculate the mean and standard deviation of V_T in each ROI. Then, ten ground truth V_T values were defined for each ROI, so that they, when combined, resulted in the same mean and standard deviation as the previously defined true V_T s in the da Cunha-Bang dataset. Finally, the hard-coded V_T values were assigned to ten simulated subjects in an ascending fashion, so that the relative magnitude of each subject's V_T values was consistent across regions. All hard-coded V_T s are listed in Table 7.

As mentioned, true values for Δ_{\max} and IC_{50} were kept constant, at 85% and $2\mu\text{g}/\text{L}$, throughout all simulations. For each target occupancy (Δ), the corresponding C_P s were calculated from these values, by rearranging the Emax model as,

$$C_P = \frac{\text{IC}_{50} \cdot \Delta}{\Delta_{\max} - \Delta}. \quad (13)$$

9.1.5 Applying Unique and Realistic Noise to the Data

To simulate V_T values with realistic noise properties, an estimate of the covariance structure of V_T in the selected ROIs was produced. This calculation was based on the same seven subjects, with pre- and post placebo intervention scans, as the ground truth values (da Cunha-Bang et al., 2019). Regional V_T s for both scans were calculated using the 2TCM with AIF. It was assumed that the placebo had no, or negligible, effect on the V_T estimates, and the dataset was treated as a test-retest. The 6×6 covariance matrix, Σ , describing the covariance of V_T values across the six regions was estimated as,

$$\Sigma = \text{cov}(\mathbf{V}_T^{\text{test}} - \mathbf{V}_T^{\text{retest}}). \quad (14)$$

Where $\mathbf{V}_T^{\text{test}}$ and $\mathbf{V}_T^{\text{retest}}$ are 6×7 matrices of V_T estimates across 6 ROIs (those listed in Table 7) for 7 subjects.

THA	INS	ACC	PCC	ORB	OCC	V_{ND}
11.0	27.0	30.0	24.0	27.0	24.0	8.5
13.0	29.0	33.0	27.0	31.0	27.0	9.5
15.0	31.0	34.0	30.0	35.0	29.0	10.5
17.0	34.0	37.0	31.0	38.5	31.0	12.0
18.0	36.0	38.0	34.0	39.5	33.0	12.5
19.0	37.0	38.5	36.0	40.0	34.0	13.0
20.0	40.0	39.5	39.0	41.0	36.0	14.0
22.0	43.0	42.5	40.0	44.5	38.0	15.0
24.0	45.0	43.5	43.0	48.5	41.0	16.0
25.0	47.0	46.0	45.0	52.5	43.0	17.0

Table 7: Hard-coded V_T values for 10 subjects, in thalamus (THA), Insula (INS), anterior cingulate cortex (ACC), posterior cingulate cortex (PCC), orbitofrontal cortex (ORB), occipital cortex (OCC), and cerebellum (V_{ND}).

Subsequently, the covariance matrix, Σ , was used to apply noise with a realistic covariance structure to the simulated data. Cholesky decomposition of the covariance matrix results in an upper triangular matrix $\mathbf{\Gamma}^T$, consistent with $\Sigma = \mathbf{\Gamma}^T \mathbf{\Gamma}$. To ensure random noise, a 6×1000 matrix, \mathbf{B} , was filled with random numbers sampled from a unit normal distribution (mean = 0, standard deviation = 1). $\mathbf{\Gamma}^T \mathbf{B}$ is then a 6×1000 matrix with covariance Σ . By adding each column in $\mathbf{\Gamma}^T \mathbf{B}$ to a 6×1 matrix of hard coded V_T values, 1000 unique datasets, each with a covariance structure defined by Σ is generated.

To ensure realistic proportions of the added noise, all rows in $\mathbf{\Gamma}^T \mathbf{B}$ were scaled by multiplication with $V_{T,k}^{\text{true}}/34$, where $V_{T,k}^{\text{true}}$ is the hard-coded true value for V_T in region k . Across all regions and scans in the placebo intervention dataset 34 was the mean V_T value.

9.1.6 Simulating Baseline-Block Data

To define the true V_T values for a baseline-block experiment, N subjects were chosen, by simple random sampling without replacement, from the ten hard-coded subjects in Table 7. For experiments with $N > 10$, all predefined subjects were included once, and subsequent subjects were sampled from the same 10. For $N > 20$, $N > 30$ and $N > 40$, all subjects were included 2, 3, and 4 times before randomly sampling remaining subjects. N C_{PS} corresponding to the desired occupancies were calculated according to Equation 13, and randomly

assigned to the N subjects. For each subject, the true baseline and block V_T s were defined as,

$$\begin{cases} V_{T,true}^{\text{base}} = V_{ND}\mathbf{1} + V_S \\ V_{T,true}^{\text{block}} = V_{ND}\mathbf{1} + \left(1 - \Delta_{\max} \frac{C_p}{C_p + IC_{50}}\right) V_S, \end{cases} \quad (15)$$

where $V_{T,true}^{\text{base}}$ and $V_{T,true}^{\text{block}}$ are 6×1 vectors of true V_T values, V_{ND} is the true cerebellum V_T for the subject, and V_S is a 6×1 vector of true V_S values for the subject, calculated as the difference between the true V_T and V_{ND} for each ROI.

Then, 1000 unique instances of each subject were generated by adding noise to $V_{T,true}^{\text{base}}$ and $V_{T,true}^{\text{block}}$ as in described in section 9.1.5.

9.1.7 Simulating Test-Retest Data for Estimation of Covariance Structure

For each simulated baseline-block dataset, a unique test-retest dataset, was simulated, and used for estimation of a covariance matrix. All simulated test-retest datasets consisted of ten subjects. The same ten hard-coded subjects presented in Table 7 were used for this purpose. Noise was added to the ten subjects as described in section 9.1.5.

Using each simulated dataset of ten test and retest V_T s, a covariance matrix, $\hat{\Sigma}$, was estimated by nonlinear shrinkage (Ledoit and Wolf, 2015; Schain, Zanderigo, and Ogden, 2018).

9.2 ANALYSIS OF BASELINE-BLOCK DATA

We compared three different approaches to estimate Δ_{\max} and IC_{50} from a PET baseline-block dataset:

- i Lassen plot applied to regional V_T values to obtain occupancy estimates, followed by fitting the dose-occupancy data to the Emax model
- ii Likelihood Estimation of Occupancy to obtain occupancy estimates, followed by dose-occupancy plot, followed by fitting the dose-occupancy data to the Emax model
- iii Likelihood Estimation of Affinity

All three approaches were applied to all simulated data. Approach (i) is the established method for estimation of drug interaction parameters from V_T values. Approach (ii) is a relatively recent addition to the field, that has already been shown to improve occupancy estimation (Naganawa et al., 2019; Schain, Zanderigo, and Ogden, 2018). Approach (iii) was developed for this paper, and introduced and evaluated for the first time.

All analyses were done in MATLAB (version 9.10; MathWorks).

9.2.1 *The Lassen Plot*

The theoretical framework for the Lassen plot is explained in Section 4.3.1. We used the Cunningham formulation of the Lassen plot, presented in Equation 7 (Cunningham et al., 2010). For each simulated subject, we fitted the Lassen plot equation to the regional V_T s. In the fitting procedure, V_{ND} was constrained to be positive, and Δ was constrained to be between 0 and 1.

9.2.2 *Likelihood Estimation of Occupancy*

Likelihood Estimation of Occupancy (LEO) is a maximum likelihood-based approach for estimation of V_{ND} and occupancy, based on the same key assumptions as the Lassen plot (Schain, Zanderigo, and Ogden, 2018). The method is outlined in Section 4.3.2.

For each simulated subject, the Matlab function `fminsearch` was used to find the minimum of the negative LEO log-likelihood function (Equation 9), with V_{ND} constrained to be positive, and Δ constrained to be between 0 and 1.

9.2.3 *Dose-Occupancy Plot*

The dose-occupancy portion of the data was both simulated and solved using the Emax model (Equation 11). For each simulated dataset, the simulated plasma drug concentration measurements and estimated occupancies (from Lassen plot or LEO), were fitted to Equation 11 using nonlinear curve fitting (`lsqcurvefit` in Matlab). IC_{50} was constrained to be positive, and Δ_{max} was constrained to be between 0 and 1.

9.2.4 *Likelihood Estimation of Affinity*

In Paper II, we introduced Likelihood Estimation of Affinity (LEA), a maximum likelihood-based estimator for calculation of drug interaction parameters from a PET baseline-block dataset with multiple subjects. LEA is based on LEO, in combination with the Emax model (Equation 11). Similar to LEO, it uses the regional V_T values as input. In addition, it also uses each subject's C_P as input. However, the method only accounts for the errors in the V_T estimates, and not for those in the C_P estimates. For the V_T estimates, LEA assumes, like LEO, that they are normally distributed, and that the variance is the same in both the baseline and block scans (see Equation 8).

LEA assumes, like the Emax model, that all subjects in the dataset share one global IC_{50} and one global Δ_{max} .

The data from all subjects in a baseline-block dataset are combined into one log-likelihood function. The LEA log-likelihood function for a dataset with N subjects is given by,

$$\begin{aligned}
& l(\text{IC}_{50}, \Delta_{\text{max}}, V_{\text{ND},1}, V_{\text{ND},2}, \dots, V_{\text{ND},N}, \mathbf{V}_{\text{S},1}, \mathbf{V}_{\text{S},2}, \dots, \mathbf{V}_{\text{S},N} \mid \\
& \mathbf{V}_{\text{T},1}^{\text{baseline}}, \mathbf{V}_{\text{T},2}^{\text{baseline}}, \dots, \mathbf{V}_{\text{T},2}^{\text{block}}, \dots, \mathbf{V}_{\text{T},N}^{\text{baseline}}, \mathbf{V}_{\text{T},1}^{\text{block}}, \mathbf{V}_{\text{T},2}^{\text{block}}, \dots, \mathbf{V}_{\text{T},N}^{\text{block}}, \\
& C_{\text{P},1}, C_{\text{P},2}, \dots, C_{\text{P},N}) \\
& = \sum_{j=1}^N \left[\left(\mathbf{V}_{\text{T},j}^{\text{baseline}} - (V_{\text{ND},j} \mathbf{1} + \mathbf{V}_{\text{S},j}) \right)^{\text{T}} \Sigma^{-1} \left(\mathbf{V}_{\text{T},j}^{\text{baseline}} - (V_{\text{ND},j} \mathbf{1} + \mathbf{V}_{\text{S},j}) \right) \right. \\
& + \left(\mathbf{V}_{\text{T},j}^{\text{block}} - \left(V_{\text{ND},j} \mathbf{1} + \left(1 - \Delta_{\text{max}} \frac{C_{\text{P},j}}{C_{\text{P},j} + \text{IC}_{50}} \right) \mathbf{V}_{\text{S},j} \right) \right)^{\text{T}} \Sigma^{-1} \\
& \left. \left(\mathbf{V}_{\text{T},j}^{\text{block}} - \left(V_{\text{ND},j} \mathbf{1} + \left(1 - \Delta_{\text{max}} \frac{C_{\text{P},j}}{C_{\text{P},j} + \text{IC}_{50}} \right) \mathbf{V}_{\text{S},j} \right) \right) \right].
\end{aligned} \tag{16}$$

$V_{\text{ND},j}$ is the estimated V_{ND} for subject j . $\mathbf{V}_{\text{T},j}^{\text{baseline}}$ and $\mathbf{V}_{\text{T},j}^{\text{block}}$ are $k \times 1$ arrays of k baseline and block V_{T} values for subject j . $C_{\text{P},j}$ is the block-scan plasma drug concentration for subject j . Σ is the covariance matrix of the regional V_{T} values.

Similar to LEO, the dimensionality of the log-likelihood function can be reduced by solving $\frac{\partial}{\partial \mathbf{V}_{\text{S},j}} l = 0$, which yields the following expression for $\mathbf{V}_{\text{S},j}$:

$$\mathbf{V}_{\text{S},j} = \frac{\mathbf{V}_{\text{T},j}^{\text{baseline}} - V_{\text{ND},j} \mathbf{1} + \left(1 - \Delta_{\text{max}} \frac{C_{\text{P},j}}{C_{\text{P},j} + \text{IC}_{50}} \right) \left(\mathbf{V}_{\text{T},j}^{\text{block}} - V_{\text{ND},j} \mathbf{1} \right)}{1 + \left(1 - \Delta_{\text{max}} \frac{C_{\text{P},j}}{C_{\text{P},j} + \text{IC}_{50}} \right)^2}. \tag{17}$$

As a result, the log-likelihood function is just a function of IC_{50} , Δ_{max} , and each subjects V_{ND} , giving a dimensionality of $N + 2$ for N subjects.

The full derivation of the LEA log-likelihood function is presented in Appendix D. The log-likelihood function presented in Equation 16 uses data from one baseline and one block scan per subject. However, the function can easily be extended to account for several block scans per subject.

For each simulated subject, the Matlab function `fminsearch` was used to find the minimum of the negative LEA log-likelihood function, with IC_{50} and V_{ND} constrained to be positive, and Δ_{max} constrained to be between 0 and 1.

9.2.5 Comparison of Parameter Estimates

In Paper II, box plots of parameter estimates were used to compare the IC_{50} estimates from the three different methods. Here, in the the-

sis, the median estimates and interquartile ranges (75th - 25th percentiles) for both the IC_{50} and Δ_{max} estimates are presented in tables.

Throughout this project the emphasis was on estimation of IC_{50} , as that was deemed the most interesting parameter. In many dose-occupancy studies a one-parameter Emax model is employed, where Δ_{max} is constrained to be 100%.

RESULTS AND DISCUSSION

In Paper II we evaluated different study designs and data analysis methods for PET baseline-block studies. The main outcome measure was IC_{50} , and box plots illustrating the distribution of IC_{50} estimates can be found in Paper II (Appendix B).

In this chapter, results are presented in tables of the median and interquartile range of parameter estimates. In the Paper II figures, only the results for IC_{50} were reported. Here, both IC_{50} and Δ_{max} estimates are presented. The true underlying values in the simulations were 2 $\mu\text{g/L}$ for IC_{50} , and 85% for Δ_{max} .

10.1 OCCUPANCY RANGE

In the first simulation experiment we investigated the contribution of low-occupancy datapoints on the estimation of IC_{50} . The median parameter estimates and interquartile ranges for both IC_{50} and Δ_{max} , estimated with all three methods are presented in Table 8. The first additional datapoint ($\Delta = 46.7\%$) clearly improved the estimation of both parameters with all three methods. However, when the subsequent datapoints were added, no obvious improvements were observed.

The results suggest that collecting data at these lower occupancies makes little economical sense. Realistically, most people would probably want to collect some lower-occupancy datapoints to confirm that the assumed model aligns with the *in vivo* kinetics of the drug. However, it seems that such datapoints would likely not contribute to the accurate characterization of the dose-occupancy relationship.

Here, the simulations are based on [^{11}C]Cimbi-36. It is possible that with another radiotracer, with less noise, lower doses could contribute more to the parameter estimation. Also, all methods evaluated here estimates drug interaction parameters based on V_T s. Generally, BP_{ND} estimates have lower test-retest variability than V_T estimates. It is possible that BP_{ND} -based estimates would have allowed for lower occupancies to contribute meaningfully to the IC_{50} and Δ_{max} estimates.

Still, lower doses also mean that accurate estimation of the plasma drug concentrations is more challenging. This will always be an issue with low-occupancy datapoints, irrespective of data collection and quantification methods.

Occupancy range [%]	Lassen [med(iqr)]	LEO [med(iqr)]	LEA [med(iqr)]
IC_{50}			
53.3-80.0	1.92(2.18)	1.92(1.09)	1.92(1.23)
46.7-80.0	1.87(1.51)	1.96(0.76)	1.93(0.76)
40.0-80.0	1.93(1.42)	1.99(0.81)	1.96(0.78)
33.3-80.0	1.83(1.37)	1.96(0.78)	1.93(0.75)
26.7-80.0	1.92(1.42)	1.98(0.74)	1.94(0.77)
20.0-80.0	1.90(1.40)	1.95(0.75)	1.92(0.73)
Δ_{max}			
53.3-80.0	85.9(15.8)	85.5(8.98)	85.9(9.94)
46.7-80.0	85.2(12.7)	85.3(6.53)	85.3(6.38)
40.0-80.0	85.9(13.5)	85.7(6.78)	86.0(6.82)
33.3-80.0	84.4(12.8)	85.4(6.86)	85.7(6.71)
26.7-80.0	85.7(14.2)	85.9(7.62)	86.0(7.81)
20.0-80.0	85.5(13.8)	85.5(7.28)	85.6(7.11)

Table 8: Results of simulation experiment 1, where the effect of adding additional datapoints at lower occupancies was evaluated. The true underlying values in the simulations were 2 $\mu\text{g/L}$ for IC_{50} , and 85% for Δ_{max} .

Lassen = Lassen plot followed by dose-occupancy plot; LEO = Likelihood estimation of occupancy followed by dose-occupancy plot; LEA = Likelihood estimation of affinity; med = median; iqr = interquartile range (difference between 75th and 25th percentiles); IC_{50} = Half-maximal inhibitory concentration; Δ_{max} = Maximal attainable occupancy.

10.2 NUMBER OF SUBJECTS

In the second simulation experiment we investigated the effect of the number of subjects in the dataset on the parameter estimation. For a few of the evaluated sample sizes, median parameter estimates and interquartile ranges, for all three methods, are presented in Table 9.

As expected, including more subjects generally led to more precise parameter estimation. We could see no clear cut-off after which including more subjects did not discernibly improve parameter estimation.

To better imitate a real life scenario, we also used the estimated dose-occupancy relationships from this simulation experiment to evaluate how each method performed at determining the correct plasma concentration corresponding to a target dose. We defined three different therapeutic windows, 20-30%, 45-55%, and 70-80%. Then, for all different sample sizes, and all three methods, we calculated the C_p that should correspond to the mid-point of each therapeutic window according to each of the 1000 estimated dose-occupancy relationships. In supplementary figure 1 of Paper II (Appendix B), the success rates for each method across increasing sample sizes was plotted. Here, we observed some ceiling effect, especially for LEO and LEA, where the benefit of increasing the sample size flattened out after approximately 20 subjects. In general, nearly four times the number of subjects were required for the Lassen plot to reach the same success rate as the likelihood-based methods.

10.3 NOISE IN PLASMA DRUG CONCENTRATION MEASUREMENTS

In the third simulation experiment, we evaluated the effect of noise in the measurements of plasma drug concentrations. The median parameter estimates and interquartile ranges, for some of the evaluated noise levels, are presented in Table 10.

The error of the parameter estimates increased with increased noise in the C_p measurements. At moderate noise levels, there was a negative bias on both parameters with all three methods. At the highest evaluated noise levels, there was a positive bias in the parameter estimates, although slightly less for LEA compared to the other two methods.

It is unclear which of our simulated plasma noise factors (κ) best match the typical errors in real-life measurements of plasma drug concentrations. Based on literature (Pea et al., 2019), we believe that it is likely in the range of 0.2 – 0.4. At these noise levels there is no clear benefit of using LEA over LEO.

The noise in the plasma drug concentration measurements is not accounted for in the LEA log-likelihood function. Ideally, we would have wanted to develop a maximum likelihood based estimator that

N	Lassen [med(iqr)]	LEO [med(iqr)]	LEA [med(iqr)]
IC₅₀			
5	1.92(1.66)	1.95(0.98)	1.93(0.98)
10	1.86(1.24)	1.94(0.66)	1.87(0.68)
15	1.94(1.16)	2.00(0.61)	1.94(0.60)
20	1.96(0.98)	1.99(0.52)	1.93(0.50)
25	1.98(0.87)	1.99(0.51)	1.93(0.48)
30	1.93(0.85)	1.97(0.42)	1.91(0.41)
Δ_{\max}			
5	85.3(14.6)	85.5(8.51)	85.5(8.45)
10	85.4(11.7)	85.1(6.39)	85.2(6.18)
15	85.6(11.3)	85.7(5.88)	85.7(5.75)
20	84.5(9.65)	85.6(4.80)	85.6(4.87)
25	85.4(8.33)	85.6(4.64)	85.6(4.83)
30	85.0(7.79)	85.5(3.91)	85.5(4.10)

Table 9: Results of simulation experiment 2, where the effect of adding additional subjects was evaluated. The true underlying values in the simulations were 2 $\mu\text{g/L}$ for IC_{50} , and 85% for Δ_{\max} .

N = number of subjects; Lassen = Lassen plot followed by dose-occupancy plot; LEO = Likelihood estimation of occupancy followed by dose-occupancy plot; LEA = Likelihood estimation of affinity; med = median; iqr = interquartile range (difference between 75th and 25th percentiles); IC_{50} = Half-maximal inhibitory concentration; Δ_{\max} = Maximal attainable occupancy.

	Lassen [med(iqr)]	LEO [med(iqr)]	LEA [med(iqr)]
IC ₅₀			
0	1.90(1.36)	1.97(0.73)	1.93(0.70)
0.3	1.49(1.31)	1.58(0.87)	1.59(0.87)
0.6	1.67(3.45)	1.52(3.23)	1.52(2.61)
0.9	4.75(10.6)	4.70(10.5)	3.41(5.99)
Δ _{max}			
0	85.3(12.1)	85.6(6.53)	85.8(5.79)
0.3	81.6(12.9)	82.4(7.80)	82.9(7.86)
0.6	82.3(27.7)	80.3(25.5)	80.3(24.5)
0.9	93.3(28.6)	92.4(28.5)	88.0(26.9)

Table 10: Results of simulation experiment 3, where the effect of noise on the plasma drug concentration measurements was evaluated. The true underlying values in the simulations were 2 μg/L for IC₅₀, and 85% for Δ_{max}.

κ = plasma noise factor; Lassen = Lassen plot followed by dose-occupancy plot; LEO = Likelihood estimation of occupancy followed by dose-occupancy plot; LEA = Likelihood estimation of affinity; med = median; iqr = interquartile range (difference between 75th and 25th percentiles); IC₅₀ = Half-maximal inhibitory concentration; Δ_{max} = Maximal attainable occupancy.

also accounts for this noise, but we were unable to identify a suitable strategy for this. Estimating the true C_Ps from the measured values would dramatically increase the dimensionality of the method. Also, it is not entirely clear how to realistically characterize the noise. Unlike V_T, the noise in C_P does not seem to be normally distributed (Pea et al., 2019).

10.4 ANALYTICAL METHODS

Throughout all three simulation experiments, the maximum likelihood based methods, consistently outperformed the Lassen plot. The differences between the LEO- and LEA-based parameter estimates were minimal, but we observed a small tendency for LEO to estimate values closer to the true underlying values.

In the two first simulation experiments, the accuracy was comparable across the three methods, with generally very similar median parameter estimates. The precision was much higher with LEO and LEA than with the Lassen plot. In simulation experiment 2, the interquartile ranges of the LEO- and LEA-based IC₅₀ estimates were

similar to those that the Lassen plot achieved with four times the number of subjects.

The maximum likelihood based methods rely on estimation of the covariance structure of regional V_T estimates. In this study, that was estimated from a test-retest dataset with ten subjects. Without a good estimate of the covariance structure, these methods would perform comparably with the Lassen plot (Schain, Zanderigo, and Ogden, 2018). This is a clear limitation of these methods. Although test-retest studies are a natural part of the evaluation of new PET tracers, it is not given that such a dataset would be available for all tracers. Even if an appropriate test-retest dataset exists for a tracer, it would not necessarily be available for use.

Still, at the noise levels we have simulated here, it seems that collecting 10 test-retest subjects and 5 baseline-block subjects and analyzing the data with LEO or LEA, would yield more precise parameter estimates than collecting 15 baseline-block subjects and analyzing the data with the Lassen plot.

Unfortunately, extending the existing likelihood based method did not improve the parameter estimation, and the results obtained with LEO and LEA were generally very similar. LEA did perform better at very high levels of noise in C_p . However, we believe that these noise levels are unrealistically high. At the noise levels we expect to be closer to reality, LEA performs comparably to LEO.

It is difficult to imagine that someone would prefer to use LEA over LEO. Not only because it does not add precision to the parameter estimates, but also because it represents an unrealistic study design. The standard approach for collection of PET occupancy data is an adaptive study design, where each drug dose is determined based on the occupancies achieved in previous scans (Takano et al., 2016). As such, the two step approach of first calculating occupancies with LEO or the Lassen plot, and later pooling all the occupancy data makes more sense.

Because the strength of the likelihood-based approaches lies in the fact that they account for noise, the relative performance we have reported in Paper II is naturally dependent on the magnitude of the noise in the simulated data. We have done our best to add a realistic level of noise to the V_T values. Nevertheless, it is entirely possible that we have simulated an excessive level of noise. If that is the case, the outperformance of the Lassen plot by LEO and LEA reported here would be exaggerated. Naturally, the noise in V_T is a complex combination of several factors, and highly dependent on the radiotracer.

Part VI

PAPER III

You become responsible, forever, for what you have
tamed.

— Antoine de Saint-Exupéry,
The Little Prince

METHODS

In Paper III, we present and evaluate a new model for arterial input function (AIF) based quantification of data from a PET displacement study. In this type of study, a competing drug is administered during an ongoing PET-scan, with the intention of measuring the displacement of the PET tracer by the drug.

11.1 KINETIC MODELS FOR PET DISPLACEMENT STUDIES

In the classic baseline-block occupancy study design, the drug intervention occurs between two separate PET scans. When the competing drug is instead administered during an ongoing scan, the system is dynamically altered during data collection. Thus, the kinetics of the PET tracer can no longer be accurately modeled by a linear system. Instead, a different type of model must be used, that accounts for the changes to the system.

In the two-tissue compartment model (2TCM), the rate constant k_3 is linearly related to the concentration of available targets, B_{avail} (Innis et al., 2007; Slifstein and Laruelle, 2001):

$$k_3 = f_{\text{ND}} k_{\text{on}} B_{\text{avail}}, \quad (18)$$

where f_{ND} is the fraction of free radioligand in the nondisplaceable compartment, and k_{on} is the association rate constant for the radioligand to its specific target. When a competing drug is introduced, B_{avail} is fractionally reduced with the occupancy of the drug. Given the linear relationship between B_{avail} and k_3 , it follows that as long as f_{ND} and k_{on} remains unchanged, the same fractional reduction will also apply to k_3 . Thus, we assumed that following the intervention k_3 will fractionally decrease with the target occupancy. In our model, we have also assumed that the other rate constants (k_1, k_2 , and k_4) are unperturbed by the intervention. This model assumptions, of occupancy acting solely on k_3 , was also proposed by Endres and Carson (1998).

Based on these assumptions we have developed two kinetic models for PET displacement studies, one based on the one-tissue compartment model (1TCM) and one based on the 2TCM. Only the 1TC displacement model was evaluated in Paper III.

11.1.1.1 The Occupancy Model

We modeled the occupancy as a function of time, $\partial(t)$. The occupancy was assumed to be zero before the time of the intervention (beginning time, t_b), then to increase up to some max value, ∂^{\max} , until time t_e (end time), after which it was assumed to be constant at ∂^{\max} throughout the rest of the scan.

We assumed that the occupancy function would be monotonically non-decreasing between t_b and t_e . We also needed the function to be differentiable at all time points. A sigmoid-shaped function, developed for the prediction of crop growth rates, met our conditions (Yin et al., 2003):

$$\partial(t) = \partial^{\max} \left(1 + \frac{t_e - t}{t_e - t_m} \right) \left(\frac{t - t_b}{t_e - t_b} \right)^{\frac{t_e - t_b}{t_e - t_m}}. \quad (19)$$

t_m is some time point between t_b and t_e , where the derivative of $\partial(t)$ is at its maximum. In order to limit the number of estimated parameters, t_m was arbitrarily constrained to be the mid-point between t_b and t_e throughout this study. Thus, t_m in Equation 19 can be replaced with $\frac{1}{2}(t_b + t_e)$, yielding,

$$\partial(t) = \partial^{\max} \left(1 + 2 \frac{t_e - t}{t_e - t_b} \right) \left(\frac{t - t_b}{t_e - t_b} \right)^2. \quad (20)$$

Examples of $\partial(t)$ with different t_e are illustrated in Figure 1 of Paper III.

11.1.1.2 The One-Tissue Compartment Displacement Model

In our models, the occupancy function, $\partial(t)$, acts on k_3 , a parameter that is not part of the 1TCM. In order to allow occupancy to be estimated from a 1TC displacement model, we adopted a framework similar to the simplified reference tissue model (SRTM; Lammertsma and Hume (1996)). In the SRTM, the combined forward rate constant k_{2a} can be expressed in terms of the 2TCM rate constants as,

$$k_{2a} = \frac{k_2}{1 + BP_{ND}} = \frac{k_2}{1 + k_3/k_4}, \quad (21)$$

where k_2, k_3 , and k_4 are the 2TCM rate constants. By replacing the 1TCM k_2 in the 1TCM differential equation with the expression for k_{2a} in Equation 21, it is possible to incorporate a time-varying occupancy function acting on k_3 . The differential equation for the 1TC displacement model then becomes,

$$\frac{dC_T(t)}{dt} = K_1 C_P(t) - \frac{k_2}{1 + (1 - \partial(t)) BP_{ND}} \quad (22)$$

11.1.3 The Two-Tissue Compartment Displacement Model

In the 2TC implementation of the displacement model, the occupancy function, $\vartheta(t)$ acts directly on k_3 . Thus, the differential equations for the 2TC displacement model are:

$$\frac{dC_{ND}(t)}{dt} = K_1 C_P(t) - (k_2 + (1 - \vartheta(t)) k_3) C_{ND}(t) + k_4 C_S(t), \quad (23)$$

$$\frac{dC_S(t)}{dt} = (1 - \vartheta(t)) k_3 C_{ND}(t) - k_4 C_S(t). \quad (24)$$

The 2TC version of the displacement model was not evaluated in Paper III. However, a more detailed description of the model and its proposed solutions can be found in Section A of the paper's supplementary material (Appendix C).

11.2 SIMULATION OF PET TACS WITH DISPLACEMENT

Data was simulated using the 1TC displacement model (see Section 11.1.2), and a AIF from one of the [^{11}C]UCB-J pig displacement scans (see Section 11.1.3). For the first eight minutes a smoothed version of the pig AIF was used. For the remainder of the scan, a tri-exponential function was fitted to the AIF, to allow for the scan duration to be extended in simulations.

Time-activity curves (TAC) for seven regions of interest (ROI) were simulated: cerebellum, frontal cortex, hippocampus, occipital cortex, putamen, temporal cortex and thalamus. The rate constants were chosen from published [^{11}C]UCB-J rate constants, and chosen to result in $V_{ND} = 4$ in all ROIs (Finnema et al., 2018).

Throughout all simulations, the time of intervention (t_b) was set to 60 min, and the scan duration was set to 120 min. Three different drugs were simulated, one fast, one slow, and one very slow, with max occupancy (ϑ^{max}) reached at 65, 90 and 180 min, respectively. For each drug, scans at three different occupancies were simulated, with ϑ^{max} at 25%, 50% and 75% occupancy.

For each condition (combination of drug speed and occupancy), 1000 sets of 7 TACs were simulated.

All simulations were done in MATLAB (version 9.10; MathWorks).

11.2.1 Generation of Noise-Free Time-Activity Curves

The noise-free TACs for all conditions and ROIs were generated by numerically solving the 1TC displacement model differential equation (Equation 22), using the Euler forward method, with [^{11}C]UCB-J based parameter values and pig AIF as outlined above.

11.2.2 Adding Realistic Noise

A previously proposed noise model, that accounts for frame duration, radionuclide decay and activity concentration, was used to add realistic noise to all frames of the simulated TACs (Logan et al., 2001; Varga and Szabo, 2002). In frame j , the simulated noisy activity concentrations $C_{\text{noise}}(t_j)$ was given by,

$$C_{\text{noise}}(t_j) = C_{\text{true}}(t_j) \left(1 + \alpha \sqrt{\frac{e^{\lambda t_j^{\text{mid}}}}{C_{\text{true}}(t_j) \Delta t_j}} G(0, 1) \right), \quad (25)$$

where $C_{\text{true}}(t_j)$ is the simulated true activity concentration in frame j , λ is the decay constant for ^{11}C , t_j^{mid} is the mid-time of frame j , Δt_j is the frame duration of frame j , and $G(0, 1)$ is a random number sampled from a unit normal distribution (mean = 0, standard deviation = 1). α is a scaling factor for the noise. It was set to 5 throughout all simulations, in order to achieve a realistic magnitude of the noise.

11.3 PIG DISPLACEMENT EXPERIMENTS

For evaluation of the displacement model on real data, [^{11}C]UCB-J PET intervention scans were conducted in six pig. All scans were acquired on a HRRT scanner, with a scan duration of 150 min. After 60 min, brivaracetam was administered intravenously over 20 seconds, at doses corresponding to 0.1, 0.2, 0.75, 1, 2, and 5 mg/kg body mass. Two of the pigs (0.1 and 2 mg/kg), underwent 120-min baseline and block scans immediately before and after the intervention scans. No additional drug was given prior to the block scans. Arterial blood was automatically (first 30 min) and manually (14 samples) collected during all scans, for estimation of AIFs.

For estimation of plasma brivaracetam concentrations, seven arterial samples were collected during the intervention scans (at approximately 1, 5, 15, 30, 45, 60 and 90 min after the intervention), and five samples were collected during the block scans (at approximately 3, 15, 45, 75 and 90 min after radioligand injection).

More details on the pig data acquisition and processing can be found in Paper III and its supplementary material.

11.4 ANALYSIS OF PET DISPLACEMENT SCANS

The 1TC displacement model was fitted to all TACs, both simulated and pig data, using both a numerical and an analytical approach. With both methods, all TACs from a single scan were fitted simultaneously using a nested approach, where global parameters were fitted in an outer layer, and ROI-specific parameters were fitted in an inner layer. Simultaneous fitting of regions is a necessary to iden-

tify a global minimum, because the free parameters k_2 , BP_{ND} and $\partial(t)$, only appear as a ratio in the 1TC displacement model differential equation. This is explained in greater detail in the supplementary material of Paper III.

∂^{\max} , V_{ND} , and t_e were assumed to be the same in all ROIs. ∂^{\max} was constrained to be between 0 and 1, V_{ND} was constrained to be positive, and t_e was constrained to be after t_b . The time of intervention, t_b , was also assumed to be the same in all ROIs. This parameter, was not fitted, but assumed to be known. For the simulated data, the true t_b from the simulations was used. For the pig data, t_b was set to the start of the brivaracetam injection.

K_1 , V_S and the fractional blood volume, v_B , were estimated separately for each ROI. In the fitting, K_1 and V_S were constrained to be positive, and v_B was constrained to be between 0 and 1.

For both the simulated data and the pig data the same seven ROIs were used: cerebellum, frontal cortex, hippocampus, occipital cortex, putamen, temporal cortex and thalamus.

All analyses were done in Matlab (version 9.10). Both the inner-layer and outer-layer fits, with both the numerical and analytical approaches, were fitted using the Matlab function `lsqnonlin`.

11.4.1 *The Numerical Solution*

The displacement model was fitted numerically to the data using the Euler forward method. Euler forward is a first-order numerical method for solving ordinary differential equations. Starting at known initial conditions, the next data point is estimated by taking a small step according to the curve's tangent at that point. In this manner, TACs based on a set of parameter estimates can be drawn. In the fitting, the combination of parameter estimates that yields the most similar curves to the subject's TACs is identified.

For the numerical solution a fixed step size of 0.5 seconds was used.

11.4.2 *The Single Step Approximation*

Because the displacement models describe a time-invariant system the analytical methods used to solve classic PET compartment model differential equations (e.g. the Laplace transform) cannot be used. In order to solve the displacement model differential equations analytically, we introduced a simplified model variation, where the occupancy function, $\partial(t)$, is approximated as a step function, with $\partial(t) = 0$ before some time t_s and $\partial(t) = \partial^{\max}$ after. This allows the TACs to be separated into two separate time-invariant systems, where the initial values in the second system will be given by the final values of the first.

In the fitting, all parameters except the occupancy were constrained to be the same in both systems. The time of the step, t_s , was fitted, with the constraint that it occurs after the time of the intervention, t_b . t_s replaces t_e in this solution, but they are not the same parameter.

RESULTS AND DISCUSSION

In Paper III, we presented and evaluated a new kinetic model, based on the 1TCM, for AIF-based analysis of data from PET displacement studies. We evaluated the model in simulations, and tested it on pig [^{11}C]UCB-J scans with brivaracetam intervention.

12.1 ESTIMATION OF OCCUPANCY

In the simulation experiment we simulated three different drug speeds ($t_e - t_b = 5, 30,$ and 120 min) and three different occupancies ($\partial^{\max} = 25, 50,$ and 75%). For the two faster drugs, the distributions of occupancy estimates are presented in histograms in Figure 2 of Paper III. The precision of the occupancy estimates improved with higher occupancies.

For the slowest drug speed ($t_e - t_b = 120$), the distribution of ∂^{\max} estimates are presented in Supplementary figure 5 of Paper III. The model was unable to provide reasonable estimates, even at higher occupancies. In these simulations, the max occupancy was reached a full hour after the end of the PET scans. As such, it is not surprising that the parameter estimation failed in this case. This condition was included in the study, not because we expected it to be useful for occupancy calculations, but because we wanted to test the limitations of the model and the solutions.

The results from the pig experiment are presented in Figure 4 of Paper III. To make an assessment on the quality of the occupancy estimates, the Emax model was fitted to the occupancies and plasma brivaracetam concentrations. The Emax model has previously been shown to provide good fits to brivaracetam occupancies estimated with [^{11}C]UCB-J PET (Finnema et al., 2019). The model fitted well with our estimated occupancies.

We used the peak plasma values for the dose-occupancy plots. However, it is not clearly established which plasma concentrations to use when occupancies have been estimated from a displacement scan. In a classic baseline-block setup either the plasma concentration at the start of the scan, at the end of the scan, or the mean plasma concentration could be used (Takano et al., 2016). It does not matter much, as the concentrations will often be relatively constant. During an intervention scan, the plasma drug concentration will vary much more throughout the scan. This is illustrated in Figure 4, which shows the plasma brivaracetam time course for one of the pigs that underwent both an intervention scan and a subsequent block scan.

For comparison, we also fitted the Emax model with mean plasma concentrations. This resulted in parameter estimates that were more in line with those that have previously been reported. With peak plasma concentrations the IC_{50} estimate was $1.26 \mu\text{g/mL}$, and with mean plasma concentrations we got an IC_{50} estimate of $0.47 \mu\text{g/mL}$. Previously, a brivaracetam IC_{50} , calculated from human [^{11}C]UCB-J occupancy data, of $0.46 \mu\text{g/mL}$ has been reported (Finnema et al., 2019).

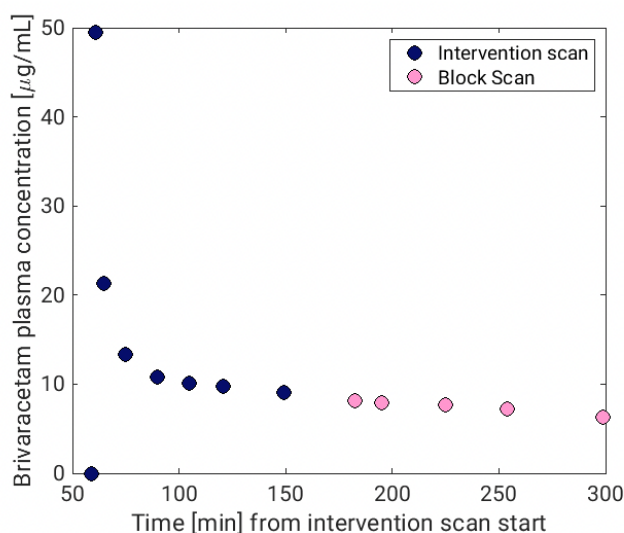


Figure 4: Plasma brivaracetam concentration over time for the pig that received a 2 mg/kg brivaracetam dose. The samples collected during the intervention scan are indicated by blue markers, and those collected during the block scan by pink markers.

Four of the pigs were scanned just once (the intervention scan). Two pigs were scanned three times in one day, but brivaracetam was administered just once per pig. Consequently, the occupancies were lower in the block scans than in the corresponding intervention scans as brivaracetam had undergone some washout (see the first tile of Figure 4 in Paper III). In order to compare the intervention model occupancies to the baseline-block Lassen occupancies, we plotted them versus their corresponding drug plasma level at the time of the respective scan in the same dose-occupancy plots. The block-scan occupancies seemed to agree well with the dose-occupancy relationship established from the intervention scans.

12.2 THE MODEL

The proposed model seems to be appropriate for describing displacement of [^{11}C]UCB-J by brivaracetam in pig scans.

We employed a function developed for crop growth rates to model the occupancy. This function is sigmoidal in shape, which is proba-

bly not a good representation of the true underlying time course of occupancy. However, we demonstrate here that it is a useful approximation for brivaracetam in pigs. The occupancy function we have used here has only two parameters (t_e , ∂^{\max}), which means that fitting the model is relatively simple.

In the simulation study, the proposed occupancy function was used both to simulate the data, and in the numerical solution. Although the numerical solution also worked well in the pig study, brivaracetam is a relatively fast drug. It seems likely that the exact shape of the occupancy curve would not be of great significance for a drug which rapidly reaches its peak occupancy.

The main assumptions of our model are not new to the field (Endres and Carson, 1998), and have been employed by other groups. Very recently, a similar, though more complex, model for PET displacement studies has been introduced (Naganawa et al., 2022), and evaluated on [^{11}C]UCB-J data with brivaracetam intervention. That model, also includes kinetic modeling of the drug, including both nondisplaceable and specific drug binding compartments, and relies on plasma drug concentrations to be used as an input function in addition to the PET AIF. Although this, in all likelihood, is a much more accurate representation of how a drug behaves in the body, the model could not offer stable parameter estimates without fixing several of the model parameters to previously reported population values (Naganawa et al., 2022).

Regarding our model, it is possible, maybe even probable, that it will not be applicable to all drugs and drug administration approaches. Although simulations showed promising results also with a slower drug, the pig experiments only considered brivaracetam, which is a relatively fast drug. Future work will have to show whether the model also can be useful for displacement studies with other drugs and radiotracers. We are currently applying the model to human [^{11}C]UCB-J scans with levetiracetam, which, compared to brivaracetam, displaces [^{11}C]UCB-J at a slower rate (Finnema et al., 2019).

The 2TC variant of the displacement model has not yet been implemented and evaluated. This will be an important next step, as a validated 2TC-based model would open up for PET displacement studies with tracers that are best described by 2TC kinetics.

12.3 MODEL SOLUTIONS

We have proposed two different solutions to our model: one based on numerical methods and one based on analytical methods. In both the simulation study and the pig study, they yielded near-identical results. In the pig study, the numerical approach led to an IC_{50} estimate of 1.26 $\mu\text{g}/\text{mL}$, and the analytical approach led to an IC_{50} estimate of 1.27 $\mu\text{g}/\text{mL}$. Only for the lowest occupancies (25%) is there a clear

difference in the distributions of occupancy estimates (see Figure 2 in Paper III, Appendix C).

The default in PET kinetic modeling is to use analytical methods to solve models. However, some recent publications have employed numerical approaches to analyze PET displacement data (Mandeville et al., 2022; Naganawa et al., 2022). With our implementations of the model solutions, the numerical approach was much faster than the analytical. Further, this approach also offers substantial flexibility to the displacement model, as the particular form of the occupancy curve can easily be changed for other applications.

However, we still think that there is value in analytically solving the model. This is the approach that is closest to the established solutions to time-invariant compartment models, and the implementation should be easier and more familiar for most people with experience in PET kinetic modeling. The single-step approximation in itself is interesting to evaluate, as it is an already established one for reference region based quantification of PET displacement scan data (ESRTM; Zhou et al. (2006)).

We also briefly evaluated a multi-step solution, where the PET scan was divided into several time-invariant systems with different occupancies. Surprisingly, reducing the multistep approach to only a single step did not appear to add bias, even for very slow-acting drugs.

Part VII

CONCLUSION

It is much more difficult to judge oneself than to judge others. If you succeed in judging yourself rightly, then you are indeed a man of true wisdom.

— Antoine de Saint-Exupéry,
The Little Prince

CONCLUDING REMARKS AND FUTURE PERSPECTIVES

The aim of the thesis work was to improve the utility of PET for quantification of drug interactions in the living human brain. This has been endeavoured through the assessment of existing assumptions and methods, evaluation of the effects of study design, and development of novel methods.

13.1 NONDISPLACEABLE BINDING

In brain PET, it is common to assume that V_{ND} is uniform across regions, and at least comparable across subjects. In fact, most of the established methods for data quantification rely on these assumptions. The assumption of constant V_{ND} , like many other assumptions made in PET kinetic modeling, is often useful or even necessary. Still, for improved interpretability of results, it is important to fully understand the boundaries and limitations of these assumptions. I personally feel that this is an area where a lot of work still remains to be done.

In Paper I, we conclude, based on several [^{11}C]PBR28 datasets, that in some instances V_{ND} may be different between groups: we found that subjects with alcohol use disorder and Parkinson's disease both had significantly lower V_{ND} than their matched controls.

This raises a big question, which is relevant for all PET studies: when and why is it meaningful to assume that the nondisplaceable radiotracer binding is constant across groups and following interventions? Both V_T , BP_{ND} , and semiquantitative outcomes such as SUV and SUVR, are directly dependent on the level of nondisplaceable uptake. As such, no widely used PET outcome measure is resistant to the possible confounding effects of V_{ND} . Simultaneous estimation of V_{ND} (SIME), which was used in Paper I to show the between-group differences in V_{ND} , itself assumes that V_{ND} is constant within subjects. This assumption might also not hold in all situations.

SIME should in the future be applied to other tracers and datasets in order to increase the confidence in results, or reveal possible group differences in V_{ND} . This is especially important for comparison of results between patient populations and controls in conditions that could affect the structure and function of the brain.

The main focus of the thesis project is pharmacological competition studies. Although Paper I lies slightly outside this scope, assessment

of V_{ND} is also very important in the context of PET occupancy studies. With V_T -based occupancy estimation, occupancy and V_{ND} are highly correlated parameters, and an overestimation of V_{ND} will also lead to an overestimation of the occupancy. Also, blocking of the specific binding by a competing unlabeled ligand is the current gold standard method for estimation of V_{ND} .

In the future, I would like to study V_{ND} in the context of occupancy studies more closely. It might, for example, be interesting to investigate how the altered tracer kinetics in a block scan relative to a baseline scan might effect V_{ND} estimation. Also, improved estimation and better understanding of V_{ND} could also contribute to improved estimation of occupancy.

13.2 DRUG OCCUPANCY STUDIES

Throughout the thesis work, we have employed two different experimental setups for PET pharmacological competition studies. In Paper II we used the standard baseline-block setup, and in Paper III we used within-scan displacement.

In Paper II we were able to quantitatively demonstrate that low-occupancy datapoints in baseline-block studies contribute minimally to estimation of the dose-occupancy relationship. I hope that this, together with our findings from the other simulation experiments, can be of assistance to PET researchers planning future occupancy studies.

Many PET occupancy studies are performed with reference region based quantification. This presents a different set of advantages and challenges compared to the AIF-based quantification employed in Paper II. Going forward, I would like to repeat a similar simulation study for BP_{ND} -based occupancy. Ideally, this could also entail a head-to-head comparison of BP_{ND} -based and V_T -based occupancy estimates. Data from such a study could facilitate deliberations on whether or not to collect blood data as part of PET occupancy experiments.

In Paper III, we confirmed that for [^{11}C]UCB-J PET, in-scan displacement presents a viable option for quantification of brivaracetam occupancy. We presented and validated a new kinetic model for analysis of displacement scan PET data. The in-scan intervention setup can be especially useful for rapidly acting drugs, where the washout might be too fast for accurate occupancy estimation with the traditional baseline-block setup.

I believe that the potential applications of the displacement model reach far beyond what was revealed in Paper III. For example, by changing the time-varying occupancy function, drugs with different kinetics might be characterized more accurately. Future work should

implement and evaluate the two-tissue compartment version of this model, and evaluate the models for different radiotracers and drugs. I also hope to apply the displacement model to pure block scans in order to estimate the time-varying occupancy of drugs with a fast washout.

Although some important contributions have been made with the papers included in this thesis, much work still remains in optimizing both baseline-block and in-scan intervention occupancy studies. Ultimately, my ambition is to develop a framework in which the two study designs can be compared head-to-head. This could hopefully aid in future decisions on the experimental setup of drug occupancy studies.

Part VIII

BIBLIOGRAPHY

"People where you live," the little prince said, "grow five thousand roses in one garden... Yet they don't find what they're looking for [...] And yet what they're looking for could be found in a single rose."

— Antoine de Saint-Exupéry,
The Little Prince

BIBLIOGRAPHY

- Abbott, N. Joan, Adjanie A. K. Patabendige, Diana E. M. Dolman, Siti R. Yusof, and David J. Begley (Jan. 2010). "Structure and Function of the Blood-Brain Barrier." In: *Neurobiology of Disease* 37.1, pp. 13–25. ISSN: 1095-953X. DOI: [10.1016/j.nbd.2009.07.030](https://doi.org/10.1016/j.nbd.2009.07.030). pmid: [19664713](https://pubmed.ncbi.nlm.nih.gov/19664713/).
- Albrecht, Daniel S et al. (Jan. 2018). "Pseudoreference Regions for Glial Imaging with (11)C-PBR28: Investigation in 2 Clinical Cohorts." In: *Journal of nuclear medicine : official publication, Society of Nuclear Medicine* 59.1, pp. 107–114. ISSN: 1535-5667. DOI: [10.2967/jnumed.116.178335](https://doi.org/10.2967/jnumed.116.178335). PMID: [28818984](https://pubmed.ncbi.nlm.nih.gov/28818984/).
- Alpert, Nathaniel M., Rajendra D. Badgaiyan, Elijah Livni, and Alan J. Fischman (July 2003). "A Novel Method for Noninvasive Detection of Neuromodulatory Changes in Specific Neurotransmitter Systems." In: *NeuroImage* 19.3, pp. 1049–1060. ISSN: 1053-8119. DOI: [10.1016/s1053-8119\(03\)00186-1](https://doi.org/10.1016/s1053-8119(03)00186-1). pmid: [12880831](https://pubmed.ncbi.nlm.nih.gov/12880831/).
- Antoni, Gunnar (2019). "The Radiopharmaceutical Chemistry of Carbon-11: Basic Principles." In: *Radiopharmaceutical Chemistry*. Ed. by Jason S. Lewis, Albert D. Windhorst, and Brian M. Zeglis. Cham: Springer International Publishing, pp. 207–220. ISBN: 978-3-319-98946-4 978-3-319-98947-1. DOI: [10.1007/978-3-319-98947-1_11](https://doi.org/10.1007/978-3-319-98947-1_11). URL: http://link.springer.com/10.1007/978-3-319-98947-1_11 (visited on 01/01/2023).
- Badawi, Ramsey D. et al. (Mar. 2019). "First Human Imaging Studies with the EXPLORER Total-Body PET Scanner." In: *Journal of Nuclear Medicine: Official Publication, Society of Nuclear Medicine* 60.3, pp. 299–303. ISSN: 1535-5667. DOI: [10.2967/jnumed.119.226498](https://doi.org/10.2967/jnumed.119.226498). pmid: [30733314](https://pubmed.ncbi.nlm.nih.gov/30733314/).
- Belarbi, Karim, Elodie Cuvelier, Marie-Amandine Bonte, Mazarine Desplanque, Bernard Gressier, David Devos, and Marie-Christine Chartier-Harlin (Oct. 17, 2020). "Glycosphingolipids and Neuroinflammation in Parkinson's Disease." In: *Molecular Neurodegeneration* 15.1, p. 59. ISSN: 1750-1326. DOI: [10.1186/s13024-020-00408-1](https://doi.org/10.1186/s13024-020-00408-1). pmid: [33069254](https://pubmed.ncbi.nlm.nih.gov/33069254/).
- Benavides, J., D. Quarteronet, F. Imbault, C. Malgouris, A. Uzan, C. Renault, M. C. Dubroeuq, C. Guerey, and G. Le Fur (Dec. 1983). "Labelling of "Peripheral-Type" Benzodiazepine Binding Sites in the Rat Brain by Using [3H]PK 11195, an Isoquinoline Carboxamide Derivative: Kinetic Studies and Autoradiographic Localization." In: *Journal of Neurochemistry* 41.6, pp. 1744–1750. ISSN: 0022-3042. DOI: [10.1111/j.1471-4159.1983.tb00888.x](https://doi.org/10.1111/j.1471-4159.1983.tb00888.x). pmid: [6315880](https://pubmed.ncbi.nlm.nih.gov/6315880/).
- Bhagwagar, Zubin, Rainer Hinz, Matthew Taylor, Sabrina Fancy, Philip Cowen, and Paul Grasby (Sept. 2006). "Increased 5-HT(2A) Receptor Binding in Euthymic, Medication-Free Patients Recovered from Depression: A Positron Emission Study with [(11)C]MDL 100,907." In: *The American Journal of Psychiatry* 163.9, pp. 1580–1587. ISSN: 0002-953X. DOI: [10.1176/ajp.2006.163.9.1580](https://doi.org/10.1176/ajp.2006.163.9.1580). pmid: [16946184](https://pubmed.ncbi.nlm.nih.gov/16946184/).
- Bretin, Florian et al. (May 7, 2013). "Preclinical Radiation Dosimetry for the Novel SV2A Radiotracer [18F]UCB-H." In: *EJNMMI research* 3.1, p. 35. ISSN: 2191-219X. DOI: [10.1186/2191-219X-3-35](https://doi.org/10.1186/2191-219X-3-35). pmid: [23647774](https://pubmed.ncbi.nlm.nih.gov/23647774/).
- Briard, Emmanuelle, Sami S. Zoghbi, Masao Imaizumi, Jonathan P. Gourley, H. Umesha Shetty, Jinsoo Hong, Vanessa Cropley, Masahiro Fujita, Robert B. Innis, and Victor W. Pike (Jan. 10, 2008). "Synthesis and Evaluation in Monkey of Two Sensitive 11C-labeled Aryloxyanilide Ligands for Imaging Brain Peripheral Benzodiazepine Receptors in Vivo." In: *Journal of Medicinal Chemistry* 51.1, pp. 17–30. ISSN: 0022-2623. DOI: [10.1021/jm0707370](https://doi.org/10.1021/jm0707370). pmid: [18067245](https://pubmed.ncbi.nlm.nih.gov/18067245/).
- Carson, Richard E., Michael A. Channing, Ronald G. Blasberg, Bonnie B. Dunn, Robert M. Cohen, Kenner C. Rice, and Peter Herscovitch (Jan. 1993). "Comparison of Bolus and Infusion Methods for Receptor Quantitation: Application to [18 F]Cyclofoxy and Positron Emission Tomography." In: *Journal of Cere-*

- bral Blood Flow & Metabolism* 13.1, pp. 24–42. ISSN: 0271-678X, 1559-7016. DOI: [10.1038/jcbfm.1993.6](https://doi.org/10.1038/jcbfm.1993.6). URL: <http://journals.sagepub.com/doi/10.1038/jcbfm.1993.6> (visited on 01/01/2023).
- Casellas, Pierre, Sylvaine Galiegue, and Anthony S. Basile (2002). “Peripheral Benzodiazepine Receptors and Mitochondrial Function.” In: *Neurochemistry International* 40.6, pp. 475–486. ISSN: 01970186. DOI: [10.1016/S0197-0186\(01\)00118-8](https://doi.org/10.1016/S0197-0186(01)00118-8).
- Charbonneau, P., A. Syrota, C. Crouzel, J. M. Valois, C. Prenant, and M. Crouzel (Mar. 1986). “Peripheral-Type Benzodiazepine Receptors in the Living Heart Characterized by Positron Emission Tomography.” In: *Circulation* 73.3, pp. 476–483. ISSN: 0009-7322. DOI: [10.1161/01.cir.73.3.476](https://doi.org/10.1161/01.cir.73.3.476). pmid: [3004781](https://pubmed.ncbi.nlm.nih.gov/3004781/).
- Cherry, Simon R., James A. Sorenson, and Michael E. Phelps (2012a). “Interaction of Radiation with Matter.” In: *Physics in Nuclear Medicine*. Elsevier, pp. 63–85. ISBN: 978-1-4160-5198-5. DOI: [10.1016/B978-1-4160-5198-5.00006-X](https://doi.org/10.1016/B978-1-4160-5198-5.00006-X). URL: <https://linkinghub.elsevier.com/retrieve/pii/B978141605198500006X> (visited on 12/09/2022).
- Cherry, Simon R., James A. Sorenson, and Michael E. Phelps (2012b). “Modes of Radioactive Decay.” In: *Physics in Nuclear Medicine*. Elsevier, pp. 19–30. ISBN: 978-1-4160-5198-5. DOI: [10.1016/B978-1-4160-5198-5.00006-X](https://doi.org/10.1016/B978-1-4160-5198-5.00006-X). URL: <https://linkinghub.elsevier.com/retrieve/pii/B978141605198500006X> (visited on 12/09/2022).
- Cherry, Simon R., James A. Sorenson, and Michael E. Phelps (2012c). “Positron Emission Tomography.” In: *Physics in Nuclear Medicine*. Elsevier, pp. 307–344. ISBN: 978-1-4160-5198-5. DOI: [10.1016/B978-1-4160-5198-5.00006-X](https://doi.org/10.1016/B978-1-4160-5198-5.00006-X). URL: <https://linkinghub.elsevier.com/retrieve/pii/B978141605198500006X> (visited on 12/09/2022).
- Cherry, Simon R., James A. Sorenson, and Michael E. Phelps (2012d). “Radiation Detectors.” In: *Physics in Nuclear Medicine*. Elsevier, pp. 87–106. ISBN: 978-1-4160-5198-5. DOI: [10.1016/B978-1-4160-5198-5.00006-X](https://doi.org/10.1016/B978-1-4160-5198-5.00006-X). URL: <https://linkinghub.elsevier.com/retrieve/pii/B978141605198500006X> (visited on 12/09/2022).
- Cherry, Simon R., James A. Sorenson, and Michael E. Phelps (2012e). “Radionuclide and Radiopharmaceutical Production.” In: *Physics in Nuclear Medicine*. Elsevier, pp. 43–62. ISBN: 978-1-4160-5198-5. DOI: [10.1016/B978-1-4160-5198-5.00006-X](https://doi.org/10.1016/B978-1-4160-5198-5.00006-X). URL: <https://linkinghub.elsevier.com/retrieve/pii/B978141605198500006X> (visited on 12/09/2022).
- Collste, K., A. Forsberg, A. Varrone, N. Amini, S. Aeinehband, I. Yakushev, C. Halldin, L. Farde, and S. Cervenka (2016). “Test-Retest Reproducibility of [(11)C]PBR28 Binding to TSPO in Healthy Control Subjects.” In: *European Journal of Nuclear Medicine and Molecular Imaging* 43.1, pp. 173–183.
- Collste, Karin et al. (2017). “Lower Levels of the Glial Cell Marker TSPO in Drug-Naive First-Episode Psychosis Patients as Measured Using PET and [11C]PBR28.” In: *Molecular Psychiatry* 22.6, pp. 850–856. ISSN: 14765578. DOI: [10.1038/mp.2016.247](https://doi.org/10.1038/mp.2016.247). pmid: [28194003](https://pubmed.ncbi.nlm.nih.gov/28194003/). URL: <http://dx.doi.org/10.1038/mp.2016.247>.
- Cosenza-Nashat, M., M.-L. Zhao, H.-S. Suh, J. Morgan, R. Natividad, S. Morgello, and S. C. Lee (June 2009). “Expression of the Translocator Protein of 18 kDa by Microglia, Macrophages and Astrocytes Based on Immunohistochemical Localization in Abnormal Human Brain.” In: *Neuropathology and Applied Neurobiology* 35.3, pp. 306–328. ISSN: 1365-2990. DOI: [10.1111/j.1365-2990.2008.01006.x](https://doi.org/10.1111/j.1365-2990.2008.01006.x). pmid: [19077109](https://pubmed.ncbi.nlm.nih.gov/19077109/).
- Costes, Nicolas, Alain Dagher, Kevin Larcher, Alan C. Evans, D. Louis Collins, and Anthonin Reilhac (Oct. 1, 2009). “Motion Correction of Multi-Frame PET Data in Neuroreceptor Mapping: Simulation Based Validation.” In: *NeuroImage* 47.4, pp. 1496–1505. ISSN: 1095-9572. DOI: [10.1016/j.neuroimage.2009.05.052](https://doi.org/10.1016/j.neuroimage.2009.05.052). pmid: [19481154](https://pubmed.ncbi.nlm.nih.gov/19481154/).
- Cunningham, Vincent J., Susan P. Hume, Gary R. Price, Randall G. Ahier, Jill E. Cremer, and Anthony K. P. Jones (Jan. 1991). “Compartmental Analysis of Diprenorphine Binding to Opiate Receptors in the Rat in Vivo and Its Comparison with Equilibrium Data in Vitro.” In: *Journal of Cerebral Blood Flow & Metabolism* 11.1,

- pp. 1–9. ISSN: 0271-678X, 1559-7016. DOI: [10.1038/jcbfm.1991.1](https://doi.org/10.1038/jcbfm.1991.1). URL: <http://journals.sagepub.com/doi/10.1038/jcbfm.1991.1> (visited on 01/01/2023).
- Cunningham, Vincent J, Eugenii A Rabiner, Mark Slifstein, Marc Laruelle, and Roger N Gunn (Jan. 2010). "Measuring Drug Occupancy in the Absence of a Reference Region: The Lassen Plot Re-Visited." In: *Journal of cerebral blood flow and metabolism : official journal of the International Society of Cerebral Blood Flow and Metabolism* 30.1, pp. 46–50. ISSN: 1559-7016. DOI: [10.1038/jcbfm.2009.190](https://doi.org/10.1038/jcbfm.2009.190). PMID: [19738632](https://pubmed.ncbi.nlm.nih.gov/19738632/).
- D'Souza, Deepak Cyril et al. (July 2021). "Preliminary in Vivo Evidence of Lower Hippocampal Synaptic Density in Cannabis Use Disorder." In: *Molecular Psychiatry* 26.7, pp. 3192–3200. ISSN: 1476-5578. DOI: [10.1038/s41380-020-00891-4](https://doi.org/10.1038/s41380-020-00891-4). pmid: [32973170](https://pubmed.ncbi.nlm.nih.gov/32973170/).
- Da Cunha-Bang, Sofi et al. (Apr. 11, 2019). "Measuring Endogenous Changes in Serotonergic Neurotransmission with [(11)C]Cimbi-36 Positron Emission Tomography in Humans." In: *Translational psychiatry* 9.1, p. 134. ISSN: 2158-3188. DOI: [10.1038/s41398-019-0468-8](https://doi.org/10.1038/s41398-019-0468-8). PMID: [30975977](https://pubmed.ncbi.nlm.nih.gov/30975977/).
- De Picker, Livia and Manuel Morrens (2020). "Perspective: Solving the Heterogeneity Conundrum of TSPO PET Imaging in Psychosis." In: *Frontiers in Psychiatry* 11, p. 362. ISSN: 1664-0640. DOI: [10.3389/fpsyt.2020.00362](https://doi.org/10.3389/fpsyt.2020.00362). pmid: [32425835](https://pubmed.ncbi.nlm.nih.gov/32425835/).
- De la Monte, Suzanne M. and Jillian J. Kril (Jan. 2014). "Human Alcohol-Related Neuropathology." In: *Acta Neuropathologica* 127.1, pp. 71–90. ISSN: 1432-0533. DOI: [10.1007/s00401-013-1233-3](https://doi.org/10.1007/s00401-013-1233-3). pmid: [24370929](https://pubmed.ncbi.nlm.nih.gov/24370929/).
- De Lange, Charlotte, Rønnaug Solberg, Jon Erik Holtedahl, Andreas Tulipan, Jon Barlinn, William Trigg, Torild Wickstrøm, Ola Didrik Saugstad, Eirik Malinen, and Mona Elisabeth Revheim (2018). "Dynamic TSPO-PET for Assessing Early Effects of Cerebral Hypoxia and Resuscitation in New Born Pigs." In: *Nuclear Medicine and Biology* 66, pp. 49–57. ISSN: 18729614. DOI: [10.1016/j.nucmedbio.2018.08.004](https://doi.org/10.1016/j.nucmedbio.2018.08.004). URL: <https://doi.org/10.1016/j.nucmedbio.2018.08.004>.
- Dickens, Alex M et al. (Mar. 1, 2014). "Detection of Microglial Activation in an Acute Model of Neuroinflammation Using PET and Radiotracers ¹¹C-(R)-PK11195 and ¹⁸F-GE-180." In: *Journal of Nuclear Medicine* 55.3, pp. 466–472. DOI: [10.2967/jnumed.113.125625](https://doi.org/10.2967/jnumed.113.125625). URL: <http://jnm.snmjournals.org/content/55/3/466.abstract>.
- Dupont, Anne Claire, Bérenger Largeau, Maria Joao Santiago Ribeiro, Denis Guilleau, Claire Tronel, and Nicolas Arlicot (2017). "Translocator Protein-18 kDa (TSPO) Positron Emission Tomography (PET) Imaging and Its Clinical Impact in Neurodegenerative Diseases." In: *International Journal of Molecular Sciences* 18.4, pp. 1–37. ISSN: 14220067. DOI: [10.3390/ijms18040785](https://doi.org/10.3390/ijms18040785).
- Durazzo, Timothy C., Stefan Gazdzinski, Anderson Mon, and Dieter J. Meyerhoff (May 2010). "Cortical Perfusion in Alcohol-Dependent Individuals during Short-Term Abstinence: Relationships to Resumption of Hazardous Drinking after Treatment." In: *Alcohol (Fayetteville, N.Y.)* 44.3, pp. 201–210. ISSN: 1873-6823. DOI: [10.1016/j.alcohol.2010.03.003](https://doi.org/10.1016/j.alcohol.2010.03.003). pmid: [20682188](https://pubmed.ncbi.nlm.nih.gov/20682188/).
- Endres, C. J. and R. E. Carson (Nov. 1998). "Assessment of Dynamic Neurotransmitter Changes with Bolus or Infusion Delivery of Neuroreceptor Ligands." In: *Journal of Cerebral Blood Flow and Metabolism: Official Journal of the International Society of Cerebral Blood Flow and Metabolism* 18.11, pp. 1196–1210. ISSN: 0271-678X. DOI: [10.1097/00004647-199811000-00006](https://doi.org/10.1097/00004647-199811000-00006). pmid: [9809509](https://pubmed.ncbi.nlm.nih.gov/9809509/).
- Ermer, Johannes and Bernd Neumaier (2019). "The Radiopharmaceutical Chemistry of Fluorine-18: Nucleophilic Fluorinations." In: *Radiopharmaceutical Chemistry*. Ed. by Jason S. Lewis, Albert D. Windhorst, and Brian M. Zeglis. Cham: Springer International Publishing, pp. 273–283. ISBN: 978-3-319-98946-4 978-3-319-98947-1. DOI: [10.1007/978-3-319-98947-1_15](https://doi.org/10.1007/978-3-319-98947-1_15). URL: http://link.springer.com/10.1007/978-3-319-98947-1_15 (visited on 01/01/2023).
- Erritzoe, David et al. (Apr. 2020). "Serotonin Release Measured in the Human Brain: A PET Study with [¹¹C]CIMBI-36 and d-Amphetamine Challenge." In: *Neuropsychopharmacology: Official Publication of the American College of Neuropsychopharmacology*

- macology* 45.5, pp. 804–810. ISSN: 1740-634X. DOI: [10.1038/s41386-019-0567-5](https://doi.org/10.1038/s41386-019-0567-5). pmid: [31715617](https://pubmed.ncbi.nlm.nih.gov/31715617/).
- Ettrup, Anders et al. (Apr. 2011). “Radiosynthesis and in Vivo Evaluation of a Series of Substituted ¹¹C-phenethylamines as 5-HT (2A) Agonist PET Tracers.” In: *European Journal of Nuclear Medicine and Molecular Imaging* 38.4, pp. 681–693. ISSN: 1619-7089. DOI: [10.1007/s00259-010-1686-8](https://doi.org/10.1007/s00259-010-1686-8). pmid: [21174090](https://pubmed.ncbi.nlm.nih.gov/21174090/).
- Ettrup, Anders et al. (July 2014). “Serotonin 2A Receptor Agonist Binding in the Human Brain with [¹¹C]Cimbi-36.” In: *Journal of cerebral blood flow and metabolism : official journal of the International Society of Cerebral Blood Flow and Metabolism* 34.7, pp. 1188–1196. ISSN: 1559-7016. DOI: [10.1038/jcbfm.2014.68](https://doi.org/10.1038/jcbfm.2014.68). PMID: [24780897](https://pubmed.ncbi.nlm.nih.gov/24780897/).
- Ettrup, Anders et al. (2016). “Serotonin 2A Receptor Agonist Binding in the Human Brain with [¹¹C]Cimbi-36: Test-retest Reproducibility and Head-to-Head Comparison with the Antagonist [¹⁸F]Altanserin.” In: *NeuroImage* 130, pp. 167–174. ISSN: 10959572. DOI: [10.1016/j.neuroimage.2016.02.001](https://doi.org/10.1016/j.neuroimage.2016.02.001). pmid: [26876490](https://pubmed.ncbi.nlm.nih.gov/26876490/).
- Farde, L., F. A. Wiesel, C. Halldin, and G. Sedvall (Jan. 1988). “Central D₂-dopamine Receptor Occupancy in Schizophrenic Patients Treated with Antipsychotic Drugs.” In: *Archives of General Psychiatry* 45.1, pp. 71–76. ISSN: 0003-990X. DOI: [10.1001/archpsyc.1988.01800250087012](https://doi.org/10.1001/archpsyc.1988.01800250087012). pmid: [2892477](https://pubmed.ncbi.nlm.nih.gov/2892477/).
- Finnema, Sjoerd J., Vladimir Stepanov, Anders Ettrup, Ryuji Nakao, Nahid Amini, Marie Svedberg, Charlotte Lehmann, Martin Hansen, Gitte M. Knudsen, and Christer Halldin (Jan. 1, 2014). “Characterization of [(11)C]Cimbi-36 as an Agonist PET Radioligand for the 5-HT(2A) and 5-HT(2C) Receptors in the Non-human Primate Brain.” In: *NeuroImage* 84, pp. 342–353. ISSN: 1095-9572. DOI: [10.1016/j.neuroimage.2013.08.035](https://doi.org/10.1016/j.neuroimage.2013.08.035). pmid: [23994452](https://pubmed.ncbi.nlm.nih.gov/23994452/).
- Finnema, Sjoerd J et al. (July 2016). “Imaging Synaptic Density in the Living Human Brain.” In: *Science translational medicine* 8.348, 348ra96. ISSN: 1946-6242 (Electronic). DOI: [10.1126/scitranslmed.aaf6667](https://doi.org/10.1126/scitranslmed.aaf6667). pmid: [27440727](https://pubmed.ncbi.nlm.nih.gov/27440727/).
- Finnema, Sjoerd J et al. (Nov. 2018). “Kinetic Evaluation and Test-Retest Reproducibility of [(11)C]UCB-J, a Novel Radioligand for Positron Emission Tomography Imaging of Synaptic Vesicle Glycoprotein 2A in Humans.” In: *Journal of cerebral blood flow and metabolism : official journal of the International Society of Cerebral Blood Flow and Metabolism* 38.11, pp. 2041–2052. ISSN: 1559-7016 (Electronic). DOI: [10.1177/0271678X17724947](https://doi.org/10.1177/0271678X17724947). pmid: [28792356](https://pubmed.ncbi.nlm.nih.gov/28792356/).
- Finnema, Sjoerd J. et al. (May 2019). “A Single-Center, Open-Label Positron Emission Tomography Study to Evaluate Brivaracetam and Levetiracetam Synaptic Vesicle Glycoprotein 2A Binding in Healthy Volunteers.” In: *Epilepsia* 60.5, pp. 958–967. ISSN: 1528-1167. DOI: [10.1111/epi.14701](https://doi.org/10.1111/epi.14701). pmid: [30924924](https://pubmed.ncbi.nlm.nih.gov/30924924/).
- Finnema, Sjoerd J. et al. (Oct. 2020). “Reduced Synaptic Vesicle Protein 2A Binding in Temporal Lobe Epilepsy: A [¹¹C]UCB-J Positron Emission Tomography Study.” In: *Epilepsia* 61.10, pp. 2183–2193. ISSN: 1528-1167. DOI: [10.1111/epi.16653](https://doi.org/10.1111/epi.16653). pmid: [32944949](https://pubmed.ncbi.nlm.nih.gov/32944949/).
- Fujita, Masahiro, Masao Imaizumi, Sami S. Zoghbi, Yota Fujimura, Amanda G. Farris, Tetsuya Suhara, Jinsoo Hong, Victor W. Pike, and Robert B. Innis (Mar. 1, 2008). “Kinetic Analysis in Healthy Humans of a Novel Positron Emission Tomography Radioligand to Image the Peripheral Benzodiazepine Receptor, a Potential Biomarker for Inflammation.” In: *NeuroImage* 40.1, pp. 43–52. ISSN: 1053-8119. DOI: [10.1016/j.neuroimage.2007.11.011](https://doi.org/10.1016/j.neuroimage.2007.11.011). pmid: [18093844](https://pubmed.ncbi.nlm.nih.gov/18093844/).
- Fujita, Masahiro et al. (Oct. 16, 2017). “Comparison of Four (¹¹C)-labeled PET Ligands to Quantify Translocator Protein 18 kDa (TSPO) in Human Brain: (R)-PK11195, PBR28, DPA-713, and ER176-based on Recent Publications That Measured Specific-to-Non-Displaceable Ratios.” In: *EJNMMI research* 7.1, p. 84. ISSN: 2191-219X. DOI: [10.1186/s13550-017-0334-8](https://doi.org/10.1186/s13550-017-0334-8). PMID: [29038960](https://pubmed.ncbi.nlm.nih.gov/29038960/).
- Gao, Yuyuan et al. (2017). “Changes of Brain Structure in Parkinson’s Disease Patients with Mild Cognitive Impairment Analyzed via VBM Technology.” In: *Neuroscience Letters* 658, pp. 121–132. ISSN: 0304-3940. DOI: [10.1016/j.neulet.](https://doi.org/10.1016/j.neulet.)

- 2017.08.028. URL: <http://www.sciencedirect.com/science/article/pii/S0304394017306754>.
- Ghadery, Christine, Yuko Koshimori, Sarah Coakeley, Madeleine Harris, Pablo Rusjan, Jinhee Kim, Sylvain Houle, and Antonio P Strafella (Jan. 11, 2017). "Microglial Activation in Parkinson's Disease Using [(18)F]-FEPPA." In: *Journal of neuroinflammation* 14.1, p. 8. ISSN: 1742-2094. DOI: [10.1186/s12974-016-0778-1](https://doi.org/10.1186/s12974-016-0778-1). PMID: [28086916](https://pubmed.ncbi.nlm.nih.gov/28086916/).
- Ginovart, N., A. A. Wilson, J. H. Meyer, D. Hussey, and S. Houle (Nov. 2001). "Positron Emission Tomography Quantification of [(11)C]-DASB Binding to the Human Serotonin Transporter: Modeling Strategies." In: *Journal of Cerebral Blood Flow and Metabolism: Official Journal of the International Society of Cerebral Blood Flow and Metabolism* 21.11, pp. 1342-1353. ISSN: 0271-678X. DOI: [10.1097/00004647-200111000-00010](https://doi.org/10.1097/00004647-200111000-00010). pmid: [11702049](https://pubmed.ncbi.nlm.nih.gov/11702049/).
- González-Maeso, Javier and Stuart C. Sealton (Apr. 2009). "Psychedelics and Schizophrenia." In: *Trends in Neurosciences* 32.4, pp. 225-232. ISSN: 01662236. DOI: [10.1016/j.tins.2008.12.005](https://doi.org/10.1016/j.tins.2008.12.005). URL: <https://linkinghub.elsevier.com/retrieve/pii/S016622360900037X> (visited on 12/22/2022).
- Gunn, R. N., S. R. Gunn, and V. J. Cunningham (June 2001). "Positron Emission Tomography Compartmental Models." In: *Journal of Cerebral Blood Flow and Metabolism: Official Journal of the International Society of Cerebral Blood Flow and Metabolism* 21.6, pp. 635-652. ISSN: 0271-678X. DOI: [10.1097/00004647-200106000-00002](https://doi.org/10.1097/00004647-200106000-00002). pmid: [11488533](https://pubmed.ncbi.nlm.nih.gov/11488533/).
- Gunn, Roger N and Eugenii A Rabiner (2017). "Imaging in Central Nervous System Drug Discovery." In: *Seminars in Nuclear Medicine* 47.1, pp. 89-98. ISSN: 0001-2998. DOI: [10.1053/j.semnuclmed.2016.09.001](https://doi.org/10.1053/j.semnuclmed.2016.09.001). URL: <http://www.sciencedirect.com/science/article/pii/S000129981630071X>.
- Gunn, Roger N, Mark Slifstein, Graham E Searle, and Julie C Price (Nov. 21, 2015). "Quantitative Imaging of Protein Targets in the Human Brain with PET." In: *Physics in Medicine and Biology* 60.22, R363-R411. ISSN: 0031-9155, 1361-6560. DOI: [10.1088/0031-9155/60/22/R363](https://doi.org/10.1088/0031-9155/60/22/R363). URL: <https://iopscience.iop.org/article/10.1088/0031-9155/60/22/R363> (visited on 12/31/2022).
- Guo, Qi, Alessandro Colasanti, David R. Owen, Mayca Onega, Aruloly Kamalakaran, Idriss Bennacef, Paul M. Matthews, Eugenii A. Rabiner, Federico E. Turkheimer, and Roger N. Gunn (Nov. 2013). "Quantification of the Specific Translocator Protein Signal of ¹⁸F-PBR111 in Healthy Humans: A Genetic Polymorphism Effect on In Vivo Binding." In: *Journal of Nuclear Medicine* 54.11, pp. 1915-1923. ISSN: 0161-5505, 2159-662X. DOI: [10.2967/jnumed.113.121020](https://doi.org/10.2967/jnumed.113.121020). URL: <http://jnm.snmjournals.org/lookup/doi/10.2967/jnumed.113.121020> (visited on 12/15/2022).
- Gómez-Vallejo, Vanessa, Luka Rejc, Fernando López-Gallego, and Jordi Llop (2019). "The Radiopharmaceutical Chemistry of Nitrogen-13 and Oxygen-15." In: *Radiopharmaceutical Chemistry*. Ed. by Jason S. Lewis, Albert D. Windhorst, and Brian M. Zeglis. Cham: Springer International Publishing, pp. 237-254. ISBN: 978-3-319-98946-4 978-3-319-98947-1. DOI: [10.1007/978-3-319-98947-1_13](https://doi.org/10.1007/978-3-319-98947-1_13). URL: http://link.springer.com/10.1007/978-3-319-98947-1_13 (visited on 01/01/2023).
- Halberstadt, Adam L. (Jan. 15, 2015). "Recent Advances in the Neuropsychopharmacology of Serotonergic Hallucinogens." In: *Behavioural Brain Research* 277, pp. 99-120. ISSN: 1872-7549. DOI: [10.1016/j.bbr.2014.07.016](https://doi.org/10.1016/j.bbr.2014.07.016). pmid: [25036425](https://pubmed.ncbi.nlm.nih.gov/25036425/).
- Hallare, Jericho and Valerie Gerriets (2022). "Half Life." In: *StatPearls*. Treasure Island (FL): StatPearls Publishing. pmid: [32119385](https://pubmed.ncbi.nlm.nih.gov/32119385/). URL: <http://www.ncbi.nlm.nih.gov/books/NBK554498/> (visited on 12/30/2022).
- Hurling, Kerstin, Antoine Leuzy, My Jonasson, Andreas Frick, Eduardo R. Zimmer, Agneta Nordberg, and Mark Lubberink (Sept. 2017). "Quantitative Positron Emission Tomography in Brain Research." In: *Brain Research* 1670, pp. 220-234. ISSN: 00068993. DOI: [10.1016/j.brainres.2017.06.022](https://doi.org/10.1016/j.brainres.2017.06.022). URL: <https://doi.org/10.1016/j.brainres.2017.06.022>.

- [//linkinghub.elsevier.com/retrieve/pii/S0006899317302706](http://linkinghub.elsevier.com/retrieve/pii/S0006899317302706) (visited on 01/01/2023).
- Hillmer, A. T. et al. (2017a). "In Vivo Imaging of Translocator Protein, a Marker of Activated Microglia, in Alcohol Dependence." In: *Molecular Psychiatry* 22.12, pp. 1759–1766. ISSN: 14765578. DOI: [10.1038/mp.2017.10](https://doi.org/10.1038/mp.2017.10). URL: <http://dx.doi.org/10.1038/mp.2017.10>.
- Hillmer, Ansel T, Daniel Holden, Krista Fowles, Nabeel Nabulsi, Brian L West, Richard E Carson, and Kelly P Cosgrove (Dec. 2017b). "Microglial Depletion and Activation: A [(11)C]PBR28 PET Study in Nonhuman Primates." In: *EJN-MMI research* 7.1, p. 59. ISSN: 2191-219X. DOI: [10.1186/s13550-017-0305-0](https://doi.org/10.1186/s13550-017-0305-0). PMID: [28741281](https://pubmed.ncbi.nlm.nih.gov/28741281/).
- Holford, Nick (2016). "Absorption and Half-Life." In: *Translational and Clinical Pharmacology* 24.4, p. 157. ISSN: 2289-0882, 2383-5427. DOI: [10.12793/tcp.2016.24.4.157](https://doi.org/10.12793/tcp.2016.24.4.157). URL: <https://tcpharm.org/DOIx.php?id=10.12793/tcp.2016.24.4.157> (visited on 12/30/2022).
- Holmes, Sophie E. et al. (Apr. 4, 2019). "Lower Synaptic Density Is Associated with Depression Severity and Network Alterations." In: *Nature Communications* 10.1, p. 1529. ISSN: 2041-1723. DOI: [10.1038/s41467-019-09562-7](https://doi.org/10.1038/s41467-019-09562-7). pmid: [30948709](https://pubmed.ncbi.nlm.nih.gov/30948709/).
- Ikawa, Masamichi et al. (Feb. 2017). "¹¹C-ER176, a Radioligand for 18-kDa Translocator Protein, Has Adequate Sensitivity to Robustly Image All Three Affinity Genotypes in Human Brain." In: *Journal of Nuclear Medicine: Official Publication, Society of Nuclear Medicine* 58.2, pp. 320–325. ISSN: 1535-5667. DOI: [10.2967/jnumed.116.178996](https://doi.org/10.2967/jnumed.116.178996). pmid: [27856631](https://pubmed.ncbi.nlm.nih.gov/27856631/).
- Innis, Robert B et al. (May 9, 2007). "Consensus Nomenclature for in Vivo Imaging of Reversibly Binding Radioligands." In: *Journal of Cerebral Blood Flow & Metabolism* 27.9, pp. 1533–1539. ISSN: 0271-678X. DOI: [10.1038/sj.jcbfm.9600493](https://doi.org/10.1038/sj.jcbfm.9600493). URL: <https://doi.org/10.1038/sj.jcbfm.9600493>.
- Jain, Poorva, Aisling M. Chaney, Mackenzie L. Carlson, Isaac M. Jackson, Anoushka Rao, and Michelle L. James (Aug. 2020). "Neuroinflammation PET Imaging: Current Opinion and Future Directions." In: *Journal of Nuclear Medicine* 61.8, pp. 1107–1112. ISSN: 0161-5505, 2159-662X. DOI: [10.2967/jnumed.119.229443](https://doi.org/10.2967/jnumed.119.229443). URL: <http://jnm.snmjournals.org/lookup/doi/10.2967/jnumed.119.229443> (visited on 12/20/2022).
- Jørgensen, Louise M et al. (Feb. 2017). "Cerebral 5-HT Release Correlates with [(11)C]Cimbi36 PET Measures of 5-HT_{2A} Receptor Occupancy in the Pig Brain." In: *Journal of cerebral blood flow and metabolism : official journal of the International Society of Cerebral Blood Flow and Metabolism* 37.2, pp. 425–434. ISSN: 1559-7016. DOI: [10.1177/0271678X16629483](https://doi.org/10.1177/0271678X16629483). PMID: [26825776](https://pubmed.ncbi.nlm.nih.gov/26825776/).
- Kalk, N J et al. (Jan. 10, 2017). "Decreased Hippocampal Translocator Protein (18 kDa) Expression in Alcohol Dependence: A [(11)C]PBR28 PET Study." In: *Translational psychiatry* 7.1, e996–e996. ISSN: 2158-3188. DOI: [10.1038/tp.2016.264](https://doi.org/10.1038/tp.2016.264). PMID: [28072413](https://pubmed.ncbi.nlm.nih.gov/28072413/).
- Kim, Sung Won et al. (Aug. 2018). "Influence of Alcoholism and Cholesterol on TSPO Binding in Brain: PET [(11)C]PBR28 Studies in Humans and Rodents." In: *Neuropsychopharmacology : official publication of the American College of Neuropsychopharmacology* 43.9, pp. 1832–1839. ISSN: 1740-634X. DOI: [10.1038/s41386-018-0085-x](https://doi.org/10.1038/s41386-018-0085-x). PMID: [29777199](https://pubmed.ncbi.nlm.nih.gov/29777199/).
- Knoll, Glenn F. (2010). "Radiation Sources." In: *Radiation Detection and Measurement*. 4th Edition. Wiley, pp. 1–27.
- Koole, Michel, June van Aalst, Martijn Devrome, Nathalie Mertens, Kim Serdons, Brigitte Lacroix, Joel Mercier, David Sciberras, Paul Maguire, and Koen Van Laere (Feb. 2019). "Quantifying SV_{2A} Density and Drug Occupancy in the Human Brain Using [¹¹C]UCB-J PET Imaging and Subcortical White Matter as Reference Tissue." In: *European Journal of Nuclear Medicine and Molecular Imaging* 46.2, pp. 396–406. ISSN: 1619-7089. DOI: [10.1007/s00259-018-4119-8](https://doi.org/10.1007/s00259-018-4119-8). pmid: [30121895](https://pubmed.ncbi.nlm.nih.gov/30121895/).

- Koshimori, Yuko et al. (Sept. 18, 2015). "Imaging Striatal Microglial Activation in Patients with Parkinson's Disease." In: *PLoS ONE* 10.9, e0138721–e0138721. ISSN: 19326203. DOI: [10.1371/journal.pone.0138721](https://doi.org/10.1371/journal.pone.0138721). PMID: 26381267.
- Kumar, Ajay, Otto Muzik, Varun Shandal, Diane Chugani, Pulak Chakraborty, and Harry T. Chugani (Oct. 4, 2012). "Evaluation of Age-Related Changes in Translocator Protein (TSPO) in Human Brain Using (11)C-[R]-PK11195 PET." In: *Journal of Neuroinflammation* 9, p. 232. ISSN: 1742-2094. DOI: [10.1186/1742-2094-9-232](https://doi.org/10.1186/1742-2094-9-232). pmid: 23035793.
- Kyme, Andre Z. and Roger R. Fulton (Sept. 15, 2021). "Motion Estimation and Correction in SPECT, PET and CT." In: *Physics in Medicine and Biology* 66.18. ISSN: 1361-6560. DOI: [10.1088/1361-6560/ac093b](https://doi.org/10.1088/1361-6560/ac093b). pmid: 34102630.
- Lagarde, Julien, Marie Sarazin, and Michel Bottlaender (2018). "In Vivo PET Imaging of Neuroinflammation in Alzheimer's Disease." In: *Journal of Neural Transmission* 125.5, pp. 847–867. ISSN: 14351463. DOI: [10.1007/s00702-017-1731-x](https://doi.org/10.1007/s00702-017-1731-x).
- Lammertsma, A. A. and S. P. Hume (Dec. 1996). "Simplified Reference Tissue Model for PET Receptor Studies." In: *NeuroImage* 4 (3 Pt 1), pp. 153–158. ISSN: 1053-8119. DOI: [10.1006/nimg.1996.0066](https://doi.org/10.1006/nimg.1996.0066). pmid: 9345505.
- Lammertsma, Adriaan A. (July 2017). "Forward to the Past: The Case for Quantitative PET Imaging." In: *Journal of Nuclear Medicine: Official Publication, Society of Nuclear Medicine* 58.7, pp. 1019–1024. ISSN: 1535-5667. DOI: [10.2967/jnumed.116.188029](https://doi.org/10.2967/jnumed.116.188029). pmid: 28522743.
- Lassen, N. A. et al. (1995). "Benzodiazepine Receptor Quantification in Vivo in Humans Using [11C]Flumazenil and PET: Application of the Steady-State Principle." In: *Journal of Cerebral Blood Flow and Metabolism* 15.1, pp. 152–165. ISSN: 0271678X. DOI: [10.1038/jcbfm.1995.17](https://doi.org/10.1038/jcbfm.1995.17). pmid: 7798333.
- Lavis, Sonia et al. (Jan. 2021). "Increased Microglial Activation in Patients with Parkinson Disease Using [18F]-DPA714 TSPO PET Imaging." In: *Parkinsonism & Related Disorders* 82, pp. 29–36. ISSN: 1873-5126. DOI: [10.1016/j.parkreldis.2020.11.011](https://doi.org/10.1016/j.parkreldis.2020.11.011). pmid: 33242662.
- Ledoit, Olivier and Michael Wolf (2015). "Spectrum Estimation: A Unified Framework for Covariance Matrix Estimation and PCA in Large Dimensions." In: *Journal of Multivariate Analysis* 139, pp. 360–384. ISSN: 0047-259X. DOI: [10.1016/j.jmva.2015.04.006](https://doi.org/10.1016/j.jmva.2015.04.006). URL: <http://www.sciencedirect.com/science/article/pii/S0047259X15000949>.
- Lee, Tzu C., Adam M. Alessio, Robert M. Miyaoka, and Paul E. Kinahan (Mar. 2016). "Morphology Supporting Function: Attenuation Correction for SPECT/CT, PET/CT, and PET/MR Imaging." In: *The quarterly journal of nuclear medicine and molecular imaging: official publication of the Italian Association of Nuclear Medicine (AIMN) [and] the International Association of Radiopharmacology (IAR), [and] Section of the Society of...* 60.1, pp. 25–39. ISSN: 1827-1936. pmid: 26576737.
- Logan, J., J. S. Fowler, N. D. Volkow, Y. S. Ding, G. J. Wang, and D. L. Alexoff (Mar. 2001). "A Strategy for Removing the Bias in the Graphical Analysis Method." In: *Journal of Cerebral Blood Flow and Metabolism: Official Journal of the International Society of Cerebral Blood Flow and Metabolism* 21.3, pp. 307–320. ISSN: 0271-678X. DOI: [10.1097/00004647-200103000-00014](https://doi.org/10.1097/00004647-200103000-00014). pmid: 11295885.
- Lubberink, Mark and Kerstin Heurling (2019). "Kinetic Modeling of Radiotracers." In: *Radiopharmaceutical Chemistry*. Ed. by Jason S. Lewis, Albert D. Windhorst, and Brian M. Zeglis. Cham: Springer International Publishing, pp. 501–514. ISBN: 978-3-319-98946-4 978-3-319-98947-1. DOI: [10.1007/978-3-319-98947-1_28](https://doi.org/10.1007/978-3-319-98947-1_28). URL: http://link.springer.com/10.1007/978-3-319-98947-1_28 (visited on 01/01/2023).
- Madsen, Martin K. et al. (June 1, 2019). "Psychedelic Effects of Psilocybin Correlate with Serotonin 2A Receptor Occupancy and Plasma Psilocin Levels." In: *Neuropsychopharmacology* 44.7, pp. 1328–1334. ISSN: 1740-634X. DOI: [10.1038/s41386-019-0324-9](https://doi.org/10.1038/s41386-019-0324-9). URL: <https://doi.org/10.1038/s41386-019-0324-9>.

- Malpetti, Maura et al. (Nov. 2, 2022). "Synaptic Loss in Frontotemporal Dementia Revealed by [¹¹C]UCB-J Positron Emission Tomography." In: *Annals of Neurology*. ISSN: 1531-8249. DOI: [10.1002/ana.26543](https://doi.org/10.1002/ana.26543). PMID: [36321699](https://pubmed.ncbi.nlm.nih.gov/36321699/).
- Mandeville, Joseph B., Michael A. Levine, John T. Arsenault, Wim Vanduffel, Bruce R. Rosen, and Christin Y. Sander (June 2022). "A Reference Tissue Forward Model for Improved PET Accuracy Using Within-Scan Displacement Studies." In: *Journal of Cerebral Blood Flow and Metabolism: Official Journal of the International Society of Cerebral Blood Flow and Metabolism* 42.6, pp. 1007–1019. ISSN: 1559-7016. DOI: [10.1177/0271678X211065212](https://doi.org/10.1177/0271678X211065212). PMID: [34894821](https://pubmed.ncbi.nlm.nih.gov/34894821/).
- Marner, Lisbeth et al. (June 2009). "Kinetic Modeling of ¹¹C-SB207145 Binding to 5-HT₄ Receptors in the Human Brain in Vivo." In: *Journal of Nuclear Medicine: Official Publication, Society of Nuclear Medicine* 50.6, pp. 900–908. ISSN: 0161-5505. DOI: [10.2967/jnumed.108.058552](https://doi.org/10.2967/jnumed.108.058552). PMID: [19470850](https://pubmed.ncbi.nlm.nih.gov/19470850/).
- Marques, Tiago Reis, Abhishekh H Ashok, Toby Pillinger, Mattia Veronese, Federico E. Turkheimer, Paola Dazzan, Iris E.C. Sommer, and Oliver D Howes (Oct. 2019). "Neuroinflammation in Schizophrenia: Meta-Analysis of *in Vivo* Microglial Imaging Studies." In: *Psychological Medicine* 49.13, pp. 2186–2196. ISSN: 0033-2917, 1469-8978. DOI: [10.1017/S0033291718003057](https://doi.org/10.1017/S0033291718003057). URL: https://www.cambridge.org/core/product/identifier/S0033291718003057/type/journal_article (visited on 12/20/2022).
- Marques, Tiago Reis, Mattia Veronese, David R. Owen, Eugenii A. Rabiner, Graham E. Searle, and Oliver D. Howes (Oct. 2021). "Specific and Non-Specific Binding of a Tracer for the Translocator-Specific Protein in Schizophrenia: An [¹¹C]-PBR28 Blocking Study." In: *European Journal of Nuclear Medicine and Molecular Imaging* 48.11, pp. 3530–3539. ISSN: 1619-7089. DOI: [10.1007/s00259-021-05327-x](https://doi.org/10.1007/s00259-021-05327-x). PMID: [33825022](https://pubmed.ncbi.nlm.nih.gov/33825022/).
- Martin, Crescent B and Cynthia L Ogden (2019). "Prescription Drug Use in the United States, 2015–2016." In: 334.
- Matheson, Granville J., Pontus Plavén-Sigra, Anton Forsberg, Andrea Varrone, Lars Farde, and Simon Cervenka (2017). "Assessment of Simplified Ratio-Based Approaches for Quantification of PET [¹¹C]PBR28 Data." In: *EJNMMI Research* 7, pp. 1–6. ISSN: 2191219X. DOI: [10.1186/s13550-017-0304-1](https://doi.org/10.1186/s13550-017-0304-1).
- Mercier, Joël et al. (Apr. 2014). "Discovery of Heterocyclic Nonacetamide Synaptic Vesicle Protein 2A (SV2A) Ligands with Single-Digit Nanomolar Potency: Opening Avenues towards the First SV2A Positron Emission Tomography (PET) Ligands." In: *ChemMedChem* 9.4, pp. 693–698. ISSN: 18607179. DOI: [10.1002/cmdc.201300482](https://doi.org/10.1002/cmdc.201300482). URL: <https://onlinelibrary.wiley.com/doi/10.1002/cmdc.201300482> (visited on 12/22/2022).
- Milak, Matthew S., Christine DeLorenzo, Francesca Zanderigo, Jaya Prabhakaran, J. S. Dileep Kumar, Vattoly J. Majo, J. John Mann, and Ramin V. Parsey (Dec. 2010). "In Vivo Quantification of Human Serotonin 1A Receptor Using ¹¹C-CUMI-101, an Agonist PET Radiotracer." In: *Journal of Nuclear Medicine: Official Publication, Society of Nuclear Medicine* 51.12, pp. 1892–1900. ISSN: 1535-5667. DOI: [10.2967/jnumed.110.076257](https://doi.org/10.2967/jnumed.110.076257). PMID: [21098796](https://pubmed.ncbi.nlm.nih.gov/21098796/).
- Minter, Myles R., Juliet M. Taylor, and Peter J. Crack (Feb. 2016). "The Contribution of Neuroinflammation to Amyloid Toxicity in Alzheimer's Disease." In: *Journal of Neurochemistry* 136.3, pp. 457–474. ISSN: 1471-4159. DOI: [10.1111/jnc.13411](https://doi.org/10.1111/jnc.13411). PMID: [26509334](https://pubmed.ncbi.nlm.nih.gov/26509334/).
- Mintun, M. A., M. E. Raichle, M. R. Kilbourn, G. F. Wooten, and M. J. Welch (Mar. 1984). "A Quantitative Model for the *in Vivo* Assessment of Drug Binding Sites with Positron Emission Tomography." In: *Annals of Neurology* 15.3, pp. 217–227. ISSN: 0364-5134. DOI: [10.1002/ana.410150302](https://doi.org/10.1002/ana.410150302). PMID: [6609679](https://pubmed.ncbi.nlm.nih.gov/6609679/).
- Morgan, Paul, Piet H. Van Der Graaf, John Arrowsmith, Doug E. Feltner, Kira S. Drummond, Craig D. Wegner, and Steve D. A. Street (May 2012). "Can the Flow of Medicines Be Improved? Fundamental Pharmacokinetic and Pharmacological Principles toward Improving Phase II Survival." In: *Drug Discovery Today*

- 17.9-10, pp. 419-424. ISSN: 1878-5832. DOI: [10.1016/j.drudis.2011.12.020](https://doi.org/10.1016/j.drudis.2011.12.020). pmid: 22227532.
- Mullard, Asher (July 2016). "Parsing Clinical Success Rates." In: *Nature Reviews Drug Discovery* 15.7, pp. 447-447. ISSN: 1474-1776, 1474-1784. DOI: [10.1038/nrd.2016.136](https://doi.org/10.1038/nrd.2016.136). URL: <http://www.nature.com/articles/nrd.2016.136> (visited on 12/30/2022).
- Mutch, Sarah A. et al. (Jan. 26, 2011). "Protein Quantification at the Single Vesicle Level Reveals That a Subset of Synaptic Vesicle Proteins Are Trafficked with High Precision." In: *The Journal of Neuroscience: The Official Journal of the Society for Neuroscience* 31.4, pp. 1461-1470. ISSN: 1529-2401. DOI: [10.1523/JNEUROSCI.3805-10.2011](https://doi.org/10.1523/JNEUROSCI.3805-10.2011). pmid: 21273430.
- Nabulsi, Nabeel B. et al. (May 2016). "Synthesis and Preclinical Evaluation of ¹¹C-UCB-J as a PET Tracer for Imaging the Synaptic Vesicle Glycoprotein 2A in the Brain." In: *Journal of Nuclear Medicine: Official Publication, Society of Nuclear Medicine* 57.5, pp. 777-784. ISSN: 1535-5667. DOI: [10.2967/jnumed.115.168179](https://doi.org/10.2967/jnumed.115.168179). pmid: 26848175.
- Naganawa, Mika, Jean-Dominique Gallezot, Samantha Rossano, and Richard E Carson (Sept. 2019). "Quantitative PET Imaging in Drug Development: Estimation of Target Occupancy." In: *Bulletin of mathematical biology* 81.9, pp. 3508-3541. ISSN: 1522-9602. DOI: [10.1007/s11538-017-0374-2](https://doi.org/10.1007/s11538-017-0374-2). URL: <https://pubmed.ncbi.nlm.nih.gov/29230702>.
- Naganawa, Mika et al. (Nov. 8, 2022). "Drug Characteristics Derived from Kinetic Modeling: Combined ¹¹C-UCB-J Human PET Imaging with Levetiracetam and Brivaracetam Occupancy of SV2A." In: *EJNMMI Research* 12.1, p. 71. ISSN: 2191-219X. DOI: [10.1186/s13550-022-00944-5](https://doi.org/10.1186/s13550-022-00944-5). URL: <https://ejnmires.springeropen.com/articles/10.1186/s13550-022-00944-5> (visited on 11/23/2022).
- Narayanaswami, Vidya, Kenneth Dahl, Vadim Bernard-Gauthier, Lee Josephson, Paul Cumming, and Neil Vasdev (2018). "Emerging PET Radiotracers and Targets for Imaging of Neuroinflammation in Neurodegenerative Diseases: Outlook Beyond TSPO." In: *Molecular Imaging* 17, p. 1536012118792317. ISSN: 1536-0121. DOI: [10.1177/1536012118792317](https://doi.org/10.1177/1536012118792317). pmid: 30203712.
- Normandin, Marc D., Wynne K. Schiffer, and Evan D. Morris (Feb. 1, 2012). "A Linear Model for Estimation of Neurotransmitter Response Profiles from Dynamic PET Data." In: *NeuroImage* 59.3, pp. 2689-2699. ISSN: 1095-9572. DOI: [10.1016/j.neuroimage.2011.07.002](https://doi.org/10.1016/j.neuroimage.2011.07.002). pmid: 21767654.
- Nutma, Erik et al. (Nov. 1, 2019). "A Quantitative Neuropathological Assessment of Translocator Protein Expression in Multiple Sclerosis." In: *Brain: A Journal of Neurology* 142.11, pp. 3440-3455. ISSN: 1460-2156. DOI: [10.1093/brain/awz287](https://doi.org/10.1093/brain/awz287). pmid: 31578541.
- Nørgaard, Martin, Melanie Ganz, Claus Svarer, Vibe G. Frokjaer, Douglas N. Greve, Stephen C. Strother, and Gitte M. Knudsen (Sept. 2020). "Different Preprocessing Strategies Lead to Different Conclusions: A [¹¹C]DASB-PET Reproducibility Study." In: *Journal of Cerebral Blood Flow and Metabolism: Official Journal of the International Society of Cerebral Blood Flow and Metabolism* 40.9, pp. 1902-1911. ISSN: 1559-7016. DOI: [10.1177/0271678X19880450](https://doi.org/10.1177/0271678X19880450). pmid: 31575336.
- Ogden, R. Todd, Francesca Zanderigo, and Ramin V. Parsey (2015). "Estimation of in Vivo Nonspecific Binding in Positron Emission Tomography Studies without Requiring a Reference Region." In: *NeuroImage* 108, pp. 234-242. ISSN: 10959572. DOI: [10.1016/j.neuroimage.2014.12.038](https://doi.org/10.1016/j.neuroimage.2014.12.038). URL: <http://dx.doi.org/10.1016/j.neuroimage.2014.12.038>.
- Okazawa, Hidehiko, Yoshifumi Higashino, Tetsuya Tsujikawa, Hidetaka Arishima, Tetsuya Mori, Yasushi Kiyono, Hirohiko Kimura, and Ken-ichiro Kikuta (Aug. 2018). "Noninvasive Method for Measurement of Cerebral Blood Flow Using O-15 Water PET/MRI with ASL Correlation." In: *European Journal of Radiology* 105, pp. 102-109. ISSN: 0720048X. DOI: [10.1016/j.ejrad.2018.05.033](https://doi.org/10.1016/j.ejrad.2018.05.033). URL: <https://linkinghub.elsevier.com/retrieve/pii/S0720048X18302043> (visited on 01/01/2023).

- Olesen, J., A. Gustavsson, M. Svensson, H.-U. Wittchen, B. Jönsson, on behalf of the CDBE2010 study group, and the European Brain Council (Jan. 2012). "The Economic Cost of Brain Disorders in Europe: Economic Cost of Brain Disorders in Europe." In: *European Journal of Neurology* 19.1, pp. 155–162. ISSN: 13515101. DOI: [10.1111/j.1468-1331.2011.03590.x](https://doi.org/10.1111/j.1468-1331.2011.03590.x). URL: <https://onlinelibrary.wiley.com/doi/10.1111/j.1468-1331.2011.03590.x> (visited on 12/26/2022).
- Olesen, J. and M. Leonardi (Sept. 2003). "The Burden of Brain Diseases in Europe." In: *European Journal of Neurology* 10.5, pp. 471–477. ISSN: 1351-5101. DOI: [10.1046/j.1468-1331.2003.00682.x](https://doi.org/10.1046/j.1468-1331.2003.00682.x). PMID: [12940825](https://pubmed.ncbi.nlm.nih.gov/12940825/).
- Olin, Anders B., Adam E. Hansen, Jacob H. Rasmussen, Björn Jakoby, Anne K. Berthelsen, Claes N. Ladefoged, Andreas Kjær, Barbara M. Fischer, and Flemming L. Andersen (Mar. 16, 2022). "Deep Learning for Dixon MRI-based Attenuation Correction in PET/MRI of Head and Neck Cancer Patients." In: *EJNMMI physics* 9.1, p. 20. ISSN: 2197-7364. DOI: [10.1186/s40658-022-00449-z](https://doi.org/10.1186/s40658-022-00449-z). PMID: [35294629](https://pubmed.ncbi.nlm.nih.gov/35294629/).
- Owen, David R et al. (Sept. 2010). "Two Binding Sites for [³H]PBR28 in Human Brain: Implications for TSPO PET Imaging of Neuroinflammation." In: *Journal of cerebral blood flow and metabolism : official journal of the International Society of Cerebral Blood Flow and Metabolism* 30.9, pp. 1608–1618. ISSN: 1559-7016. DOI: [10.1038/jcbfm.2010.63](https://doi.org/10.1038/jcbfm.2010.63). PMID: [20424634](https://pubmed.ncbi.nlm.nih.gov/20424634/).
- Owen, David R et al. (Jan. 2012). "An 18-kDa Translocator Protein (TSPO) Polymorphism Explains Differences in Binding Affinity of the PET Radioligand PBR28." In: *Journal of cerebral blood flow and metabolism : official journal of the International Society of Cerebral Blood Flow and Metabolism* 32.1, pp. 1–5. ISSN: 1559-7016. DOI: [10.1038/jcbfm.2011.147](https://doi.org/10.1038/jcbfm.2011.147). PMID: [22008728](https://pubmed.ncbi.nlm.nih.gov/22008728/).
- Owen, David R et al. (June 2014). "Determination of [(11)C]PBR28 Binding Potential in Vivo: A First Human TSPO Blocking Study." In: *Journal of cerebral blood flow and metabolism : official journal of the International Society of Cerebral Blood Flow and Metabolism* 34.6, pp. 989–994. ISSN: 1559-7016. DOI: [10.1038/jcbfm.2014.46](https://doi.org/10.1038/jcbfm.2014.46). PMID: [24643083](https://pubmed.ncbi.nlm.nih.gov/24643083/).
- Palpagama, Thulani H., Henry J. Waldvogel, Richard L. M. Faull, and Andrea Kwakowsky (2019). "The Role of Microglia and Astrocytes in Huntington's Disease." In: *Frontiers in Molecular Neuroscience* 12, p. 258. ISSN: 1662-5099. DOI: [10.3389/fnmol.2019.00258](https://doi.org/10.3389/fnmol.2019.00258). PMID: [31708741](https://pubmed.ncbi.nlm.nih.gov/31708741/).
- Parkinson Study Group (Apr. 3, 2002). "Dopamine Transporter Brain Imaging to Assess the Effects of Pramipexole vs Levodopa on Parkinson Disease Progression." In: *JAMA* 287.13, pp. 1653–1661. ISSN: 0098-7484. DOI: [10.1001/jama.287.13.1653](https://doi.org/10.1001/jama.287.13.1653). PMID: [11926889](https://pubmed.ncbi.nlm.nih.gov/11926889/).
- Parsey, R. V., M. Slifstein, D. R. Hwang, A. Abi-Dargham, N. Simpson, O. Mawlawi, N. N. Guo, R. Van Heertum, J. J. Mann, and M. Laruelle (July 2000). "Validation and Reproducibility of Measurement of 5-HT_{1A} Receptor Parameters with [Carbonyl-¹¹C]WAY-100635 in Humans: Comparison of Arterial and Reference Tissue Input Functions." In: *Journal of Cerebral Blood Flow and Metabolism: Official Journal of the International Society of Cerebral Blood Flow and Metabolism* 20.7, pp. 1111–1133. ISSN: 0271-678X. DOI: [10.1097/00004647-200007000-00011](https://doi.org/10.1097/00004647-200007000-00011). PMID: [10908045](https://pubmed.ncbi.nlm.nih.gov/10908045/).
- Pea, Federico, Robert Krause, Carsten Müller, Benjamin Hennart, Malcolm Richardson, Andreas Meintzer, Martin H.J. Wiesen, Tatiana Wiktorowicz, Jochen Spickermann, and Anne S. Henriksen (2019). "Interlaboratory Analysis of Isavuconazole Plasma Concentration Assays among European Laboratories." In: *Therapeutic Drug Monitoring* 41.5, pp. 657–664. ISSN: 15363694. DOI: [10.1097/FTD.0000000000000632](https://doi.org/10.1097/FTD.0000000000000632). PMID: [30950933](https://pubmed.ncbi.nlm.nih.gov/30950933/).
- Phelps, M. E., S. C. Huang, E. J. Hoffman, C. Selin, L. Sokoloff, and D. E. Kuhl (Nov. 1979). "Tomographic Measurement of Local Cerebral Glucose Metabolic Rate in Humans with (F-18)2-Fluoro-2-Deoxy-D-glucose: Validation of Method." In: *Annals of Neurology* 6.5, pp. 371–388. ISSN: 0364-5134, 1531-8249. DOI: [10.1002/](https://doi.org/10.1002/)

- ana. 410060502. URL: <https://onlinelibrary.wiley.com/doi/10.1002/ana.410060502> (visited on 01/01/2023).
- Pike, V. W., J. A. McCarron, A. A. Lammerstma, S. P. Hume, K. Poole, P. M. Grasby, A. Malizia, I. A. Cliffe, A. Fletcher, and C. J. Bench (Sept. 5, 1995). "First Delimitation of 5-HT_{1A} Receptors in Human Brain with PET and [¹¹C]WAY-100635." In: *European Journal of Pharmacology* 283.1-3, R1-3. ISSN: 0014-2999. DOI: [10.1016/0014-2999\(95\)00438-q](https://doi.org/10.1016/0014-2999(95)00438-q). pmid: 7498295.
- Plavén-Sigray, Pontus, Granville James Matheson, Zsolt Cselényi, Aurelija Jucaite, Lars Farde, and Simon Cervenka (Nov. 29, 2018a). "Test-Retest Reliability and Convergent Validity of (R)-[(¹¹C)]PK11195 Outcome Measures without Arterial Input Function." In: *EJNMMI research* 8.1, p. 102. ISSN: 2191-219X. DOI: [10.1186/s13550-018-0455-8](https://doi.org/10.1186/s13550-018-0455-8). PMID: 30498919.
- Plavén-Sigray, Pontus et al. (2018b). "Positron Emission Tomography Studies of the Glial Cell Marker Translocator Protein in Patients With Psychosis: A Meta-analysis Using Individual Participant Data." In: *Biological Psychiatry* 84.6, pp. 433-442. ISSN: 0006-3223. DOI: [10.1016/j.biopsych.2018.02.1171](https://doi.org/10.1016/j.biopsych.2018.02.1171). URL: <http://www.sciencedirect.com/science/article/pii/S0006322318312988>.
- Plavén-Sigray, Pontus et al. (2019). "Accuracy and Reliability of [¹¹C]PBR28 Specific Binding Estimated without the Use of a Reference Region." In: *NeuroImage* 188 (June 2018), pp. 102-110. ISSN: 10959572. DOI: [10.1016/j.neuroimage.2018.11.020](https://doi.org/10.1016/j.neuroimage.2018.11.020).
- Poon, Jonathan K., Magnus L. Dahlbom, William W. Moses, Karthik Balakrishnan, Wenli Wang, Simon R. Cherry, and Ramsey D. Badawi (July 7, 2012). "Optimal Whole-Body PET Scanner Configurations for Different Volumes of LSO Scintillator: A Simulation Study." In: *Physics in Medicine and Biology* 57.13, pp. 4077-4094. ISSN: 1361-6560. DOI: [10.1088/0031-9155/57/13/4077](https://doi.org/10.1088/0031-9155/57/13/4077). pmid: 22678106.
- Radford, Lauren L. and Suzanne E. Lapi (2019). "Methods for the Production of Radionuclides for Medicine." In: *Radiopharmaceutical Chemistry*. Ed. by Jason S. Lewis, Albert D. Windhorst, and Brian M. Zeglis. Cham: Springer International Publishing, pp. 63-83. ISBN: 978-3-319-98946-4 978-3-319-98947-1. DOI: [10.1007/978-3-319-98947-1_4](https://doi.org/10.1007/978-3-319-98947-1_4). URL: http://link.springer.com/10.1007/978-3-319-98947-1_4 (visited on 01/01/2023).
- Radhakrishnan, Rajiv et al. (Dec. 2021). "In Vivo Evidence of Lower Synaptic Vesicle Density in Schizophrenia." In: *Molecular Psychiatry* 26.12, pp. 7690-7698. ISSN: 1476-5578. DOI: [10.1038/s41380-021-01184-0](https://doi.org/10.1038/s41380-021-01184-0). pmid: 34135473.
- Rahmim, Arman, Jing Tang, and Habib Zaidi (July 10, 2009). "Four-Dimensional (4D) Image Reconstruction Strategies in Dynamic PET: Beyond Conventional Independent Frame Reconstruction: Four-dimensional PET Imaging." In: *Medical Physics* 36.8, pp. 3654-3670. ISSN: 00942405. DOI: [10.1118/1.3160108](https://doi.org/10.1118/1.3160108). URL: <http://doi.wiley.com/10.1118/1.3160108> (visited on 01/01/2023).
- Rang, H. P. (Jan. 2006). "The Receptor Concept: Pharmacology's Big Idea." In: *British Journal of Pharmacology* 147 Suppl 1 (Suppl 1), S9-16. ISSN: 0007-1188. DOI: [10.1038/sj.bjp.0706457](https://doi.org/10.1038/sj.bjp.0706457). pmid: 16402126.
- Rinne, Juha O. et al. (Apr. 2010). "¹¹C-PiB PET Assessment of Change in Fibrillar Amyloid-Beta Load in Patients with Alzheimer's Disease Treated with Bapineuzumab: A Phase 2, Double-Blind, Placebo-Controlled, Ascending-Dose Study." In: *The Lancet. Neurology* 9.4, pp. 363-372. ISSN: 1474-4465. DOI: [10.1016/S1474-4422\(10\)70043-0](https://doi.org/10.1016/S1474-4422(10)70043-0). pmid: 20189881.
- Ritter, James M., Rod Flower, Graeme Henderson, Yoon Kong Loke, David MacEwan, and Humphrey P. Rang (2020a). "Chemical Transmission and Drug Action in the Central Nervous System." In: *Rang & Dale's Pharmacology*. Ninth Edition. Elsevier, pp. 480-485. ISBN: 978-0-7020-7448-6.
- Ritter, James M., Rod Flower, Graeme Henderson, Yoon Kong Loke, David MacEwan, and Humphrey P. Rang (2020b). "Drug Discovery and Development." In: *Rang & Dale's Pharmacology*. Ninth Edition. Elsevier, pp. 750-755. ISBN: 978-0-7020-7448-6.

- Ritter, James M., Rod Flower, Graeme Henderson, Yoon Kong Loke, David MacEwan, and Humphrey P. Rang (2020c). "Pharmacokinetics." In: *Rang & Dale's Pharmacology*. Ninth Edition. Elsevier, pp. 143–151. ISBN: 978-0-7020-7448-6.
- Rizzo, Gaia, Mattia Veronese, Matteo Tonietto, Paolo Zanotti-Fregonara, Federico E Turkheimer, and Alessandra Bertoldo (June 2014). "Kinetic Modeling without Accounting for the Vascular Component Impairs the Quantification of [(11)C]PBR28 Brain PET Data." In: *Journal of cerebral blood flow and metabolism : official journal of the International Society of Cerebral Blood Flow and Metabolism* 34.6, pp. 1060–1069. ISSN: 1559-7016. DOI: [10.1038/jcbfm.2014.55](https://doi.org/10.1038/jcbfm.2014.55). PMID: 24667911.
- Rousset, Olivier, Arman Rahmim, Abass Alavi, and Habib Zaidi (Apr. 2007). "Partial Volume Correction Strategies in PET." In: *PET Clinics* 2.2, pp. 235–249. ISSN: 15568598. DOI: [10.1016/j.cpet.2007.10.005](https://doi.org/10.1016/j.cpet.2007.10.005). URL: <https://linkinghub.elsevier.com/retrieve/pii/S1556859807000338> (visited on 01/01/2023).
- Saba, Wadad, Sébastien Goutal, Sylvain Auvity, Bertrand Kuhnast, Christine Coulon, Virginie Kouyoumdjian, Irène Buvat, Claire Leroy, and Nicolas Tournier (Sept. 1, 2018). "Imaging the Neuroimmune Response to Alcohol Exposure in Adolescent Baboons: A TSPO PET Study Using 18F-DPA-714." In: *Addiction Biology* 23.5, pp. 1000–1009. ISSN: 1355-6215. DOI: [10.1111/adb.12548](https://doi.org/10.1111/adb.12548). URL: <https://doi.org/10.1111/adb.12548>.
- Sadzot, B., C. Lemaire, P. Maquet, E. Salmon, A. Plenevaux, C. Degueldre, J. P. Hermanne, M. Guillaume, R. Cantineau, and D. Comar (Sept. 1995). "Serotonin 5HT₂ Receptor Imaging in the Human Brain Using Positron Emission Tomography and a New Radioligand, [18F]Altanserin: Results in Young Normal Controls." In: *Journal of Cerebral Blood Flow and Metabolism: Official Journal of the International Society of Cerebral Blood Flow and Metabolism* 15.5, pp. 787–797. ISSN: 0271-678X. DOI: [10.1038/jcbfm.1995.99](https://doi.org/10.1038/jcbfm.1995.99). pmid: 7673371.
- Saeed, Usman, Anthony E. Lang, and Mario Masellis (2020). "Neuroimaging Advances in Parkinson's Disease and Atypical Parkinsonian Syndromes." In: *Frontiers in Neurology* 11, p. 572976. ISSN: 1664-2295. DOI: [10.3389/fneur.2020.572976](https://doi.org/10.3389/fneur.2020.572976). pmid: 33178113.
- Sander, Christin Y., Stefano Bovo, Angel Torrado-Carvajal, Daniel Albrecht, Hongping Deng, Vitaly Napadow, Julie C. Price, Jacob M. Hooker, and Marco L. Loggia (Nov. 2021). "[11C]PBR28 Radiotracer Kinetics Are Not Driven by Alterations in Cerebral Blood Flow." In: *Journal of Cerebral Blood Flow and Metabolism: Official Journal of the International Society of Cerebral Blood Flow and Metabolism* 41.11, pp. 3069–3084. ISSN: 1559-7016. DOI: [10.1177/0271678X211023387](https://doi.org/10.1177/0271678X211023387). pmid: 34159823.
- Sandiego, Christine M. et al. (2015). "Imaging Robust Microglial Activation after Lipopolysaccharide Administration in Humans with PET." In: *Proceedings of the National Academy of Sciences* 112.40, pp. 12468–12473. ISSN: 0027-8424. DOI: [10.1073/pnas.1511003112](https://doi.org/10.1073/pnas.1511003112).
- Sasaki, Takeshi et al. (July 2012). "Quantification of Dopamine Transporter in Human Brain Using PET with 18F-FE-PE2I." In: *Journal of Nuclear Medicine: Official Publication, Society of Nuclear Medicine* 53.7, pp. 1065–1073. ISSN: 1535-5667. DOI: [10.2967/jnumed.111.101626](https://doi.org/10.2967/jnumed.111.101626). pmid: 22689927.
- Schain, Martin, Francesca Zanderigo, J. John Mann, and R. Todd Ogden (2017). "Estimation of the Binding Potential BPND without a Reference Region or Blood Samples for Brain PET Studies." In: *NeuroImage* 146 (October 2016), pp. 121–131. ISSN: 10959572. DOI: [10.1016/j.neuroimage.2016.11.035](https://doi.org/10.1016/j.neuroimage.2016.11.035). URL: <http://dx.doi.org/10.1016/j.neuroimage.2016.11.035>.
- Schain, Martin, Francesca Zanderigo, and R. Todd Ogden (2018). "Likelihood Estimation of Drug Occupancy for Brain PET Studies." In: *NeuroImage* 178, pp. 255–265. ISSN: 1053-8119. DOI: [10.1016/j.neuroimage.2018.05.017](https://doi.org/10.1016/j.neuroimage.2018.05.017). URL: <http://www.sciencedirect.com/science/article/pii/S1053811918304154>.
- Schain, Martin, Francesca Zanderigo, R. Todd Ogden, and William C. Kreisl (2018). "Non-Invasive Estimation of [11C]PBR28 Binding Potential." In: *NeuroImage* 169

- (October 2017), pp. 278–285. ISSN: 10959572. DOI: [10.1016/j.neuroimage.2017.12.002](https://doi.org/10.1016/j.neuroimage.2017.12.002). URL: <https://doi.org/10.1016/j.neuroimage.2017.12.002>.
- Selleri, S., F. Bruni, C. Costagli, A. Costanzo, G. Guerrini, G. Ciciani, B. Costa, and C. Martini (Oct. 2001). “2-Arylpyrazolo[1,5-a]Pyrimidin-3-Yl Acetamides. New Potent and Selective Peripheral Benzodiazepine Receptor Ligands.” In: *Bioorganic & Medicinal Chemistry* 9.10, pp. 2661–2671. ISSN: 0968-0896. DOI: [10.1016/S0968-0896\(01\)00192-4](https://doi.org/10.1016/S0968-0896(01)00192-4). PMID: 11557354.
- Serrano, Maria Elisa, Eugene Kim, Marija M. Petrinovic, Federico Turkheimer, and Diana Cash (2022). “Imaging Synaptic Density: The Next Holy Grail of Neuroscience?” In: *Frontiers in Neuroscience* 16, p. 796129. ISSN: 1662-4548. DOI: [10.3389/fnins.2022.796129](https://doi.org/10.3389/fnins.2022.796129). PMID: 35401097.
- Slifstein, Mark and Marc Laruelle (2001). “Models and Methods for Derivation of in Vivo Neuroreceptor Parameters with PET and SPECT Reversible Radiotracers.” In: *Nuclear Medicine and Biology* 28.5, pp. 595–608. ISSN: 0969-8051. DOI: [10.1016/S0969-8051\(01\)00214-1](https://doi.org/10.1016/S0969-8051(01)00214-1). URL: <http://www.sciencedirect.com/science/article/pii/S0969805101002141>.
- Slomka, Piotr J., Tinsu Pan, Daniel S. Berman, and Guido Germano (2015). “Advances in SPECT and PET Hardware.” In: *Progress in Cardiovascular Diseases* 57.6, pp. 566–578. ISSN: 1873-1740. DOI: [10.1016/j.pcad.2015.02.002](https://doi.org/10.1016/j.pcad.2015.02.002). PMID: 25721706.
- Smart, Kelly et al. (May 2021). “Binding of the Synaptic Vesicle Radiotracer [¹¹C]UCB-J Is Unchanged during Functional Brain Activation Using a Visual Stimulation Task.” In: *Journal of Cerebral Blood Flow and Metabolism: Official Journal of the International Society of Cerebral Blood Flow and Metabolism* 41.5, pp. 1067–1079. ISSN: 1559-7016. DOI: [10.1177/0271678X20946198](https://doi.org/10.1177/0271678X20946198). PMID: 32757741.
- Smietana, Katarzyna, Marcin Siatkowski, and Martin Møller (June 2016). “Trends in Clinical Success Rates.” In: *Nature Reviews. Drug Discovery* 15.6, pp. 379–380. ISSN: 1474-1784. DOI: [10.1038/nrd.2016.85](https://doi.org/10.1038/nrd.2016.85). PMID: 27199245.
- Srinivas, Nithya, Kaitlyn Maffuid, and Angela D. M. Kashuba (Sept. 2018). “Clinical Pharmacokinetics and Pharmacodynamics of Drugs in the Central Nervous System.” In: *Clinical Pharmacokinetics* 57.9, pp. 1059–1074. ISSN: 0312-5963, 1179-1926. DOI: [10.1007/s40262-018-0632-y](https://doi.org/10.1007/s40262-018-0632-y). URL: <http://link.springer.com/10.1007/s40262-018-0632-y> (visited on 12/26/2022).
- Stuckey, Shannon M., Lin Kooi Ong, Lyndsey E. Collins-Praino, and Renée J. Turner (Dec. 3, 2021). “Neuroinflammation as a Key Driver of Secondary Neurodegeneration Following Stroke?” In: *International Journal of Molecular Sciences* 22.23, p. 13101. ISSN: 1422-0067. DOI: [10.3390/ijms222313101](https://doi.org/10.3390/ijms222313101). PMID: 34884906.
- Svarer, Claus, Karine Madsen, Steen G. Hasselbalch, Lars H. Pinborg, Steven Haugbøl, Vibe G. Frøkjær, Søren Holm, Olaf B. Paulson, and Gitte M. Knudsen (Feb. 15, 2005). “MR-based Automatic Delineation of Volumes of Interest in Human Brain PET Images Using Probability Maps.” In: *NeuroImage* 24.4, pp. 969–979. ISSN: 1053-8119. DOI: [10.1016/j.neuroimage.2004.10.017](https://doi.org/10.1016/j.neuroimage.2004.10.017). PMID: 15670674.
- Takano, Akihiro, Andrea Varrone, Balázs Gulyás, Piero Salvadori, Antony Gee, Albert Windhorst, Johnny Vercouillie, Guy Bormans, Adriaan A. Lammertsma, and Christer Halldin (Nov. 1, 2016). “Guidelines to PET Measurements of the Target Occupancy in the Brain for Drug Development.” In: *European Journal of Nuclear Medicine and Molecular Imaging* 43.12, pp. 2255–2262. ISSN: 16197089. DOI: [10.1007/s00259-016-3476-4](https://doi.org/10.1007/s00259-016-3476-4). PMID: 27514528.
- Talbot, Peter S., Mark Slifstein, Dah-Ren Hwang, Yiyun Huang, Erica Scher, Anissa Abi-Dargham, and Marc Laruelle (Jan. 2, 2012). “Extended Characterisation of the Serotonin 2A (5-HT_{2A}) Receptor-Selective PET Radiotracer ¹¹C-MDL100907 in Humans: Quantitative Analysis, Test-Retest Reproducibility, and Vulnerability to Endogenous 5-HT Tone.” In: *NeuroImage* 59.1, pp. 271–285. ISSN: 1095-9572. DOI: [10.1016/j.neuroimage.2011.07.001](https://doi.org/10.1016/j.neuroimage.2011.07.001). PMID: 21782029.
- Terada, Tatsuhiro, Masamichi Yokokura, Etsuji Yoshikawa, Masami Futatsubashi, Satoshi Kono, Takashi Konishi, Hiroaki Miyajima, Takanori Hashizume, and Yasuomi Ouchi (Oct. 2016). “Extrastriatal Spreading of Microglial Activation

- in Parkinson's Disease: A Positron Emission Tomography Study." In: *Annals of Nuclear Medicine* 30.8, pp. 579–587. ISSN: 1864-6433. DOI: [10.1007/s12149-016-1099-2](https://doi.org/10.1007/s12149-016-1099-2). pmid: [27299437](https://pubmed.ncbi.nlm.nih.gov/27299437/).
- Thie, Joseph A. (Sept. 2004). "Understanding the Standardized Uptake Value, Its Methods, and Implications for Usage." In: *Journal of Nuclear Medicine: Official Publication, Society of Nuclear Medicine* 45.9, pp. 1431–1434. ISSN: 0161-5505. pmid: [15347707](https://pubmed.ncbi.nlm.nih.gov/15347707/).
- Tournier, Nicolas, Géraldine Pottier, Fabien Caillé, Christine Coulon, Maud Goislard, Benoit Jégo, Julia Negroni, Claire Leroy, and Wadad Saba (May 2021). "Nalmefene Alleviates the Neuroimmune Response to Repeated Binge-like Ethanol Exposure: A TSPO PET Imaging Study in Adolescent Rats." In: *Addiction Biology* 26.3, e12962. ISSN: 1369-1600. DOI: [10.1111/adb.12962](https://doi.org/10.1111/adb.12962). pmid: [32896074](https://pubmed.ncbi.nlm.nih.gov/32896074/).
- Tuisku, Jouni et al. (Oct. 2019). "Effects of Age, BMI and Sex on the Glial Cell Marker TSPO - a Multicentre [¹¹C]PBR28 HRRT PET Study." In: *European Journal of Nuclear Medicine and Molecular Imaging* 46.11, pp. 2329–2338. ISSN: 1619-7089. DOI: [10.1007/s00259-019-04403-7](https://doi.org/10.1007/s00259-019-04403-7). pmid: [31363804](https://pubmed.ncbi.nlm.nih.gov/31363804/).
- Tuncel, Hayel et al. (June 2021). "Kinetics and 28-Day Test-Retest Repeatability and Reproducibility of [¹¹C]UCB-J PET Brain Imaging." In: *Journal of Cerebral Blood Flow and Metabolism: Official Journal of the International Society of Cerebral Blood Flow and Metabolism* 41.6, pp. 1338–1350. ISSN: 1559-7016. DOI: [10.1177/0271678X20964248](https://doi.org/10.1177/0271678X20964248). pmid: [34013797](https://pubmed.ncbi.nlm.nih.gov/34013797/).
- Tyler, Ryan E. et al. (2019). "Detecting Neuroinflammation in the Brain Following Chronic Alcohol Exposure in Rats: A Comparison between in Vivo and in Vitro TSPO Radioligand Binding." In: *European Journal of Neuroscience* (October 2018), pp. 1831–1842. ISSN: 14609568. DOI: [10.1111/ejn.14392](https://doi.org/10.1111/ejn.14392).
- Vaquero, Juan José and Paul Kinahan (2015). "Positron Emission Tomography: Current Challenges and Opportunities for Technological Advances in Clinical and Preclinical Imaging Systems." In: *Annual Review of Biomedical Engineering* 17, pp. 385–414. ISSN: 1545-4274. DOI: [10.1146/annurev-bioeng-071114-040723](https://doi.org/10.1146/annurev-bioeng-071114-040723). pmid: [26643024](https://pubmed.ncbi.nlm.nih.gov/26643024/).
- Varga, József and Zsolt Szabo (Feb. 2002). "Modified Regression Model for the Logan Plot." In: *Journal of Cerebral Blood Flow and Metabolism: Official Journal of the International Society of Cerebral Blood Flow and Metabolism* 22.2, pp. 240–244. ISSN: 0271-678X. DOI: [10.1097/00004647-200202000-00012](https://doi.org/10.1097/00004647-200202000-00012). pmid: [11823722](https://pubmed.ncbi.nlm.nih.gov/11823722/).
- Varnäs, Katarina, Zsolt Cselényi, Aurelija Jucaite, Christer Halldin, Per Svenningsson, Lars Farde, and Andrea Varrone (2019). "PET Imaging of [¹¹C]PBR28 in Parkinson's Disease Patients Does Not Indicate Increased Binding to TSPO despite Reduced Dopamine Transporter Binding." In: *European Journal of Nuclear Medicine and Molecular Imaging* 46.2, pp. 367–375. ISSN: 16197089. DOI: [10.1007/s00259-018-4161-6](https://doi.org/10.1007/s00259-018-4161-6).
- Varnäs, Katarina, Vladimir Stepanov, and Christer Halldin (Oct. 2020). "Autoradiographic Mapping of Synaptic Vesicle Glycoprotein 2A in Non-Human Primate and Human Brain." In: *Synapse (New York, N.Y.)* 74.10, e22157. ISSN: 1098-2396 (Electronic). DOI: [10.1002/syn.22157](https://doi.org/10.1002/syn.22157). pmid: [32259300](https://pubmed.ncbi.nlm.nih.gov/32259300/).
- Varnäs, Katarina et al. (Jan. 2011). "Quantitative Analysis of [¹¹C]AZ10419369 Binding to 5-HT_{1B} Receptors in Human Brain." In: *Journal of Cerebral Blood Flow and Metabolism: Official Journal of the International Society of Cerebral Blood Flow and Metabolism* 31.1, pp. 113–123. ISSN: 1559-7016. DOI: [10.1038/jcbfm.2010.55](https://doi.org/10.1038/jcbfm.2010.55). pmid: [20424633](https://pubmed.ncbi.nlm.nih.gov/20424633/).
- Varrone, Andrea, Christoffer Bundgaard, and Benny Bang-Andersen (Apr. 2022). "PET as a Translational Tool in Drug Development for Neuroscience Compounds." In: *Clinical Pharmacology and Therapeutics* 111.4, pp. 774–785. ISSN: 1532-6535. DOI: [10.1002/cpt.2548](https://doi.org/10.1002/cpt.2548). pmid: [35201613](https://pubmed.ncbi.nlm.nih.gov/35201613/).
- Vendel, Esmée, Vivi Rottschäfer, and Elizabeth C. M. de Lange (May 16, 2019). "The Need for Mathematical Modelling of Spatial Drug Distribution within the Brain." In: *Fluids and barriers of the CNS* 16.1, p. 12. ISSN: 2045-8118. DOI: [10.1186/s12987-019-0133-x](https://doi.org/10.1186/s12987-019-0133-x). pmid: [31092261](https://pubmed.ncbi.nlm.nih.gov/31092261/).

- Venkataraman, Ashwin V. et al. (Aug. 17, 2022). "Widespread Cell Stress and Mitochondrial Dysfunction Occur in Patients with Early Alzheimer's Disease." In: *Science Translational Medicine* 14.658, eabk1051. ISSN: 1946-6242. DOI: [10.1126/scitranslmed.abk1051](https://doi.org/10.1126/scitranslmed.abk1051). pmid: 35976998.
- Vignal, Nicolas, Salvatore Cisternino, Nathalie Rizzo-Padoin, Carine San, Fortune Hontonnou, Thibaut Gelé, Xavier Declèves, Laure Sarda-Mantel, and Benoît Hosten (June 7, 2018). "[¹⁸F]FEPPA a TSPO Radioligand: Optimized Radiosynthesis and Evaluation as a PET Radiotracer for Brain Inflammation in a Peripheral LPS-Injected Mouse Model." In: *Molecules (Basel, Switzerland)* 23.6, p. 1375. ISSN: 1420-3049. DOI: [10.3390/molecules23061375](https://doi.org/10.3390/molecules23061375). PMID: 29875332.
- Weiss, Julian J. et al. (Oct. 20, 2021). "Preliminary In Vivo Evidence of Reduced Synaptic Density in Human Immunodeficiency Virus (HIV) Despite Antiretroviral Therapy." In: *Clinical Infectious Diseases: An Official Publication of the Infectious Diseases Society of America* 73.8, pp. 1404–1411. ISSN: 1537-6591. DOI: [10.1093/cid/ciab484](https://doi.org/10.1093/cid/ciab484). pmid: 34050746.
- Wilson, Alan A., Armando Garcia, Jun Parkes, Patrick McCormick, Karin A. Stephenson, Sylvain Houle, and Neil Vasdev (Apr. 2008). "Radiosynthesis and Initial Evaluation of [¹⁸F]-FEPPA for PET Imaging of Peripheral Benzodiazepine Receptors." In: *Nuclear Medicine and Biology* 35.3, pp. 305–314. ISSN: 0969-8051. DOI: [10.1016/j.nucmedbio.2007.12.009](https://doi.org/10.1016/j.nucmedbio.2007.12.009). pmid: 18355686.
- Wilson, Heather et al. (Aug. 2020). "Mitochondrial Complex 1, Sigma 1, and Synaptic Vesicle 2A in Early Drug-Naive Parkinson's Disease." In: *Movement Disorders: Official Journal of the Movement Disorder Society* 35.8, pp. 1416–1427. ISSN: 1531-8257. DOI: [10.1002/mds.28064](https://doi.org/10.1002/mds.28064). pmid: 32347983.
- Yang, Kai-Chun, Vladimir Stepanov, Stefan Martinsson, Anders Ettrup, Akihiro Takano, Gitte M. Knudsen, Christer Halldin, Lars Farde, and Sjoerd J. Finnema (Sept. 1, 2017). "Fenfluramine Reduces [¹¹C]Cimbi-36 Binding to the 5-HT_{2A} Receptor in the Nonhuman Primate Brain." In: *The International Journal of Neuropsychopharmacology* 20.9, pp. 683–691. ISSN: 1469-5111. DOI: [10.1093/ijnp/pyx051](https://doi.org/10.1093/ijnp/pyx051). pmid: 28911007.
- Yang, Kai-Chun et al. (Sept. 2019). "Effect of Clinically Relevant Doses of Vortioxetine and Citalopram on Serotonergic PET Markers in the Nonhuman Primate Brain." In: *Neuropsychopharmacology: Official Publication of the American College of Neuropsychopharmacology* 44.10, pp. 1706–1713. ISSN: 1740-634X. DOI: [10.1038/s41386-019-0442-4](https://doi.org/10.1038/s41386-019-0442-4). pmid: 31216565.
- Yin, Xinyou, Jan Goudriaan, Egbert A. Lantinga, Jan Vos, and Huub J. Spiertz (Feb. 2003). "A Flexible Sigmoid Function of Determinate Growth." In: *Annals of Botany* 91.3, pp. 361–371. ISSN: 0305-7364. DOI: [10.1093/aob/mcg029](https://doi.org/10.1093/aob/mcg029). pmid: 12547689.
- Zanotti-Fregonara, Paolo, Kewei Chen, Jieih-San Liow, Masahiro Fujita, and Robert B Innis (Oct. 2011). "Image-Derived Input Function for Brain PET Studies: Many Challenges and Few Opportunities." In: *Journal of Cerebral Blood Flow & Metabolism* 31.10, pp. 1986–1998. ISSN: 0271-678X, 1559-7016. DOI: [10.1038/jcbfm.2011.107](https://doi.org/10.1038/jcbfm.2011.107). URL: <http://journals.sagepub.com/doi/10.1038/jcbfm.2011.107> (visited on 01/01/2023).
- Zhou, Yun, Ming-Kai Chen, Christopher J. Endres, Weiguo Ye, James R. Brasić, Mohab Alexander, Andrew H. Crabb, Tomás R. Guilarte, and Dean F. Wong (Nov. 1, 2006). "An Extended Simplified Reference Tissue Model for the Quantification of Dynamic PET with Amphetamine Challenge." In: *NeuroImage* 33.2, pp. 550–563. ISSN: 1053-8119. DOI: [10.1016/j.neuroimage.2006.06.038](https://doi.org/10.1016/j.neuroimage.2006.06.038). pmid: 16920365.

Part IX

STATEMENTS

Look up at the sky. Ask yourself, “Has the sheep eaten the flower or not?” And you’ll see how everything changes. . .

— Antoine de Saint-Exupéry,
The Little Prince

ETHICS STATEMENT

The data used in Paper I was collected at the Yale PET Center (New haven, Connecticut, USA) and at Karolinska Institutet (Solna, Sweden). All four studies were approved by their respective local ethics committees. We refer to the original publications of the datasets for further details (Collste et al., 2017; Hillmer et al., 2017; Sandiego et al., 2015; Varnäs et al., 2019).

In Paper II, the simulations were based on existing [^{11}C]Cimbi-36 data (da Cunha-Bang et al., 2019). That study was approved by the Ethics committee for the Capital Region of Denmark (Journal number: H-4-2012-105).

The pig experiments that were part of Paper III were approved by The Danish Council of Animal Ethics (Journal number: 2016-15-0201-01149), and conformed to the ARRIVE guidelines and European Commission's Directive 2010/63/EU.

DATA AVAILABILITY

The [^{11}C]PBR28 datasets that were included in Paper I were kindly provided by groups at Karolinska Institutet (Solna, Sweden) and The Yale PET Center (New Haven, Connecticut, USA). For this data, we refer to the corresponding authors of the original publications (Collste et al., 2017; Hillmer et al., 2017; Sandiego et al., 2015; Varnäs et al., 2019).

The simulations in Paper II were based on a previously published [^{11}C]Cimbi-36 dataset (da Cunha-Bang et al., 2019). For research purposes, all data from the Cimbi database (Knudsen et al., 2016) are made available upon request.

The simulations in Paper III are based on previously published rate constant estimates for [^{11}C]UCB-J (Finnema et al., 2018).

The [^{11}C]UCB-J pig dataset with in-scan intervention from Paper III is made available for research purposes upon request.

CODE AVAILABILITY

Matlab code for Simultaneous estimation of V_{ND} (SIME) is available at <https://github.com/martinschain/SIME>.

Matlab code for Likelihood Estimation of Occupancy (LEO) is available at <https://github.com/martinschain/LEO>.

Matlab code for Likelihood Estimation of Affinity (LEA) is available at <https://github.com/Gjertrud/LEA>.

Matlab code and test data for PET displacement models is available at <https://github.com/Gjertrud/ISI>.

ACKNOWLEDGEMENTS

First, I want to thank my spectacular team of supervisors for their encouragement and guidance. *Gitte*, I feel so honored to have been working so closely with you over the past years. Thank you for having my back, and for all your insightful comments and suggestions. *Claus*, I don't really understand why you trust my intuition so much, but I'm so happy that you do. Working with you has made me both smarter, and more confident. *Pontus*, thank you for the train rides, for the espressos, and for always letting me dump my stress on you. I have grown so much as a researcher - and as a person - under your guidance. *Todd*, you have impressed me from the first time we met. Thank you for always finding time to listen to my half-baked ideas, and for hosting me at Columbia/NYSPI during my change or research environment. *Martin*, thank you for being so generous with your time and with your ideas. Discussing kinetic modeling with you has been the highlight of my time as a PhD student. If I could, I'd have you supervise all my projects until the day I retire.

NRU has been such a fun and inspiring place to work. I owe a big thank you, to all my bright and considerate colleagues. *Annette*, thank you for all the interesting discussions. No matter where our careers take us next, I hope that we can find a space to discuss PET for many years to come. To the rest of the Pink Ladies - *Clara, Drummond, Søren, & Sara* - I'm so incredibly happy that you invited me into your office! To past and present PhD students - especially *Sophia, Silvia, Maja, Vibeke & Sanjay* - thank you for brightening my days. Thank you to the NRU data analysis group for listening to more presentations on PET occupancy studies than anyone should ever have to endure, and for sharing your own interesting work. Special thanks to *Melanie & Hanne*, for always being so inspirational and encouraging.

Thanks to contacts and collaborators from other universities. To *Mark & My* in Uppsala, for inspiring me to pursue a career in research, and for setting the bar so incredibly high on supervision. And to *Francesca, Betsy & Granville* at Columbia, for interesting discussions and inspiring work.

To the coauthors on my papers, thank you for sharing your ideas and your data. In addition to those already mentioned, they are Adriaan A. Lammertsmaa, Andrea Varrone, Ansel T. Hillmer, Arafat Nasser, Aurelija Jucaite, Jacob Madsen, Kelly P. Cosgrove, Lene L. Donovan, Nakul R. Raval, Simon Cervenka, and the Karolinska Schizophrenia

Project consortium.

Una, thank you for keeping me company over the phone for hours every week, for always encouraging me to be ambitious, and for allowing me to apply my analytical skills to all possible fields outside of neuroimaging. *Simen*, thank you for providing me with a social life in Copenhagen. Your friendship means so much to me! Thank you *Louise*, for helping me get through my bachelor studies, and *Ayman*, for helping me get through my master studies.

Thanks to my brilliant mom *Vibeke* and dad *Harald*, who showed me from an early age that working hard pays off. I wish you were geographically closer, and that we saw each other more often. Thank you for being such great babysitters whenever we do. Thanks to my brothers - *Yrjar*, *Trym* & *Trygg* - for always entertaining and inspiring me with your curiosity, creativity and sarcastic humor. I'm so grateful for my grandma, *Marit*, who will always be my biggest fan and closest ally! If I could, I would also thank my grandpa *Terje* for constantly feeding my curiosity and teaching me how to teach myself. Although he has been gone for a decade, no one has left a bigger imprint on my life.

Thanks to my family in-law, for all of the fun times spent together. I'm especially grateful for *Anna-Karin*, who must surely be the best mother in-law in the world. Thank you for all the help and support.

I owe my biggest thanks to *Hugo* – my best friend, the love of my life, and the world's best dad. Thank you for taking an interest in my work, and for always being up for discussing Matlab functions and mathematical models. Thank you for facilitating my crazy commute by doing all the preschool drop-offs and pick-ups. Sharing my life with you truly makes everything so much easier, and so much more fun.

Tarjei and *Skule*, you're the best distractions, and the best comfort. Thank you!

Gjertrud Louise Laurell,
Lund, January 1st, 2023

Part X

APPENDICES

Sometimes, there is no harm in putting off a piece of
work until another day.

— Antoine de Saint-Exupéry,
The Little Prince

Gjertrud Louise Laurell, Pontus Plavén-Sigra, Aurelija Jucaite, Andrea Varrone, Kelly P. Cosgrove, Claus Svarer, Gitte Moos Knudsen, Karolinska Schizophrenia Project Consortium, R. Todd Ogden, Francesca Zanderigo, Simon Cervenka, Ansel T. Hillmer, Martin Schain. Nondisplaceable binding is a potential confounding factor in ^{11}C -PBR28 translocator PET studies. *The Journal of Nuclear Medicine*. 2021; 62:412-417.
DOI: 10.2967/jnumed.120.243717.
PMID: 32680926

Nondisplaceable Binding Is a Potential Confounding Factor in ^{11}C -PBR28 Translocator Protein PET Studies

Gjertrud L. Laurell¹, Pontus Plavén-Sigra^{1,2}, Aurelija Jucaite^{2,3}, Andrea Varrone², Kelly P. Cosgrove^{4,5}, Claus Svarer¹, Gitte M. Knudsen^{1,6}, Karolinska Schizophrenia Project Consortium⁷, R. Todd Ogden^{8,9}, Francesca Zanderigo^{8,10}, Simon Cervenka², Ansel T. Hillmer^{4,5,11}, and Martin Schain¹

¹Neurobiology Research Unit, Copenhagen University Hospital Rigshospitalet, Copenhagen, Denmark; ²Centre for Psychiatry Research, Department of Clinical Neuroscience, Karolinska Institutet, and Stockholm Health Care Services, Region Stockholm, Stockholm, Sweden; ³PET Science Centre, Precision Medicine and Genomics, R&D, AstraZeneca, Stockholm, Sweden; ⁴PET Center, Department of Radiology and Biomedical Imaging, Yale University, New Haven, Connecticut; ⁵Department of Psychiatry, Yale University, New Haven, Connecticut; ⁶Faculty of Health and Medical Sciences, University of Copenhagen, Copenhagen, Denmark; ⁷Karolinska Schizophrenia Project Consortium, Stockholm, Sweden; ⁸Department of Biostatistics, Columbia University, New York, New York; ⁹Molecular Imaging and Neuropathology Area, New York State Psychiatric Institute, New York, New York; ¹⁰Department of Psychiatry, Columbia University College of Physicians and Surgeons, New York, New York; and ¹¹Department of Radiology and Biomedical Imaging, Yale University School of Medicine, New Haven, Connecticut

The PET ligand ^{11}C -PBR28 (*N*-((2-(methoxy- ^{11}C)-phenyl)methyl)-*N*-(6-phenoxy-3-pyridinyl)acetamide) binds to the 18-kDa translocator protein (TSPO), a biomarker of glia. In clinical studies of TSPO, the ligand total distribution volume, V_T , is frequently the reported outcome measure. Since V_T is the sum of the ligand-specific distribution volume (V_S) and the nondisplaceable-binding distribution volume (V_{ND}), differences in V_{ND} across subjects and groups will have an impact on V_T . **Methods:** Here, we used a recently developed method for simultaneous estimation of V_{ND} (SIME) to disentangle contributions from V_{ND} and V_S . Data from 4 previously published ^{11}C -PBR28 PET studies were included: before and after a lipopolysaccharide challenge (8 subjects), in alcohol use disorder (14 patients, 15 controls), in first-episode psychosis (16 patients, 16 controls), and in Parkinson disease (16 patients, 16 controls). In each dataset, regional V_T estimates were obtained with a standard 2-tissue-compartment model, and brain-wide V_{ND} was estimated with SIME. V_S was then calculated as $V_T - V_{ND}$. V_{ND} and V_S were then compared across groups, within each dataset. **Results:** A lower V_{ND} was found for individuals with alcohol-use disorder (34%, $P = 0.00084$) and Parkinson disease (34%, $P = 0.0032$) than in their corresponding controls. We found no difference in V_{ND} between first-episode psychosis patients and their controls, and the administration of lipopolysaccharide did not change V_{ND} . **Conclusion:** Our findings suggest that in TSPO PET studies, nondisplaceable binding can differ between patient groups and conditions and should therefore be considered.

Key Words: PET; translocator protein; ^{11}C -PBR28; simultaneous estimation; kinetic modeling

J Nucl Med 2021; 62:412–417
DOI: 10.2967/jnumed.120.243717

PET with radioligands for the glial marker 18-kDa translocator protein (TSPO) has been extensively used over the past 2 decades to assess brain immune function in vivo (1). ^{11}C -PBR28 (*N*-((2-(methoxy- ^{11}C)-phenyl)methyl)-*N*-(6-phenoxy-3-pyridinyl)acetamide) is a second-generation TSPO radioligand with signal-to-noise characteristics superior to those of the first-generation radioligand ^{11}C -PK11195 (2). As with other second-generation TSPO tracers, the affinity of ^{11}C -PBR28 to TSPO is affected by a single-nucleotide polymorphism on the TSPO gene (rs6971), and in clinical studies, TSPO genotype is used to classify subjects as low-, mixed-, or high-affinity binders (3,4).

PET ligand binding to TSPO is often quantified by fitting a 2-tissue-compartment model (2TCM), or variants thereof (5), to the PET time-activity curves, using parent radioligand concentration in arterial plasma as the input function. The 2TCM describes the ligand kinetics using 2 tissue compartments, one for ligand that is bound specifically to the target of interest and one for nondisplaceable binding. The nondisplaceable compartment includes both free and nonspecifically bound radioligand. The standard outcome measure reported using 2TCM is the total distribution volume (V_T), which represents the ratio of total activity concentration in tissue to that in plasma at equilibrium. V_T is the sum of the nondisplaceable and specific distribution volumes ($V_T = V_{ND} + V_S$). Some radioligands display negligible specific binding in a certain brain region (i.e., $V_S = 0$). Such a region is usually referred to as a reference region and can be used to estimate V_{ND} , which is assumed to be constant throughout the brain. When a reference region is available, the binding potential with nondisplaceable uptake as a reference, $BP_{ND} (=V_S/V_{ND})$, is typically the reported

Received Feb. 17, 2020; revision accepted Jun. 23, 2020.
For correspondence or reprints contact: Gjertrud L. Laurell, Neurobiology Research Unit, Rigshospitalet, Blegdamsvej 9, DK-2100, Copenhagen, Denmark.
E-mail: gjertrud.laurell@nru.dk
Published online Jul. 17, 2020.
COPYRIGHT © 2021 by the Society of Nuclear Medicine and Molecular Imaging.

outcome measure. TSPO is expressed throughout the brain, and thus, no reference region exists for this target. It is therefore challenging to obtain reliable estimates of the relative contributions from the specific and nondisplaceable binding, leaving a degree of uncertainty about the interpretation of V_T .

Recently, a method for simultaneous estimation of V_{ND} (SIME) (6) was developed to estimate V_{ND} for tracers without a reference region. SIME uses the assumption that nondisplaceable binding is constant throughout the brain and estimates a global value for V_{ND} by fitting a constrained 2TCM for several brain regions simultaneously. The performance of SIME with ^{11}C -PBR28 has been thoroughly tested in healthy human subjects (7). Using simulations, pharmacologic competition data, and test–retest data, SIME-derived estimates of V_{ND} and V_S (calculated using 2TCM V_T and SIME V_{ND}) were shown to be accurate and reliable (7).

For comparison of V_T between groups to be meaningful, there must be an underlying assumption that V_{ND} is the same across the groups. Currently, there is limited scientific evidence to back up this assumption. Hence, our aim with this study was to investigate whether nondisplaceable binding can be a confounding factor in TSPO PET studies that use V_T as an outcome measure. To achieve this aim, SIME was used to quantify V_{ND} in ^{11}C -PBR28 data from 4 different published datasets. In the first dataset, an immune stimulator was administered to healthy subjects (8). The 3 remaining datasets contain controls and subjects with alcohol-use disorder (AUD) (9), first-episode psychosis (FEP) (10), and Parkinson disease (PD) (11).

MATERIALS AND METHODS

This study includes 4 datasets obtained at 2 PET centers. All subjects underwent a ^{11}C -PBR28 PET scan in a high-resolution research tomograph (Siemens). Metabolite-corrected arterial input functions were collected for all scans. T1-weighted MRI scans were acquired to define regions of interest (ROIs). All subjects were genotyped for the rs6971 polymorphism, and low-affinity binders were excluded. In previous publications, V_T has been the primary reported

outcome measure. A list of the datasets, with subject information, is reported in Table 1, and the reader is referred to the original publications for further details on data acquisition and processing.

Lipopolysaccharide

The lipopolysaccharide dataset (8) was collected at the Yale PET Center. Eight healthy men were scanned twice on the same day, at baseline and 3 h after injection of lipopolysaccharide (dose 1.0 ng/kg), an acute immune stimulus. ^{11}C -PBR28 was injected as a 1-min bolus, and the PET scan duration was 120 min.

AUD

The AUD dataset (9) was collected at the Yale PET center. It consists of 14 subjects with AUD and 15 age-matched control subjects. Five of the control subjects also participated in the lipopolysaccharide experiment. AUD subjects were imaged 1–4 d (in 1 case, 24 d) after intake of their last alcoholic beverage. ^{11}C -PBR28 was injected as a 1-min bolus, and the PET scan duration was 120 min.

FEP

The FEP dataset (10) was collected at Karolinska Institutet. It consists of 16 FEP patients and 16 age-matched controls. All patients were naïve to antipsychotic drugs. ^{11}C -PBR28 was injected as a 10-s bolus, and the PET scan duration was approximately 90 min.

PD

The PD dataset (11) was collected at Karolinska Institutet. It consists of 16 patients with PD and 16 age-matched controls. ^{11}C -PBR28 was injected as a 10-s bolus, and the PET scan duration was 72 min.

SIME

The SIME method (6) works by first defining a grid of possible V_{ND} values. Then, for each value in the grid, a 2TCM is fitted to the time–activity curves with the constraint that $K_1 = V_{ND} \cdot k_2$ in all ROIs, reducing the number of rate constants from 4 to 3. The residual sum of squares is then computed for all ROIs and frames, and the V_{ND} that yields the lowest residual sum of squares is selected as the estimate of a brain-wide V_{ND} .

TABLE 1
Dataset Summary

Dataset	Group	Subjects (n)		Age	
		HABs	MABs	HABs	MABs
Sandiego, 2015	Lipopolysaccharide	3	5	28.0 ± 6.0 (22.7–34.5)	23.6 ± 5.1 (19.1–31.1)
Hillmer, 2017	AUD				
	Controls	8	7	37.4 ± 9.0 (26.3–48.4)	32.8 ± 14.6 (19.1–55.6)
	Patients	7	7	40.9 ± 7.9 (31.6–55.2)	37.9 ± 10.4 (26.9–51.0)
Collste, 2017	FEP				
	Controls	9	7	27.8 ± 9.3 (22–50)	25.7 ± 8.2 (20–43)
	Patients	6	10	29.8 ± 8.2 (20–40)	27.7 ± 8.8 (19–47)
Varnäs, 2019	PD				
	Controls	8	8	64.9 ± 4.9 (57.8–71.5)	62.1 ± 5.3 (56.1–72.0)
	Patients	8	8	63.6 ± 4.3 (57.1–69.1)	63.4 ± 6.4 (55.2–73.2)

HAB = high-affinity binder; MAB = mixed-affinity binder.

Age is given as mean ± SD, followed by range in parentheses.

For all datasets, we used a V_{ND} grid from 0.01 to 5, with steps of 0.01, based on previous studies with SIME and ^{11}C -PBR28 (7,12). Initial evaluation of the data indicated that this range covers the cost function minimum. The residual sum of squares was weighted by the square root of the frame duration. Fractional blood volume was fitted for each ROI separately. SIME V_{ND} was calculated using time-activity curves from the cerebellum, parietal cortex, frontal cortex, occipital cortex, temporal cortex, putamen, caudate, and thalamus, thus covering various brain structures and tissue types.

Calculation of Outcome Measures and ROIs

In each ROI, V_T was calculated using a standard 2TCM, including fitting of the fractional blood volume. $V_S (=V_T - V_{ND})$ was calculated from the 2TCM V_T estimates and the SIME V_{ND} estimates. For all datasets except the PD dataset, we report ROI-specific outcome measures (V_T , V_S) in the cerebellum and frontal cortex. For PD, we report V_T and V_S in the striatum instead of the frontal cortex, because the striatum is considered a key region in the pathophysiology of PD and is more frequently reported in PET studies.

Statistical Analysis

Statistical analyses were performed using MATLAB (version 9.5; MathWorks). For the lipopolysaccharide data, a paired-sample t test was used for all outcome measures (V_{ND} , V_T , and V_S) to test for a difference between the pre- and postlipopolysaccharide scans. The percentage change in the outcome measures for each subject was calculated as $100 \cdot (\text{pre} - \text{post})/\text{pre}$. For the remaining datasets, a univariate 2-way ANOVA without an interaction term was applied for each outcome measure (V_{ND} , V_T , and V_S) to determine the group differences between controls and patients, with log-transformed outcome measures as a dependent variable and diagnosis and genotype as fixed factors, as described earlier (12). Using the regression coefficients, β , from the ANOVA, the percentage difference between patients and controls across genotypes was calculated as $100 \cdot (e^{\beta_{\text{patient}}} - e^{\beta_{\text{control}}} - 1)$. The α -level was set to 0.05. Reported P values were not corrected for multiple comparisons.

RESULTS

For all datasets, the results obtained for V_T are in accordance with those in the original publications. Below, we report the results for V_T , V_S , and V_{ND} for each dataset separately. The results for the ROIs presented below are consistent with the remaining ROIs included in the SIME calculation (Supplemental Tables 1–4; supplemental materials are available at <http://jnm.snmjournals.org>). Results were also unchanged when an interaction term was included in the ANOVA (Supplemental Tables 5–7) and when volume-based weights were used in the SIME analysis (Supplemental Tables 8–11).

Lipopolysaccharide

Lipopolysaccharide injection was associated with a significant increase in V_T in both the cerebellum (mean, 40% [SD, 34%]; $P = 0.016$) and the frontal cortex (mean, 46% [SD, 23%]; $P = 0.0012$). V_{ND} was not affected by lipopolysaccharide (mean, 15% [SD, 40%]; $P = 0.38$). The mean increase in V_S was 59% (SD, 51%) ($P = 0.0052$) in the cerebellum and 66% (SD, 35%) ($P = 0.00026$) in the frontal cortex. The results are summarized in Figure 1.

AUD

V_T was significantly lower in AUD subjects than in controls, both in the cerebellum (18%, $P = 0.012$) and in the frontal cortex (23%, $P = 0.0048$). V_{ND} was 34% lower in patients than in controls ($P = 0.00084$). V_S did not differ significantly between the groups. These results are shown in Figure 2. Genotype had a significant effect on both V_T and V_S ($P < 0.0005$) but not on V_{ND} .

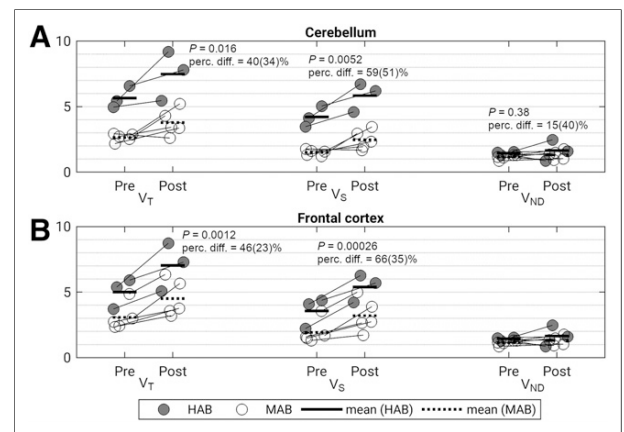


FIGURE 1. Change in outcome measures (V_T , V_S , and V_{ND}) between pre- and postlipopolysaccharide scans in cerebellum (A) and frontal cortex (B). Individual subjects are connected with a line. P values and percentage difference (perc. diff.) between pre- and postlipopolysaccharide scans are shown. HAB = high-affinity binder; MAB = mixed-affinity binder.

FEP

In the FEP dataset, V_T was overall lower in patients than in controls (32%, $P = 0.060$ in the cerebellum; 36%, $P = 0.045$ in the frontal cortex). There was no significant difference in V_{ND} between patients and controls ($P = 0.30$). V_S exhibited a larger percentage separation between patients and controls than that observed for V_T in both the cerebellum (44%, $P = 0.054$) and the frontal cortex (57%, $P = 0.033$). The results are shown in Figure 3. The effect of genotype was statistically significant for V_T in the cerebellum and frontal cortex ($P = 0.011$ and 0.017 , respectively), for V_{ND} in the ■■■ ($P = 0.0043$), and for V_S in the frontal cortex ($P = 0.017$) but not in the cerebellum ($P = 0.099$).

PD

In the PD dataset, we found no statistically significant difference in V_T or V_S between patients and controls, in either the cerebellum ($P = 0.74$ for V_T ; $P = 0.11$ for V_S) or the striatum ($P = 0.32$ for V_T ; $P = 0.42$ for V_S). V_{ND} was, however, lower in patients than in

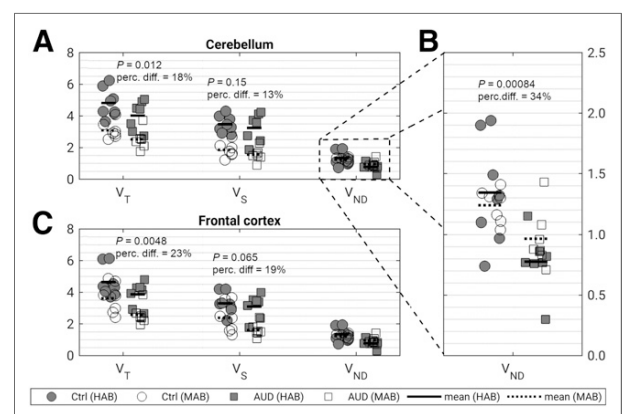


FIGURE 2. (A and C) Difference in outcome measures (V_T , V_S , and V_{ND}) between controls (Ctrl) and subjects with AUD in cerebellum (A) and frontal cortex (C). (B) Zoomed view of results for V_{ND} . P values and percentage difference (perc. diff.) between controls and patients are shown. HAB = high-affinity binder; MAB = mixed-affinity binder.

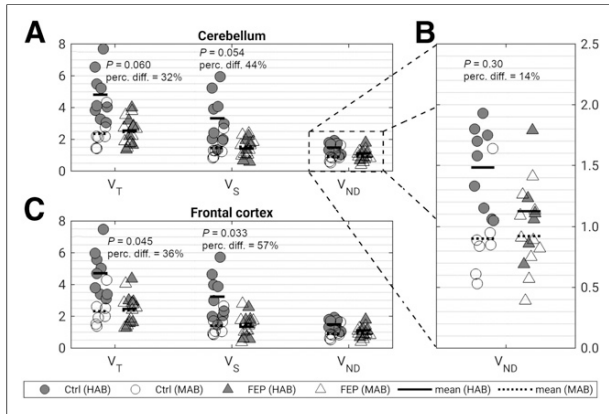


FIGURE 3. (A and C) Difference in outcome measures (V_T , V_S , and V_{ND}) between controls (Ctrl) and FEP patients in cerebellum (A) and frontal cortex (C). (B) Zoomed view of results for V_{ND} . P values and percentage difference (perc. diff.) between controls and patients are shown. HAB = high-affinity binder; MAB = mixed-affinity binder.

controls (34%, $P = 0.0032$). These results are shown in Figure 4. Across all outcome measures and ROIs, there was a significant effect of genotype ($P = 0.012$ for V_{ND} , $P < 10^{-6}$ for V_T and V_S).

DISCUSSION

In this study, we used a new method to estimate V_{ND} in 4 clinical ^{11}C -PBR28 datasets. We found that V_{ND} estimated with this method was lower in AUD and PD than in their matched controls, whereas no difference was found between FEP patients and their controls or in subjects before and after lipopolysaccharide injection. This was, to our knowledge, the first attempt to disentangle the extent by which differences in nondisplaceable binding may contribute to the observed differences in V_T .

Lipopolysaccharide

Although leading to a pronounced increase in V_T , administration of lipopolysaccharide had no apparent effect on SIME V_{ND} . Lipopolysaccharide is a useful model to study an acute immune

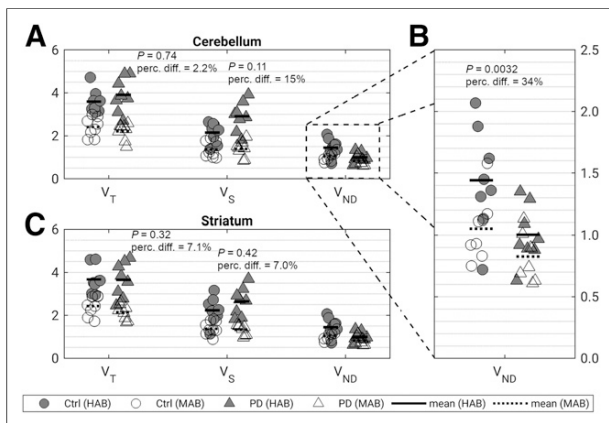


FIGURE 4. (A and C) Difference in outcome measures (V_T , V_S , and V_{ND}) between controls (Ctrl) and PD patients in cerebellum (A) and striatum (C). (B) Zoomed view of results for V_{ND} . P values and percentage difference (perc. diff.) between controls and patients are shown. HAB = high-affinity binder; MAB = mixed-affinity binder.

response, and upregulation of TSPO has been observed in vivo in several species, including mice (13), rats (14), pigs (15), and non-human primates (16). When using V_S as an outcome measure, we observed a larger percentage separation between the pre- and post-lipopolysaccharide scans, with mean differences of 59% and 66% in the cerebellum and frontal cortex, respectively, and with variability similar to that of V_T (coefficient of variation [SD/mean] was 0.85 for V_T and 0.86 for V_S). This higher percentage difference occurred because V_{ND} is not affected by the challenge. In a scenario in which V_{ND} is unaffected by a particular disease, and V_T consists of one third of V_{ND} and two thirds of V_S , a 50% difference in specific TSPO binding translates to only a 33% difference in V_T . In such a scenario, though the effect sizes might likely be the same, it follows that changes in V_S more directly reflect changes in TSPO densities, whereas changes in V_T are attenuated by the contribution from V_{ND} .

AUD

Both V_T and V_{ND} were lower in AUD subjects than in their age-matched controls, with a similar trend in V_S . This finding may explain a previous report in which mixed-affinity binders with AUD had a lower ^{11}C -PBR28 V_T than mixed-affinity binder controls across several brain regions, whereas no difference was seen in high-affinity binders (17), since V_{ND} composes a larger fraction of V_T in mixed-affinity binders than in high-affinity binders. In a separate cohort, Kalk et al. reported a lower ^{11}C -PBR28 hippocampal V_T in alcohol-dependent subjects than in controls, across both genotypes (18). In the present analysis, although some of the differences in V_T between AUD and controls were ascribed to differences in V_{ND} , frontal cortex V_S still showed a sizeable (albeit nonsignificant) percentage difference between AUD subjects and their controls. We can only speculate why V_{ND} would be lower in AUD subjects; pharmacologic competition studies in this population would be needed to conclusively establish levels of specific and nondisplaceable radiotracer uptake. Chronic alcohol exposure induces brain tissue atrophy, reduces cerebral perfusion, and accelerates aging (19,20). Including gray matter volume as a covariate in the statistical analysis did not change the results, indicating that the findings are not driven by partial-volume effects (Supplemental Table 12). Age-related alterations in tissue composition have been proposed as an explanation for differences in V_{ND} observed with the 5-hydroxytryptamine receptor 2A ligand ^{18}F -altanserin (21). Although these questions remain unanswered, the findings here reported illustrate how separation of V_{ND} and V_S could change the interpretation of results from TSPO PET studies.

FEP

Patients with FEP had SIME V_{ND} estimates similar to those of their matched controls. Frontal cortex V_T and V_S values were lower in patients. Using V_S as an outcome measure resulted in a larger percentage difference between the groups. Most previous TSPO PET studies of FEP and schizophrenia have found no significant differences in V_T (22–24), whereas a recent metaanalysis, which pooled PET data from 5 studies on psychosis and schizophrenia using second-generation TSPO radioligands (152 subjects in total), found strong evidence for lower V_T values in patients than in controls (25). If V_S had been used as the outcome measure in previous TSPO PET studies of FEP and schizophrenia, it is possible that the power to detect the population effect of a lower TSPO also in the individual samples of patients would have been higher.

PD

We found that SIME V_{ND} was lower in PD patients than in controls, but we observed no significant differences in V_T , consistent with findings in TSPO PET studies using another second-generation radioligand (26,27). One study, using ^{11}C -PK11195 and a basis-function implementation of the simplified reference tissue model, found a higher BP_{ND} in PD patients than in controls (28). Since BP_{ND} is defined as V_S/V_{ND} , and given our findings, it is possible that the higher BP_{ND} reported in the ^{11}C -PK11195 study was due to lower nondisplaceable binding rather than higher specific binding. This possibility illustrates that V_{ND} is a potential confounding factor not only in studies using V_T as an outcome measure but also in those reporting BP_{ND} . By using ratio-based methods to provide BP_{ND} in TSPO PET studies, one may mistakenly interpret a decrease in V_{ND} as an increase in TSPO binding. Similar to the finding in the AUD dataset, PD might be associated with increased global atrophy (29), and it is possible that altered tissue composition could explain the lower V_{ND} in PD patients. Further studies are required to establish the reason for this observed group difference.

Effect of V_{ND} on Genotype

We observed a pronounced effect of genotype on SIME V_{ND} in both the FEP and the PD datasets but not in the AUD data. The observed effect, if true, complicates interpretation of our current understanding of the TSPO polymorphism, by implicating effects both on the tracer's affinity to TSPO and on nondisplaceable uptake. When all the controls in this study were pooled, a difference in V_{ND} between genotypes was quite evident ($P = 0.00016$). We identify 3 potential interpretations for this observation. One possibility is that SIME-derived estimates of V_{ND} are artifactually contaminated by estimates of V_S , so that high specific binding results in an overestimation of V_{ND} . However, this spillover across compartments has previously been tested and discarded using simulations (7). This finding is also supported by the lipopolysaccharide experiment, in which increased V_S is not reflected in V_{ND} . A second interpretation is that the higher affinity of the radioligand in high-affinity binders leads to a higher nondisplaceable binding because equilibrium conditions are achieved at a later time for a high-affinity versus a low-affinity radioligand. The same mechanisms could potentially lead to higher nondisplaceable tracer binding in high-target-density brain regions than in regions with low target densities. For ^{11}C -raclopride, it has been suggested that regional differences in observed occupancy could in fact be attributable to spatially varying nondisplaceable uptake (30,31). The third possibility is that SIME-derived V_{ND} estimates are affected by other features, which are, in turn, dependent on the genotype. For instance, it has previously been shown that V_{ND} estimated with SIME may be sensitive to the shapes of the arterial input function (32). The fact that input functions may differ between genotypes has been shown for both ^{11}C -PBR28 (7) and the TSPO SPECT radioligand ^{123}I -CLINDE (33), as is to be expected from the different levels of binding to TSPO in peripheral tissue (34). Irrespective of cause, estimates of V_{ND} (and, as a consequence, of BP_{ND}) may not be directly comparable across genotype groups, and their difference could itself be a confounder in clinical studies if the cohort is not balanced across genotypes. The datasets included in this study, however, are well balanced across genotypes; as such, a potential influence of differences in V_{ND} estimates is unlikely. Pharmacologic competition data would be needed to conclusively establish any effect of genotype on V_{ND} .

However, previous ^{11}C -PBR28 blocking studies have included only high-affinity-binder individuals (35) and therefore cannot provide insights into potential differences between genotypes.

Limitations

For any arterial input model, including SIME, V_{ND} estimates are sensitive to the input function shape. Further, similar to reference-tissue modeling, we did not consider spatial variations in V_{ND} . SIME was additionally executed on a larger set of ROIs, which resulted in close-to-identical findings (Supplemental Table 13). Yet, a formal procedure on how to establish a suitable ROI set for estimation of V_{ND} remains to be investigated.

CONCLUSION

Our findings suggest that V_{ND} may be a potential confounding factor in ^{11}C -PBR28 PET studies. This outcome warrants further studies to establish the observed V_{ND} differences and, if possible, reveal their causes. We recommend the use of V_S as an additional outcome parameter in TSPO PET studies since this measure more directly reflects binding to TSPO.

DISCLOSURE

Martin Schain was supported by a NARSAD young investigator grant from the Brain & Behavior Research Foundation. Pontus Plavén-Sigra was supported by the Lundbeck Foundation and the Swedish Society for Medical Research. Ansel Hillmer was supported by NIH grant K01AA024788. Simon Cervenka was supported by Swedish Research Council grant 523-2014-3467. No other potential conflict of interest relevant to this article was reported.

ACKNOWLEDGMENTS

The Karolinska Schizophrenia Project consortium consists of Lars Farde, Lena Flyckt, Göran Engberg, Sophie Erhardt, Helena Fatouros-Bergmann, Simon Cervenka, Lilly Schwieler, Fredrik Piehl, Ingrid Agartz, Karin Collste, Pauliina Victorsson, Anna Malmqvist, Mikael Hedberg, and Funda Orhan.

KEY POINTS

QUESTION: Is nondisplaceable binding a confounding factor in ^{11}C -PBR28 PET studies?

PERTINENT FINDINGS: Nondisplaceable uptake was estimated for 4 ^{11}C -PBR28 PET datasets. In 2 of these (AUD and PD) there was a significant difference in nondisplaceable uptake between patients and controls.

IMPLICATIONS FOR PATIENT CARE: The possibility of obtaining estimates of specific binding to TSPO may improve the interpretability of nuclear imaging studies addressing the role of neuroinflammation in several disorders.

REFERENCES

1. Liu GJ, Middleton RJ, Hatty CR, et al. The 18 kDa translocator protein, microglia and neuroinflammation. *Brain Pathol.* 2014;24:631–653.
2. Fujita M, Kobayashi M, Ikawa M, et al. Comparison of four ^{11}C -labeled PET ligands to quantify translocator protein 18 kDa (TSPO) in human brain: (*R*)-PK11195, PBR28, DPA-713, and ER176-based on recent publications that measured specific-to-non-displaceable ratios. *EJNMMI Res.* 2017;7:84.

3. Owen DR, Howell OW, Tang S-P, et al. Two binding sites for [³H]PBR28 in human brain: implications for TSPO PET imaging of neuroinflammation. *J Cereb Blood Flow Metab.* 2010;30:1608–1618.
4. Owen DR, Yeo AJ, Gunn RN, et al. An 18-kDa translocator protein (TSPO) polymorphism explains differences in binding affinity of the PET radioligand PBR28. *J Cereb Blood Flow Metab.* 2012;32:1–5.
5. Rizzo G, Veronese M, Tonietto M, Zanotti-Fregonara P, Turkheimer FE, Bertoldo A. Kinetic modeling without accounting for the vascular component impairs the quantification of [¹¹C]PBR28 brain PET data. *J Cereb Blood Flow Metab.* 2014;34:1060–1069.
6. Ogden RT, Zanderigo F, Parsey RV. Estimation of in vivo nonspecific binding in positron emission tomography studies without requiring a reference region. *Neuroimage.* 2015;108:234–242.
7. Plavén-Sigra P, Schain M, Zanderigo F, et al. Accuracy and reliability of [¹¹C]PBR28 specific binding estimated without the use of a reference region. *Neuroimage.* 2019;188:102–110.
8. Sandiego CM, Gallezot J-D, Pittman B, et al. Imaging robust microglial activation after lipopolysaccharide administration in humans with PET. *Proc Natl Acad Sci USA.* 2015;112:12468–12473.
9. Hillmer AT, Sandiego CM, Hannestad J, et al. In vivo imaging of translocator protein, a marker of activated microglia, in alcohol dependence. *Mol Psychiatry.* 2017;22:1759–1766.
10. Collste K, Plavén-Sigra P, Fatouros-Bergman H, et al. Lower levels of the glial cell marker TSPO in drug-naïve first-episode psychosis patients as measured using PET and [¹¹C]PBR28. *Mol Psychiatry.* 2017;22:850–856.
11. Varnäs K, Cselényi Z, Jucaite A, et al. PET imaging of [¹¹C]PBR28 in Parkinson's disease patients does not indicate increased binding to TSPO despite reduced dopamine transporter binding. *Eur J Nucl Med Mol Imaging.* 2019;46:367–375.
12. Schain M, Zanderigo F, Ogden RT, Kreisl WC. Non-invasive estimation of [¹¹C]PBR28 binding potential. *Neuroimage.* 2018;169:278–285.
13. Vignal N, Cisternino S, Rizzo-Padoin N, et al. [¹⁸F]FEPPA a TSPO radioligand: optimized radiosynthesis and evaluation as a PET radiotracer for brain inflammation in a peripheral LPS-injected mouse model. *Molecules.* 2018;23:1375.
14. Dickens AM, Vainio S, Marjamäki P, et al. Detection of microglial activation in an acute model of neuroinflammation using PET and radiotracers [¹¹C]-(R)-PK11195 and [¹⁸F]-GE-180. *J Nucl Med.* 2014;55:466–472.
15. de Lange C, Solberg R, Holtedahl JE, et al. Dynamic TSPO-PET for assessing early effects of cerebral hypoxia and resuscitation in new born pigs. *Nucl Med Biol.* 2018;66:49–57.
16. Hillmer AT, Holden D, Fowles K, et al. Microglial depletion and activation: A [¹¹C]PBR28 PET study in nonhuman primates. *EJNMMI Res.* 2017;7:59.
17. Kim SW, Wiers CE, Tyler R, et al. Influence of alcoholism and cholesterol on TSPO binding in brain: PET [¹¹C]PBR28 studies in humans and rodents. *Neuropsychopharmacology.* 2018;43:1832–1839.
18. Kalk NJ, Guo Q, Owen D, et al. Decreased hippocampal translocator protein (18 kDa) expression in alcohol dependence: a [¹¹C]PBR28 PET study. *Transl Psychiatry.* 2017;7:e996.
19. Oscar-Berman M, Valmas MM, Sawyer KS, Ruiz SM, Luhar RB, Gravit ZR. Profiles of impaired, spared, and recovered neuropsychologic processes in alcoholism. *Handb Clin Neurol.* 2014;125:183–210.
20. Luo A, Jung J, Longley M, et al. Epigenetic aging is accelerated in alcohol use disorder and regulated by genetic variation in APOE2. *Neuropsychopharmacology.* 2020;45:327–336.
21. Adams KH, Pinborg LH, Svare C, et al. A database of [¹⁸F]-altanserin binding to 5-HT_{2A} receptors in normal volunteers: normative data and relationship to physiological and demographic variables. *Neuroimage.* 2004;21:1105–1113.
22. Bloomfield PS, Selvaraj S, Veronese M, et al. Microglial activity in people at ultra high risk of psychosis and in schizophrenia: a [¹¹C]PBR28 PET brain imaging study. *Am J Psychiatry.* 2016;173:44–52.
23. Kenk M, Selvanathan T, Rao N, et al. Imaging neuroinflammation in gray and white matter in schizophrenia: an in-vivo PET study with [¹⁸F]-FEPPA. *Schizophr Bull.* 2015;41:85–93.
24. Hafizi S, Tseng H-H, Rao N, et al. Imaging microglial activation in untreated first-episode psychosis: a PET study with [¹⁸F]-FEPPA. *Am J Psychiatry.* 2017;174:118–124.
25. Plavén-Sigra P, Matheson GJ, Collste K, et al. Positron emission tomography studies of the glial cell marker translocator protein in patients with psychosis: a meta-analysis using individual participant data. *Biol Psychiatry.* 2018;84:433–442.
26. Ghadery C, Koshimori Y, Coakeley S, et al. Microglial activation in Parkinson's disease using [¹⁸F]-FEPPA. *J Neuroinflammation.* 2017;14:8.
27. Koshimori Y, Ko J-H, Mizrahi R, et al. Imaging striatal microglial activation in patients with Parkinson's disease. *PLoS One.* 2015;10:e0138721.
28. Ouchi Y, Yoshikawa E, Sekine Y, et al. Microglial activation and dopamine terminal loss in early Parkinson's disease. *Ann Neurol.* 2005;57:168–175.
29. Gao Y, Nie K, Huang B, et al. Changes of brain structure in Parkinson's disease patients with mild cognitive impairment analyzed via VBM technology. *Neurosci Lett.* 2017;658:121–132.
30. Mawlawi O, Martinez D, Slifstein M, et al. Imaging human mesolimbic dopamine transmission with positron emission tomography: I. Accuracy and precision of D₂ receptor parameter measurements in ventral striatum. *J Cereb Blood Flow Metab.* 2001;21:1034–1057.
31. Svensson JE, Schain M, Plavén-Sigra P, et al. Validity and reliability of extrastriatal [¹¹C]raclopride binding quantification in the living human brain. *Neuroimage.* 2019;202:116143.
32. Schain M, Zanderigo F, Mann JJJ, Ogden RTT. Estimation of the binding potential BPND without a reference region or blood samples for brain PET studies. *Neuroimage.* 2017;146:121–131.
33. Feng L, Jensen P, Thomsen G, et al. The variability of translocator protein signal in brain and blood of genotyped healthy humans using in vivo ¹²³I-CLINDE SPECT imaging: a test-retest study. *J Nucl Med.* 2017;58:989–995.
34. Kreisl WC, Fujita M, Fujimura Y, et al. Comparison of [¹¹C]-(R)-PK 11195 and [¹¹C]PBR28, two radioligands for translocator protein (18 kDa) in human and monkey: implications for positron emission tomographic imaging of this inflammation biomarker. *Neuroimage.* 2010;49:2924–2932.
35. Owen DR, Guo Q, Kalk NJ, et al. Determination of [¹¹C]PBR28 binding potential in vivo: a first human TSPO blocking study. *J Cereb Blood Flow Metab.* 2014;34:989–994.

Supplementary material

1. Results of statistical analyses for all ROIs

Results of the statistical tests in all eight regions in the SIME analysis, for V_{ND} , V_T and V_S can be found in the following tables. Table 1 shows the results of the paired-sample t-test for the lipopolysaccharide dataset. ANOVA results are displayed in Table 2 for alcohol use disorder, in Table 3 for first-episode psychosis, and in Table 4 for Parkinson's disease.

Table 1: Results of the paired-sample t-test for the lipopolysaccharide (LPS) dataset

	P(LPS)		
	V_{ND}	V_T	V_S
Caudate	0.38	0.0034	0.0014
Cerebellum		0.016	0.0052
Frontal cortex		0.0012	2.6E-4
Occipital cortex		0.036	0.044
Parietal cortex		0.047	0.055
Putamen		0.0015	6.4E-4
Temporal cortex		0.0067	0.0075
Thalamus		0.022	0.022

Table 2: Results of the ANOVA for the alcohol use disorder dataset. * One subject removed due to fitting failure of the two-tissue compartment model.

	P(diagnosis)			P(genotype)		
	V_{ND}	V_T	V_S	V_{ND}	V_T	V_S
Caudate	8.4E-4	0.089	0.85	0.36	0.0032	1.4E-4
Cerebellum		0.012	0.15		2.3E-6	5.7E-8
Frontal cortex		0.0048	0.065		4.4E-4	8.0E-5
Occipital cortex*		0.011	0.11		4.5E-4	4.9E-5
Parietal cortex		0.022	0.31		2.7E-5	2.6E-6
Putamen		0.085	0.89		1.2E-5	9.3E-7
Temporal cortex		0.023	0.36		1.8E-5	9.9E-7
Thalamus		0.081	0.57		2.0E-5	1.1E-6

Table 3: Results of the ANOVA for the first episode psychosis dataset

	P(diagnosis)			P(genotype)		
	V _{ND}	V _T	V _S	V _{ND}	V _T	V _S
Caudate	0.30	0.047	0.030	0.0043	0.022	0.17
Cerebellum		0.060	0.054		0.011	0.073
Frontal cortex		0.045	0.033		0.017	0.099
Occipital cortex		0.050	0.051		0.0094	0.057
Parietal cortex		0.034	0.023		0.012	0.066
Putamen		0.050	0.033		0.0061	0.023
Temporal cortex		0.060	0.049		0.0071	0.044
Thalamus		0.042	0.029		0.0071	0.018

Table 4: Results of the ANOVA for the Parkinson's disease dataset

	P(diagnosis)			P(genotype)		
	V _{ND}	V _T	V _S	V _{ND}	V _T	V _S
Caudate	0.0032	0.15	0.47	0.012	3.7E-7	2.9E-6
Cerebellum		0.78	0.17		4.3E-8	6.7E-7
Frontal cortex		0.36	0.38		6.9E-9	8.5E-9
Occipital cortex		0.73	0.12		1.1E-8	2.2E-8
Parietal cortex		0.50	0.21		1.2E-8	2.1E-8
Putamen		0.35	0.48		3.1E-7	9.1E-7
Temporal cortex		0.59	0.17		7.0E-9	1.9E-8
Thalamus		0.78	0.25		5.4E-9	1.5E-9

2. ANOVA for V_{ND} with gray matter volume as covariate

Table 5 holds the results for V_{ND} of an ANOVA which includes gray matter volume as a covariate.

Table 5: Results for ANOVA on V_{ND} with gray matter volume as covariate, for the alcohol use disorder, first episode psychosis and Parkinson's disease datasets

Dataset	P(diagnosis)	P(genotype)	P(volume)
Alcohol use disorder	0.0026	0.52	0.53
First episode psychosis	0.30	0.0053	0.38
Parkinson's disease	0.0039	0.038	0.63

3. ANOVA with diagnosis*genotype interaction

In the following tables the results of an ANOVA which includes a diagnosis*genotype interaction term are presented; in Table 6 for alcohol use disorder, in Table 7 for first-episode psychosis, and in Table 8 for Parkinson's disease.

Table 6: Results of ANOVA with an interaction term for the alcohol use disorder dataset

	P(diagnosis)			P(genotype)			P(diagnosis*genotype)		
	V _{ND}	V _T	V _S	V _{ND}	V _T	V _S	V _{ND}	V _T	V _S
Caudate	8.4E-4			0.33			0.18		
Cerebellum		0.014	0.15		3.5E-6	9.3E-8		0.86	0.64
Frontal cortex		0.0048	0.058		4.5E-4	6.8E-5		0.38	0.21
Occipital cortex		0.011	0.097		4.7E-4	4.4E-5		0.42	0.24
Parietal cortex		0.025	0.32		3.9E-5	4.1E-6		0.89	0.99
Putamen		0.093	0.90		1.8E-5	1.5E-6		0.78	0.80
Temporal cortex		0.026	0.37		2.6E-5	1.6E-6		0.89	0.95
Thalamus		0.088	0.59		2.7E-5	1.5E-6		0.47	0.44

Table 7: Results of ANOVA with an interaction term for the first episode psychosis dataset. * one subject excluded du to fitting failure of the two-tissue compartment model.

	P(diagnosis)			P(genotype)			P(diagnosis*genotype)		
	V _{ND}	V _T	V _S	V _{ND}	V _T	V _S	V _{ND}	V _T	V _S
Caudate	0.26	0.018	0.011	0.0043	0.013	0.14	0.20	0.0069	0.0089
Cerebellum		0.024	0.020		0.0061	0.052		0.0073	0.0059
Frontal cortex		0.019	0.014		0.011	0.083		0.011	0.015
Occipital cortex *		0.025	0.023		0.0064	0.046		0.013	0.0089
Parietal cortex		0.016	0.011		0.0081	0.056		0.019	0.026
Putamen		0.023	0.014		0.0037	0.016		0.016	0.015
Temporal cortex		0.025	0.019		0.0038	0.030		0.0085	0.0070
Thalamus		0.020	0.013		0.0046	0.013		0.021	0.019

Table 8: Results of ANOVA with an interaction term for the Parkinson's disease dataset

	P(diagnosis)			P(genotype)			P(diagnosis*genotype)		
	V _{ND}	V _T	V _S	V _{ND}	V _T	V _S	V _{ND}	V _T	V _S
Caudate	0.0036	0.16	0.48	0.013	5.8E-7	4.2E-6	0.57	0.81	0.91
Cerebellum		0.78	0.16		4.5E-8	5.4E-7		0.23	0.14
Frontal cortex		0.37	0.38		1.2E-8	1.4E-8		0.70	0.53
Occipital cortex		0.73	0.13		1.8E-8	3.0E-8		0.63	0.41
Parietal cortex		0.51	0.22		2.2E-8	3.5E-8		0.92	0.74
Putamen		0.35	0.47		3.7E-7	7.3E-7		0.32	0.14
Temporal cortex		0.59	0.17		1.0E-8	2.3E-8		0.46	0.27
Thalamus		0.78	0.25		8.8E-9	2.2E-9		0.54	0.40

4. Results for SIME with ROI weights

The following tables presents the results of the statistical testing when SIME V_{ND} was estimated using size-based ROI weights. The contribution of each ROI was weighted by the ratio of the region volume to the volume of the largest included region. The results for LPS are presented in Table 9, for alcohol use disorder in Table 10, for first-episode psychosis in Table 11, and for Parkinson's Disease in Table 12.

Table 9: Results of a pair-sample t-test on the lipopolysaccharide (LPS) dataset, where SIME V_{ND} was estimated with size-based ROI weights

	P(LPS)	
	V _{ND}	V _S
Caudate	0.41	0.0011
Cerebellum		0.0050
Frontal cortex		2.3E-4
Occipital cortex		0.043
Parietal cortex		0.054
Putamen		7.0E-4
Temporal cortex		0.0076
Thalamus		0.026

Table 10: Results of the ANOVA on the alcohol use disorder dataset, where SIME V_{ND} was estimated using size-based ROI weights.

	P(diagnosis)		P(genotype)	
	V_{ND}	V_S	V_{ND}	V_S
Caudate	0.0010	0.86	0.20	1.4E-4
Cerebellum		0.15		6.3E-8
Frontal cortex		0.068		6.3E-5
Occipital cortex		0.11		3.7E-5
Parietal cortex		0.31		2.0E-6
Putamen		0.93		1.6E-6
Temporal cortex		0.38		1.2E-6
Thalamus		0.60		1.2E-6

Table 11: Results of the ANOVA on the first episode psychosis dataset, where SIME V_{ND} was estimated using size-based ROI weights

	P(diagnosis)		P(genotype)	
	V_{ND}	V_S	V_{ND}	V_S
Caudate	0.33	0.031	0.0045	0.15
Cerebellum		0.050		0.065
Frontal cortex		0.031		0.090
Occipital cortex		0.047		0.050
Parietal cortex		0.022		0.059
Putamen		0.033		0.022
Temporal cortex		0.046		0.039
Thalamus		0.029		0.017

Table 12: Results of the ANOVA on the Parkinson's disease dataset, where SIME V_{ND} was estimated using size-based ROI weights

	P(diagnosis)		P(genotype)	
	V_{ND}	V_S	V_{ND}	V_S
Caudate	0.0014	0.47	0.017	2.9E-6
Cerebellum		0.17		6.7E-7
Frontal cortex		0.38		8.5E-9
Occipital cortex		0.12		2.2E-8
Parietal cortex		0.21		2.1E-8
Putamen		0.48		9.1E-7
Temporal cortex		0.17		1.9E-8
Thalamus		0.25		1.5E-9

5. Results for SIME executed on a larger ROI set

For the two datasets from Karolinska Institutet we additionally calculated V_{ND} using a larger ROI set than the one presented in the manuscript. These ROIs were frontal cortex, temporal cortex, parietal cortex, occipital cortex, limbic lobe, striatum, thalamus, insula, anterior cingulate cortex, posterior cingulate cortex, and cerebellum. The results of the ANOVA for these V_{ND} values are presented in Table 13.

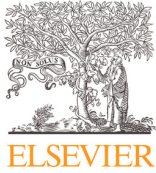
Table 13: Results of the ANOVA for V_{ND} calculated on a larger ROI set

Dataset	P(diagnosis)	P(genotype)
First episode psychosis	0.35	0.0074
Parkinson's disease	0.0023	0.010

Gjertrud Louise Laurell, Pontus Plavén-Sigray, Claus Svarer, R. Todd Ogden, Gitte Moos Knudsen, Martin Schain. Designing drug occupancy studies with PET neuroimaging: Sample size, occupancy ranges and analytical methods. *NeuroImage*. 2022; 263:119620.

DOI: [10.1016/j.neuroimage.2022.119620](https://doi.org/10.1016/j.neuroimage.2022.119620).

PMID: 36087903



Contents lists available at ScienceDirect

NeuroImage

journal homepage: www.elsevier.com/locate/neuroimage

Designing drug occupancy studies with PET neuroimaging: Sample size, occupancy ranges and analytical methods

Gjertrud Louise Laurell^{a,b,*}, Pontus Plavén-Sigra^a, Claus Svarer^a, R. Todd Ogden^{c,d}, Gitte Moos Knudsen^{a,b}, Martin Schain^{a,e}

^a Neurobiology Research Unit, Copenhagen University Hospital Rigshospitalet, 6-8 Inge Lehmanns Vej, Rigshospitalet, Copenhagen DK-2100, Denmark

^b Faculty of Health and Medical Sciences, University of Copenhagen, Copenhagen, Denmark

^c Department of Biostatistics, Columbia University, New York, NY, United States

^d Molecular Imaging and Neuropathology Area, New York State Psychiatric Institute, New York, NY, United States

^e Antaros Medical AB, Mölndal, Sweden

ARTICLE INFO

Keywords:

Receptor occupancy

IC_{50}

PET study design

[¹¹C]Cimbi-36

Kinetic modeling

Lassen plot

ABSTRACT

Molecular neuroimaging is today considered essential for evaluation of novel CNS drugs; it is used to quantify blood-brain barrier permeability, verify interaction with key target and determine the drug dose resulting in 50% occupancy, IC_{50} . In spite of this, there has been limited data available to inform on how to optimize study designs.

Through simulations, we here evaluate how IC_{50} estimation is affected by the (i) range of drug doses administered, (ii) number of subjects included, and (iii) level of noise in the plasma drug concentration measurements. Receptor occupancy is determined from PET distribution volumes using two different methods: the Lassen plot and Likelihood estimation of occupancy (LEO). We also introduce and evaluate a new likelihood-based estimator for direct estimation of IC_{50} from PET distribution volumes.

For estimation of IC_{50} , we find very limited added benefit in scanning individuals who are given drug doses corresponding to less than 40% receptor occupancy. In the range of typical PET sample sizes (5–20 subjects) each extra individual clearly reduces the error of the IC_{50} estimate.

In all simulations, likelihood-based methods gave more precise IC_{50} estimates than the Lassen plot; four times the number of subjects were required for the Lassen plot to reach the same IC_{50} precision as LEO.

1. Introduction

Drug development is an expensive and time-consuming process. It has been estimated that the development of drugs targeting the brain on average costs close to USD 800 million (Wouters et al., 2020). One factor contributing to the high costs is the relatively low probability of success; only 15% of central nervous system (CNS) drug candidates entering clinical trials make it to market (Wong et al., 2019). Recent years have seen an increase in the use of molecular imaging in general, and positron emission tomography (PET) in particular, as a tool for facilitating the drug development process (Son et al., 2019). PET is particularly useful in the early parts of the process, because of its ability to locate and quantify potential CNS drug targets, such as receptors, transporters, and enzymes (Takano et al., 2016). This allows for both a fast identification of drug candidate failure, and can help prioritize candidates for subsequent testing (Gunn and Rabiner, 2017). With PET pharmacoki-

netic competition studies, it is also possible to quantify the relationship between drug dose or, even better, plasma concentration and target occupancy by, e.g., estimating the affinity with which a drug binds to its target. This information can then be used to guide dosing in phase II studies, which is of importance since inappropriate dosing can lead to failure of phase II and III studies (Matthews et al., 2012; Takano et al., 2016). Consequently, the use of PET in CNS drug development has the potential to greatly reduce costs and increase efficiency.

PET pharmacokinetic competition studies are typically used to determine the percentage of target molecules that are engaged by a drug at a certain dose ('the occupancy'). In these studies, each subject is scanned at least twice with a radioligand that binds to the same target as the drug; first at baseline, and then again after administration of the drug. The occupancy (i.e., the percentage of available target molecules bound by the drug during the second scan) is determined by comparing the outcome measures from the two scans. For radioligands for which no

Abbreviations: LEA, Likelihood Estimation of Affinity; LEO, Likelihood Estimation of Occupancy; Δ , Occupancy; Δ_{max} , Maximum attainable target occupancy; C_p , Plasma drug concentration.

* Corresponding author at: Neurobiology Research Unit, 6-8 Inge Lehmanns Vej, Rigshospitalet, DK-2100, Copenhagen, Denmark.

E-mail address: gjertrud.laurell@nru.dk (G.L. Laurell).

<https://doi.org/10.1016/j.neuroimage.2022.119620>

Received 25 May 2022; Received in revised form 18 August 2022; Accepted 6 September 2022

Available online 7 September 2022.

1053-8119/© 2022 The Authors. Published by Elsevier Inc. This is an open access article under the CC BY-NC-ND license

(<http://creativecommons.org/licenses/by-nc-nd/4.0/>)

suitable reference region exists, the total distribution volume (V_T) is often the outcome measure of choice (Innis et al., 2007).

In the presence of a suitable reference region for the radiotracer, the binding potential with respect to the non-displaceable compartment (BP_{ND}) can be reliably determined. In these cases, the receptor occupancy is the percentage reduction of BP_{ND} between the baseline and block scans. For radiotracers without an appropriate reference region, the occupancy must be based on V_T . Because V_T contains both target-specific and non-displaceable binding, the decrease in V_T observed in the blocked scan is most often not proportional to the target occupancy. The standard method to analyze such data is the Lassen plot, which estimates occupancy (Δ) and non-displaceable distribution volume (V_{ND}) using linear regression (Cunningham et al., 2010; Lassen et al., 1995). The association between a subject's occupancy and the corresponding plasma drug level is then typically quantified with the dose-occupancy plot, sometimes referred to as the E_{max} model. In the E_{max} model, the data are fitted to the equation,

$$\Delta = \Delta_{max} \frac{C_P}{C_P + IC_{50}}. \quad (1)$$

where C_P is the plasma concentration of the drug, Δ_{max} denotes the maximum attainable receptor occupancy, and IC_{50} denotes the plasma drug level at which 50% of the Δ_{max} is reached. In this context, IC_{50} is taken as a measure of the drug's affinity to the target receptor.

The currently applied study design to estimate drug occupancies and IC_{50} leaves room for improvement. In both the Lassen plot and in the dose-occupancy plot, there are non-negligible errors in the independent variables. For the Lassen plot, the uncertainty in the independent variable (i.e., V_T) can be as high as 20%, as estimated from test-retest studies (Arakawa et al., 2020; Collste et al., 2016; Zanderigo et al., 2018). In the E_{max} model, the measured plasma drug level is the independent variable, which also comes with measurement errors. When the independent variables in a linear model are noisy, the outcome parameters can be influenced by "regression dilution", that is, a systematic underestimation of the regression slope (Spearman, 1904).

When planning a target engagement study, it is important to take these shortcomings into account to ensure that reasonable conclusions are drawn from the observed results. From a data-analysis perspective, some alternative tools have been proposed to reduce the error induced by the Lassen plot (Naganawa et al., 2019; Schain et al., 2018). However, for estimation of IC_{50} , no alternative to fitting Eq. (1) has, to our knowledge, been presented.

From a data acquisition point of view, the range of administered doses and the number of included subjects should be optimized and balanced with the research budget and the ethical considerations associated with the exposure of humans to radioactivity. In practice, it is not trivial to make these decisions. With regard to administered dose, guidelines from the European Association of Nuclear Medicine Drug Development Committee recommend that doses should 'cover the entire range from low to high occupancy' (Takano et al., 2016). In the context of using PET for dose selection for clinical trials, they suggest that occupancies could range from 20% through 80%. In our experience, estimating occupancies as low as 20% is difficult because at such low occupancies, the noise in the V_T estimates is large in relation to the true difference in V_T between the two PET scans. In addition, at low occupancies, the level of drug in plasma can approach the lower limit of quantification, which may lead to a situation where data from additional scans add little value to the study. It is therefore important to assess how feasible and informative it is to conduct PET scans at low occupancies considering the associated costs and radiation exposure.

Regarding sample size, there is currently no good procedure to determine a suitable sample size a priori. Here, the guidelines from the European Association of Nuclear Medicine Drug Development Committee simply advise that as many data points as possible should be included (Takano et al., 2016). Clearly, parameter estimation improves with increasing N , but it would be useful to identify the sample size where

the improvement is too incremental to motivate additional expense and exposure.

In this study, our objective is to provide data-driven recommendations on how to plan and analyze pharmacological intervention PET studies where V_T is the PET outcome measure. Using simulations, we determine a suitable occupancy range that optimizes the IC_{50} estimate and evaluate the extent by which the estimate improves with increasing sample size. Using simulated V_T values, both the Lassen plot and a maximum-likelihood based estimator are used to calculate corresponding occupancies, which are then combined in dose-occupancy plots to determine IC_{50} for the entire population. We also test the extent by which errors in the measurements of drug level in plasma affect the IC_{50} estimates. Finally, we present a new maximum-likelihood estimator that makes use of V_T values at baseline and block conditions for all subjects as input and estimates the IC_{50} and Δ_{max} in a single step.

2. Methods

2.1. Simulations

We conducted a total of three simulation experiments, each aiming to answer one of the following questions:

1. Is it worthwhile to acquire data at lower occupancies when the goal is to determine the dose-occupancy relationship as precisely as possible?
2. Is there an upper limit of the sample size, above which acquisition of additional data is not justified to establish the dose-occupancy relationship?
3. Are measurement errors in plasma drug levels causing a bias in IC_{50} estimates when fitting Eq. (1)?

Each experiment consisted of running a set of simulations, in which some parameters were varied. In each case, V_T values with realistic noise properties for a set of brain regions at baseline and blocking conditions were simulated. For each choice of parameters, 1000 iterations of the simulation were performed. The true underlying values for IC_{50} and Δ_{max} were kept constant throughout all three experiments, at $2\mu\text{g/L}$ and 85%, respectively. These values are based on the IC_{50} and Δ_{max} of psilocin binding to the serotonin 2A receptor, which have been estimated to be $1.95\mu\text{g/L}$ and 77% in a [^{11}C]Cimbi-36 baseline-block study (Madsen et al., 2019).

In each instance, occupancies were estimated using both Lassen plot and a likelihood-based estimator for occupancy (LEO, see Section 2.3.2 Likelihood estimation of occupancy) and pooled in a dose-occupancy plot to estimate IC_{50} . IC_{50} was also estimated directly from the V_T values using a likelihood-based estimator for IC_{50} (LEA, see Section 2.3.3 Likelihood estimation of affinity). Thus, a total of three methods were used, each resulting in 1000 estimates of IC_{50} for every simulated scenario.

2.1.1. Simulation experiment 1: contribution of data points with low occupancy

In the first simulation experiment we investigated the extent by which occupancy estimates in the lower range improves the IC_{50} estimate. First, we simulated 1000 instances of V_T values at baseline and blocking conditions for 5 subjects, with occupancies evenly distributed between 53.3% and 80%. Subsequently, we added a subject with 6.7% lower occupancy than the lowest occupancy in the last run and re-ran the simulation. This procedure was repeated until, in the last simulation, the dataset consisted of V_T values from 10 subjects, with occupancies evenly distributed between 20% and 80%. This design is illustrated in Fig. 1B.

2.1.2. Simulation experiment 2: number of subjects

In the second experiment we investigated the impact of the number of subjects on the estimate of IC_{50} . First, we simulated 1000 instances

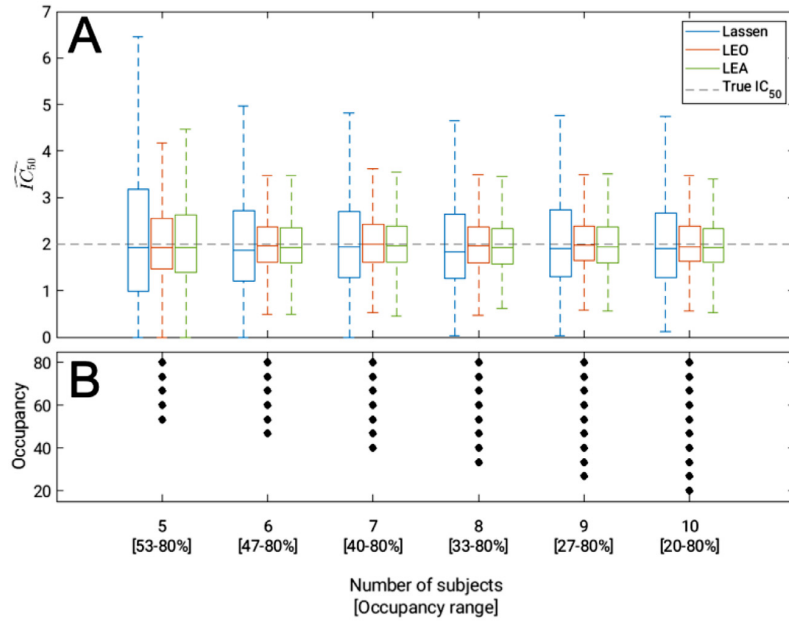


Fig. 1. Simulation experiment 1. (A) Boxplots illustrating the distribution of IC_{50} estimates obtained with the three different methods: Lassen plot and dose-occupancy plot (Lassen, blue), Likelihood estimation of occupancy and dose-occupancy plot (LEO, red) and likelihood estimation of affinity (LEA, green), across increasing numbers of subjects and dose ranges. (B) Illustration of the simulation study design. The black dots indicate the block-scan occupancies for each of the subjects in the simulated study. For each additional subject, the lowest included occupancy is decreased by 6.67%. With 5 subjects the occupancy ranges from 53.3% to 80%, and with 10 subjects the occupancy ranges from 20% to 80%.

of V_T values from five subjects acquired at both baseline and block conditions. The number of subjects was then increased in steps of one up to 25 subjects, and then in steps of five up to 45 subjects. In each case, the occupancies were evenly distributed between 40% and 80%. This occupancy range was chosen based on the results of simulation experiment 1.

2.1.3. Simulation experiment 3: noise in plasma drug level measurements

In the final experiment we investigated how measurement error in the plasma drug level, C_p , affects the IC_{50} estimate. First, 1000 instances of V_T values for 10 subjects at baseline and block was simulated, with occupancies in the range 40–80%, and corresponding C_p values were calculated from Eq. (1) (i.e., no noise in C_p). The procedure was then repeated, with the value for C_p being replaced with a number sampled from a normal distribution with mean equal to the true value for C_p , and standard deviation (SD) equal to the true C_p multiplied by a scale factor. This scale factor (which represents the coefficient of variation [SD/mean] of the data) was initially set to 0.1, and then gradually increased to 1, in steps of 0.1. Thus, a total of 11 sets of V_T values in 10 subjects were generated, with increasing noise levels in C_p across the different datasets.

2.2. Simulation framework

We developed a simulation setup designed to generate V_T values with realistic noise properties for a set of brain regions. The simulated data is based on a published dataset with the serotonin 2A agonist radioligand [^{11}C]Cimbi-36 (da Cunha-Bang et al., 2019). All subjects in the dataset had provided written informed consent, and the study was approved by the Ethics committee for the Capital Region of Denmark (Journal number: H-4-2012-105). All [^{11}C]Cimbi-36 scans are included in the Cimbi database, and are available for academic purposes (Knudsen et al., 2016). A full description of the simulation framework can be found in the supplemental material.

2.3. Calculation of IC_{50}

We evaluated three approaches for estimation of IC_{50} , (i) dose-occupancy plot (Eq. (1)) with occupancy estimates from Lassen plot, (ii) dose-occupancy plots with occupancy estimates from likelihood

estimation of occupancy (LEO, see Section 2.3.2 Likelihood estimation of occupancy), and (iii) likelihood estimation of affinity (LEA, see Section 2.3.3 Likelihood estimation of affinity). For both LEO and LEA, the estimated covariance matrix, $\hat{\Sigma}$, was obtained based on a simulated test-retest dataset with ten subjects, as outlined in the supplemental material (section A.4). In both the dose-occupancy plot and in LEA, IC_{50} was constrained to be positive, and Δ_{max} was constrained to be between 0 and 1. The performance of each method was visually assessed using boxplots of the IC_{50} estimates.

2.3.1. Lassen plot

In absence of an appropriate reference region, the Lassen plot is currently the only established method to estimate occupancies from PET data. It is based on the following assumptions about V_T in the baseline and block scans:

$$\begin{cases} \mathbf{V}_T^{\text{base}} = V_{ND} + \mathbf{V}_S \\ \mathbf{V}_T^{\text{block}} = V_{ND} + (1 - \Delta)\mathbf{V}_S \end{cases} \quad (2)$$

The Lassen plot is achieved by re-arranging those equations, resulting in:

$$\mathbf{V}_T^{\text{base}} - \mathbf{V}_T^{\text{block}} = \Delta(\mathbf{V}_T^{\text{base}} - V_{ND}\mathbf{1}), \quad (3)$$

where $\mathbf{V}_T^{\text{base}}$ and $\mathbf{V}_T^{\text{block}}$ are $K \times 1$ arrays of regional V_T values in K brain regions. Plotting $\mathbf{V}_T^{\text{base}} - \mathbf{V}_T^{\text{block}}$ versus $\mathbf{V}_T^{\text{base}}$ typically results in a linear relationship, where the slope and x-intercept corresponds to estimates of Δ and V_{ND} , respectively (Cunningham et al., 2010; Lassen et al., 1995). As mentioned previously, error in the independent variable ($\mathbf{V}_T^{\text{base}}$) means that estimates of Δ and V_{ND} derived with Lassen plot may be biased. IC_{50} was obtained via nonlinear fitting of the parameters in Eq. (1), with the occupancy estimates derived from the Lassen plot.

2.3.2. Likelihood estimation of occupancy

Like the Lassen plot, LEO (Schain et al., 2018) provides estimates of Δ and V_{ND} given regional V_T values at baseline and block conditions. It is based on the same basic assumptions, but rather than relying on linear regression, LEO uses a maximum likelihood procedure, which in theory provides asymptotically unbiased estimates. An important feature of LEO is that it accounts for measurement errors in regional V_T values by including the covariance matrix Σ in the objective function. To obtain an estimate of Σ , we propose using a test-retest dataset.

The LEO log-likelihood function is

$$\begin{aligned} \ell(V_{ND}, V_S, \Delta | \mathbf{V}_T^{base}, \mathbf{V}_T^{block}) = & -(\mathbf{V}_T^{base} - V_{ND} \mathbf{1} - \mathbf{V}_S)^T \\ & \sum^{-1} (\mathbf{V}_T^{base} - V_{ND} \mathbf{1} - \mathbf{V}_S) - (\mathbf{V}_T^{block} - V_{ND} \mathbf{1} - (1 - \Delta) \mathbf{V}_S)^T \\ & \sum^{-1} (\mathbf{V}_T^{block} - V_{ND} \mathbf{1} - (1 - \Delta) \mathbf{V}_S), \end{aligned} \quad (4)$$

where constant terms have been excluded because they will not affect the optimization. The dimensionality in (4) is reduced by solving $\frac{\partial}{\partial V_S} \ell = 0$, which leads to the following expression for V_S :

$$V_S = \frac{\mathbf{V}_T^{base} + (1 + \Delta)(\mathbf{V}_T^{block} - V_{ND} \mathbf{1})}{1 + (1 + \Delta)^2}. \quad (5)$$

As a result, the number of parameters in the LEO log-likelihood is reduced from $K + 2$ to two (V_{ND} and Δ). IC_{50} was obtained via nonlinear fitting of the parameters in Eq. (1), with the occupancy estimates derived from LEO.

LEO Matlab code, and instructions on how to use it, are available at <https://github.com/martinschain/LEO>.

2.3.3. Likelihood estimation of affinity

LEA is an extension of LEO, where IC_{50} and Δ_{max} are calculated in a single step from the regional V_T values. If we combine the assumptions of the Lassen plot/LEO (Eq. (2)) and the dose-occupancy response curve (Eq. (1)), we get the following expressions for V_T in the baseline and block scans

$$\begin{cases} \mathbf{V}_T^{base} = V_{ND} \mathbf{1} + \mathbf{V}_S + \epsilon^{base} \\ \mathbf{V}_T^{block} = V_{ND} \mathbf{1} + \left(1 - \Delta_{max} \frac{C_p}{C_p + IC_{50}}\right) \mathbf{V}_S + \epsilon^{block}, \end{cases} \quad (6)$$

where ϵ^{base} and ϵ^{block} are arrays of errors for each region in the baseline and block scans respectively. If we assume that the error in V_T is normally distributed, and that the variance is constant within each region between scans, the measured V_T 's can be expressed as

$$\begin{cases} \mathbf{V}_T^{base} \sim N(V_{ND} \mathbf{1} + \mathbf{V}_S, \Sigma) \\ \mathbf{V}_T^{block} \sim N\left(V_{ND} \mathbf{1} + \left(1 - \Delta_{max} \frac{C_p}{C_p + IC_{50}}\right) \mathbf{V}_S, \Sigma\right), \end{cases} \quad (7)$$

where Σ is the covariance matrix of the data. Based on this, we derive a log-likelihood function where V_{ND} , IC_{50} and Δ_{max} are estimated from all subjects' V_T values. For a dataset of N subjects, where each subject has undergone one baseline and one block scan, the log-likelihood function becomes.

$$\begin{aligned} \ell(IC_{50}, \Delta_{max}, V_{ND,1}, V_{ND,2}, \dots, V_{ND,N} \\ | \mathbf{V}_{T,1}^{base}, \mathbf{V}_{T,2}^{base}, \dots, \mathbf{V}_{T,N}^{base}, \mathbf{V}_{T,1}^{block}, \mathbf{V}_{T,2}^{block}, \dots, \mathbf{V}_{T,N}^{block}, \\ C_{P,1}, C_{P,2}, \dots, C_{P,N}) \\ = \sum_{n=1}^N \left[-(\mathbf{V}_{T,n}^{base} - V_{ND,n} \mathbf{1} - \mathbf{V}_{S,n})^T \sum^{-1} (\mathbf{V}_{T,n}^{base} - V_{ND,n} \mathbf{1} - \mathbf{V}_{S,n}) \right. \\ \left. - \left(\mathbf{V}_{T,n}^{block} - V_{ND,n} \mathbf{1} - \left(1 - \Delta_{max} \frac{C_{P,n}}{C_{P,n} + IC_{50}}\right) \mathbf{V}_{S,n} \right)^T \right. \\ \left. \sum^{-1} \left(\mathbf{V}_{T,n}^{block} - V_{ND,n} \mathbf{1} - \left(1 - \Delta_{max} \frac{C_{P,n}}{C_{P,n} + IC_{50}}\right) \mathbf{V}_{S,n} \right) \right] \end{aligned} \quad (8)$$

Constant terms have been excluded from (8), because they do not affect the optimization. Similar to LEO, solving $\frac{\partial}{\partial V_S} \ell = 0$ provides a closed form expression for V_S , which can be substituted to reduce the dimensionality when fitting (8).

$$V_{S,n} = \frac{\mathbf{V}_{T,n}^{base} - V_{ND,n} \mathbf{1} + \left(1 - \Delta_{max} \frac{C_{P,n}}{C_{P,n} + IC_{50}}\right) (\mathbf{V}_{T,n}^{block} - V_{ND,n} \mathbf{1})}{1 + \left(1 - \Delta_{max} \frac{C_{P,n}}{C_{P,n} + IC_{50}}\right)^2}. \quad (9)$$

LEA treats IC_{50} and Δ_{max} as global parameters shared by all subjects, whereas V_{ND} may differ across subjects. Thus, LEA provides N estimates of V_{ND} and single estimates of IC_{50} and Δ_{max} ($N + 2$ parameters in total).

LEA Matlab code, and instructions on how to use it, are available at <https://github.com/Gjertrud/LEA>.

3. Results

3.1. Simulation experiment 1: contribution of data points with low occupancy

The distribution of IC_{50} estimates for each method is presented in Fig. 1. For all three methods (Lassen plot, LEO, and LEA), inclusion of subjects with low occupancy typically had little impact on the result; for example, including 7 subjects with occupancy ranging from 40 to 80% resulted in roughly similar distribution of IC_{50} estimates as including 10 subjects with occupancy ranging from 20 to 80%.

Using the Lassen plot to estimate occupancy consistently resulted in markedly higher errors than the likelihood-based methods, while minimal difference between LEO and LEA was observed.

3.2. Simulation experiment 2: number of subjects

The distribution of IC_{50} estimates for increasingly larger datasets is presented in Fig. 2. In general, increasing the sample size resulted in more narrow distributions around the true IC_{50} value for all three methods. The sample size has no obvious effect on bias. Each consecutive increment had less effect on the distribution than the previous one, and each added subject beyond approximately 20–30 resulted in only marginal improvements.

As in experiment 1, the Lassen plot resulted in substantially larger errors compared to the likelihood-based methods. For example, the Lassen plot requires 40–45 subjects to achieve a IC_{50} distribution that is equally narrow around the true IC_{50} as the one observed for the likelihood-based methods at 10 subjects.

3.3. Simulation experiment 3: noise in plasma drug level measurements

The distribution of IC_{50} for increasing levels of noise in the plasma drug measurements is shown in Fig. 3A. As expected, the IC_{50} error increases with increasing plasma error for all three methods. For low or no noise in measurement of drug plasma concentration, LEO and LEA showed comparable IC_{50} distributions. These were narrower than those seen with the Lassen plot. When the plasma error scale factor (SD/mean) exceeds approximately 0.5 the IC_{50} distributions become much wider for all three methods, although less so for LEA than for Lassen and LEO. At these high noise levels there is also a clear bias, with a tendency to overestimate IC_{50} . Again, this is more pronounced for Lassen and LEO than for LEA. The effect of noise on the estimated dose-occupancy curve is illustrated in Fig. 3C, which shows the mean and SD of the curve fits for each of the methods at the max noise level. At this noise level the LEO curve is completely overlapping with the Lassen curve, while for no plasma noise (Fig. 3B) the LEO mean and SD curves are almost identical to the LEA ones.

4. Discussion

In this study, we provide data to inform the design and analysis of a PET occupancy study. Using simulated data, we evaluated how different experimental setups and analytical methods affected the error in IC_{50} estimation. Throughout all simulations the likelihood-based estimators considerably outperformed the traditional Lassen plot.

In drug development, the relationship between plasma drug concentration and occupancy established by the IC_{50} and Δ_{max} is often used to further inform about doses relevant for clinical trials. To illustrate how

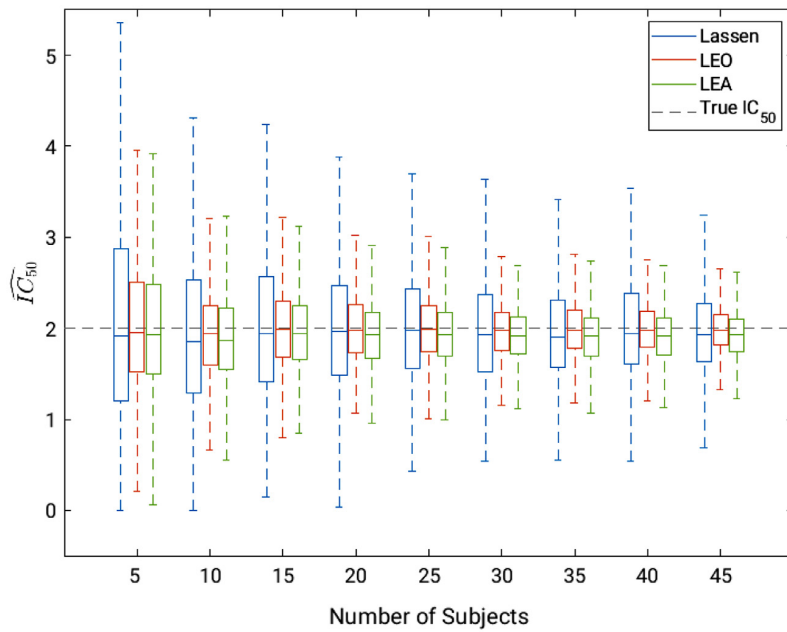


Fig. 2. Simulation experiment 2. Boxplots illustrating the distribution of the IC_{50} estimates obtained with the three different methods: Lassen plot and dose-occupancy plot (Lassen, blue). Likelihood estimation of occupancy and dose-occupancy plot (LEO, red) and likelihood estimation of affinity (LEA, green), across increasing numbers of subjects. For all different numbers of subjects, the occupancies within each dataset ranges from 40% to 80%.

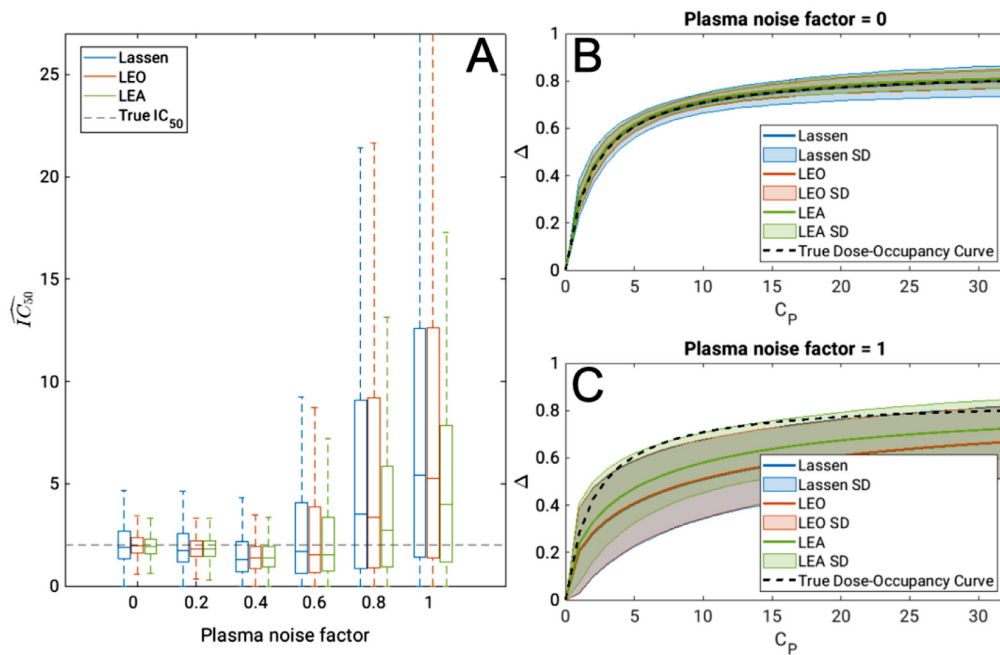


Fig. 3. Simulation experiment 3. (A) Boxplots illustrating the distribution of IC_{50} estimates obtained with three different methods: Lassen plot and dose-occupancy plot (Lassen, blue). Likelihood estimation of occupancy and dose-occupancy plot (LEO, red) and likelihood estimation of affinity (LEA, green), across increasing noise in the plasma drug concentration (C_p) measurements. (B & C) The mean and standard deviation (SD) of the dose-occupancy plot estimates for (B) no noise in C_p , and (C) maximum simulated noise in C_p .

the differences in IC_{50} estimation presented here translate to a clinical setting, we present an example of a drug development experiment:

Assume that we have a drug with a therapeutic window between 70 and 80% occupancy. We want to administer a dose resulting in 75% occupancy to hit this desired range. We therefore need to conduct a PET occupancy study to estimate IC_{50} and Δ_{max} to describe the relationship between the plasma drug concentration and target occupancy. The data from simulation experiment 2 can help inform how many subjects we want to include in that occupancy study. For each analytical method

and iteration in the simulation experiment, we have calculated IC_{50} and Δ_{max} . With those parameter estimates, we can calculate the plasma drug concentration that corresponds to 75% occupancy. Using the true underlying parameter values, and assuming that the correlation between administered dose and plasma drug concentration is established without error, we can investigate whether the calculated plasma concentration results in an occupancy within the therapeutic window. The results from this are illustrated in Fig. 4. When using LEO to estimate IC_{50} and Δ_{max} , 10 subjects are sufficient to correctly predict a suitable dose in

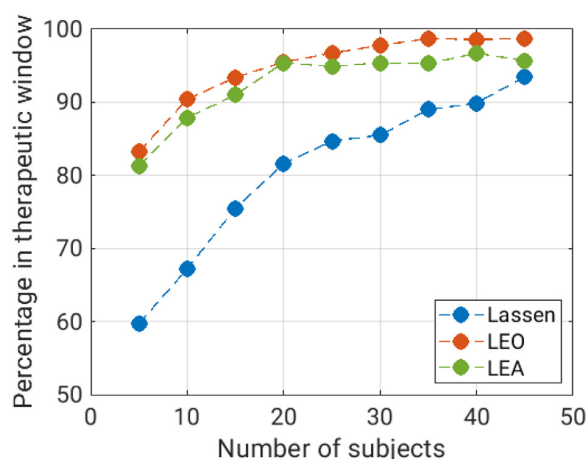


Fig. 4. Illustration of the example introduced in the discussion. For each iteration in simulation experiment 2, we calculate the plasma drug concentration corresponding to 75% occupancy from the estimated parameter values. The figure shows how large percentage of those plasma drug concentrations result in occupancies within the therapeutic window of 70–80% for different numbers of subjects in the study and for different analytical methods; Lassen (blue), LEO (red), and LEA (green).

90.4% of the cases. By comparison, when the Lassen plot is used for quantifying outcomes, a sample size of 40 subjects is necessary to establish a dose-occupancy relationships that results in a dose in the desired range for 89.9% of the cases. The same experiment was repeated for two other therapeutic windows, 20–30% and 45–55%, both resulting in approximately the same relative performance of the three methods (Supplementary Fig. 1).

4.1. Simulation experiment 1: contribution of data points with low occupancy

In the first experiment, we explored the degree to which the inclusion of additional subjects with very low occupancy improves the IC_{50} estimate. Six simulations were performed. The first had five subjects, and block scan occupancies in the range 53.3% to 80%. In each consecutive simulation, a lower-occupancy data point was added.

As expected, additional datapoints lead to more precise IC_{50} estimates. For each additional subject, the improvement became smaller. Especially the last three datapoints ($\Delta < 40\%$) had very little effect on the IC_{50} error. This trend was apparent with all three analytical methods. Consequently, the recommendations from the European Association of Nuclear Medicine Drug Development Committee that ‘low’ occupancies should be included in these types of studies may not be justified. Rather than including datapoints at occupancies below 40%, if feasible with regards to potential drug effects, it is more valuable to aim at attaining occupancies larger than 40% for all subjects. In cases in which it is unclear whether the data conforms to a single-site binding model (i.e., the E_{max} -model), the inclusion of lower-occupancy datapoints could be justified to confirm the shape of the dose-occupancy curve. However, in our experience, going below approximately 20% is associated with very unreliable occupancy estimates, as well as increased difficulty with accurately measuring the plasma drug concentration, limiting any conclusions that can be drawn from such data.

4.2. Simulation experiment 2: number of subjects

In the second experiment, we examine the degree to which the IC_{50} estimate improves with increasing sample size. We performed simulations with datasets ranging from 5 to 45 subjects, while keeping the range of occupancies constant (40–80%). Within the range of typical

sample sizes for PET pharmacokinetic competition studies, there is a linear relationship between the addition of subjects and the reduction in error. The decrease in error flattens out after approximately 20 subjects for the likelihood-based methods, and 30 subjects for the Lassen plot. Above this, the inclusion of additional subjects will likely rarely be justified when weighing the expected reduction in error against cost and radiation exposure. We do, however, recognize that the inclusion of 20–30 subjects is far beyond the regular sample sizes seen with this type of PET study. If the goal is to determine parameter values with the smallest possible error, the recommendation to include ‘as many points as possible’ (Takano et al., 2016) could still hold true. Yet, in our opinion, including approximately 10 subjects should usually be sufficient, especially if the resulting data is analyzed with a likelihood-based method.

4.3. Simulation experiment 3: noise in plasma drug level measurements

In the third simulation experiment, we saw that the increase in IC_{50} error with increased error in the drug plasma level, C_p , was more moderate for LEA than for LEO and the Lassen plot. It is difficult to determine the magnitude and nature of measurement error in C_p noise in a practical setting, but for a typical PET pharmacokinetic competition study it is likely that the magnitude is in the lower half of the range evaluated in this study. The error in C_p is influenced by a number of parameters, including the kinetics of the drug, the sampling site (Huang and Isoheranen, 2020), sampling materials (Krischke et al., 2014), and analytical methods (Pea et al., 2019). Guidelines from the US Food and Drug Administration (Food and Drug Administration, 2018) and The European Medicines Agency (European Medicines Agency, 2011) suggest that the accuracy and precision of a bioanalytical method should fall within a 15% threshold. However, in a recent study in which drug spiked plasma samples were analyzed by 27 different European laboratories, only 54% of the 112 samples were within the 15% margins (Pea et al., 2019). The ratio of the standard deviation to the mean in that study corresponded to a plasma noise scale factor of approximately 0.2. However, they also found a considerable bias, where 38% of the samples were overestimated, and only 8% were underestimated (Pea et al., 2019). Because we have simulated plasma drug concentrations with no bias, the standard deviations reported in that study are not necessarily directly comparable to our simulation experiment.

With increased noise in C_p , we saw not only wider distributions of estimated IC_{50} values, but also a clear tendency to overestimate the IC_{50} , especially for the two methods that use the traditional dose-occupancy plot. Fig. 3B and 3C, which display the mean estimated dose-occupancy relationship for each method at no noise and maximum noise respectively, clearly illustrate how the curves are underestimated at high errors in C_p .

4.4. Choice of analytical methods

In all three experiments, we found that the likelihood-based approaches lead to markedly lower errors in the IC_{50} estimate, as compared to the Lassen plot. Simulation experiment 2 revealed that when using the Lassen plot to calculate occupancy, approximately four times as many subjects must be scanned to obtain errors comparable to the likelihood-based methods.

It should be noted that the demonstrated performance of LEO and LEA relies on the presence of a test-retest dataset of ten subjects. In our experience, such datasets should be available for many, if not most, PET radioligands. If no test-retest dataset for the radioligand is available, it would probably still be less taxing on resources to first perform a test-retest study, and then apply likelihood-based methods. Based on the results in this study, one would still expect a better IC_{50} estimate from scanning both ten test-retest subjects and ten baseline-block subjects, and subsequently analyzing the data with a likelihood-based method,

compared to scanning 20 baseline-block subjects, and calculating occupancies with the Lassen plot. The former strategy will not only lead to better occupancy parameter estimates but would also provide information on the test-retest variability of the radioligand. It should also be noted that, because the estimation of the covariance matrix improves with the size of the test-retest dataset, the likelihood-based methods would perform even better than demonstrated here if more than ten test-retest subjects were available (Schain et al., 2018). Strategies to approximate the covariance structure of the data in the absence of a test-retest dataset also exist (Naganawa et al., 2019).

Throughout most of the simulations the two likelihood-based methods LEO and LEA performed comparably. However, when very high noise in the plasma drug level measurements was simulated, LEA resulted in better IC_{50} estimates than LEO. In fact, at these noise levels, the performance of LEO is comparable to that of the Lassen plot. Although it is clear that LEO provides improved occupancy estimates compared to the Lassen plot (Schain et al., 2018), it seems that if the plasma drug concentration is poorly estimated, the improved occupancy estimate does not lead to an improved estimation of the Emax model curve.

4.5. Limitations

Although LEA handles noise in the measurement of plasma drug concentration better than the other approaches, the LEA log-likelihood function does not explicitly account for the measurement error in C_p , as it does for V_T . This was not included in the model, in part because it would nearly double the number of model parameters in the LEA likelihood function. Also, the magnitude and nature of the measurement errors are not as easily accessible for C_p as it is for V_T .

Both LEO and LEA build on the same assumptions as the Lassen plot and the dose-occupancy response curve; namely that occupancy and V_{ND} are constant in all included brain regions. This assumption has faced some criticism (Svensson et al., 2019). Also, all three methods assume that IC_{50} and max occupancy are constant, not only across the brain, but also between subjects which are conditions that are not necessarily met. Voxel-wise application of the Lassen plot and E_{max} model to [^{11}C]flumazenil scans of healthy humans, has suggested that there may be regional variation in vivo CVL-865 affinity for the GABA_A receptor (de Laat et al., 2022). Assumptions could be violated for, e.g., radiotracers sensitive to endogenous ligands or for comparisons between groups that have genetic differences in the protein structure which are associated with differences in the radioligand affinity to its target. These violations would also, however, apply to occupancy measures based on the Lassen plot or on BP_{ND} .

We have evaluated study designs and analytical methods in a simulation framework based on the serotonin 2A receptor PET tracer [^{11}C]Cimbi-36. The error in the occupancy, and therefore also IC_{50} , estimates will depend on the characteristics of the PET radioligand, such as the test-retest variability and the signal-to-background ratio. For instance, we expect that a lower signal-to-background ratio would result in less well-determined estimates of occupancy. Our work focuses on V_T -based estimates of occupancy and since the complexity in the determination of a correct input function is prone to noise, one can expect V_T 's to yield less reliable occupancy estimates, through worse test-retest reliability (Naganawa et al., 2019). We based our simulations on the agonist radiotracer [^{11}C]Cimbi-36 because it previously has turned out to generate excellent occupancy data (Madsen et al., 2019). It is unknown if agonist radioligands, everything else being equal, generate different occupancy measures than antagonist radioligands, but we find it unlikely that simulations based on an antagonist radiotracer would have changed the outcome of our study. That is, our findings do most likely generalize to other radiotracers.

This work addresses estimation of drug interaction parameters based on PET V_T 's. Because of its simplicity, many PET studies use regional BP_{ND} estimates to calculate these parameters. Although this is a more straight-forward approach, it is not valid for radiotracers without a suit-

able reference region. Further research is required to assess whether the results regarding study design (occupancy ranges and sample sizes) would hold true also for simulated BP_{ND} values.

5. Conclusion

Our results suggest that when designing a PET occupancy study to quantify a drug's interaction with its target from distribution volumes, it is not justified to administer drug doses corresponding to what can be expected to give less than 40% occupancy. We also demonstrate that within the range of typical PET sample sizes each additional subject clearly contributes to reduced IC_{50} error. Excessive noise in determination of the drug plasma levels leads to an underestimation of the dose-occupancy curve. Finally, we show in all our experiments that the maximum likelihood-based methods are superior to the Lassen plot; where the likelihood-based methods require five subjects only, the Lassen plot will require 20 subjects to achieve the same IC_{50} accuracy.

Data and code availability statement

The simulations presented in our manuscript are based on a published dataset with the serotonin 2A radioligand [^{11}C]Cimbi-36 (da Cunha-Bang et al., 2019). All [^{11}C]Cimbi-36 scans are included in the Cimbi database, and are available for academic purposes (Knudsen et al., 2016).

Matlab code for *Likelihood Estimation of Occupancy* (LEO) is available at <https://github.com/martinschain/LEO>. Matlab code for *Likelihood Estimation of Affinity* (LEA) is available at <https://github.com/Gjertrud/LEA>.

Funding

GLL was supported by Rigshospitalet's Research Council (R197-A8956) and The Lundbeck Foundation (R317-2019-787 & R290-2018-756). PPS was supported by the Lundbeck Foundation (R303-2018-3263). The funding sources have had no involvement in the design, conduct, or dissemination of the research presented in this article.

Declarations of Competing Interest

GMK has received honoraria as a speaker for Sage Biogen and H. Lundbeck, and as a consultant for Sanos. MS has received compensation from Roche as a key opinion leader, and is an employee and owns stock options in Antares Medical.

Credit authorship contribution statement

Gjertrud Louise Laurell: Conceptualization, Methodology, Software, Investigation, Visualization, Writing – original draft. **Pontus Plavén-Sigra:** Conceptualization, Data curation, Writing – review & editing. **Claus Svarer:** Conceptualization, Resources, Writing – review & editing. **R. Todd Ogden:** Conceptualization, Methodology, Supervision, Writing – review & editing. **Gitte Moos Knudsen:** Funding acquisition, Conceptualization, Supervision, Writing – review & editing. **Martin Schain:** Funding acquisition, Conceptualization, Methodology, Resources, Supervision, Writing – original draft.

Supplementary materials

Supplementary material associated with this article can be found, in the online version, at doi:[10.1016/j.neuroimage.2022.119620](https://doi.org/10.1016/j.neuroimage.2022.119620).

References

- Arakawa, R., Takano, A., Stenkrona, P., Stepanov, V., Nag, S., Jahan, M., Grybäck, P., Bolin, M., Chen, L., Zhang, L., He, P., Villalobos, A., McCarthy, T.J., Hallidin, C., Varrone, A., 2020. PET imaging of beta-secretase 1 in the human brain: radiation dosimetry, quantification, and test-retest examination of [^{18}F]PF-06684511. *Eur. J. Nucl. Med. Mol. Imaging* 47, 2429–2439. doi:[10.1007/s00259-020-04739-5](https://doi.org/10.1007/s00259-020-04739-5).

- Collste, K., Forsberg, A., Varrone, A., Amini, N., Aeineband, S., Yakushev, I., Halldin, C., Farde, L., Cervenka, S., 2016. Test-retest reproducibility of [¹¹C]PBR28 binding to TSPO in healthy control subjects. *Eur. J. Nucl. Med. Mol. Imaging* 43, 173–183. doi:10.1007/s00259-015-3149-8.
- Cunningham, V.J., Rabiner, E.A., Slifstein, M., Laruelle, M., Gunn, R.N., 2010. Measuring drug occupancy in the absence of a reference region: the Lassen plot re-visited. *J. Cereb. Blood Flow Metab.* 30, 46–50. doi:10.1038/jcbfm.2009.190.
- da Cunha-Bang, S., Ettrup, A., Mc Mahon, B., Skibsted, A.P., Schain, M., Lehel, S., Dyssegaard, A., Jørgensen, L.M., Møller, K., Gillings, N., Svarer, C., Knudsen, G.M., 2019. Measuring endogenous changes in serotonergic neurotransmission with [¹¹C]Cimbi-36 positron emission tomography in humans. *Transl. Psychiatry* 9, 134. doi:10.1038/s41398-019-0468-8.
- de Laat, B., Hoyer, J., Liu, H., Morris, E.D., 2022. EC50 images, a novel endpoint from PET target occupancy studies, reveal spatial variation in apparent drug affinity. *Eur. J. Nucl. Med. Mol. Imaging* 49, 1232–1241.
- European Medicines Agency, 2011. Guideline on bioanalytical method validation.
- Food and Drug Administration, 2018. Bioanalytical Method Validation Guidance for Industry.
- Gunn, R.N., Rabiner, E.A., 2017. Imaging in central nervous system drug discovery. *Semin. Nucl. Med.* 47, 89–98. doi:10.1053/j.semnuclmed.2016.09.001.
- Huang, W., Isoherranen, N., 2020. Sampling site has a critical impact on physiologically based pharmacokinetic modeling. *J. Pharmacol. Exp. Ther.* 372, 30–45. doi:10.1124/jpet.119.262154.
- Innis, R.B., Cunningham, V.J., Delforge, J., Fujita, M., Gjedde, A., Gunn, R.N., Holden, J., Houle, S., Huang, S.-C., Ichise, M., Iida, H., Ito, H., Kimura, Y., Koeppe, R.A., Knudsen, G.M., Knuuti, J., Lammertsma, A.A., Laruelle, M., Logan, J., Maguire, R.P., Mintun, M.A., Morris, E.D., Parsey, R., Price, J.C., Slifstein, M., Sossi, V., Suhara, T., Votaw, J.R., Wong, D.F., Carson, R.E., 2007. Consensus nomenclature for in vivo imaging of reversibly binding radioligands. *J. Cereb. Blood Flow Metab.* 27, 1533–1539. doi:10.1038/sj.jcbfm.9600493.
- Knudsen, G.M., Jensen, P.S., Erritzoe, D., Baaré, W.F.C., Ettrup, A., Fisher, P.M., Gillings, N., Hansen, H.D., Hansen, L.K., Hasselbalch, S.G., Henningson, S., Herth, M.M., Holst, K.K., Iversen, P., Kessing, L.V., Macoveanu, J., Madsen, K.S., Mortensen, E.L., Nielsen, F.Å., Paulson, O.B., Siebner, H.R., Stenbæk, D.S., Svarer, C., Jernigan, T.L., Strother, S.C., Frokjaer, V.G., 2016. The Center for Integrated Molecular Brain Imaging (Cimbi) database. *Shar. Wealth Brain Imaging Repos.* 2015 124, 1213–1219. doi:10.1016/j.neuroimage.2015.04.025.
- Krischke, M., Boddy, A.V., Boos, J., 2014. Sources of preanalytical error in pharmacokinetic analyses—focus on intravenous drug administration and collection of blood samples. *Expert Opin. Drug Metab. Toxicol.* 10, 825–838. doi:10.1517/17425255.2014.907273.
- Lassen, N.A., Bartenstein, P.A., Lammertsma, A.A., Pevett, M.C., Turton, D.R., Luthra, S.K., Osman, S., Bloomfield, P.M., Jones, T., Patsalos, P.N., O'Connell, M.T., Duncan, J.S., Andersen, J.V., 1995. Benzodiazepine receptor quantification in vivo in humans using [¹¹C]Flumazenil and PET: application of the steady-state principle. *J. Cereb. Blood Flow Metab.* 15, 152–165. doi:10.1038/jcbfm.1995.17.
- Madsen, M.K., Fisher, P.M., Burmester, D., Dyssegaard, A., Stenbæk, D.S., Kristiansen, S., Johansen, S.S., Lehel, S., Linnet, K., Svarer, C., Erritzoe, D., Ozenne, B., Knudsen, G.M., 2019. Psychedelic effects of psilocybin correlate with serotonin 2A receptor occupancy and plasma psilocin levels. *Neuropsychopharmacology* 44, 1328–1334. doi:10.1038/s41386-019-0324-9.
- Matthews, P.M., Rabiner, E.A., Passchier, J., Gunn, R.N., 2012. Positron emission tomography molecular imaging for drug development: PET for drug development. *Br. J. Clin. Pharmacol.* 73, 175–186. doi:10.1111/j.1365-2125.2011.04085.x.
- Naganawa, M., Gallezot, J.-D., Rossano, S., Carson, R.E., 2019. Quantitative PET imaging in drug development: estimation of target occupancy. *Bull. Math. Biol.* 81, 3508–3541. doi:10.1007/s11538-017-0374-2.
- Pea, F., Krause, R., Müller, C., Hennart, B., Richardson, M., Meinitzer, A., Wiesen, M.H.J., Wiktorowicz, T., Spickermann, J., Henriksen, A.S., 2019. Interlaboratory analysis of isavuconazole plasma concentration assays among European laboratories. *Ther. Drug Monit.* 41, 657–664. doi:10.1097/FTD.0000000000000632.
- Schain, M., Zanderigo, F., Todd Ogden, R., 2018. Likelihood estimation of drug occupancy for brain PET studies. *Neuroimage* 178, 255–265. doi:10.1016/j.neuroimage.2018.05.017.
- Son, H., Jang, K., Lee, Heechan, Kim, S.E., Kang, K.W., Lee, Howard, 2019. Use of molecular imaging in clinical drug development: a systematic review. *Nucl. Med. Imaging* 53, 208–215. doi:10.1007/s13139-019-00593-y.
- Spearman, C., 1904. The proof and measurement of association between two things. *Am. J. Psychol.* 15, 72–101. doi:10.2307/1412159.
- Svensson, J.E., Schain, M., Plavén-Sigra, P., Cervenka, S., Tiger, M., Nord, M., Halldin, C., Farde, L., Lundberg, J., 2019. Validity and reliability of extrastriatal [¹¹C]raclopride binding quantification in the living human brain. *Neuroimage* 202, 116143. doi:10.1016/j.neuroimage.2019.116143.
- Takano, A., Varrone, A., Gulyás, B., Salvadori, P., Gee, A., Windhorst, A., Vercoillie, J., Bormans, G., Lammertsma, A.A., Halldin, C., 2016. Guidelines to PET measurements of the target occupancy in the brain for drug development. *Eur. J. Nucl. Med. Mol. Imaging* 43, 2255–2262. doi:10.1007/s00259-016-3476-4.
- Wong, C.H., Siah, K.W., Lo, A.W., 2019. Estimation of clinical trial success rates and related parameters. *Biostatistics* 20, 273–286. doi:10.1093/biostatistics/kxx069.
- Wouters, O.J., McKee, M., Luyten, J., 2020. Estimated research and development investment needed to bring a new medicine to market, 2009–2018. *JAMA* 323, 844–853. doi:10.1001/jama.2020.1166.
- Zanderigo, F., D'Agostino, A.E., Joshi, N., Schain, M., Kumar, D., Parsey, R.V., DeLorenzo, C., Mann, J.J., 2018. [¹¹C]Harmine binding to brain monoamine oxidase A: test-retest properties and noninvasive quantification. *Mol. Imaging Biol.* 20, 667–681. doi:10.1007/s11307-018-1165-3.

Supplemental material

A. Simulation framework

In this section we provide a detailed account of how we have simulated PET V_T values for baseline-block, as well as test-retest, studies. As stated in the main manuscript, for each changed conditions 1000 unique baseline-block datasets, and 1000 unique corresponding test-retest datasets, were simulated.

A.1 Definition of covariance structure

In order to generate simulated data with realistic noise properties, we used a test-retest (pre- and post- placebo intervention) dataset for the serotonin 2A radioligand [^{11}C]Cimbi-36 (da Cunha-Bang et al., 2019). The dataset consists of 8 human subjects scanned before and after a placebo treatment. One subject was excluded, due to missing data in the first PET scan. Six brain regions of interests (ROIs) were included: thalamus, insula, anterior cingulate cortex, posterior cingulate cortex, orbitofrontal cortex, and occipital cortex. Plasma samples were collected for all subjects and used to calculate regional V_T values with the two-tissue compartment model. The test-retest data was used to define a true covariance matrix, Σ , as $\Sigma = \text{cov}(\mathbf{V}_T^{\text{test}} - \mathbf{V}_T^{\text{retest}})/2$, where $\mathbf{V}_T^{\text{test}}$ and $\mathbf{V}_T^{\text{retest}}$ are $K \times N$ matrices holding the measured V_T values in $K = 6$ ROIs for $N = 7$ subjects. This covariance matrix was then used to generate noise with a realistic covariance structure (see section 1.3 *Generation of noise*).

A.2 Definition of true parameter values

The [^{11}C]Cimbi-36 dataset was also used to define true V_T values for the simulations. First, for each subject and ROI (those mentioned in section 1.1 *Definition of covariance structure*, and cerebellum), the mean V_T across the two PET scans, was computed. Then, for each ROI, those values from all 7 subjects were pooled, and the mean and SD calculated. We then defined (i.e., hardcoded) true V_T values in 10 simulated subjects, so that the mean and SD matched those calculated based on the test-retest dataset. These hardcoded values for V_T are shown in Table 1.

Table 1: Overview of the hardcoded subjects and their distribution volume (V_T) in each of the included brain regions. V_{ND} corresponds to Cerebellum V_T . ACC: anterior cingulate cortex, PCC: posterior cingulate cortex, OrbC: orbitofrontal cortex, OccC: occipital cortex.

Region	Subject									
	1	2	3	4	5	6	7	8	9	10
Thalamus	11.0	13.0	15.0	17.0	18.0	19.0	20.0	22.0	24.0	25.0
Insula	27.0	29.0	31.0	34.0	36.0	37.0	40.0	43.0	45.0	47.0
ACC	30.0	33.0	34.0	37.0	38.0	38.5	39.5	42.5	43.5	46.0
PCC	24.0	27.0	30.0	31.0	34.0	36.0	39.0	40.0	43.0	45.0
OrbC	27.0	31.0	35.0	38.5	39.5	40.0	41.0	44.5	48.5	52.5
OccC	24.0	27.0	29.0	31.0	33.0	34.0	36.0	38.0	41.0	43.0
V_{ND}	8.5	9.5	10.5	12.0	12.5	13.0	14.0	15.0	16.0	17.0

In each simulation experiment, the true V_T values were selected from these 10 subjects by random sampling. For the experiments in which more than ten subjects were simulated, all hardcoded subjects were included, and additional subjects were randomly sampled from those same 10. Cerebellum V_T was used as an estimate of V_{ND} , and ROI-specific values for V_S was calculated as $V_T - V_{ND}$. Thus, to set V_T values at baseline and block condition for subject i , one subject was taken from Table 1, and

$$\begin{cases} \mathbf{V}_{T,true,i}^{base} = V_{ND} \mathbf{1} + \mathbf{V}_{S,i} \\ \mathbf{V}_{T,true,i}^{block} = V_{ND} \mathbf{1} + \left(1 - \Delta_{max} \frac{C_P}{C_P + IC_{50}}\right) \mathbf{V}_{S,i} \end{cases}, \quad (2)$$

where $\mathbf{V}_{T,true}^{base}$ and $\mathbf{V}_{T,true}^{block}$ are $K \times 1$ vectors with V_T values at baseline and block conditions, \mathbf{V}_S is a $K \times 1$ vector with V_S for each ROI (as derived from table 1), and $\mathbf{1}$ is a $K \times 1$ vector of ones. Further, Δ_{max} and IC_{50} are global parameters that remain constant in every simulation, and the plasma drug level, C_p , was set to result in a desired occupancy.

A.3 Generation of noise

Subsequently, noise was added to $\mathbf{V}_{T,true}^x$, using the covariance matrix Σ . The Cholesky factorization of Σ produces an upper triangular matrix $\mathbf{\Gamma}^T$, so that $\Sigma = \mathbf{\Gamma}^T \mathbf{\Gamma}$. If \mathbf{B} denotes a $K \times 1000$ matrix with random numbers sampled from a normal distribution with mean = 0 and

SD = 1, it follows that $\mathbf{\Gamma}^T \mathbf{B}$ will be a $K \times 1000$ matrix with covariance equal to $cov(\mathbf{\Gamma}^T \mathbf{B}) = \mathbf{\Gamma}^T cov(\mathbf{B}) \mathbf{\Gamma} = \mathbf{\Gamma}^T \mathbf{\Gamma} = \mathbf{\Sigma}$. Thus, adding the columns of $\mathbf{\Gamma}^T \mathbf{B}$ to $\mathbf{V}_{T,true}^x$ creates a $K \times 1000$ matrix, where each column holds one simulated measurement of V_T values in all K ROIs, for subject i . This process ensures that each simulated set of V_T values has unique noise and covariance structure according to $\mathbf{\Sigma}$. However, it does not guarantee that the added noise will be of realistic proportions (e.g., a subject with low V_T values likely has a low noise level as well). Therefore, the rows of $\mathbf{\Gamma}^T \mathbf{B}$ was scaled with $\frac{V_{T,true,k}}{34}$, where $V_{T,true,k}$ is the true V_T value in ROI k for subject i . This scaling ensured that the added noise was proportional to the true V_T , and constructed to be one at $V_T=34$, because 34 was the mean V_T value in the test-retest dataset. To create a complete dataset, this procedure was then repeated for all N subjects.

A.4 Simulation of test-retest data for likelihood-based approaches

The maximum-likelihood based estimators improve when a test-retest dataset of the radioligand is available (Schain et al., 2018). To assess their performance, test-retest data was also simulated in parallel to the baseline-block data, using the same method, but with the exception that Δ was set to 0. Throughout the simulations, a test-retest sample size of 10 was used. The effect of varying the test-retest sample size has been assessed previously (Schain et al., 2018).

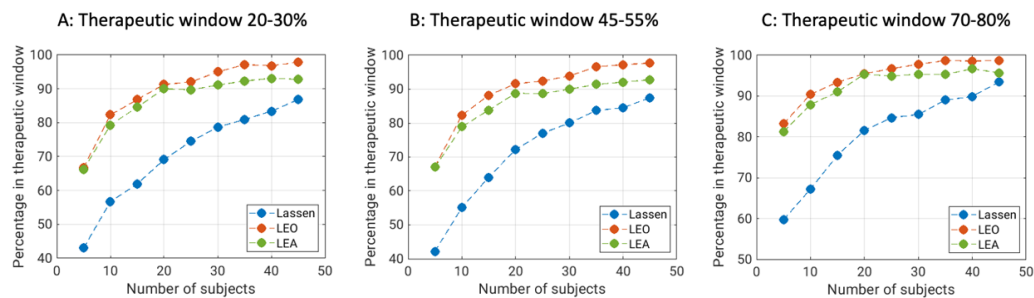
$\mathbf{V}_{T,true}^{test}$ and $\mathbf{V}_{T,true}^{retest}$ were defined in the same manner as $\mathbf{V}_{T,true}^{base}$ in equation 7, and noise was added according to section 2.2.3. This simulated test-retest data was then used to estimate a covariance matrix to be used in the maximum-likelihood based estimators.

In our previous assessment, it was clear that using the raw estimate of the covariance matrix is not advisable, as it would not be well determined from a small-sampled test-retest study. Instead, we propose to use a nonlinear shrinkage method to derive an estimate of $\mathbf{\Sigma}$, denoted $\hat{\mathbf{\Sigma}}$ (Ledoit and Wolf, 2015; Schain et al., 2018). Throughout the simulations, $\hat{\mathbf{\Sigma}}$ was calculated with this method applied to the simulated test-retest data.

B. Therapeutic Window Experiment

In the main manuscript, the clinical implication of the difference in performance between methods is illustrated by an example, where for each method and sample size, we evaluated how many of the established drug concentration-occupancy relationships would lead to correct

dosing for a desired occupancy range between 70 and 80%. That same experiment was repeated for two other therapeutic windows; 20-30%, and 45-55%. The results for those therapeutic windows, together with the results for the therapeutic window presented in the main text (70-80%), are presented in Supplementary figure 1 and 2.



Supplementary figure 1: Illustration of results for the hypothetical drug experiment presented in the discussion, for three different therapeutic windows; 20-30% (A), 45-55% (B), and 70-80% (C). For each iteration in simulation experiment 2, we calculate the plasma drug concentration corresponding to the middle of the target therapeutic window, from the estimated parameter values. The figure shows how large percentage of those plasma drug concentrations result in occupancies within the therapeutic windows for different numbers of subjects in the study and for different analytical methods; Lassen (blue), LEO (red), and LEA (green).

References

- da Cunha-Bang, S., Ettrup, A., Mc Mahon, B., Skibsted, A.P., Schain, M., Lehel, S., Dyssegaard, A., Jørgensen, L.M., Møller, K., Gillings, N., Svarer, C., Knudsen, G.M., 2019. Measuring endogenous changes in serotonergic neurotransmission with [11C]Cimbi-36 positron emission tomography in humans. *Transl. Psychiatry* 9, 134. <https://doi.org/10.1038/s41398-019-0468-8>
- Knudsen, G.M., Jensen, P.S., Erritzoe, D., Baaré, W.F.C., Ettrup, A., Fisher, P.M., Gillings, N., Hansen, H.D., Hansen, L.K., Hasselbalch, S.G., Henningsson, S., Herth, M.M., Holst, K.K., Iversen, P., Kessing, L.V., Macoveanu, J., Madsen, K.S., Mortensen, E.L., Nielsen, F.Å., Paulson, O.B., Siebner, H.R., Stenbæk, D.S., Svarer, C., Jernigan, T.L., Strother, S.C., Frokjaer, V.G., 2016. The Center for Integrated Molecular Brain Imaging (Cimbi) database. *Shar. Wealth Brain Imaging Repos.* 2015 124, 1213–1219. <https://doi.org/10.1016/j.neuroimage.2015.04.025>
- Ledoit, O., Wolf, M., 2015. Spectrum estimation: A unified framework for covariance matrix estimation and PCA in large dimensions. *J. Multivar. Anal.* 139, 360–384. <https://doi.org/10.1016/j.jmva.2015.04.006>
- Schain, M., Zanderigo, F., Todd Ogden, R., 2018. Likelihood estimation of drug occupancy for brain PET studies. *NeuroImage* 178, 255–265. <https://doi.org/10.1016/j.neuroimage.2018.05.017>

Gjertrud Louise Laurell, Pontus Plavén-Sigra, Annette Johansen, Nakul Ravi Raval, Arafat Nasser, Clara Aabye Madsen, Jacob Madsen, Hanne Demant Hansen, Lene Lundgaard Donovan, Gitte Moos Knudsen, Adriaan A. Lammertsma, R. Todd Ogden, Claus Svarer, Martin Schain. Kinetic Models for PET Displacement Studies. *In review at The Journal of Cerebral Blood Flow and Metabolism*

DOI: 10.1101/2022.11.25.517914

Kinetic models for PET displacement studies

Gjertrud Louise Laurell^{1,2}, Pontus Plavén-Sigra¹, Annette Johansen^{1,2}, Nakul Ravi Raval^{1,2}, Arafat Nasser¹, Clara Aabye Madsen,^{1,2} Jacob Madsen³, Hanne Demant Hansen^{1,4}, Lene Lundgaard Donovan^{1,2}, Gitte Moos Knudsen^{1,2}, Adriaan A Lammertsma^{1,5,6}, R Todd Ogden^{1,7,8}, Claus Svarer¹, Martin Schain^{1,9}.

1 Neurobiology Research Unit, Copenhagen University Hospital, Copenhagen, Denmark

2 Faculty of Health and Medical Sciences, Copenhagen University, Copenhagen, Denmark

3 Department of Clinical Physiology, Nuclear Medicine & PET, Copenhagen University, Denmark

4 A. A. Martinos Center for Biomedical Imaging, Massachusetts General Hospital, Charlestown, MA, USA

5 Department of Radiology and Nuclear Medicine, Amsterdam UMC, Vrije Universiteit Amsterdam, Amsterdam, Netherlands

6 Department of Nuclear Medicine and Molecular Imaging, University of Groningen, University Medical Center Groningen, Groningen, Netherlands

7 Molecular Imaging and Neuropathology Division, The New York State Psychiatric Institute, New York, USA

8 Department of Biostatistics, Mailman School of Public Health, Columbia University, New York, New York

9 Antaros Medical, Mölndal, Sweden

Corresponding author:

Claus Svarer

claus.svarer@nru.dk

Phone: +45 3545 6712

Neurobiology Research Unit

6-8 Inge Lehmanns Vej

Rigshospitalet, building 8057

DK-2100 Copenhagen, Denmark

Abstract

The traditional design of PET target engagement studies is based on a baseline scan and one or more scans after drug administration. We here evaluate an alternative design in which the drug is administered during an on-going scan (i.e., a displacement study). This approach results both in lower radiation exposure and lower costs. Existing kinetic models assume steady state. This condition is not present during a drug displacement and consequently, our aim here was to develop kinetic models for analysing PET displacement data.

We modified existing compartment models to accommodate a time-variant increase in occupancy following the pharmacological in-scan intervention. Since this implies the use of differential equations that cannot be solved analytically, we developed instead one approximate and one numerical solution. Through simulations, we show that if the occupancy is relatively high, it can be estimated without bias and with good accuracy. The models were applied to PET data from six pigs where [¹¹C]UCB-J was displaced by intravenous brivaracetam. The dose-occupancy relationship estimated from these scans showed good agreement with occupancies calculated with Lassen plot applied to baseline-block scans of two pigs. In summary, the proposed models provide a framework to determine target occupancy from a single displacement scan.

Keywords: Displacement, Drug Occupancy, Kinetic Modelling, PET, Synaptic Density

1. Introduction

The discovery and development of drugs for the treatment of brain disorders is a challenging process requiring extensive resources, long timelines and significant investments.¹ Over the past decades, imaging with positron emission tomography (PET) has become a valuable tool in CNS drug development. PET imaging with appropriate radioligands makes it possible to determine at an early stage whether a candidate drug penetrates the blood-brain barrier and binds to the target of interest *in vivo*. This helps to ensure that only suitable candidates will be advanced to subsequent trial phases, saving substantial resources.²

In the traditional experimental set-up for determination of target occupancy, two (or more) PET scans are acquired in each subject using a radiotracer that binds to the same target as the drug. Usually, one scan is acquired at baseline (i.e., without drug), and subsequent scan(s) after administration of the drug. The difference between outcome measures from baseline and follow-up scans is then used to determine occupancy, i.e., the fraction of targets occupied by the drug.³

The analysis of data from a PET occupancy study typically follows a three-step approach. First, a mathematical model (either based on arterial blood samples or a reference region) is used to quantify radiotracer uptake for each scan.⁴ Second, outcome measures from the different scans are combined to estimate the occupancy at the time of the post-drug scan.^{3,5} Last, all subjects are pooled in a occupancy plot (sometimes referred to as the E_{max} model) where the administered doses or plasma concentrations of the drug are related to the measured occupancies. This final step provides information of the drug's affinity to the target, defined as the half maximum inhibitory concentration, IC_{50} .

This established methodology leaves room for improvement. First, relying on multiple PET measurements may introduce unwanted variance in the data. It is often difficult to design the experiment in such a way that the intervention is the only difference between the scans, as other (e.g., time-related) factors may affect radiotracer uptake.⁶⁻⁹ Second, the test person is exposed to multiple doses of ionizing radiation. Third, PET is a relatively expensive research tool, so a method that requires two scans for each data point places an unnecessary burden on the research budget.

An alternative approach to determine drug occupancy is to administer the drug during an on-going PET scan and based on a single injection of radioligand. When the drug is administered, competitive binding causes displacement of the radiotracer. Deriving occupancy from such a study would result in reduced costs and lower radiation exposure, as each subject would need to undergo only one scan.

Unfortunately, standard pharmacokinetic models, routinely used to analyse PET data, cannot be applied to data obtained from a displacement scan, as these models rely on the assumption of steady-state throughout a scan.¹⁰ This assumption implies that all model parameters remain constant over time, i.e., the modelled system is assumed to be time-invariant. This assumption is violated when a competing drug is administered during an on-going scan. To quantify displacement studies, a new class of pharmacokinetic models needs to be developed to incorporate the perturbation of the steady state.

The idea to model competitive binding was already pioneered in the 1990s, when models to quantify release of endogenous dopamine were developed.¹¹⁻¹⁴ Of the models relying on bolus injection, the only established model today is the neurotransmitter PET (ntPET), which has been used to evaluate dopamine release under various conditions.¹⁵⁻¹⁸ The ntPET, and variants thereof,¹⁹⁻²³ rely on reference tissue models, i.e., quantification is performed using a reference region rather than an arterial input

function. For many radiotracers, true reference regions do not exist for, due to ubiquitous expression of the target, although some degree of specific binding in the reference region may be tolerable in clinical studies. In pharmacological intervention studies, however, specific binding in the reference region is particularly problematic, as blocking in both target and reference region can result in a complicated bias in the occupancy estimates.

Here, we present a pharmacokinetic model that describes radiotracer kinetics during a displacement scan based on an arterial input function rather than a reference region. The model is based on one-tissue compartment model (ITCM) kinetics. The corresponding two-tissue compartment model (2TCM) is presented in section A of the supplementary material. Because the competing drug will perturb the system's steady state, analytical solutions to the model equations do not exist. Instead, we present two alternative approaches: an approximate analytical solution that is derived by introducing assumptions on the accumulation of the competing drug in brain, and one numerical solution. The performance of the model and solutions are evaluated using simulations, and applied to pig [^{11}C]UCB-J PET scans,²⁴ with brivaracetam displacement.

2. Materials and methods

2.1 Theory

2.1.1 The occupancy model

When radioligand displacement is induced by the introduction of a competing cold ligand (drug) it is assumed that the change is caused by reduction in specific radioligand binding only. This can be modelled by defining an occupancy function, $\partial(t)$, with $0 \leq \partial(t) \leq 1$, that acts on the concentration of available binding sites, B_{avail} . We typically have little knowledge about the drug concentration time profile in brain tissue *in vivo*. To set $\partial(t)$, we defined a set of conditions to be fulfilled. The occupancy model should

- 1) be monotone non-decreasing
- 2) be continuous and differentiable in all time points (i.e., a smooth growth)
- 3) be 0 at the time of drug administration

To fulfil the conditions above, we modified a model originally developed in agricultural sciences to predict crop growth rates.²⁵ Our model for the occupancy function $\partial(t)$ is

$$\partial(t) = \partial^{max} \left(1 + \frac{t_e - t}{t_e - t_m} \right) \left(\frac{t - t_b}{t_e - t_b} \right)^{\frac{t_e - t_b}{t_e - t_m}}, \quad t_b \leq t \leq t_e, \quad (1)$$

where ∂^{max} is the maximal occupancy reached ($0 \leq \partial^{max} \leq 1$), t_e is the end time of the growth (i.e., the time at which ∂^{max} is reached), t_b is the begin-time of the growth (i.e., the time of intervention), and t_m is the time during which $\partial'(t)$ reaches a maximum (i.e., t_m will control the steepness of $\partial(t)$). The function $\partial(t)$ will show a sigmoidal growth within the interval $t_b \leq t \leq t_e$, is exactly 0 at $t = t_b$, and can allow asymmetric or symmetric growth curves depending on the choices of t_e and t_m . Examples of $\partial(t)$ are shown in Figure 1.

2.1.2 Displacement model

The 2TCM is the most common pharmacokinetic model used in quantification of brain PET data. In the 2TCM, the rate of exchange between compartments is determined by the constants K_1 , k_2 , k_3 and k_4 (Figure 1). The rate constant k_3 is linearly dependent on the concentration of available targets (B_{avail}), $k_3 = f_{ND} k_{on} B_{avail}$.^{3,4} We assume that a reduction of available targets will have a negligible impact on

both the association rate constant k_{on} and the fraction of free tracer in the non-displaceable compartment, f_{ND} . It follows that a time dependent reduction of available targets, i.e., $(1 - \partial(t))B_{avail}$ will affect k_3 equally, i.e., $f_{ND}k_{on} \cdot (1 - \partial(t))B_{avail} = (1 - \partial(t))k_3$. With this, the 2TCM can be modified to accommodate an increase in occupancy, starting at some time t_b after radiotracer injection (details and equations provided in section A of the supplementary material).

The pharmacokinetics of some radiotracers are reasonably well approximated by a 1TCM. In the 1TCM, the compartments corresponding to specific and non-displaceable uptake are collapsed into a single compartment, where rate constants K_1 and k_2 describe the transfer rate of radiotracer to and from that compartment. To modify the 1TCM to accommodate displacement, we adapted the framework of the simplified reference tissue model, where the compartments for specific and non-displaceable binding are presumed to latently reside within the model configuration (Figure 1).²⁶ Setting equal the distribution volumes for the 1- and 2 tissue compartment configurations, a relationship between the apparent efflux rate constant, k_{2a} , and k_2/k_4 from the latently present 2TCM configuration can be derived, $k_{2a} = k_2 / \left(1 + \frac{k_3}{k_4}\right)$. This modification enables the introduction of an occupancy parameter to act on k_3 in the 1TCM configuration. A schematic for the model is shown in Figure 1, and the corresponding differential equation becomes

$$\frac{dC_T(t)}{dt} = K_1 C_p(t) - \frac{k_2}{1 + (1 - \partial(t))BP_{ND}} C_T(t), \quad (2)$$

where $C_p(t)$ is the metabolite corrected arterial plasma input function, $BP_{ND} = k_3/k_4$, and $\partial(t)$ as defined by

$$\partial(t) = \begin{cases} 0, & t < t_b \\ \partial^{max} \left(1 + \frac{t_e - t}{t_e - t_m}\right) \left(\frac{t - t_b}{t_e - t_b}\right)^{\frac{t_e - t_b}{t_e - t_m}}, & t_b \leq t < t_e \\ \partial^{max}, & t \geq t_e \end{cases} \quad (3)$$

As indicated in equation (3), the competing drug is assumed not to wash out during the course of the scan (see Discussion).

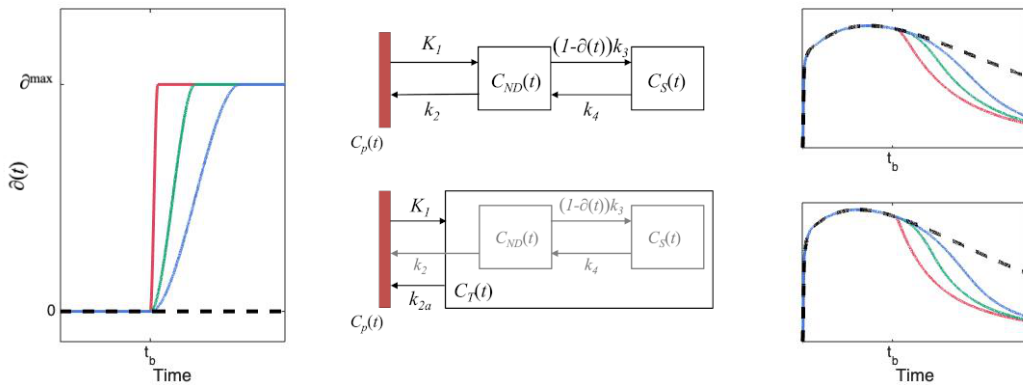


Figure 1: The left panel shows the occupancy function, $\partial(t)$ as defined in Eq.1, for 3 different choices of t_e . The middle panels show schematic diagrams of the intervention models for 2TCM and 1TCM, respectively. The right panels show time-activity curves originating from each compartmental model using the choices for $\partial(t)$ depicted in the left panel.

2.1.3 The single step solution

In contrast to the standard kinetic models, equations (2) describe a time-variant system, and common tools for finding analytical solutions are not strictly defined. To find solutions for the differential equations (2), we placed some restrictions on the occupancy function, $\partial(t)$.

For a drug acting rapidly on the target, i.e., quickly reaching the maximal occupancy attainable at the administered dose, we assume that $\partial(t)$ takes the form of a step function, i.e.,

$$\partial(t) = \begin{cases} 0, & t \leq t_s \\ \partial^{max}, & t > t_s \end{cases}.$$

With this simplification, we can partition the PET time-activity curve (TAC) into two segments (i.e., before and after the time at which the drug is assumed to act on the system, t_s) and apply the 1TCM separately to each segment. We assume that the rate constants are the same for the two segments, but the differential equation for the segment after the step ($t > t_s$) will come with non-zero initial values. The initial values for the $t > t_s$ segment are set to the values at the endpoint of the $t \leq t_s$ segment.

Let $C_T^0(t)$ and $C_T^1(t)$ denote the tissue concentrations before and after administration of the competing drug. The equations describing $C_T^0(t)$ are the standard differential equations for the 1TCM (see equation 2, with $\partial(t) = 0$). Setting $\tau = t - t_s$, the differential equation for $t > t_s$ becomes

$$\begin{cases} \frac{dC_T^1(\tau)}{d\tau} = K_1 C_p(\tau + t_s) - \frac{k_2}{1+(1-\partial^{max})BP_{ND}} C_T^1(\tau), & \tau > 0. \\ C_T^1(t_s) = C_T^0(t_s) \end{cases}$$

The solution to these differential equations becomes

$$C_T(t) = \begin{cases} K_1 C_p(t) \otimes e^{-\frac{k_2}{1+BP_{ND}}t}, & t \leq t_s \\ K_1 C_p(t) \otimes e^{-\frac{k_2}{1+(1-\partial^{max})BP_{ND}}(t-t_s)} + C_T^0(t_s) \cdot e^{-\frac{k_2}{1+(1-\partial^{max})BP_{ND}}(t-t_s)}, & t > t_s \end{cases} \quad (6)$$

Fitting the single step solution thus means estimating a total of 4 model parameters: K_1 , k_2 and BP_{ND} and ∂^{max} . In our implementation, we also included the fractional blood volume (v_B), and the time at which the occupancy step occurs (t_s), as free parameters. The reason to include t_s as a free parameter is to reduce errors caused by setting $\partial(t)$ to be a step function: by allowing the model to perform the step later than the time of intervention we submit that a better description of the data can be obtained. The equations for the single step solution of the 2TCM is provided in the supplementary material (section A.2).

2.1.4 The Numerical Solution

The Euler Forward method was used to obtain a numerical solution to equation (2).

Starting at known initial conditions, each next point on the model curves is calculated by,

$$C(t_n) = C(t_{n-1}) + hC'(t_{n-1}),$$

where $h = t_n - t_{n-1}$ (i.e., linearity is assumed in the small time interval $t_{n-1} < t < t_n$). Insertion of the model equations in (2) gives

$$C_T(t_n) = h \cdot K_1 C_p(t_{n-1}) + \left(1 - \frac{h \cdot k_2}{1 + (1 - \partial(t_{n-1})) BP_{ND}}\right) C_T(t_{n-1}).$$

The occupancy function shown in equation 3 (Figure 1) was used for $\partial(t_n)$, and h was set to 0.5 seconds. The corresponding numerical solution for the 2TCM is presented in the supplementary material (section A.3).

2.1.4 Fitting of multiple regions simultaneously

As seen in equation (2), the free model parameters k_2 , $\partial(t)$, and BP_{ND} appear only as a ratio, and as such, each of these parameters are free to take any value as long as the term $\frac{k_2}{(1 + \partial(t)) BP_{ND}}$ results in an adequate fit. Consequently, unless some constraints are placed in the optimization, neither of these parameters can be properly identified (see supplementary material, section B and supplementary figures 1 and 2).

In PET kinetic modelling, it is common to assume that the non-displaceable distribution volume (V_{ND}) is the same across all included brain regions. In dose-occupancy studies, it is also common to assume that the fractional occupancy is the same across the brain. In fact, these two assumptions form the basis for many quantification strategies, including all reference tissue modelling as well as the Lassen Plot.²⁷ We therefore constructed our optimizer so that V_{ND} and ∂^{max} are shared across all included brain regions, whereas the other model parameters, i.e., K_1 , BP_{ND} , and v_B , are free to vary across the brain. For the single step approach, the estimated time at which the model performs the jump, t_s , was also treated as a global parameter. Similarly for the numerical solution, the estimated time at which the growth of the occupancy ends, t_e , was estimated globally. For both methods, we used a nested approach to fit the models to the data. In an outer layer, the global parameters (V_{ND} , ∂^{max} , t_e/t_s) were estimated with non-linear least squares. For each iteration of the outer layer, the remaining model parameters (K_1 , V_{ND} , v_B) were fitted for each ROI separately. More details about models and implementation can be found in the supplementary material (section C).

2.2 Simulations

2.2.1 Generation of noise-free time activity curves

In simulations, we attempted to mimic the behaviour of [¹¹C]UCB-J.²⁴ For $C_p(t)$, we used an arterial input function measured from a pig scan (baseline scan of experiment 1 in Table 1), where the measured activities after the peak were fitted with a tri-exponential function. The tissue rate constants were taken from table 1 in (Finnema et al., 2018)²⁸, and set to result in $V_{ND} = 4$, and V_T ranging between 14.2 and 22.4. We simulated TACs for seven regions: putamen, temporal cortex, occipital cortex, frontal cortex, thalamus, cerebellum, and hippocampus.

To evaluate the performance of our methods, we simulated displacement TACs with two different types of drugs: one fast and one slower. In both cases, the time of injection of the drug was set at 60 minutes after radiotracer administration. For the fast-acting drug, the time t_e at which the drug reached it maximal occupancy was set to 65 minutes, for the slow-acting drug, t_e was set to 90 minutes. Scan durations were set to 150 minutes. For each of the drugs, we simulated displacement scans at three different occupancies (∂^{max}): 25%, 50% and 75%. For each of the six different cases (combination of drug and occupancy) we simulated 1000 unique scans, with noise added as explained in 2.2.2 *Generation of noise*. To generate the TACs we used the Euler Forward method and the differential

equation for the 1TC displacement model (Equations 2 and 3). Some example TACs with different t_e are shown in Figure 1.

2.2.2 Generation of noise

To create realistic noise, a previously proposed noise-model was used that allows for time-dependent variance.^{29,30}

$$C_{noisy}(t_k) = C_{true}(t_k) \cdot \left(1 + \alpha \sqrt{\frac{e^{\lambda t_k^{mid}}}{C_{true}(t_k) \Delta t_k}} \cdot G(0,1) \right),$$

where λ is the decay constant for the isotope (in this case ^{11}C), t_k^{mid} and Δt_k are the mid-time and duration of frame k , respectively, and $G(0,1)$ is a number sampled from a Gaussian distribution centered on 0 with a SD of 1. The scaling factor α was set to 5 in order to create noise on par with that of real experiments. Figures of example TACs at different noise levels can be found in the supplementary material (supplementary figures 3 and 4).

2.3 PET experiments

2.3.1 Experimental procedure

[^{11}C]UCB-J was largely synthesized as in Nabulsi et al., 2016,²⁴ with some modifications.³¹ All animal experiments conformed to the European Commission's Directive 2010/63/EU and the ARRIVE guidelines. The Danish Council of Animal Ethics had approved all procedures (Journal no. 2016-15-0201-01149). Six female domestic pigs (crossbreed of Yorkshire \times Duroc \times Landrace, mean weight 23.3 [range: 18-27] kg) were fully anesthetized and scanned using [^{11}C]UCB-J administered as a bolus injection (injected dose: 441 [range: 344-528] MBq; injected mass: 0.69 [range: 0.08-2.77] μg). Two of the pigs (experiments 1 and 2) underwent three scans, i.e., baseline (120 min), displacement (150 min) and blocking (120 min) scans, on the same day. Brivaracetam (Briviact®, 10 mg/mL, UCB Pharma, Belgium) was administered i.v. during the displacement scan and served as a traditional blocking agent in the third scan, which was started approximately 120 min after the brivaracetam intervention. The remaining four pigs only underwent displacement scans. In all displacement scans, brivaracetam was administered i.v. over 20 seconds, 60 min after radioligand injection. A list of all experiments is shown in Table 1.

Table 1 Overview of pig PET experiments.

Experiment	Type	Dose [mg/kg]
Experiment 1	Baseline scan	
	Intervention scan	0.1
	Block scan	
Experiment 2	Baseline scan	
	Intervention scan	2
	Block scan	
Experiment 3	Intervention scan	5
Experiment 4	Intervention scan	1
Experiment 5	Intervention scan	0.75
Experiment 6	Intervention scan	0.2

2.3.3 PET data processing

PET scans were acquired on a High Resolution Research Tomograph (HRRT; Siemens, USA) and reconstructed using OP-3D-OSEM, including modelling of the point-spread function, with 16 subsets, 10 iterations and all standard corrections.³² Data was binned into the following time frames: 6 x 10, 6 x 20, 3 x 30, 9 x 60, 8 x 120, 4 x 180, 2 x 240, 1 x 360, 1 x 420, 1 x 600, 1 x 900 and 1 x 1680 s for the 120 min scans, and 6 x 10, 6 x 20, 6 x 30, 6 x 60, 4 x 120, 14 x 300, 8 x 150 s and 8 x 300 s for the 150 min scans. Attenuation correction was performed using the MAP-TR μ -map.³³ Definition of brain regions of interests (ROIs) was performed using a dedicated pig brain template.³⁴ The seven regions from the simulation experiment were also used here: putamen, temporal cortex, occipital cortex, frontal cortex, thalamus, cerebellum and hippocampus.

2.3.4 Blood and plasma analyses

Radioactivity in arterial whole blood was measured continuously for the first 30 min of each scan using an Allogg ABSS autosampler (Allogg Technology, Sweden). Arterial blood was manually drawn at 3, 8, 10, 15, 30, 45, 59, 61, 65, 75, 90, 105, 120 and 150 min for measuring radioactivity in whole blood and plasma using a gamma counter (Cobra, 5003, Packard Instruments, Meriden, USA) that was cross-calibrated against the HRRT. Radio-HPLC was used to measure radioligand parent fractions.³⁵ A more detailed account of the blood and plasma analyses can be found in the supplementary material (Section D).

In the baseline scan of experiment 2, (see Table 1), the parent fraction could not be estimated due to a technical failure. The parent fractions from the displacement and blocking scans conducted in the same animal were, however, very similar (absolute difference averaged across time was $6.0 \pm 4.1\%$, and difference in AUC was 2%). Therefore, for the baseline scan in experiment 2, the mean parent fraction from the corresponding displacement and blocking scans was used.

The concentration of brivaracetam in arterial plasma was analysed using UPLC-MS/MS (Filadelfia Epilepsy Hospital, Denmark). During the displacement scans seven blood samples (at approximately 1,

5, 15, 30, 45, 60 and 90 min after brivaracetam injection) were collected for this purpose, and during the block scans five samples (at approximately 3, 15, 45, 75 and 90 min after scan start) were collected.

3. Results

3.1 Simulation results

Figure 2 summarises results from the simulation experiment. It shows that occupancy estimation improves both with increasing drug speed and with increasing dose. The performance of the two methods (numerical solution and single-step approximation) were comparable throughout, especially for the higher occupancies, where the histograms are almost identical. While the occupancy estimates are approximately normally distributed for the higher occupancies, the distributions of estimates are slightly skewed for both methods at 25% occupancy. At this lower occupancy, there is also a bigger difference between the distributions, with the single-step solution, unlike the numerical solution, showing a slight tendency to overestimate $\hat{\rho}^{\max}$ (for the fast drug, median $\hat{\rho}^{\max}$ estimates were 25.2% with the numerical solution and 30.2% with the single step solution). Corresponding results for V_{ND} and V_S are found in supplementary figures 8 and 9, respectively.

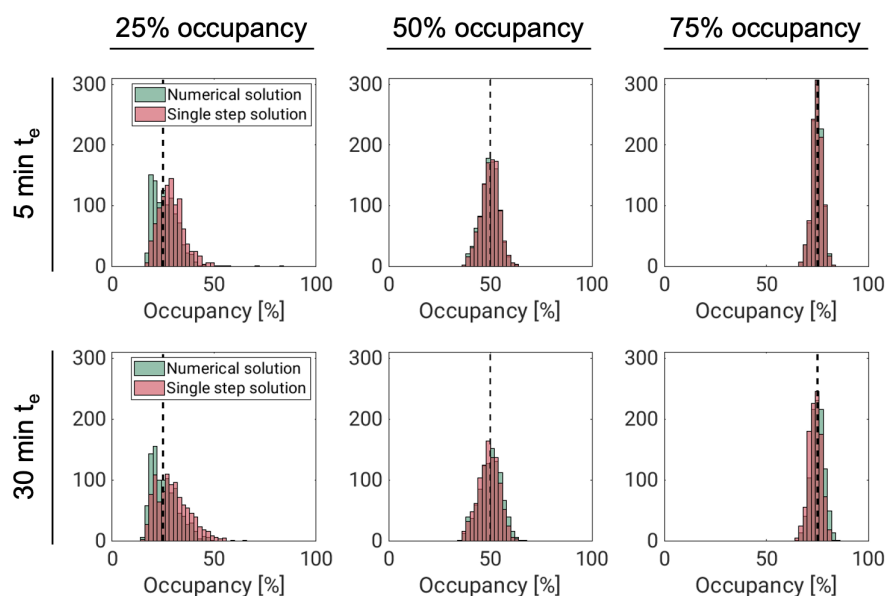


Figure 2: Results from simulating fast- ($t_e = 5$ min) and slow-acting ($t_e = 30$ min) drugs, displacing $[^{11}\text{C}]\text{UCB-J}$ binding. Each panel shows histograms of occupancy ($\hat{\rho}^{\max}$) estimates from the numerical solution (green) and single-step approximation (red). In each panel, the dashed black line corresponds to the true value for $\hat{\rho}^{\max}$.

3.2 Displacement models applied to real data

3.2.1 Model fits

The 1TC displacement model was consistently able to describe the measured TACs using both the single-step approximation and the numerical solution. Figure 3 shows model fits to temporal cortex TACs, with both methods, for the largest and the lowest dose experiments. For the numerical solution, fits to all TACs, with residuals, for the same two scans can be found in supplementary figures 13 and 14, and normalized residuals for all six pig scans can be found in supplementary figure 15. The average \pm SD total distribution volume in temporal cortex, across all displacement scans was 20.2 ± 3.7 mL/cm³ for both methods. The occupancies ranged from 41% to 86%.

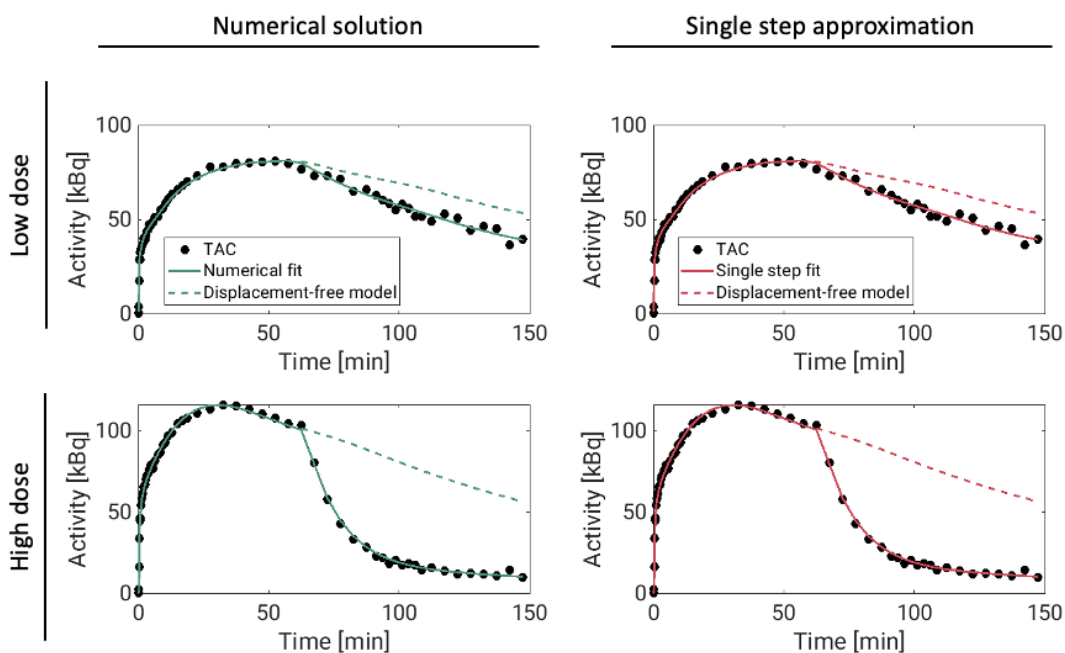


Figure 3: Displacement model fits (solid lines) to $[^{11}\text{C}]\text{UCB-J}$ temporal cortex TACs (dots) from two pig scans in which brivaracetam was administered i.v. 60 minutes after radiotracer injection. The dashed lines show model curves in the absence of displacement. These curves were generated from the estimated model parameters, with occupancy set to zero.

3.2.2 Comparison with Lassen plots

Experiment 1 and 2 each had a baseline scan before and a blocking scan after the displacement scan. These scans were analysed using the traditional ITCM, and occupancies were estimated using the Lassen plot.^{5,27} For both experiments, the Lassen occupancies in the block scans were lower than the estimates from the displacement scans (see figure 4, left panel). However, the plasma drug concentrations were also lower during the block scans, and the outcome of the Lassen-plot fit well with the dose-occupancy relationship estimated from the displacement scans (see dose-occupancy plots in figure 4). The Lassen- V_{ND} s also showed good agreement with the ones calculated with the displacement model. For the high-dose pig scan, the Lassen plot returned a V_{ND} of 2.08, while the displacement model returned a V_{ND} of 1.85 with the numerical solution and 2.15 with the single step solution. For the low-dose pig scan, the Lassen- V_{ND} was 7.46, while the displacement model returned V_{ND} estimates of 7.47 with both solutions.

3.2.3 Dose-occupancy model

Figure 4 shows occupancies (∂^{max}) estimated from the displacement models for all pigs, plotted against the maximal plasma level of brivaracetam following its injection (C_{briva}). These occupancies could be well described by the E_{max} model, $\partial^{max} = \Delta_{max} C_{briva} / (C_{briva} + IC_{50})$, where IC_{50} is the drug's half maximal inhibitory concentration, and Δ_{max} is the maximal attainable occupancy for the population. The estimated values for Δ_{max} were 87.3% for the numerical solution, and 87.6% for the single step approach. The corresponding values for IC_{50} were 1.26 $\mu\text{g}/\text{mL}$ and 1.27 $\mu\text{g}/\text{mL}$ for the numerical solution and single step, respectively.

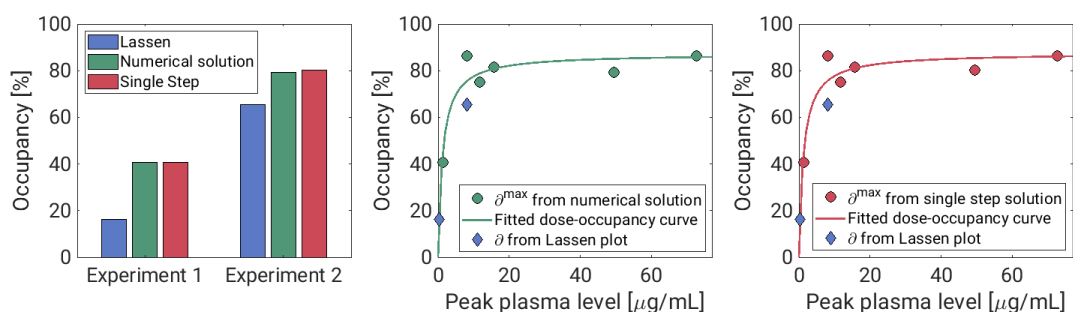


Figure 4: Results from pig experiment. The first tile show occupancy estimates for the two pigs that underwent both displacement and baseline-block scans. The Lassen plot occupancy estimates (from the block scan) are shown in blue, and the occupancy estimates from the displacement scans are shown in green (numerical solution) and red (single step solution). The two other tiles show the estimated occupancies plotted against peak plasma brivaracetam concentrations for the numerical solution and single step solutions, respectively. In both, the Lassen-occupancies plotted against the peak plasma value during the block scans are also included.

4. Discussion

In this study, we present a pharmacokinetic model capable of describing PET time-activity curves after a pharmacological intervention. We have developed a generic and flexible model that allows for increasing occupancy, and that is incorporated into the standard PET compartmental models, to describe a displacement of the radiotracer during the scan. Because the differential equations are time-variant, we present two new approaches for quantification of PET data with arterial input functions. In the single step solution, the effect of the drug intervention is approximated to be instantaneous, and the system can thus be assumed to be time-invariant both before and after the effect of the intervention occurs. The “extended simplified reference tissue model” (ESRTM) is based on the same idea, although it relies on a reference tissue rather than an arterial input function.³⁶ The other solution is to solve the model differential equations using numerical methods. Here, we used the Euler Forward method together with a monotone, continuous and differentiable occupancy model.

The present results suggest that performing displacement scans is a viable alternative to the traditional two-scan setup to determine target engagement. We demonstrate the usefulness of the methods by displacing [^{11}C]UCB-J with brivaracetam in pigs. Experiments 1 and 2 showed that the displacement model resulted in similar occupancy estimates as those obtained using the traditional Lassen plot. The estimated occupancies could be well described by the E_{max} model, which resulted in IC_{50} estimates of 1.26 $\mu\text{g/mL}$ for the single step method and 1.27 $\mu\text{g/mL}$ for the numerical solution. The E_{max} model assumes that the drug concentration in plasma is constant but plasma brivaracetam changes rapidly following intravenous injection, and it is not entirely clear how to best map occupancies to such dynamic plasma levels. Because we saw a very rapid displacement of [^{11}C]UCB-J, we used peak plasma values, i.e. plasma values immediately following injection, as they align temporally to radiotracer displacement. In basement-block experiments, where the drug is normally administered some time before the block scan, the plasma drug concentration will remain relatively constant during the scan. In these cases, the plasma concentration either at the start of the scan, the end of the scan, or the mean of the two, is often used in the E_{max} model.³⁷ For comparison, we re-ran the dose-occupancy analysis using mean plasma concentrations during each scan in place of the peak plasma values. This resulted in an IC_{50} of 0.47 $\mu\text{g/mL}$, for both the numerical solution and single-step approximation. This is nearly identical to the brivaracetam IC_{50} reported by Finnema and colleagues (0.46 $\mu\text{g/mL}$) from a [^{11}C]UCB-J baseline-block experiment in humans.³⁸

When performing drug development studies, it is common practice to use a range of doses to better characterise the dose-occupancy relationship. The displacement models presented here do not necessarily provide good estimates in the low occupancy ranges (~25%, or lower). At 25% occupancy, there is also a large uncertainty in the V_{ND} estimate (supplementary figure 8), and in several cases (especially for the numerical solution) it hits the lower bound at $V_{ND} = 0$. Due to a strong positive correlation between \mathcal{O}^{max} and V_{ND} (see supplementary tables 1 and 2, and supplementary figures 11 and 12), this leads to the apparent negative bias in occupancy that we see in figure 2. Difficulties in determining low occupancies has also been reported with the Lassen plot.³⁹⁻⁴¹ A possible solution is to fit multiple subjects simultaneously in a multilevel pharmacokinetic modelling framework, allowing the model to differentiate between displacement and normal scans.⁴² This could improve the occupancy estimates, even if normal and displacement scans were conducted in different research subjects. Such an approach could be particularly valuable if the displacement is small, e.g., when using a behavioural task to elicit neurotransmitter release rather than a pharmacological challenge.

The assumption of instantaneous occupancy (single step) that we have employed to allow the model to be solved analytically has already been shown to be a useful one for reference region quantification of displacement scans.³⁶ We emphasize that although the single step solution involves splitting TACs into two segments, each segment is not fitted independently. All rate constants are constrained to be constant throughout the scan, and they are estimated by fitting the entire TAC.

The objective of introducing a numerical solution, accounting for the time course of occupancy, was to allow better quantification of occupancy for slow-acting drugs. Unexpectedly, the two approaches performed comparably across all experiments, even for the simulated slower drug ($t_e = 30$ min). In addition to the presented data, we simulated scans with a much slower drug ($t_e = 120$ min, see supplementary figure 5), where the final occupancy was reached 30 min after the last acquired data. Even in this case, we saw no advantage of the numerical solution over the single step simplification. In fact, both approaches performed poorly in this scenario.

The performance of the single step solution presented in this paper relies on using a relatively high time resolution (0.5 s frequency) in the convolution step. In our experience, this is a much shorter step size than what is usually used when solving compartment models. Consequently, the single step approach is computationally relatively heavy, and requires approximately 30 times longer run-time than the Euler Forward-based numerical solution.

Another advantage of the numerical approach is that it allows flexibility. In this study, we have used a monotonic increasing function to explain the time course of occupancy. These assumptions appear to be reasonable for the [¹¹C]UCB-J pig scans with brivaracetam intervention. However, depending on factors like the drug, radiotracer, and experimental design, in some cases it might be preferable to use a different type of function to describe the occupancy. For instance, the numerical approach allows for an occupancy model where both drug uptake and washout happen during the scan. We chose the occupancy model in (equation 1) because it is a continuous and differentiable function that allows some key parameters to be estimated. In reality, we expect that the increase in occupancy in the time following a drug intervention is at first rapid, and then slows down as fewer binding sites remain available. In a recent study, Naganawa and colleagues present a similar displacement model for [¹¹C]UCB-J. In that study, the rate constants defining the drug's uptake and clearance in tissue were estimated, together with the radioligand's rate constants.⁴³ While this model more accurately reflects the underlying competition at the SV2A binding sites, the authors show that parameter identifiability becomes

challenging with a model of that complexity. The approach presented in the current study is thus a pragmatic solution to derive occupancy estimates from a single displacement scan.

We are confident that the simulated TACs have a level of noise that is realistic to [¹¹C]UCB-J. The level of noise could however vary for different radiotracers. In supplementary figures 6 and 7 we show histograms of $\hat{\rho}^{max}$ estimates at different levels of noise. With increasing noise, the precision of the parameter estimation is reduced, but the estimates remain unbiased. With no noise added, both solutions to the model consistently return the true $\hat{\rho}^{max}$ value.

In both solutions to the model, the time of the intervention (t_b) is treated as a known parameter and is not fitted. In the presented results, the models were solved with the true t_b values. In reality, it might be difficult to identify the exact moment when the drug reaches its target. We therefore applied the models to some of the simulated data with wrong values for t_b (1 and 5 minutes before and after the true t_b). For both solutions to the model, the $\hat{\rho}^{max}$ and V_{ND} were generally unaffected by the different values for t_b (supplementary figure 16).

A limitation of the models is that they only consider a change in available binding sites. Pharmacological interventions may also affect perfusion, which could influence some model parameters (e.g., K_I for highly permeable radiotracers). If the intervention causes, for instance, an increase in perfusion, the models presented here are likely to underestimate the occupancy due to K_I being fixed throughout the scan. Further work is needed to develop models that can account for other changes than a reduction in B_{avail} induced by the pharmacological challenge, like some of the existing reference region based methods do.^{14,19} Also, similar to available methods for baseline-block scans, the model does not account for specific binding of the radiotracer to the target, assuming that it is only present in tracer doses. Depending on the specific activity of the radiotracer, this could lead to some bias.

Although we derived displacement versions of both the 1TCM and 2TCM (see supplementary material, section A.), we only considered a tracer that can be described by 1TC kinetics. Additional work is needed to evaluate the performance of the 2TC displacement models, as well as reference tissue implementations.

A limitation of the simulation experiments is that, for the numerical solution, the same model is used both to simulate the data and solve it. This could offer an unfair advantage to the numerical solution over the single step approximation, but our pig experiments confirm that the two approaches perform well, and they are in agreement with the Lassen plot outcome. We also limited our case to a drug that after intravenous injection shows a very immediate interaction with the target. Future studies must show if the two methods perform equally well for more slow-acting drugs. For solving the proposed displacement model, both with the numerical approach and the analytical approximation, it is necessary to pool data from several brain regions. This is standard for methods of estimating occupancies in the absence of a reference region.^{5,27,39-41}

In conclusion, drug displacement PET scans constitute a promising alternative to determine occupancy, compared to baseline and follow-up studies. The kinetic models presented here enable estimation of occupancy from a single displacement scan, thereby obviating the need for two consecutive scans. This allows the number of scans required for target engagement studies to be substantially reduced, leading to lower radiation exposure and experimental costs, while also limiting the variation of biological and

experimental factors. To facilitate the implementation of these models in other research centres, the MATLAB code is freely available for download at <https://github.com/Gjertrud/ISI>.

5. Acknowledgement

This project has received funding from the European Union's Horizon 2020 research and innovation programme under the Marie Skłodowska-Curie grant agreement No 796759. GLL was supported by Rigshospitalet's Research Council (R197-A8956). PPS was supported by the Swedish Society for Medicine and the Lundbeck Foundation (R303-2018-3263). AJ was supported by The Independent Research Fund Denmark. NRR was funded by the European Union's Horizon 2020 research and innovation programme under the Marie Skłodowska-Curie grant agreement No 813528. HDH was supported by the Lundbeck Foundation (R293-2018-738). RTO and AAL were supported by visiting professorships from the Lundbeck Foundation (R317-2019-787 and R290-2018-756). The authors would like to thank the veterinarians and staff at the Department of Experimental Medicine, University of Copenhagen for their continued assistance with animal experiments.

6. Author contribution statement

MS, PPS, AAL, RTO, GMK and CS developed the theoretical framework. GLL and MS implemented the models, designed the simulations, and performed all calculations. AJ, NRR, CAM, LLD and HDH planned and conducted all PET experiments. AN analyzed all blood and plasma samples. JM led all radioligand syntheses. GLL and MS drafted the manuscript, and all authors provided critical feedback and helped shape the final version.

7. Disclosure

GMK has received honoraria as a speaker for Sage Biogen and H. Lundbeck, and as a consultant for Sanos. MS has received compensation from Roche as a key opinion leader, and is an employee and owns stock options in Antaros Medical AB.

8. Supplementary material

Supplementary material can be found in a separate file.

8. References

1. Wouters OJ, McKee M, Luyten J. Estimated Research and Development Investment Needed to Bring a New Medicine to Market, 2009-2018. *JAMA* 2020; 323: 844–853.
2. Gunn RN, Rabiner EA. Imaging in Central Nervous System Drug Discovery. *Seminars in Nuclear Medicine* 2017; 47: 89–98.
3. Innis RB, Cunningham VJ, Delforge J, et al. Consensus Nomenclature for in vivo Imaging of Reversibly Binding Radioligands. *Journal of Cerebral Blood Flow & Metabolism* 2007; 27: 1533–1539.
4. Slifstein M, Laruelle M. Models and methods for derivation of in vivo neuroreceptor parameters with PET and SPECT reversible radiotracers. *Nuclear Medicine and Biology* 2001; 28: 595–608.
5. Cunningham VJ, Rabiner EA, Slifstein M, et al. Measuring drug occupancy in the absence of a reference region: the Lassen plot re-visited. *Journal of cerebral blood flow and metabolism : official journal of the International Society of Cerebral Blood Flow and Metabolism* 2010; 30: 46–50.
6. Steinberg LJ, Rubin-Falcone H, Galfalvy HC, et al. Cortisol Stress Response and in Vivo PET Imaging of Human Brain Serotonin 1A Receptor Binding. *Int J Neuropsychopharmacol* 2019; 22: 329–338.
7. da Cunha-Bang S, Ettrup A, Mc Mahon B, et al. Measuring endogenous changes in serotonergic neurotransmission with [(11)C]Cimbi-36 positron emission tomography in humans. *Translational psychiatry* 2019; 9: 134.
8. Mc Mahon B, Andersen SB, Madsen MK, et al. Seasonal difference in brain serotonin transporter binding predicts symptom severity in patients with seasonal affective disorder. *Brain* 2016; 139: 1605–1614.
9. Matheson GJ, Schain M, Almeida R, et al. Diurnal and seasonal variation of the brain serotonin system in healthy male subjects. *NeuroImage* 2015; 112: 225–231.
10. Morris ED, Endres CJ, Schmidt KC, et al. Kinetic Modeling in Positron Emission Tomography. In: *Emission Tomography*. Elsevier, pp. 499–540.
11. Endres CJ, Kolachana BS, Saunders RC, et al. Kinetic modeling of [(11)C]raclopride: combined PET-microdialysis studies. *J Cereb Blood Flow Metab* 1997; 17: 932–942.
12. Endres CJ, Carson RE. Assessment of dynamic neurotransmitter changes with bolus or infusion delivery of neuroreceptor ligands. *J Cereb Blood Flow Metab* 1998; 18: 1196–1210.
13. Morris ED, Fisher RE, Alpert NM, et al. In vivo imaging of neuromodulation using positron emission tomography: Optimal ligand characteristics and task length for detection of activation. *Hum Brain Mapp* 1995; 3: 35–55.
14. Alpert NM, Badgaiyan RD, Livni E, et al. A novel method for noninvasive detection of neuromodulatory changes in specific neurotransmitter systems. *Neuroimage* 2003; 19: 1049–1060.
15. Yoder KK, Wang C, Morris ED. Change in binding potential as a quantitative index of neurotransmitter release is highly sensitive to relative timing and kinetics of the tracer and the endogenous ligand. *J Nucl Med* 2004; 45: 903–911.
16. Morris ED, Yoder KK, Wang C, et al. ntPET: a new application of PET imaging for characterizing the kinetics of endogenous neurotransmitter release. *Mol Imaging* 2005; 4: 473–489.
17. Morris ED, Normandin MD, Schiffer WK. Initial comparison of ntPET with microdialysis measurements of methamphetamine-induced dopamine release in rats: support for estimation of dopamine curves from PET data. *Mol Imaging Biol* 2008; 10: 67–73.
18. Normandin MD, Morris ED. Temporal resolution of ntPET using either arterial or reference region-derived plasma input functions. *Conf Proc IEEE Eng Med Biol Soc* 2006; 2006: 2005–2008.

19. Normandin MD, Schiffer WK, Morris ED. A linear model for estimation of neurotransmitter response profiles from dynamic PET data. *Neuroimage* 2012; 59: 2689–2699.
20. Kim SJ, Sullivan JM, Wang S, et al. Voxelwise lp-ntPET for detecting localized, transient dopamine release of unknown timing: sensitivity analysis and application to cigarette smoking in the PET scanner. *Hum Brain Mapp* 2014; 35: 4876–4891.
21. Wang S, Kim S, Cosgrove KP, et al. A framework for designing dynamic lp-ntPET studies to maximize the sensitivity to transient neurotransmitter responses to drugs: Application to dopamine and smoking. *Neuroimage* 2017; 146: 701–714.
22. Liu H, Zakiniaez Y, Cosgrove KP, et al. Toward whole-brain dopamine movies: a critical review of PET imaging of dopamine transmission in the striatum and cortex. *Brain Imaging Behav* 2019; 13: 314–322.
23. Irace Z, Mérida I, Redouté J, et al. Bayesian Estimation of the ntPET Model in Single-Scan Competition PET Studies. *Front Physiol* 2020; 11: 498.
24. Nabulsi NB, Mercier J, Holden D, et al. Synthesis and Preclinical Evaluation of ¹¹C-UCB-J as a PET Tracer for Imaging the Synaptic Vesicle Glycoprotein 2A in the Brain. *J Nucl Med* 2016; 57: 777–784.
25. Yin X, Goudriaan J, Lantinga EA, et al. A flexible sigmoid function of determinate growth. *Ann Bot* 2003; 91: 361–371.
26. Lammertsma AA, Hume SP. Simplified reference tissue model for PET receptor studies. *Neuroimage* 1996; 4: 153–158.
27. Lassen NA, Bartenstein PA, Lammertsma AA, et al. Benzodiazepine receptor quantification in vivo in humans using [¹¹C]flumazenil and PET: Application of the steady-state principle. *Journal of Cerebral Blood Flow and Metabolism* 1995; 15: 152–165.
28. Finnema SJ, Nabulsi NB, Mercier J, et al. Kinetic evaluation and test-retest reproducibility of [(11)C]UCB-J, a novel radioligand for positron emission tomography imaging of synaptic vesicle glycoprotein 2A in humans. *Journal of cerebral blood flow and metabolism : official journal of the International Society of Cerebral Blood Flow and Metabolism* 2018; 38: 2041–2052.
29. Logan J, Fowler JS, Volkow ND, et al. A strategy for removing the bias in the graphical analysis method. *J Cereb Blood Flow Metab* 2001; 21: 307–320.
30. Varga J, Szabo Z. Modified regression model for the Logan plot. *J Cereb Blood Flow Metab* 2002; 22: 240–244.
31. Raval NR, Gudmundsen F, Juhl M, et al. Synaptic Density and Neuronal Metabolic Function Measured by Positron Emission Tomography in the Unilateral 6-OHDA Rat Model of Parkinson’s Disease. *Front Synaptic Neurosci* 2021; 13: 715811.
32. Sureau FC, Reader AJ, Comtat C, et al. Impact of image-space resolution modeling for studies with the high-resolution research tomograph. *J Nucl Med* 2008; 49: 1000–1008.
33. Keller SH, Svarer C, Sibomana M. Attenuation correction for the HRRT PET-scanner using transmission scatter correction and total variation regularization. *IEEE Trans Med Imaging* 2013; 32: 1611–1621.
34. Villadsen J, Hansen HD, Jørgensen LM, et al. Automatic delineation of brain regions on MRI and PET images from the pig. *J Neurosci Methods* 2018; 294: 51–58.
35. Gillings N. A restricted access material for rapid analysis of [(11)C]-labeled radiopharmaceuticals and their metabolites in plasma. *Nucl Med Biol* 2009; 36: 961–965.
36. Zhou Y, Chen M-K, Endres CJ, et al. An extended simplified reference tissue model for the quantification of dynamic PET with amphetamine challenge. *Neuroimage* 2006; 33: 550–563.

37. Takano A, Varrone A, Gulyás B, et al. Guidelines to PET measurements of the target occupancy in the brain for drug development. *European Journal of Nuclear Medicine and Molecular Imaging* 2016; 43: 2255–2262.
38. Finnema SJ, Rossano S, Naganawa M, et al. A single-center, open-label positron emission tomography study to evaluate brivaracetam and levetiracetam synaptic vesicle glycoprotein 2A binding in healthy volunteers. *Epilepsia* 2019; 60: 958–967.
39. Schain M, Zanderigo F, Ogden RT. Likelihood estimation of drug occupancy for brain PET studies. *NeuroImage* 2018; 178: 255–265.
40. Naganawa M, Gallezot J-D, Rossano S, et al. Quantitative PET Imaging in Drug Development: Estimation of Target Occupancy. *Bulletin of mathematical biology* 2019; 81: 3508–3541.
41. Laurell GL, Plavén-Sigraý P, Svarer C, et al. Designing drug occupancy studies with PET neuroimaging: Sample size, occupancy ranges and analytical methods. *NeuroImage* 2022; 263: 119620.
42. Chen Y, Goldsmith J, Ogden RT. Nonlinear Mixed-Effects Models for PET Data. *IEEE Trans Biomed Eng* 2019; 66: 881–891.
43. Naganawa M, Gallezot J-D, Finnema SJ, et al. Drug characteristics derived from kinetic modeling: combined 11C-UCB-J human PET imaging with levetiracetam and brivaracetam occupancy of SV2A. *EJNMMI Res* 2022; 12: 71.

Supplementary material
Kinetic models for PET displacement studies

A. DISPLACEMENT MODEL FOR 2TCM KINETICS.....	2
A.1 Operational equations for the displacement model based on 2TCM kinetics	2
A.2 Single step approximation for the 2TCM.....	2
A.3 Numerical solution for the 2TCM.....	4
B. RATIONALE FOR SIMULTANEOUSLY FITTING SEVERAL ROIS	4
C. IMPLEMENTATION OF MODELS	5
D. BLOOD AND PLASMA ANALYSES	6
E. SUPPLEMENTARY RESULTS	6
E.1 Example of simulated data.....	6
E.2 Results for simulated drug with $t_e = 120$	7
E.3 Effect of noise on parameter estimates	8
E.4 Estimation of V_{ND} and V_T	9
E.5 Correlation between parameter estimates.....	10
E.6 Residuals of model fits to pig data.....	13
E.7 Effect of t_b on parameter estimates	14
F. REFERENCES FOR THE SUPPLEMENTARY MATERIAL	15

A. Displacement model for 2TCM kinetics

A.1 Operational equations for the displacement model based on 2TCM kinetics

In the 2TCM, the rate of exchange between compartments is determined by the constants K_1 , k_2 , k_3 and k_4 (Figure 1). The rate constant k_3 is linearly dependent on the concentration of available targets (B_{avail}), $k_3 = f_{ND}k_{on}B_{avail}$.^{1,2} We assume that a reduction of available targets will have a negligible impact on both the association rate constant k_{on} and the fraction of free radioligand in the non-displaceable compartment, f_{ND} . It follows that a time dependent reduction of available targets, i.e., $(1 - \partial(t))B_{avail}$ will affect k_3 equally, i.e., $f_{ND}k_{on} \cdot (1 - \partial(t))B_{avail} = (1 - \delta(t))k_3$. With this, the 2TCM can be modified to accommodate an increase in occupancy, starting at some time t_b after radioligand injection. A schematic diagram of the model is shown in Figure 1, with the following differential equations:

$$\begin{cases} \frac{dC_{ND}(t)}{dt} = K_1C_p(t) - (k_2 + (1 - \partial(t))k_3)C_{ND}(t) + k_4C_s(t) \\ \frac{dC_s(t)}{dt} = (1 - \partial(t))k_3C_{ND}(t) - k_4C_s(t) \end{cases}, \quad (s1)$$

where $C_p(t)$ is the metabolite corrected arterial plasma input function, C_s and C_{ND} are radioligand concentrations in the respective compartments, and

$$\partial(t) = \begin{cases} 0, & t < t_b \\ \partial^{max} \left(1 + \frac{t_e - t}{t_e - t_m} \right) \left(\frac{t - t_b}{t_e - t_b} \right)^{\frac{t_e - t_b}{t_e - t_m}}, & t_b \leq t < t_e \\ \partial^{max}, & t \geq t_e \end{cases}. \quad (s2)$$

A.2 Single step approximation for the 2TCM

Let $C_T^0(t)$ and $C_T^1(t)$ denote tissue concentrations before and after administration of the competing drug, respectively. The equations describing $C_{ND}^0(t)$ and $C_S^0(t)$ are the standard differential equations for the 2TCM. By introducing a new time variable, $\tau = t - t_s$, the differential equations for $t \geq t_s$ become

$$\begin{cases} \frac{dC_{ND}^1(\tau)}{d\tau} = K_1C_p(\tau + t_s) - (k_2 + (1 - \partial^{max})k_3)C_{ND}^1(\tau) + k_4C_S^1(\tau) \\ \frac{dC_S^1(\tau)}{d\tau} = (1 - \partial^{max})k_3C_{ND}^1(\tau) - k_4C_S^1(\tau) \\ C_{ND}^1(t_s) = C_{ND}^0(t_s), C_S^1(t_s) = C_S^0(t_s) \end{cases}, \tau \geq 0 \quad (s3)$$

Following the nomenclature provided in Gunn et al.,³ the analytical solution for total activity in tissue, $C_T(t) = C_{ND}(t) + C_S(t)$, becomes

$$C_T(t) = \begin{cases} C_p(t) \otimes (\phi_1 e^{-\theta_1 t} + \phi_2 e^{-\theta_2 t}), & t \leq t_s \\ C_p(t) \otimes (\phi_1 e^{-\theta_1(t-t_b)} + \phi_2 e^{-\theta_2(t-t_b)}) + C_{ND}^0(t_b) \frac{(\phi_1 e^{-\theta_1(t-t_b)} + \phi_2 e^{-\theta_2(t-t_b)})}{K_1} \\ \quad + C_S^0(t_b) \left(\frac{-\theta_2 e^{\theta_1(t-t_b)} + \theta_1 e^{\theta_2(t-t_b)}}{\Delta} \right), & t > t_s \end{cases}$$

(s4)

Expressions for ϕ_i , θ_i , Δ , $C_{ND}^0(t_b)$ and $C_S^0(t_b)$ are,

$$C_{ND}^0(t_b) = (H_{ND} \otimes C_p)(t_b)$$

$$C_S^0(t_b) = (H_S \otimes C_p)(t_b)$$

$$\begin{cases} \phi_1 = \frac{K_1(\theta_1 - (1 - \partial)k_3 - k_4)}{\Delta} \\ \phi_2 = \frac{K_1(\theta_2 - (1 - \partial)k_3 - k_4)}{-\Delta} \\ \theta_1 = \frac{k_2 + (1 - \partial)k_3 + k_4 + \Delta}{2} \\ \theta_2 = \frac{k_2 + (1 - \partial)k_3 + k_4 - \Delta}{2} \\ \Delta = \sqrt{(k_2 + (1 - \partial)k_3 + k_4)^2 - 4k_2k_4} \\ H_{ND}(t) = \frac{K_1}{\Delta} ((\theta_1 - k_4)e^{-\theta_1 t} - (\theta_2 - k_4)e^{-\theta_2 t}) \\ H_S(t) = \frac{K_1 k_3}{\Delta} (-e^{-\theta_1 t} + e^{-\theta_2 t}) \end{cases}$$

where,

$$\partial = \begin{cases} 0, & t < t_b \\ \partial^{max}, & t \geq t_b \end{cases}$$

A.3 Numerical solution for the 2TCM

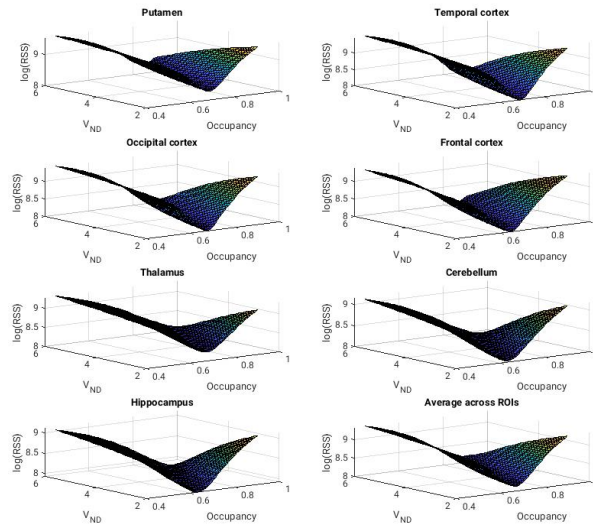
The Euler Forward Numerical solution for the 2TCM (i.e., equation s1) becomes

$$\begin{cases} C_{ND}(t_n) = hK_1 C_p(t_{n-1}) + \left(1 - h(k_2 + (1 - \partial(t_{n-1}))k_3)\right) C_{ND}(t_{n-1}) + hk_4 C_s(t_{n-1}) \\ C_s(t_n) = (1 - hk_4)C_s(t_{n-1}) + h(1 - \partial(t_{n-1}))k_3 C_{ND}(t_{n-1}) \end{cases} \quad (s5)$$

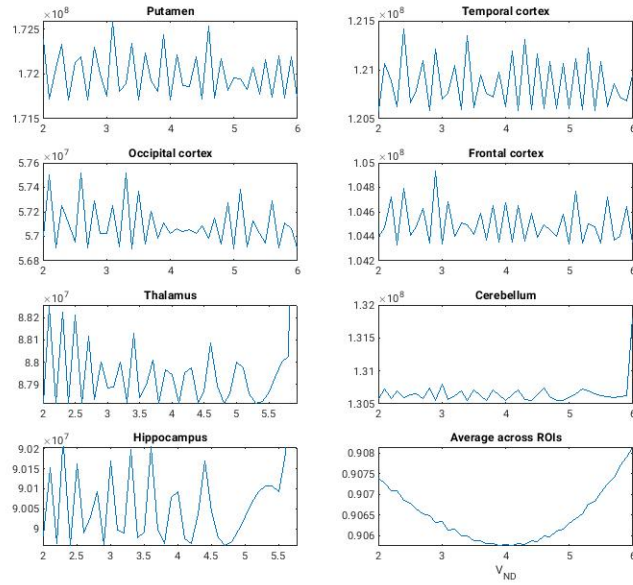
With the occupancy function $\partial(t)$ according to equation s2.

B. Rationale for simultaneously fitting several ROIs

As mentioned in the main text (section 2.1.4), the model parameters k_2 , $\partial(t)$, and BP_{ND} appear only as a ratio in the proposed model, and as a result, these parameters cannot be uniquely identified when the model is applied to a single TAC. This is illustrated in Supplementary figure 1, which shows surface plots of the model objective function for varying values for V_{ND} and occupancy, when the model is applied to each region separately. For all regions, there is a line of combinations of V_{ND} and occupancy that yield similarly low values of the objective function. Supplementary figure 2 shows the profile of the objective function through those lines. The profile does not have a clear global minimum for any of the regions. However, when all the profiles are combined, we get a clear minimum at $V_{ND} = 4$, which is the true value for V_{ND} in the simulations.



Supplementary figure 1: Objective function of model applied to a single TAC, plotted against V_{ND} and ∂^{max} (occupancy). ROIs are (left to right, top to bottom) putamen, temporal cortex, occipital cortex, frontal cortex, thalamus, cerebellum, and hippocampus. The final plot (bottom right) is the average across all ROIs.



Supplementary figure 2: Line profiles through the valleys of the objective functions in Supplementary figure 1. ROIs are (left to right, top to bottom) putamen, temporal cortex, occipital cortex, frontal cortex, thalamus, cerebellum, and hippocampus. The final plot (bottom right) is the average across all ROIs.

C. Implementation of models

All analyses were performed in Matlab (version 9.10). For both solutions to the model the fitting was run with a nested approach, where the outer layer function fitted the global parameters (∂^{max} , and V_{ND} for both solutions, t_e for the numerical solution, and t_s for the single step approximation). For each iteration of the outer function, the ROI-specific parameters (V_S , K_I and v_B) were fitted for each ROI separately. In both layers of the algorithm, lsqnonlin was used to fit the model to the data. ∂^{max} and v_B were constrained to be between 0 and 1. t_e and t_s were constrained to be higher than (after) t_b . All other parameters were constrained to be positive.

Matlab code for both models is freely available and can be found at <https://github.com/Gjertrud/ISI>.

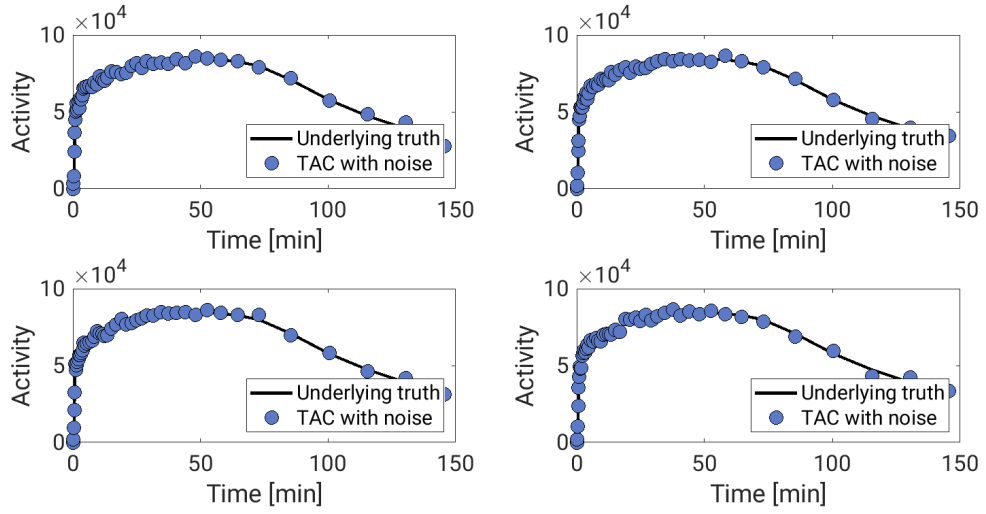
D. Blood and plasma analyses

The blood samples were centrifuged (2246xg for 7 min at 4°C), and the extracted plasma was filtered through a 0.45 µm syringe filter (Whatman GD/X 13 mm, Cytiva) and subsequently diluted 1:1 with 20 mM Phosphate buffer and 5 mM sodium-1-decanesulfonate pH 7.2 with 2% isopropanol. Samples were analysed in a fully automated column-switching HPLC system (UltiMate 3000, Thermo Fisher Scientific) connected to a radio-HPLC detector (PosiRam Model 4, LabLogic Systems).⁴ The HPLC system was equipped with a small extraction column (Shimpack MAYI-ODS 30x4.6 mm, Shimadzu Corporation) combined with an analytical column (Onyx Monolithic C18 50x4.6 mm, Phenomenex). The extraction mobile phase consisted of 100% of phosphate buffer (composition mentioned above), while the elution mobile phase consisted of 59% of 100 mM phosphate buffer and 2 mM sodium 1-decanesulfonate pH 2.6 and 41% methanol. Samples were injected in a volume of 4 mL, and the analysis was run at a flow of 5 mL/min at 25 °C. Total runtime for each sample was 8.55 min with a 4 min extraction step, 4 min elution step and 0.55 min of equilibration. Four eluate fractions were collected in 2 min intervals using a fraction collector (Foxy Jr FC144; Teledyne) and radioactivity subsequently measured using a gamma counter (Wizard 2480, Perkin Elmer). The parent tracer fraction was calculated as follow: % parent fraction = (radioactivity of parent eluate/total amount of collected radioactivity) x 100%.

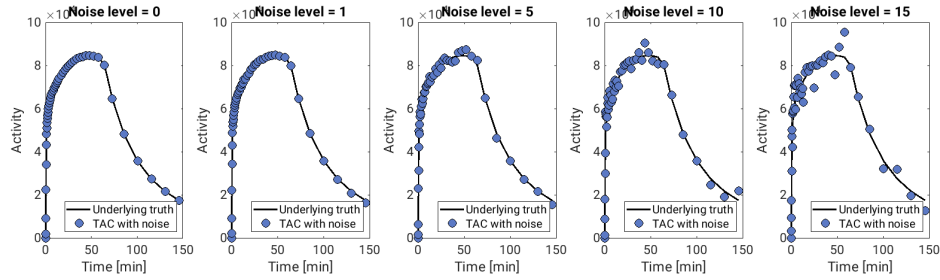
E. Supplementary results

E.1 Example of simulated data

The following two figures show examples of simulated TACs. In Supplementary figure 3, four different temporal cortex TACs from the same simulation experiment ($t_e = 30$ min, $\partial^{\max} = 50\%$, $\alpha = 5$) are shown. Supplementary figure 4 shows five simulated temporal cortex TACs with increasing noise for a simulated displacement scan with $t_e = 5$ and $\partial^{\max} = 75\%$.



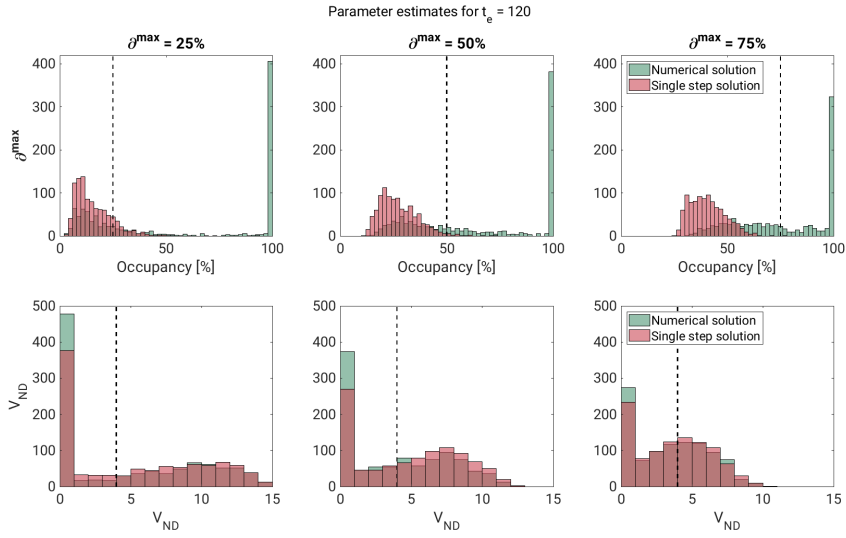
Supplementary figure 3: examples of four different simulated temporal cortex TACs for a displacement scan where 50% occupancy is reached 30 min after the intervention. The noise level (α) was 5.



Supplementary figure 4: examples of simulated temporal cortex TACs at five different noise levels ($\alpha = 0, 1, 5, 10$ & 15) for a displacement scan where 75% occupancy was reached after 5 min.

E.2 Results for simulated drug with $t_e = 120$

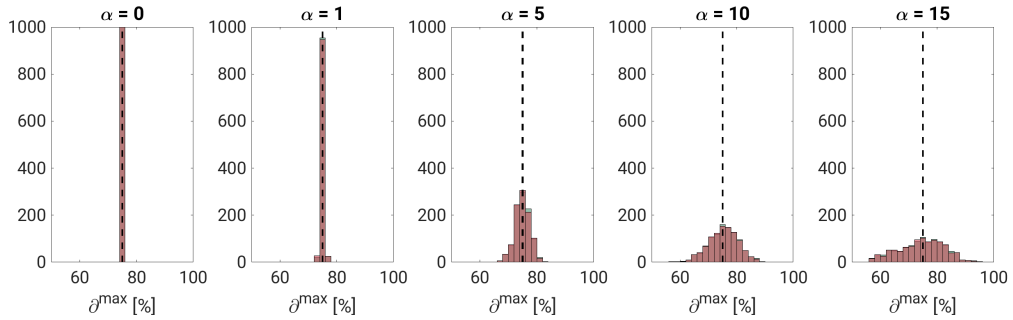
In the main text we show parameter estimates for displacement scans where full occupancy ($\hat{\rho}^{\max}$) was reached 5 or 30 minutes after the intervention. In addition, we simulated displacement TACs where full occupancy was reached after 120 minutes, i.e., 30 minutes after the end of the PET scan. The results from this experiment are illustrated in Supplementary figure 5, with $\hat{\rho}^{\max}$ estimates on the top row and V_{ND} estimates on the bottom row. For all occupancies, and both model solutions, the fitting generally failed. The single-step solution displays a tendency to underestimate $\hat{\rho}^{\max}$ (by approximately half). The numerical solution resulted in very wide distribution of $\hat{\rho}^{\max}$ estimates, frequently landing on the upper limit of 100%.



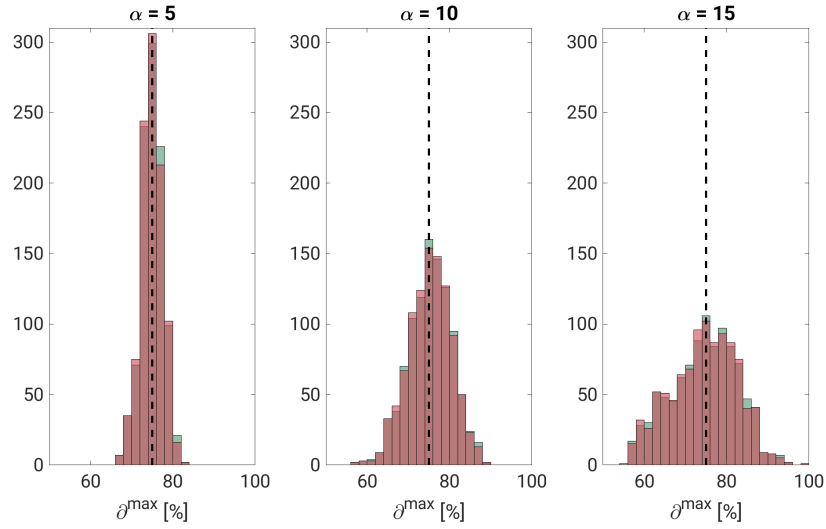
Supplementary figure 5: histograms of parameter estimates (occupancy (Δ), and V_{ND}) from a simulation experiment where full occupancy is reached after 120 minutes. The dashed lines represent the true parameter values.

E.3 Effect of noise on parameter estimates

The following figures show histograms of $\hat{\delta}^{\max}$ estimates from a simulation experiment with $\delta^{\max} = 75\%$ and $t_e = 5$ min, with increasing noise added to the TACs ($\alpha = 0, 1, 5, 10$ and 15). Supplementary figure 6 shows histograms for all five noise levels, and Supplementary figure 7 shows histograms for only the three highest noise levels ($\alpha = 5, 10$, and 15). At $\alpha = 0$ (no noise), both solutions consistently returned the true occupancy value. While the precision of the estimates deteriorated with increasing noise, the noise does not seem to induce bias.



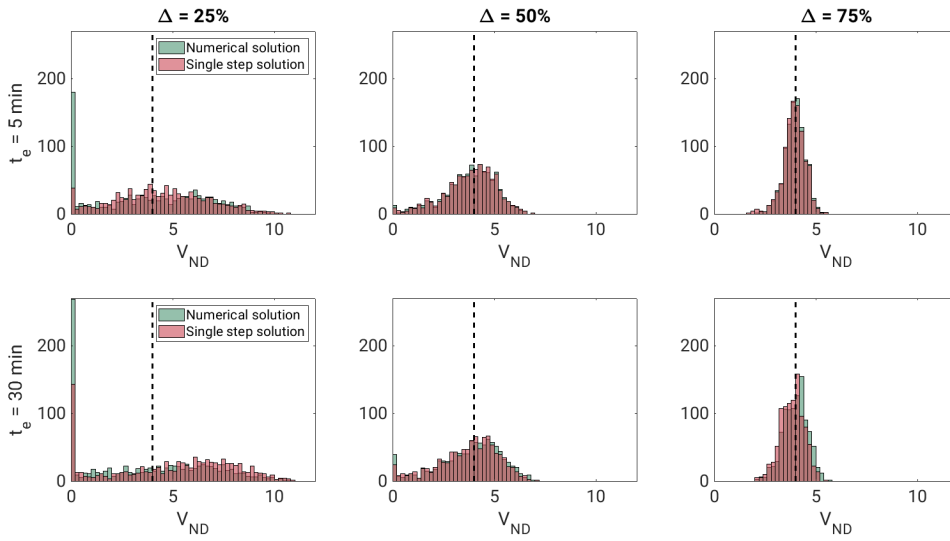
Supplementary figure 6: Histograms of occupancy estimates for increasing noise ($\alpha = 0, 1, 5, 10$ & 15). In all histograms, occupancy = 75% and $t_e = 5$ min.



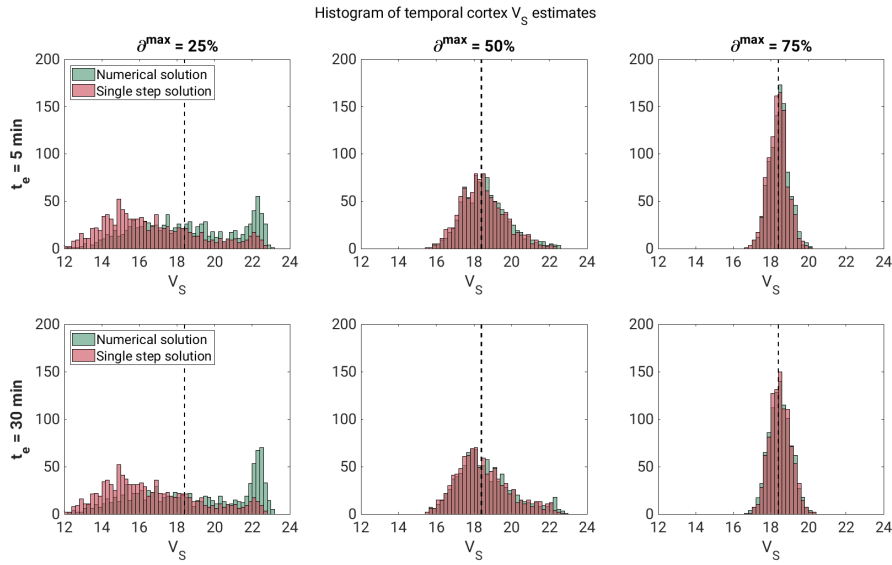
Supplementary figure 7: Histograms of occupancy estimates for increasing noise ($\alpha = 5, 10$ & 15). In all histograms, occupancy = 75% and $t_e = 5$ min.

E.4 Estimation of V_{ND} and V_T

The following figures show histograms of V_{ND} (Supplementary figure 8) and temporal cortex V_S (Supplementary figure 9), for $\delta^{\max} = 25\%$, 50% and 75% and $t_e = 5$ and 30 min, estimated with both solutions to the model.



Supplementary figure 8: Histograms of V_{ND} estimates from both the numerical solution (green) and single step solution (red), for $\delta^{\max} = 25\%$, 50% and 75% , and $t_e = 5$ and 30 min.



Supplementary figure 9: Histograms of temporal cortex V_S estimates from both the numerical solution (green) and single step solution (red), for $\delta^{\max} = 25\%$, 50% and 75% , and $t_e = 5$ and 30 min.

E.5 Correlation between parameter estimates

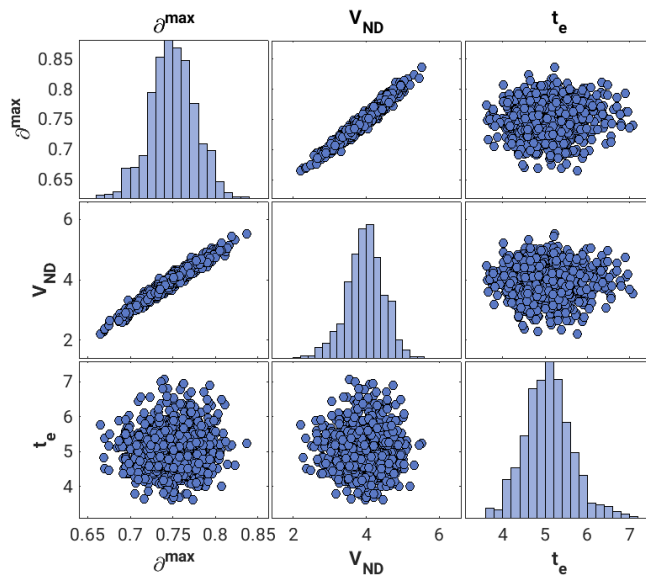
Supplementary tables 1 and 2 shows the Pearson correlation coefficients and corresponding p-values for all combinations of fitted parameters, for the numerical and single step solutions, respectively. Data from the simulations with $\delta^{\max} = 75\%$ and $t_e = 5$ min was used. For ROI-specific parameters (V_S , K_I and v_B) the temporal cortex estimates were used. Results were largely comparable between the two solutions. For the numerical solution only, scatter plots of all parameter estimates plotted against each other are presented in Supplementary figure 10 (for global parameters only) and Supplementary figure 11 (for all parameters). Again, in Supplementary figure 11, temporal cortex estimates were used for the ROI-specific parameters.

	∂^{max}	V_{ND}	t_e	V_S	K_I	v_B
∂^{max}		R = 0.98 P < 1e-100	R = 0.047 P = 0.13	R = -0.76 P < 1e-100	R = -0.15 P = 1.03e-6	R = 0.011 P = 0.74
V_{ND}	R = 0.98 P < 1e-100		R = -0.011 P = 0.74	R = -0.80 P < 1e-100	R = -0.12 P = 9.8e-5	R = 0.013 P = 0.68
t_e	R = 0.047 P = 0.13	R = -0.011 P = 0.74		R = -0.13 P = 2.2e-5	R = 0.062 P = 0.051	R = -0.051 P = 0.10
V_S	R = -0.76 P < 1e-100	R = -0.80 P < 1e-100	R = -0.13 P = 2.2e-5		R = 0.02 P = 0.47	R = 0.31 P < e-10
K_I	R = -0.15 P = 1.03e-6	R = -0.12 P = 9.8e-5	R = 0.062 P = 0.051	R = 0.02 P = 0.47		R = 0.57 P < 1e-10
v_B	R = 0.011 P = 0.74	R = 0.013 P = 0.68	R = -0.051 P = 0.10	R = 0.31 P < e-10	R = 0.57 P < 1e-10	

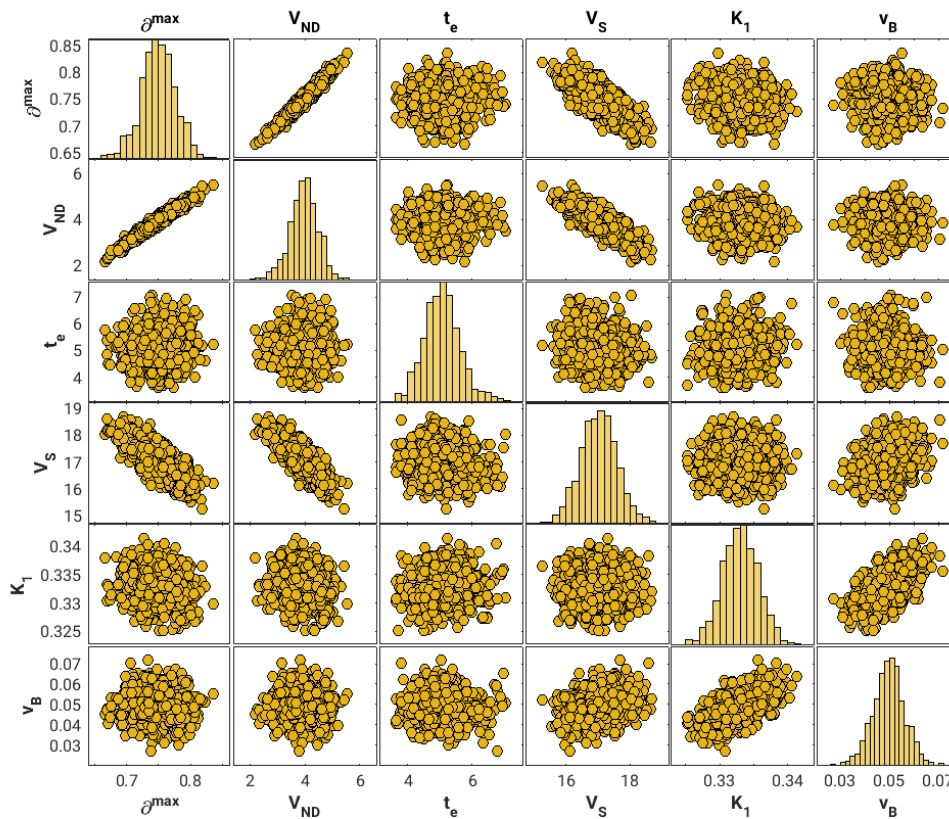
Supplementary table 1: correlation coefficients (R) and p-values (P) for the correlations for all parameters estimated with the numerical solution. Data is taken from the simulation experiment where 75% occupancy was reached after 5 min. For ROI-specific parameters (V_S , K_I and v_B), values for temporal cortex are used. Significant correlations are marked by green backgrounds.

	∂^{max}	V_{ND}	t_s	V_S	K_I	v_B
∂^{max}		R = 0.98 P < 1e-100	R = 0.024 P = 0.44	R = -0.75 P < 1e-100	R = -0.16 P = 5.8e-7	R = 0.012 P = 0.74
V_{ND}	R = 0.98 P < 1e-100		R = -0.029 P = 0.36	R = -0.79 P < 1e-100	R = -0.13 P = 6.3e-5	R = 0.014 P = 0.67
t_s	R = 0.024 P = 0.44	R = -0.029 P = 0.36		R = -0.13 P = 2.7e-5	R = 0.073 P = 0.020	R = -0.050 P = 0.12
V_S	R = -0.75 P < 1e-100	R = -0.79 P < 1e-100	R = -0.13 P = 2.7e-5		R = 0.020 P = 0.52	R = 0.32 P < 1e-10
K_I	R = -0.16 P = 5.8e-7	R = -0.13 P = 6.3e-5	R = 0.073 P = 0.020	R = 0.020 P = 0.52		R = 0.57 P < 1e-10
v_B	R = 0.012 P = 0.74	R = 0.014 P = 0.67	R = -0.050 P = 0.12	R = 0.32 P < 1e-10	R = 0.57 P < 1e-10	

Supplementary figure 10: correlation coefficients (R) and p-values for the correlations (P) for all parameters estimated with the single step solution. Data is taken from the simulation experiment where 75% occupancy was reached after 5 min. For ROI-specific parameters (V_S , K_I and v_B), values for temporal cortex are used. Significant correlations are marked by green backgrounds.



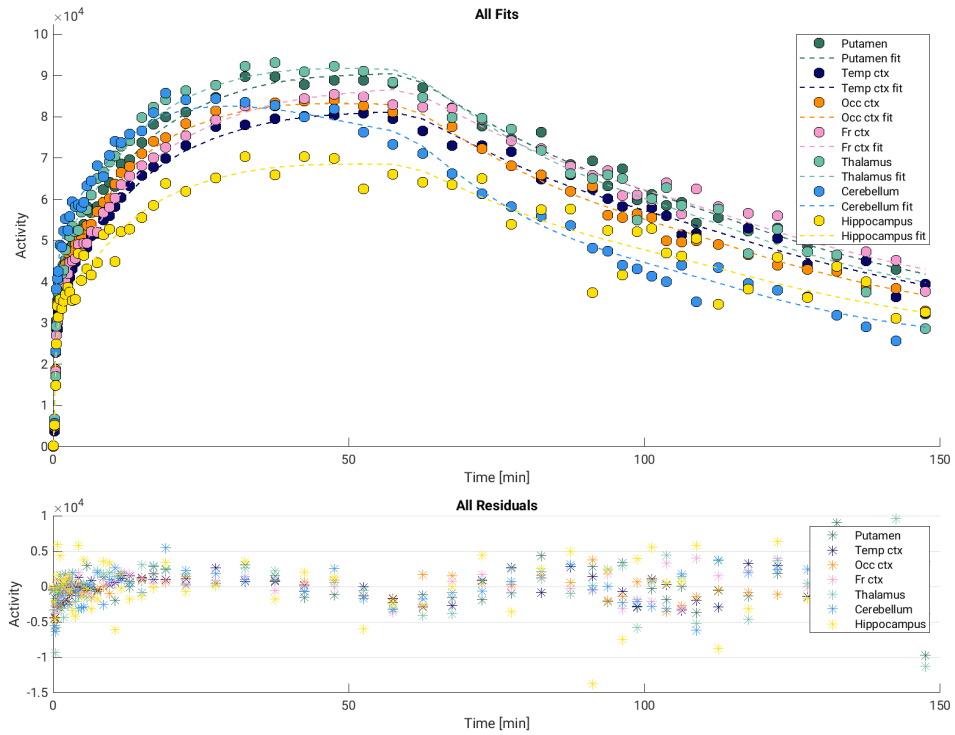
Supplementary figure 11: Scatter plots of all fitted global parameters plotted against each other. Parameters are estimated from the simulated data where $\delta^{\max} = 75\%$, and $t_e = 5$ min, using the numerical solution. On the diagonal, subplots display histograms of parameter estimates for each of the global parameters.



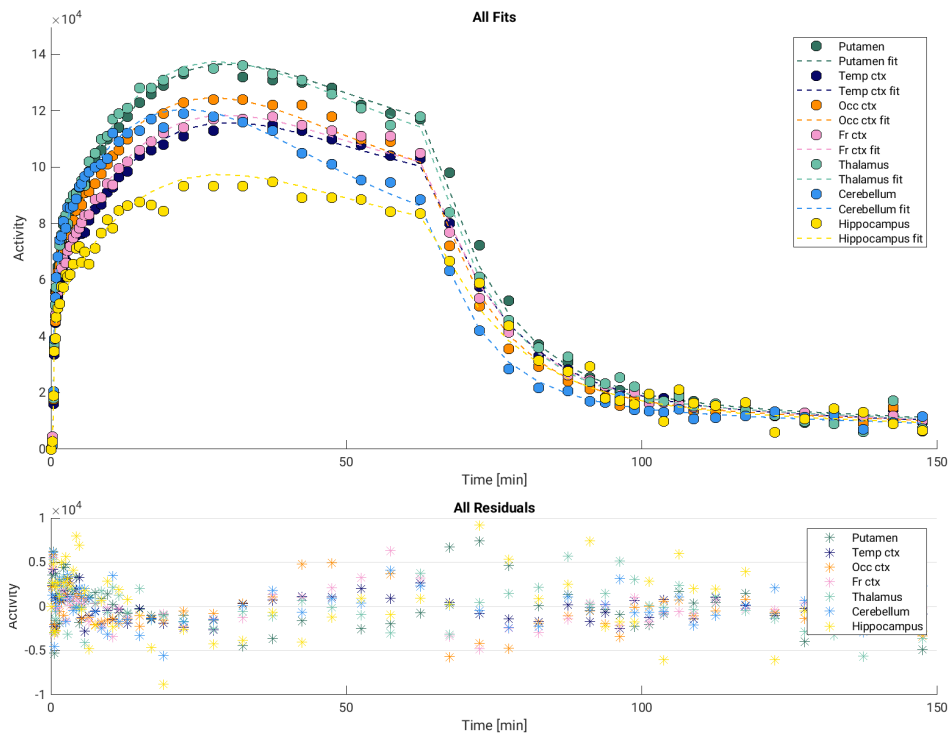
Supplementary figure 12: Scatter plots of all fitted parameters plotted against each other. Parameters are estimated from the simulated data where $\delta^{\max} = 75\%$, and $t_e = 5$ min, using the numerical solution. On the diagonal, subplots display histograms of parameter estimates for each of the parameters. For the ROI-specific parameters (V_S , K_1 and v_B) estimates for temporal cortex were used.

E.6 Residuals of model fits to pig data

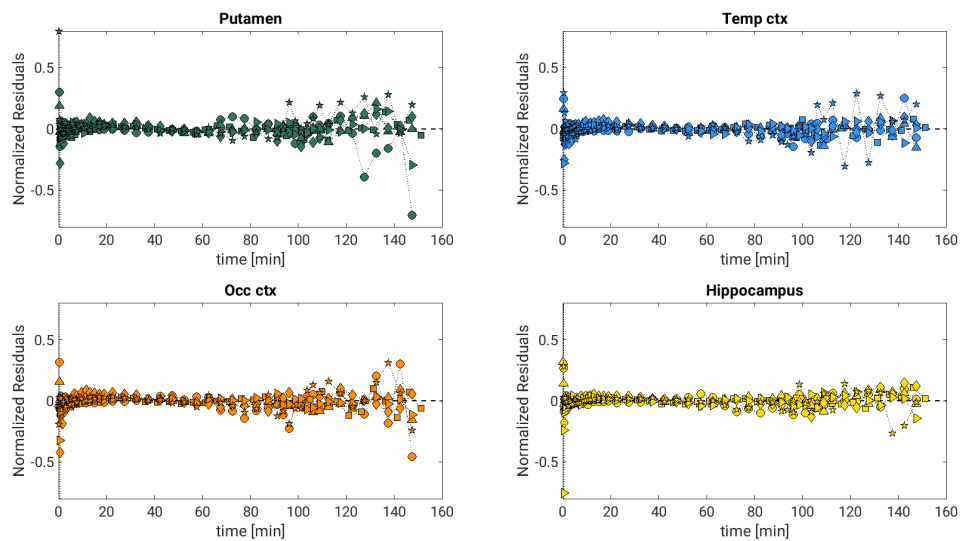
In the main text (Figure 3), we show the fits of both model solutions to temporal cortex TACs from two different pig scans with brivaracetam intervention at 60 min. Supplementary figures 13 and 14 show the model fit (numerical solution) to all included TACs in the same scans. These figures also show the residuals. In supplementary figure 15, normalized residuals for all six pig scans are shown, for putamen, temporal cortex, occipital cortex and hippocampus.



Supplementary figure 13: displacement model fits (numerical solution) to all included TACs from the pig displacement scan with the lowest brivaracetam dose (0.1 mg/kg), including residuals.



Supplementary figure 14: displacement model fits (numerical solution) to all included TACs from the pig displacement scan with the highest brivaracetam dose (5 mg/kg), including residuals.

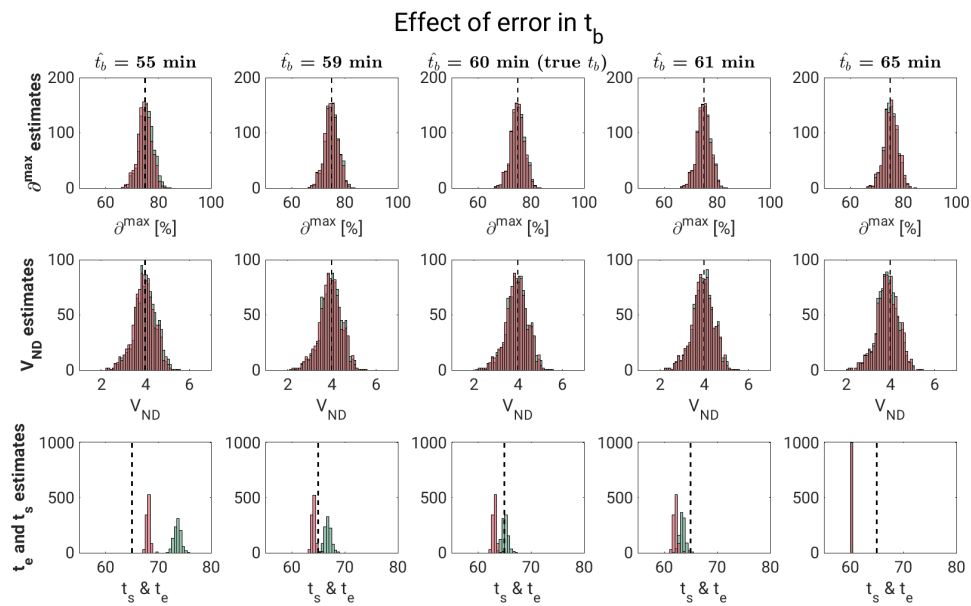


Supplementary figure 15: Normalized residuals from the model fits (numerical solution) for all six pig scans, for putamen, temporal cortex, occipital cortex and hippocampus. Each pig has a unique marker, which is consistent across the subplots. Residuals were normalized to the ROI C_T frame-by-frame.

E.7 Effect of t_b on parameter estimates

In the presented displacement model, t_b (the time of the intervention) is treated as a known parameter. In real life, the drug cannot enter the circulation instantaneously, but is typically injected over seconds-minutes. Also, there will be some delay between administration of drug, and drug reaching its brain target. Thus, choosing t_b is not trivial.

To investigate the effect of a badly defined t_b , we fitted the model to the simulated data where $\hat{\rho}^{\max} = 75\%$ and $t_e = 5$ min using different values for t_b . The data was simulated using $t_b = 60$ min. We solved the data with both the numerical and single step approaches, and t_b defined to be 55 min, 59 min, 60 min, 61 min and 65 min. The results are presented in Supplementary figure 16. Using a wrong t_b had minimal effect on both $\hat{\rho}^{\max}$ and V_{ND} estimates, and a big effect on t_e and t_s estimates.



Supplementary figure 16: The effect of wrongly defined t_b on parameter estimations. Histograms of $\hat{\rho}^{\max}$, V_{ND} , t_e (numerical solution) and t_s (single step solution) estimates for different values of t_b . The true t_b was 60 min. Estimates from the numerical solution are shown in green, and estimates from the single step solution are shown in red.

F. References for the supplementary material

1. Innis RB, Cunningham VJ, Delforge J, et al. Consensus Nomenclature for in vivo Imaging of Reversibly Binding Radioligands. *Journal of Cerebral Blood Flow & Metabolism* 2007; 27: 1533–1539.
2. Slifstein M, Laruelle M. Models and methods for derivation of in vivo neuroreceptor parameters with PET and SPECT reversible radiotracers. *Nuclear Medicine and Biology* 2001; 28: 595–608.
3. Gunn RN, Gunn SR, Cunningham VJ. Positron Emission Tomography Compartmental Models. *Journal of Cerebral Blood Flow & Metabolism* 2001; 21: 635–652.
4. Gillings N. A restricted access material for rapid analysis of [(11)C]-labeled radiopharmaceuticals and their metabolites in plasma. *Nucl Med Biol* 2009; 36: 961–965.

DERIVATION OF THE LEA LOG-LIKELIHOOD FUNCTION

Likelihood Estimation of Affinity (LEA), a maximum likelihood based estimator for calculation of IC_{50} , Δ_{max} and V_{ND} was introduced in Paper II. LEA is an extension of Likelihood Estimation of Occupancy (LEO), which also incorporates the assumptions of the Emax model, and estimates global drug interaction parameters from the V_T values of a complete baseline-block dataset in a single step.

LEA, like LEO, assumes that the errors in V_T are normally distributed, and that the magnitude of the error is the same in the baseline and block scans. Therefore, the probability density function of one subject's baseline and block V_T s in one ROI, will be given by,

$$\begin{aligned} f(V_T^{\text{baseline}} | V_{ND}, V_S) &= \frac{1}{\sqrt{2\pi\sigma^2}} e^{-\frac{(V_T^{\text{baseline}} - (V_{ND} + V_S))^2}{2\sigma^2}} \\ f(V_T^{\text{block}} | V_{ND}, V_S, \Delta) &= \frac{1}{\sqrt{2\pi\sigma^2}} e^{-\frac{(V_T^{\text{block}} - (V_{ND} + (1-\Delta)V_S))^2}{2\sigma^2}}, \end{aligned} \quad (26)$$

where σ^2 is the variance of V_T .

The likelihood function, \mathcal{L} , summarizes the evidence in the measured data about the parameters we aim to estimate. We can think of it as a surface, whose peak will indicate the combination of parameter estimates that maximizes the likelihood of the observed data. Conceptually, the likelihood function is not the same as the probability density function. The first is a function of the parameters, and the latter is a function of the data. However, algebraically, they are identical, so $f(V_T^{\text{baseline}} | V_{ND}, V_S) = \mathcal{L}(V_{ND}, V_S | V_T^{\text{baseline}})$.

The joint likelihood function for the baseline and block data will be the product of the two likelihood functions. For the simplified case presented in Equation 26 the likelihood function for V_S , V_{ND} and Δ , given the measured baseline and block V_T s will be given by:

$$\begin{aligned} \mathcal{L}(V_S, V_{ND}, \Delta | V_T^{\text{baseline}}, V_T^{\text{block}}) &= f(V_T^{\text{baseline}} | V_{ND}, V_S) \cdot f(V_T^{\text{block}} | V_{ND}, V_S, \Delta) \\ &= \frac{1}{\sqrt{2\pi\sigma^2}} e^{-\frac{(V_T^{\text{baseline}} - (V_{ND} + V_S))^2}{2\sigma^2}} e^{-\frac{(V_T^{\text{block}} - (V_{ND} + (1-\Delta)V_S))^2}{2\sigma^2}} \\ &= \frac{1}{\sqrt{2\pi\sigma^2}} e^{-\frac{(V_T^{\text{baseline}} - V_{ND} - V_S)^2 - (V_T^{\text{block}} - V_{ND} - (1-\Delta)V_S)^2}{2\sigma^2}}. \end{aligned} \quad (27)$$

This is the LEO likelihood function for one region. In LEA, LEO is extended by including the Emax model. Thus, the likelihood function

becomes a function of IC_{50} and Δ_{max} , instead of Δ . For our simplified case, the likelihood function becomes,

$$\begin{aligned} \mathcal{L}(V_S, V_{ND}, IC_{50}, \Delta_{max} | V_T^{baseline}, V_T^{block}, C_P) \\ = \frac{1}{\sqrt{2\pi\sigma^2}} e^{-\frac{(V_T^{baseline} - V_{ND} - V_S)^2 - (V_T^{block} - V_{ND} - (1 - \frac{\Delta_{max} C_P}{C_P + IC_{50}}) V_S)^2}{2\sigma^2}} \end{aligned} \quad (28)$$

If we extend the simplified case by including several ROIs, the probability density functions for one person's baseline and block V_T values would be given by,

$$\begin{aligned} f(V_T^{baseline} | V_{ND}, V_S) &= \frac{1}{\sqrt{2\pi|\Sigma|}} e^{-\frac{1}{2} A^T \Sigma^{-1} A} \\ f(V_T^{block} | V_{ND}, V_S, \Delta_{max}, IC_{50}) &= \frac{1}{\sqrt{2\pi|\Sigma|}} e^{-\frac{1}{2} B^T \Sigma^{-1} B} \end{aligned} \quad (29)$$

where $A = V_T^{baseline} - (V_{ND} \mathbf{1} + V_S)$,
and $B = V_T^{block} - \left(V_{ND} \mathbf{1} + \left(1 - \frac{\Delta_{max} C_P}{C_P + IC_{50}} \right) V_S \right)$.

Σ is the covariance matrix of the V_T data. $V_T^{baseline}$, V_T^{block} , and V_S are $k \times 1$ arrays for k ROIs. $\mathbf{1}$ is a $k \times 1$ array of ones.

The joint LEA likelihood function for one subject is the product of the two probability density functions,

$$\begin{aligned} \mathcal{L}(V_S, V_{ND}, IC_{50}, \Delta_{max} | V_T^{baseline}, V_T^{block}, C_P) \\ = \frac{1}{2\pi|\Sigma|} e^{-\frac{1}{2} [A^T \Sigma^{-1} A + B^T \Sigma^{-1} B]} \end{aligned} \quad (30)$$

where A and B are defined as in Equation 29.

Usually, the natural logarithm of the likelihood function is easier to differentiate, but the maximum value will occur at the same coordinates. The LEA log-likelihood for one subject is obtained by taking the natural logarithm of Equation 30, resulting in,

$$\begin{aligned} l(V_S, V_{ND}, IC_{50}, \Delta_{max} | V_T^{baseline}, V_T^{block}, C_P) \\ = \ln \left(\frac{1}{2\pi|\Sigma|} \right) - \frac{1}{2} [A^T \Sigma^{-1} A + B^T \Sigma^{-1} B]. \end{aligned} \quad (31)$$

Again, A and B are defined in Equation 29. Constant terms in Equation 31 will not affect the coordinates of the maximum, and can therefore be excluded without affecting the optimization. Without constant terms, the LEA log-likelihood for one subject becomes,

$$\begin{aligned} l(V_S, V_{ND}, IC_{50}, \Delta_{max} | V_T^{baseline}, V_T^{block}, C_P) \\ = \left(V_T^{baseline} - (V_{ND} \mathbf{1} + V_S) \right)^T \Sigma^{-1} \left(V_T^{baseline} - (V_{ND} \mathbf{1} + V_S) \right) \\ + \left(V_T^{block} - \left(V_{ND} \mathbf{1} + \left(1 - \frac{\Delta_{max} C_P}{C_P + IC_{50}} \right) V_S \right) \right)^T \Sigma^{-1} \\ \left(V_T^{block} - \left(V_{ND} \mathbf{1} + \left(1 - \frac{\Delta_{max} C_P}{C_P + IC_{50}} \right) V_S \right) \right). \end{aligned} \quad (32)$$

By combining the log-likelihood functions from all subjects, LEA can summarize all the evidence in the measured data about the underlying parameter values. The joint probability density function is the product of all the separate functions. In the log-domain this equates to summarizing all the log-likelihood functions. Thus, for a dataset of N subjects, the LEA log-likelihood function is given by,

$$\begin{aligned}
& \mathcal{L}(\text{IC}_{50}, \Delta_{\text{max}}, V_{\text{ND},1}, V_{\text{ND},2}, \dots, V_{\text{ND},N}, \mathbf{V}_{\text{S},1}, \mathbf{V}_{\text{S},2}, \dots, \mathbf{V}_{\text{S},N} \mid \\
& \mathbf{V}_{\text{T},1}^{\text{baseline}}, \mathbf{V}_{\text{T},2}^{\text{baseline}}, \dots, \mathbf{V}_{\text{T},N}^{\text{baseline}}, \mathbf{V}_{\text{T},1}^{\text{block}}, \mathbf{V}_{\text{T},2}^{\text{block}}, \dots, \mathbf{V}_{\text{T},N}^{\text{block}}, \\
& C_{\text{P},1}, C_{\text{P},2}, \dots, C_{\text{P},N}) \\
&= \sum_{j=1}^N \left[\left(\mathbf{V}_{\text{T},j}^{\text{baseline}} - (V_{\text{ND},j} \mathbf{1} + \mathbf{V}_{\text{S},j}) \right)^{\text{T}} \Sigma^{-1} \left(\mathbf{V}_{\text{T},j}^{\text{baseline}} - (V_{\text{ND},j} \mathbf{1} + \mathbf{V}_{\text{S},j}) \right) \right. \\
& \quad + \left(\mathbf{V}_{\text{T},j}^{\text{block}} - \left(V_{\text{ND},j} \mathbf{1} + \left(1 - \frac{\Delta_{\text{max}} C_{\text{P},j}}{C_{\text{P},j} + \text{IC}_{50}} \right) \mathbf{V}_{\text{S},j} \right) \right)^{\text{T}} \Sigma^{-1} \\
& \quad \left. \left(\mathbf{V}_{\text{T},j}^{\text{block}} - \left(V_{\text{ND},j} \mathbf{1} + \left(1 - \frac{\Delta_{\text{max}} C_{\text{P},j}}{C_{\text{P},j} + \text{IC}_{50}} \right) \mathbf{V}_{\text{S},j} \right) \right) \right].
\end{aligned} \tag{33}$$

$V_{\text{ND},j}$ is the estimated V_{ND} for subject j . $\mathbf{V}_{\text{T},j}^{\text{baseline}}$ and $\mathbf{V}_{\text{T},j}^{\text{block}}$ are $k \times 1$ arrays of k baseline and block V_{T} values for subject j . $C_{\text{P},j}$ is the block-scan plasma drug concentration for subject j .

The dimensionality of the LEA log-likelihood function can be reduced by solving $\frac{\partial}{\partial \mathbf{V}_{\text{S},j}} \mathcal{L} = 0$. By substituting the resulting expression for $\mathbf{V}_{\text{S},j}$ into the LEA log-likelihood function (Equation 33), it becomes a function of $N + 2$ parameters for a dataset of N subjects. That expression for $\mathbf{V}_{\text{S},j}$ is,

$$\mathbf{V}_{\text{S},j} = \frac{\mathbf{V}_{\text{T},j}^{\text{baseline}} - V_{\text{ND},j} \mathbf{1} + \left(1 - \Delta_{\text{max}} \frac{C_{\text{P},j}}{C_{\text{P},j} + \text{IC}_{50}} \right) \left(\mathbf{V}_{\text{T},j}^{\text{block}} - V_{\text{ND},j} \mathbf{1} \right)}{1 + \left(1 - \Delta_{\text{max}} \frac{C_{\text{P},j}}{C_{\text{P},j} + \text{IC}_{50}} \right)^2}. \tag{34}$$

GJERTRUD LOUISE LAURELL

gjertrudlaurell@gmail.com

<https://orcid.org/0000-0003-1002-0155>

<https://github.com/Gjertrud>

<https://www.researchgate.net/profile/Gjertrud-Louise-Laurell>